

THEORETICAL  
AND MATHEMATICAL PHYSICS

On the Delay Time of the Total Signal  
from a Set of Transmitters

N. S. Bukhman

Samara State Academy of Architecture and Civil Engineering, 443001 Samara, Russia

e-mail: buhman@ssaba.smr.ru

Received April 15, 2004

**Abstract**—The time dependence of the total signal from a group of closely spaced acoustic or electromagnetic transmitters radiating the same (up to an amplitude factor) signals is considered. If the duration of the partial signal is sufficiently long, the time dependence of the signal from the set of transmitters turns out to be close to that of the signal from a single transmitter up to a delay time. This delay does not necessarily coincide with the time it takes for an optical (or acoustic) signal to pass from the transmitters to the observation point. At different points of the space, this delay time may exceed, or be shorter than, the light (sound) delay time and also may be positive or negative. This follows from the backward or forward extrapolation of the time dependence of the signal when variously delayed and attenuated copies of the same signal that are produced by different transmitters are added up (i.e., interfere). One result of such an extrapolation, which arises upon transmitting a signal with its leading or trailing edge cut off, is the reconstruction of its time dependence, i.e., the detection of the nontransmitted part of the signal. © 2005 Pleiades Publishing, Inc.

INTRODUCTION

It is known that the solution of the problem of excitation of electromagnetic or acoustic waves by given sources in a homogeneous medium reduces to the solution of the inhomogeneous scalar wave equation with an appropriate right-hand side [1–3]. In particular, for the scalar potential  $\phi(x, y, z, t)$  of a time-dependent point charge  $de(t)$  located at the origin ( $\mathbf{R} = 0$ ), we have the equation [1]

$$\Delta\phi - \frac{1}{c^2} \frac{\partial^2 \phi}{\partial t^2} = -4\pi de(t)\delta(\mathbf{R}), \quad (1)$$

whose solution (the delayed potential) is well known:

$$\phi(t) = de(t - R/c)/R. \quad (2)$$

Similar relations hold for any component of the vector potential of an electromagnetic field, for Hertzian electric and magnetic vectors, for the pressure and density of a medium in a sound wave, etc. The physical meaning of the delayed potentials is straightforward: the time dependence of the potential at given point  $\phi(\mathbf{r}, t)$  of the space copies the time behavior of source  $de(t)$  with delay  $R/c$  corresponding to the time it takes for the signal to propagate from the source to the observation point. In electrodynamics, an isolated point electric charge cannot vary in time (otherwise, the charge conservation law would be violated). Nevertheless, the field produced by an arbitrary system of moving charges can be represented as a superposition of delayed potentials of type (2) [1].

A solution to Eq. (1) with an arbitrary right-hand side can be written as a superposition (i.e., as a finite,

discrete, or integral sum) of delayed potentials (2). In particular, the total potential of  $n$  point sources  $de_i(t) = q_i\phi_0(t)$  ( $i = 1, 2, \dots, n$ ) that have the same time behavior  $\phi_0(t)$  and differ from each other only by amplitude  $q_i$  and location (at points  $\mathbf{r}_i$ ) has the form

$$\phi(\mathbf{r}, t) = \sum_{i=1}^n (q_i/R_i)\phi_0(t - R_i/c), \quad (3)$$

where  $R_i = |\mathbf{r} - \mathbf{r}_i|$  is the distance between an  $i$ th source and the observation point  $\mathbf{r}$ .

Consider total field (3) of a set of closely spaced charges located near the origin. If  $T$  is the characteristic duration of the signal, the proximity condition for the transmitters (time-variable charges) can be written in the form  $\Delta t_{ij} \ll T$ , where  $\Delta t_{ij} \equiv |\mathbf{r}_i - \mathbf{r}_j|/c$  ( $i, j = 1, 2, \dots, n$ ) are the “intrinsic” delays of the system.<sup>1</sup> It is clear that, with this condition being fulfilled, the time dependence of the total field of the set of transmitters differs, to a first approximation, from the general time behavior  $\phi_0(t)$  of individual transmitters only by some delay time  $\tau$  that is dependent on the location of the observation point  $\mathbf{r}$ . It would be reasonable to expect that this delay time falls into the interval of the delays of the signals from individual transmitters,  $\Delta t_i = R_i/c$  ( $i = 1, 2, \dots, n$ ); i.e.,  $0 < \min_{i=1, \dots, n} \Delta t_i \leq \tau \leq \max_{i=1, \dots, n} \Delta t_i$ . In particular, under the condition  $r_i \ll r$  ( $i = 1, 2, \dots, n$ ), when these

<sup>1</sup> In this paper, we restrict our consideration to non-quasi-monochromatic (real) signals. The delay time of the complex envelope of a superposition of quasi-monochromatic signals is studied in [4].

delays are almost equal to each other ( $\Delta t_i = R_i/c \approx r/c$ ) and long compared with the intrinsic delays  $\Delta t_{ij}$ , one may suppose that time dependence  $\phi_0(t - r/c)$ , which regards the delay of a signal propagating from a group of closely spaced sources to the observation point, will be asymptotically exact. However, the analysis given below demonstrates that this supposition turns out to be erroneous in many cases; i.e., the delay time of the total signal may differ from (either exceed or be less than) “optical” (or, in acoustics, “sound”) delay time  $r/c$  by a value that is considerably higher than any “intrinsic” delay time  $\Delta t_{ij}$ .

## 1. GENERAL RELATIONS

First, we introduce (for now, formally) effective delay time  $\tau$  of the total signal from a set of transmitters. Let  $f_i = q_i/R_i$  be the field amplitude and  $\Delta\tau_i = \Delta t_i - \tau$  be the extra delay (an increment to the effective delay time) of the signal from an  $i$ th transmitter at a certain point in the space. Expanding the terms on the right of (3) into the Taylor series in parameter  $\Delta\tau_i$ , one can easily transform (3) to

$$\phi(\mathbf{r}, t) = f \left[ \sum_{k=0}^{\infty} \frac{(-1)^k}{k!} \phi_0^{(k)}(t - \tau) \beta_k \right], \quad (4)$$

where

$$f = \sum_{i=1}^n f_i, \quad \beta_k = \sum_{i=1}^n f_i \Delta\tau_i^k / f. \quad (5)$$

It is seen that (4) is the expansion of function  $\phi(\mathbf{r}, t)$  in powers of small parameters  $\Delta\tau_i/T$  ( $i = 1, \dots, n$ ). The zeroth-order term of this expansion has the form  $f\phi_0(t - \tau)$  and differs from initial time dependence  $\phi_0(t)$  of the signal only in amplitude factor  $f$  and as yet uncertain delay time  $\tau$ . The other terms in expansion (4) describe the  $\tau$ -dependent deviation of the total signal from the approximation  $f\phi_0(t - \tau)$ . The linear (in parameters  $\Delta\tau_i/T$ ) part of this deviation vanishes if the parameter

$$\tau = \left( \sum_{i=1}^n f_i \Delta t_i \right) / \left( \sum_{i=1}^n f_i \right) \quad (6)$$

is taken as the delay time of the total signal.

In this case,  $\beta_1 = 0$  and the error of approximation  $f\phi_0(t - \tau)$  is of the second order of smallness in  $\Delta\tau_i/T$  rather than of the first order as in the case of arbitrary  $\tau$ . Thus, in the general case, the approximation error

$$\phi(t) \approx f\phi_0(t - \tau) \quad (7)$$

is on the order of  $(\Delta\tau_i/T)^2$  ( $i = 1, 2, \dots, n$ ) in view of (5) and (6). In other words, as the signal duration increases, the approximation error infinitely decreases compared both with the signal itself (the order is one) and with the

deviation of delayed signal  $\phi_0(t - \tau)$  from undelayed one  $\phi_0(t)$  (the order is  $\Delta\tau_i/T$ ). This comes as no surprise, since it is easy to check that, in view of (5) and (6), the right-hand side of (3) can be viewed as a linear interpolation formula for the right-hand side of (7); i.e., in this case, the interference of several variously delayed copies of the same signal results in a “nonanthropogenic” interpolation of the time dependence of the signal. One can also verify that the result obtained corresponds (in terms of frequency) to the group delay approximation (the first order of the classical dispersion theory [2, 5, 6]) and, therefore, has all the merits and disadvantages of this approximation.

It is essential that, according to formula (6), the delay time  $\tau$  of the total signal may be positive, negative, or equal to zero, depending on the amplitude ratio and the arrangement of point transmitters. The last-listed case is rather specific and is hereafter called “degenerate.”

Thus, at least in the linear approximation, total signal (3) differs from the initial one only in amplitude factor (5) and delay time (6).

It is easily seen that the accuracy of approximation (7) can be improved. Provided that the conditions  $\beta_2 = \beta_3 = \dots = \beta_r = 0$  ( $r \geq 2$ ) hold, approximation (7) has an error of order  $(\Delta\tau_i/T)^{r+1}$  (i.e., instead of the moving linear interpolation (or extrapolation) of the signal, the right-hand side of (3) accomplishes moving interpolation (or extrapolation) of order  $r$ ). In terms of frequency, this situation means that the leading (up to order  $r$ , inclusive) corrections of the classical dispersion theory [2, 6] vanish. Let us analyze the time delay at various points of the space.

## 2. A GROUP OF POINT SOURCES IN AN ABSORPTION-FREE MEDIUM (NONDEGENERATE CASE)

Let us turn back to the simplest case, which we have started with, namely, a set of point transmitters in a nonabsorbing medium. Here, instead of (5) and (6), we have

$$f = \sum_{i=1}^n (q_i/R_i), \quad \tau = \left( \sum_{i=1}^n q_i \right) / (cf). \quad (8)$$

In this section, we consider the case of the nonzero total charge of the system, when the delay time of the total signal is other than zero (see (8)) and different at various points of the space ( $\tau \neq 0$ , which is the nondegenerate case in terms of the previous section). Note at once that this case cannot take place in electrodynamics, since electromagnetic radiation is always “at least” of the dipole nature. Therefore, we use the acoustic terminology [3] and treat  $q_i$  as the volume velocities of sound sources and  $c$  as the sound velocity in a given medium.

We will examine the simplest case of two point sources  $q_1$  and  $q_2$  (Fig. 1). Figure 1 (which corresponds to the volume velocities  $q_1 = 1$  and  $q_2 = -2$  of point acoustic transmitters that are  $d = 1$  apart) shows the coordinate system ( $Oxyz$ ) used below, as well as the delay time of the total signal ( $\tau$ , the thick line) and the delays of the partial signals coming from the first and second transmitters (the thin line) at various points of the abscissa. Here, instead of (8), we have

$$f = q_1/R_1 + q_2/R_2, \quad \tau = (q_1 + q_2)/(cf). \quad (9)$$

It is easy to check that, if the volume velocities are of the same sign ( $q_1 q_2 > 0$ ), the delay time of the total signal at any point of the space has a value intermediate between the delays of the signals from the first and second transmitters,  $\Delta t_{1,2} = R_{1,2}/c$ . Of greater interest is the case where the volume velocities are of opposite signs ( $q_1 q_2 < 0$ ). Then, depending on the magnitude and sign of the delay of the total signal, the whole space is subdivided into three domains by two surfaces, namely, by the “sphere of infinite delay times” (on which  $\tau = \infty$ ), which is centered at point  $x_c = [d(1 + \delta^2)]/[2(1 - \delta^2)]$  ( $\delta \equiv -q_1/q_2$ ,  $0 < \delta < 1$ ) and has radius  $R = (d\delta)/(1 - \delta^2)$ , and the “plane of equal delay times”  $x = 0$ , on which  $\Delta t_1 = \Delta t_2 = \tau$ . The former intersects the abscissa at points  $x_1 = (d/2)(1 - \delta)/(1 + \delta)$  and  $x_2 = (d/2)(1 + \delta)/(1 - \delta)$  (Fig. 1). A transmitter that is smaller in magnitude (in our case,  $q_1$ ) is inside this sphere, while the greater one ( $q_2$ ) is outside. Straight lines  $x = x_{1,2}$  are vertical asymptotes to the plot of function  $\tau(x, 0, 0)$  depicted in Fig. 1.

Inside the sphere of infinite delay times, the delay time is negative ( $\tau < 0$ , and, at any point inside this sphere, the total signal detected attains a maximum earlier than transmitted signal  $\phi(t)$ ). The rest of the space is subdivided into two parts by plane  $x = 0$ . In half-space  $x < 0$ , the delay time is positive, while smaller than the delays of the signals coming from transmitters 1 and 2 (i.e., in this “domain of advance,”  $0 < \tau < \Delta t_{1,2}$ ). In half-space  $x > 0$ , conversely, the delay time is greater than the delays of the signals from transmitters 1 and 2 (i.e., in this “domain of lag,”  $\tau > \Delta t_{1,2}$ ).

When the observation point approaches the sphere of infinite delay times from the inside, the delay time of the total signal tends to  $-\infty$ ; otherwise, it tends to  $+\infty$ .

When the observation point is infinitely far away from the set of transmitters ( $r \rightarrow \infty$ ), it follows from (9) that  $\tau \rightarrow (r/c) + (d/2c)((1 + \delta)/(1 - \delta))\cos(\theta)$ , where  $\theta$  is the angle between the abscissa and the direction towards the observation point. One can easily verify that such a delay corresponds to the signal emitted from the point  $x_0 = -(d/2)(1 + \delta)/(1 - \delta) = -x_2$  that is located to the left of point  $q_2$ . This point, together with corresponding asymptotes to curves  $\tau(x, 0, 0)$ , is shown in Fig. 1 (the dashed lines). It is clear that the point  $x_0$  of the “imaginary source” is nothing else than the “center of mass” of the set of two transmitters  $q_1$  and  $q_2$  ( $x_0 = (d/2)q_1/(q_1 + q_2) + (-d/2)q_2/(q_1 + q_2)$ ). Since one of

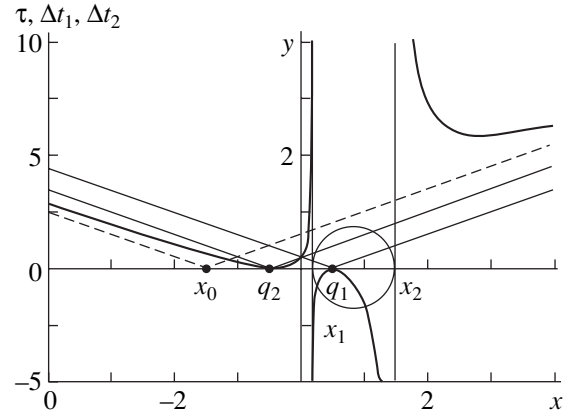


**Fig. 1.** Geometry of the problem. The space is partitioned into the domain of negative delay times (the interior of the sphere, which contains transmitter  $q_1$ ), the domain of advance (the left half-space), and the domain of lag (the right half-space except for inner and boundary points of the sphere of negative delay times). The delay time is plotted against the position of the observation point, which is located on the abscissa. The thick line shows the delay time  $\tau(x)$  of the total signal; the thin solid lines, the delay times of the signals from individual point transmitters ( $\Delta t_1$  for  $q_1$  and  $\Delta t_2$  for  $q_2$ ); and the dashed lines, the delay time of the signal from imaginary point transmitter  $x_0$ .

these “masses” is negative (in our case,  $q_2$ ), the center of mass is located outside of this system.

Thus, far away from the set of transmitters ( $r \rightarrow \infty$ ), both the time dependence and the directional pattern of the total signal approximately coincide, in the nondegenerate case, with those of the imaginary point source located outside the set of transmitters. If  $\delta \rightarrow 1$  (i.e., when approaching the degenerate case), the distance between the set of transmitters and this “imaginary” transmitter may be as larger as desired than the size of the transmitting system ( $|x_0|/d \rightarrow \infty$ ). This means that passive location of an “almost dipole” set of transmitters may lead to incorrect conclusions about its position; moreover, the distance between the true and apparent positions of the system may greatly exceed the size of the system itself.<sup>2</sup> The same is also valid for

<sup>2</sup> Here, we are dealing both with “instrumental” methods of locating a sound source and with “aural” location (which is based on the subconscious analysis of the time shift between the signals arriving at the right and left ears, the so-called binaural effect). This means that, given two spatially separated sound sources, it is basically possible (of course, at the expense of a more or less significant loss in power) to produce the effect that the sound comes from any other point that is located sufficiently far away from the real sound sources. With the superposition principle (i.e., the possibility of simultaneously transmitting several “pairs” of signals from two real transmitters with different positions of the “dummy” source) taken into consideration, this implies that, basically, two spatially separated sound sources will suffice to create an as complicated as desired system of dummy transmitters including those distant from the two real transmitters. It is also interesting that one may force the imaginary source to move even if the real sources remain motionless by varying the amplitude and phase relations between the signals from the real sound sources.

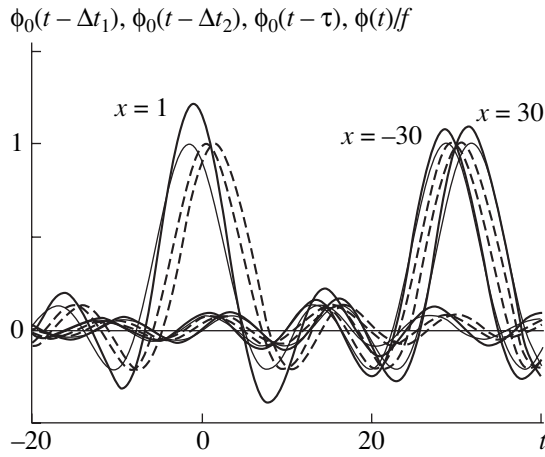


**Fig. 2.** Time dependences of the signals at various points on the abscissa ( $x = -30, 1$  and  $+30$ ). The time dependences of the total signal are shown by the thick solid line (numerical calculation) and thin solid lines (approximation (7)). The time behavior of separate sources is shown by the dotted lines.

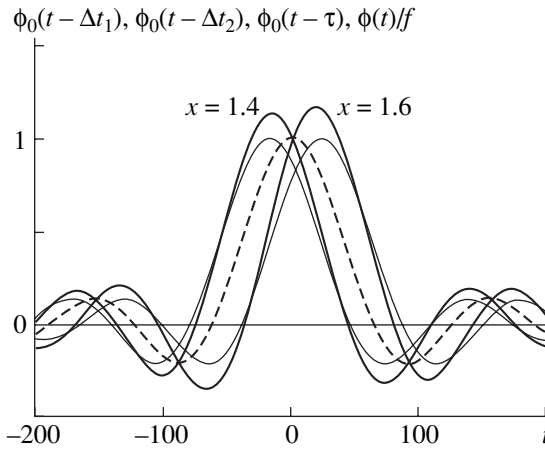


**Fig. 3.** Time dependences of the signals near the sphere of infinite delay times ( $x = 1.4$  and  $1.6$ ). The notation is the same as in Fig. 2.

active detection when a system irradiated by an external source consists of essentially dissimilar subsystems like the “tandem” of absolutely hard and absolutely soft spheres.

Figure 2 shows the time dependence of the field generated by the pair of transmitters (see Fig. 1) in a medium where the signal propagation velocity is  $c = 1$  at representative points of the domain of negative delays ( $x = 1, y = z = 0$ ), the domain of advance ( $x = -30, y = z = 0$ ), and the domain of lag ( $x = 30, y = z = 0$ ). The initial signal was taken to be  $\phi_0(t) = \sin(1/T)/(t/T)$  with duration  $T = 2$ . The abscissa is time  $t$ . Along the vertical axis, the time dependence of the field produced by both point sources ( $\phi_0(t - \Delta t_{1,2})$ , the dotted line), the time dependence of the total signal

according to approximate formula (7) ( $\phi_0(t - \tau)$ , the thin line), and the exact time dependence of the total signal resulting from interference between the fields of the point sources ( $\phi(t)/f = (f_1\phi_0(t - \Delta t_1) + f_2\phi_0(t - \Delta t_2))/f$ , the thick line) are plotted. One can see that, indeed, total signal  $\phi(t)$  may either advance or lag behind signals  $\phi_{1,2}(t)$ , which constitute the total signal on addition. Also, the delay time of the total signal may be negative (for instance, when  $x = 1$ ), positive and shorter than sound delay time  $x/c$  (for instance, when  $x = -30$ ), or positive and longer than sound delay time  $x/c$  (for instance, when  $x = 30$ ). It is little wonder, because, in this case, we observe not the violation of the causality principle but merely the nonanthropogenic (i.e., naturally occurring) forward or backward extrapolation of the signal time dependence. This extrapolation occurs (see above) as a result of interference, which can be treated as the summation of several variously delayed and attenuated copies of the same signal (note that, in essence, the anthropogenic, or intentional, extrapolation of the signal time dependence also reduces to such a summation [7]).

It is obvious that, when the signal is longer than the difference between the true delays  $\Delta t_{1,2}$  of the interfering signals and than the effective delay time  $\tau$  of the total signal, the accuracy of approximate formula (7) is rather high. As the signal becomes shorter, the accuracy of formula (7) significantly degrades. This seems to be quite reasonable, since, in this case, only two copies of the same signal are added up (interfere); in other words, we are dealing with linear extrapolation, which is reasonably accurate only when the duration of the extrapolation interval is much shorter than the signal duration [7].

The above remark is also related to the unlimited growth of the time of lag (or advance), when the observation point approaches the sphere of infinite delay time. Indeed, a lag (or advance) may be as large as desired (even as compared with the difference between the delays of the signals coming from point sources  $q_{1,2}$ ). In this case, however, the shape of the signal remains virtually undistorted for as long as the lag or advance is smaller than the signal duration. In other words, in the case of two-beam interference, the absolute lag (or advance) may be as large as desired but the relative time of lag or advance (i.e., the ratio between the lag or advance and the signal duration) must remain small [4].

This remark is illustrated by Fig. 3, which shows the time dependence of a long ( $T = 20$ ) signal near the sphere of infinite delay time ( $x = 1.4$  and  $1.6$ ). One can see that, when the delay time increases tenfold, the distortion of the time dependence of the total signal remains the same as in Fig. 2 if the signal duration is also increased tenfold. From Fig. 3, it also follows that the intrinsic delay time (i.e., the time it takes for the signal to propagate from one source to the other) may be significantly smaller than the delay (or advance) of the

total signal. In Fig. 3, in contrast to Fig. 2, the time dependences of the signals from sources  $q_1$  and  $q_2$  merge together; yet, the time dependence of the total signal exhibits a delay (or advance).<sup>3</sup>

Thus, the applicability of the effective delay time approximation depends on the characteristic duration of a signal being considered, while the effective delay time itself depends only on the geometry of a transmitting system and the position of the observation point. The present situation is quite similar to the case of applying the group velocity approximation.<sup>4</sup> The group velocity of a signal is determined only by the properties of the medium, while the applicability conditions for the group velocity approximation substantially depend on its duration and shape.

### 3. DIPOLE TRANSMITTER IN A NONABSORBING MEDIUM (DEGENERATE CASE)

Let us see how the diagram depicted in Fig. 1 will change when the amplitudes of the point sources are equal to each other ( $\delta \rightarrow 1-0$ ), i.e., in the case of a dipole transmitter. It is easy to see that the sphere of negative delays then expands and encloses the whole half-space  $x > 0$  ( $x_c \rightarrow +\infty$ ,  $R \rightarrow +\infty$ ,  $x_1 \rightarrow +0$ ,  $x_2 \rightarrow +\infty$ ). In this half-space, the delay time remains negative but infinitely decreases in magnitude ( $\tau \rightarrow -0$ ). The signal delay time in the domain of advance ( $x < 0$ ) remains positive, though infinitely decreasing ( $\tau \rightarrow +0$ ).

As a result, in the case  $q_1 + q_2 = 0$  ( $\delta = 1$ ), we come to the following “degenerate” situation: in the whole space, the delay time of the total signal is the same and equal to zero. The domain of applicability of the delay time approximation is now specified by the conditions  $|\Delta t_{1,2} - \tau| \ll T$  or, in other terms,  $r \ll cT$ . This means that we are studying the time dependence of the total field in the near-field zone of a set of point transmitters. The application of the effective delay time approximation in the far-field zone (for  $r \gg cT$ ) is merely an attempt to apply the linear extrapolation formula to ultralong (compared with the signal duration) time periods. Eventually, the linear extrapolation formula is truncated to the derivative, yielding the well-known [1] result: the field far away from a dipole transmitter is proportional to the time derivative of the dipole moment of the system.

It is not only in the dipole case that the effective delay time equals zero in the whole space. This is also valid for an arbitrary set of transmitters with a zero total

charge ( $\sum_{i=1}^n q_i = 0$ ) (see [8]). Note that such a “degenerate” case is the only possible one in electrodynamics.

Indeed, the total charge of the transmitting system is preserved ( $\sum_{i=1}^n d e_i(t) = (\sum_{i=1}^n q_i) \phi_0(t) = \text{const}$ ), which, for  $\phi_0(t) \neq \text{const}$ , is possible only when  $\sum_{i=1}^n q_i = 0$ . Of course, a closed system of electromagnetic transmitters may have an uncompensated static charge; however, this charge produces a static field with a delay time equal to zero by definition. That is why we adhere to the electrodynamics terms in this section and consider  $c$  as the velocity of light. In acoustics, the degenerate case  $\sum_{i=1}^n q_i = 0$  is also possible, though it is a particular one (dipole or multipole transmitter). The fact is that the total volume velocity [3] of a set of acoustic transmitters is not necessarily equal to zero: along with dipole and multipole transmitters, there exist acoustic monopole transmitters like a pulsating sphere.

Thus, we can state that, in a homogeneous transmission medium, the delay time of an electromagnetic signal in the near-field zone of an arbitrary set of electric charges, as well as the delay time of an acoustic signal from an arbitrary acoustic system without a monopole moment, is equal to zero.<sup>5</sup> The fact that the delay time is the same at any point of the near-field zone and precisely equals zero is, in a sense, an accident: in three-dimensional space, the field of a spherical wave geometrically decays according to the law  $(1/r)$ . In an absorbing medium (see Sect. 5), this “degeneration” is removed.

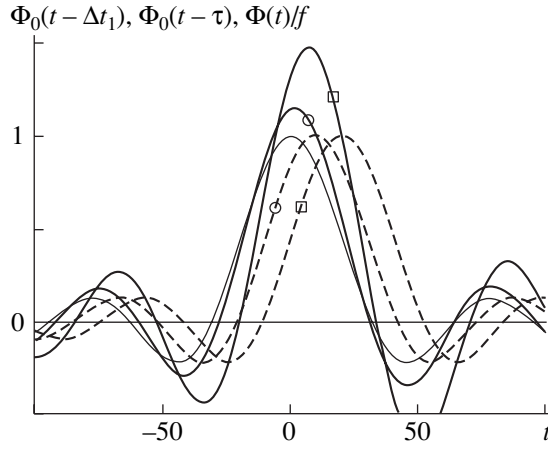
Let us corroborate our speculations by calculation. By way of example, we will consider the field of an electric or acoustic dipole ( $q_1 = -q_2 = q$ ; Fig. 1) in a homogeneous medium without dispersion and absorption.

Figure 4 shows the time dependence of the field of a dipole with point transmitters separated by a distance  $d = 0.01$  in a medium where the wave velocity is  $c = 1$  at points  $x = 10$  and  $20$  on the abscissa (the corresponding lines are labeled by circles and squares, respectively). The signal has the form  $\phi_0(t) = \sin(t/T)/(t/T)$  and duration  $T = 10$ . The notation is the same as in Figs. 2 and 3. Unlike the fields of single point transmitters, the total field “ignores” the time delay due to the finiteness of the signal propagation rate: for as long as the delay is much shorter than the signal duration, the near field almost coincides with the “undelayed” signal. It should be emphasized that the delay ignored by the total signal goes beyond the calculation accuracy and may signifi-

<sup>3</sup> The signals from two different point sources  $q_{1,2}$  merged together not only at the same observation point but also at different observation points ( $x = 1.4$  and  $1.6$ ).

<sup>4</sup> It has already been noted that the above consideration can be viewed as the group delay approximation for a signal with a zero carrier frequency (i.e., for a non-quasi-monochromatic signal) applied to the transmission from a group of point sources.

<sup>5</sup> The propagation velocity of the maximum (or any other fragment) of a signal turns out to be infinite (exceeds the velocity of light). Below, we demonstrate that this circumstance by no means contradicts the causality principle or the concept that the velocity of light in a vacuum is an ultimate (see also [4, 6, 8–11]).



**Fig. 4.** Time dependence of the dipole signal at various points on the abscissa (for  $x = 10$ , the lines are labeled by circles; for  $x = 20$ , the lines and labeled by squares). The notation is the same as in Fig. 3.

cantly exceed the time it takes for the signal to propagate between transmitters  $q_1$  and  $q_2$  (or, which is the same, may exceed the difference between the delays of the signals from individual sources.<sup>6</sup> For instance, in the case  $x = 10$ , the delay time of the signal from the closest monopole, which is ignored by the total signal, is equal to 9.995 (not that small when compared with the duration of the signal,  $T = 10$ , and in any case larger than the intrinsic delay time of the dipole, 0.01).

#### 4. MULTIPOLE TRANSMITTER IN A NONABSORBING MEDIUM

We have already mentioned that the signal can be extrapolated with a higher-than-linear accuracy. In the degenerate case,  $\tau = 0$  and extrapolation of order  $r$  can be applied (see Sect. 1) if  $\sum_{i=1}^n f_i \Delta t_i^k = 0$ ;  $k = 1, \dots, r$  (see (5)). This condition can be recast as

$$\sum_{i=1}^n q_i R_i^{k-1} = 0; \quad k = 1, \dots, r. \quad (10)$$

If the positions of the point transmitters and observation point (i.e., parameters  $R_i$  and  $r$ ) are fixed, conditions (10) can be considered as a system of  $r$  linear homogeneous algebraic equations in  $n$  variables  $q_i$ . It can be easily demonstrated that this system has nontrivial (nonzero) solutions for any values of parameters  $R_i$  if and only if  $n \geq r + 1$ . This means that we can achieve any preassigned accuracy of extrapolation of order  $r$  ( $r \leq n - 1$ ) for any preassigned arrangement of  $n$  transmitters and the position of the observation point by properly choosing the ratio of transmitter amplitudes  $q_i$ . In particular, two transmitters ( $n = 2$ ) provide for the

<sup>6</sup> Here, "individual" signals from two point sources (the dotted lines) merge together as in Fig. 3.

linear accuracy of extrapolation  $r = 1$ ; three ( $n = 3$ ), the quadratic accuracy ( $r = 2$ ); four, cubic ( $r = 3$ ); etc.

For a given extrapolation accuracy of order  $r$ , at least  $r + 1$  transmitters are required. In this case, system (10) has a unique solution (up to simultaneous scaling of all  $r + 1$  charges) in the form

$$q_p = \frac{\prod_{i \neq p} (R_{r+1} - R_i)}{\sum_{i \neq p} (R_p - R_i)} q_{r+1}, \quad (11)$$

where  $i = 1, 2, \dots, r$ ;  $p = 1, 2, \dots, r$ , and the value of charge  $q_{r+1}$  is arbitrary.

Certainly, we assume that  $R_i \neq R_j$  for  $i \neq j$ . Otherwise, transmitters  $q_i$  and  $q_j$  must be considered as a single transmitter for a given observation point, because the fields produced by them have the same time dependence at this point.

In the presence of extra (for a given accuracy of extrapolation of order  $r$ ) transmitters (the total number of transmitters is  $r + k$ ,  $k > 1$ ), the fundamental set of solutions to system (10) contains  $k$  linearly independent solutions and the general solution to system (10) has the form

$$q_p = - \sum_{l=1}^k \left( \frac{\prod_{i \neq p} (R_{r+l} - R_i)}{\sum_{i \neq p} (R_p - R_i)} \right) q_{r+l}, \quad (12)$$

where  $i = 1, 2, \dots, r$ ;  $p = 1, 2, \dots, r$ ; and the values of  $q_{r+l}$  ( $l = 1, 2, \dots, k$ ) are arbitrary.

Generally speaking, the validity of conditions (11) or (12) at some point of the space does not imply that these conditions hold in the whole space or, at least, on a certain set of points (on a line or a surface) in the space. Sometimes, however, this takes place. For instance, if  $r = 1$  (the linear accuracy), relationship (12) simplifies to the single condition  $q_1 = - \sum_{l=1}^k q_{1+l}$  ( $l = 1, 2, \dots, k$ ), which holds simultaneously at all points of the space for a system with a zero total charge (as noted above).

Another important particular case is that of aligned transmitters. It is easy to check that conditions (10) are fulfilled at any observation point that lies on the line of transmitters if the set of transmitters has no multipole moments [1] of orders  $l = 0, 1, \dots, r - 1$ :

$$Q_m^{(l)} = \sum_{i=1}^n q_i R_i^l \sqrt{\frac{4\pi}{2l+1}} Y_{lm}(\theta_i, \phi_i) = 0; \quad (13)$$

$$m = 0, \pm 1, \dots, \pm l.$$

For  $m \neq 0$ , conditions (13) hold by themselves for any linear set of transmitters; for  $m = 0$ , they coincide with (10). It is now clear that conditions (10) are (or are not) met simultaneously throughout the "line of transmitters."

Thus, an arbitrary linear system comprising any number of transmitters that has zero multipole moments of orders  $l = 0, 1, \dots, r - 1$  provides the absence of a signal delay along its axis up to order  $r$ . This means that any linear quadrupole (i.e., a linear set of charges having a zero total charge and zero dipole moment) provides second-order accuracy along its axis; any linear octupole (i.e., a linear set of charges having a zero total charge and zero dipole and quadrupole moments), the third-order accuracy; etc.

To implement such systems with a finite number of transmitters in practice, one may use relationships (11). In the case of equispaced (no matter how small or large the spacing) point transmitters, relations (11) immediately imply

$$q_p = (-1)^{n-p} C_{n-1}^{p-1} q_n; \quad p = 1, 2, \dots, n-1. \quad (14)$$

In particular, if  $n = 3$  (quadrupole), we have  $q_1 = q_3 = 1$  and  $q_2 = -2$ ; if  $n = 4$  (octupole),  $q_1 = -1$ ,  $q_2 = 3$ ,  $q_3 = -3$ , and  $q_4 = 1$ ; etc. Figure 5 shows the results of calculations for a quadrupole at points  $x = 10$  (circles) and  $x = 20$  (squares). In this case, the accuracy of formula (7) is seen to be noticeably higher than for a dipole transmitter, with distances from the set of transmitters being the same as in Fig. 4. This is because such a configuration of transmitters accomplishes the quadratic (rather than linear) extrapolation of the time dependence of the initial signal along its axis. In Fig. 6, the results of similar calculations for an octupole (the notation is the same as in Fig. 5) are presented. Here, the extrapolation along the octupole axis is cubic, which improves the accuracy of the results: the analytical (thin) line is shaded by the numerical line  $x = 10$ , and the line  $x = 20$  almost coincides with the line  $x = 10$ .

Thus, sets of transmitters that provide any preassigned accuracy of extrapolation of the signal time dependence at least on one-dimensional manifolds (curves) do exist and can be implemented, for example, using (14). At the same time, the question as to whether or not arrangements of transmitters that provide an accuracy of order higher than one on higher dimension manifolds (on surfaces or in the entire space) exist remains open.

## 5. DIPOLE TRANSMITTER IN AN ABSORBING MEDIUM

It has already been noted that degeneracy (i.e., the independence of the signal delay time from the position of the observation point) for a multipole transmitter can be removed not only by "disbalancing" the dipole (i.e., by introducing a nonzero monopole moment) in a transparent medium but also by taking into account the

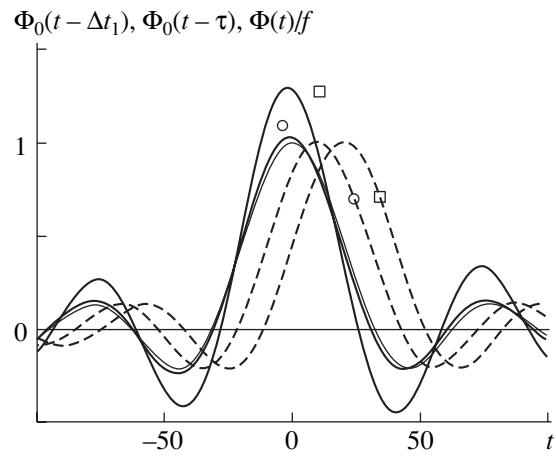


**Fig. 5.** Time dependence of the quadrupole signal at various points on the abscissa (for  $x = 10$ , the lines are labeled by circles; for  $x = 20$ , by squares). The notation is the same as in Fig. 3.

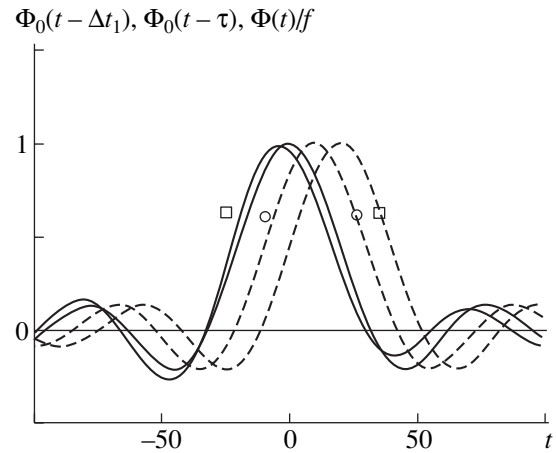


**Fig. 6.** Time dependence of the octupole signal at various points on the abscissa (for  $x = 10$ , the lines are labeled by circles; for  $x = 20$ , by squares). The notation is the same as in Fig. 3.

absorption of the medium. Consider an absorbing medium with absorption coefficient  $\lambda$ . Then, instead of (13), we have

$$\phi(\mathbf{r}, t) = \sum_{i=1}^n (q_i/R_i) \phi_0(t - R_i/c) \exp(-\lambda R_i). \quad (15)$$

In the case of a dipole ( $n = 2$ ,  $q_1 = -q_2 = q$ ), this gives, instead of (9),

$$f = q(R_1^{-1} \exp(-\lambda R_1) + R_2^{-1} \exp(-\lambda R_2)),$$

$$\tau = \frac{\exp(-\lambda R_1) - \exp(-\lambda R_2)}{c(\exp(-\lambda R_1)/R_1 - \exp(-\lambda R_2)/R_2)}. \quad (16)$$

One can easily check that the delay time of the total signal,  $\tau$ , is now different at various points of the space.

At any point, it is positive but smaller than the optical delay time of the signal from the point transmitter nearest to the observation point.<sup>7</sup> This result is quite natural. Indeed, a signal arriving at any observation point from a more distant source is attenuated more strongly. Therefore, any observation point is closer to a “more intense” (as perceived by the point) source and falls into the domain of advance (in terms of Sect. 2).

In the most interesting case  $\lambda d \ll 1$  (when the attenuation “inside the dipole” is low,<sup>8</sup> relationship (16) far from the dipole ( $r \gg d$ ) can be recast in the form

$$\tau = (r/c)(\lambda r)/(\lambda r + 1). \quad (17)$$

In the range  $\lambda r \ll 1$ , relationship (17) gives  $\tau \approx 0$ , which appears quite natural, because the absorption in this range is negligible and we actually come back to the degenerate case and a zero delay time. In the range  $\lambda r \gg 1$ , relationship (17) implies that  $\tau = (r/c) - 1/\lambda c$ . That is, the delay time is shorter than the optical time by the fixed quantity  $1/(\lambda c)$ , which is much smaller than the optical delay time of a signal propagating from the dipole to the observation point but larger than the intrinsic delay time of the dipole ( $d/c$ ). It is interesting that the latter delay is independent (contrary to the nondegenerate case considered in Sect. 2) of azimuth  $\theta$ . Hence, an imaginary point source (the same for different observation points) does not arise in this case and, at different points of the space, the signal delay time corresponds to transmission from different sources, which are always closer to the observation point than real sources of the signal.

It should also be noted that, when the condition  $T \gg 1/\lambda c$  holds, the (large) distance to the set of transmitters does not restrict the applicability of the delay time approximation. This can be interpreted as the absence of the “wave zone” for sufficiently long signals in an absorbing medium. It is for long signals ( $T \gg 1/\lambda c$ ) that the wave zone (in the normal sense) arises, the delay time approximation is applicable at infinitely long distances from signal sources, and the field at any point of the space is specified by the dipole (or multipole) moment of the transmitting system and not by its time derivative.

<sup>7</sup> Since electromagnetic waves are normally somewhat absorbed in a medium, we arrive at a conclusion that, at first glance, seems paradoxical. Namely, the maximum of an electromagnetic signal in a dispersionless absorbing medium “normally” propagates with a faster-than-light, rather than slower-than-light, velocity. In particular, this means (see below) that, when an electromagnetic signal with a steep leading or trailing edge (i.e., cut off at the front or at the rear) propagates, its tail is “reconstructed” through a “loss” in its “nose.”

<sup>8</sup> In the opposite limiting case  $\lambda d \gg 1$ , any observation point (except in the immediate vicinity of the equator,  $x \approx 0$ ) receives the signal from a single point source, namely, from the source that is closer to it. Accordingly, the signal delay time is almost equal to the optical delay.

## 6. CAUSALITY PRINCIPLE AND NEGATIVE (OR ZERO) DELAY TIME

Now let us discuss the relation between the causality principle and the fact of immediate (in the near-field zone of a multipole transmitter; Sects. 3, 4), advanced (in the domain of negative delays, Sect. 1), or faster-than-light (in the domain of advance (Sect. 1) and in an absorbing medium (Sect. 5)) arrival of the maximum (or any other fragment) of the signal. It has already been noted that these effects, being quite real and not contradicting the causality principle and the concept that the velocity of light in a vacuum is a physical limit, are due to the interference-related extrapolation of the signal time dependence.<sup>9</sup>

Nevertheless, it is the causality principle that is responsible for the reconstruction of the tail of a signal whose transmission was abruptly interrupted (see also [8, 9, 11]). In our case, the reconstruction of the nontransmitted tail of a signal is possible (and even inevitable) in the near-field zone of a dipole (or multipole) transmitter, in the domain of negative delays and in the domain of advance of a nondipole set of transmitters, as well as for a dipole (or multipole) transmitter in an absorbing medium.

Moreover, the opposite effect can be observed, which can be referred to as the effect of nose reconstruction by analogy with the previous one (such an effect for frequency-modulated signals was mentioned in [11]). In our case, the reconstruction of the nontransmitted nose of a signal occurs in the domain of lag of a nondipole set of transmitters.

As an example, Fig. 7 shows the calculation results for the propagation of the signal presented in Fig. 3, which was cut off at both ends: it abruptly arises at  $t = -60$  and disappears at  $t = 0$ . Here, panel (a) demonstrates the time dependence of the signal at point  $x = 1.4$  (the domain of negative delay times); panel (b), at point  $x = 1.6$  (the domain of lag; the delay time exceeds the acoustic delay time of the signal).

From Figs. 3 and 7, it follows that, in both cases, the total signal appears and disappears (the thick line) synchronously with interfering signals from individual point transmitters (the dashed line). This means that violation of the causality principle is out of the question. Whatever the time dependence of the signal detected, it is present at some point of the space only when its constituent delayed potentials are present at this point. The spikes of the total signal at the extremity of the time interval where it exists (see Fig. 7) are associated with the fact that the leading and trailing edges of the total signal (of duration  $d/c$ , where  $d$  is the distance between the point sources) consist of a signal from just one point source, so that signals from two

<sup>9</sup> In our opinion, this natural (interference-related) forward extrapolation of the signal time dependence underlies the nonanthropogenic prediction of this dependence and is responsible for the results predicted, such as a faster-than-light (or negative) group velocity of the signal in some types of dispersive media [6, 8–11].



sources are not partially compensated (this compensation is responsible for the backward (Fig. 7b) or forward (Fig. 7a) extrapolation of the time dependence of the total signal).

Yet, the smooth time dependence of the total signal, which exists only together with both delayed potentials (for the chosen values of the parameters, the delay of these potentials is negligible) shifts forward (Fig. 7a) or back (Fig. 7b). The future or past of the signal is reconstructed on the basis of information about the signals from the point sources that is available at a given point of the space and a given instant of time. As a result, what is actually detected is not the signal that was actually transmitted but its reconstructed past or future.

For example, in the case of a negative delay time (Fig. 7a), the detected signal (the thick line), unlike the transmitted one (the dashed line), starts from a nonzero value and has a smooth maximum, which is absent in the transmitted signal but which would appear later if the transmitted signal were smooth and exhibited no events like trailing edge cutoff. Therefore, this effect can be referred to as the reconstruction of the tail of a signal. It was shown [8, 9] that this effect arises when a signal propagates with a faster-than-light or negative group velocity in a strongly dispersive medium and is an inevitable consequence of the causality principle. If the signal transmitted is cut at both ends, the reconstruction of the time dependence of the signal tail causes a loss of information about its nose, i.e., about the time dependence of the initial part of the signal. Of course, this does not happen if the front of the signal transmitted remains intact.

When the delay time of the total signal exceeds the sound time (Fig. 7b), the signal detected (the thick line), unlike the transmitted one (the dashed line), starts from a nonzero value and is bipolar in amplitude or has a deep minimum of the intensity. The signal detected had none of these features but would have exhibited them (earlier) if its transmission had not started with the initial abrupt jump, i.e., if a smooth signal without events like leading or trailing edge cutoff were transmitted. That is why this effect is natural to be called the reconstruction of the signal nose. This effect may arise when a signal propagates with a slower-than-light (or subsonic) group velocity in a strongly dispersive medium and, unlike the effect of regeneration of the tail, may be avoided. The fact is that, in a real dispersive medium, the reconstructed nose of the signal is imposed on the response of the medium to the jump of the amplitude of the signal with the truncated leading edge. Therefore, the reconstructed nose can be distinguished only if the background is feeble.<sup>10</sup> In our case, good discernability of the truncated nose of the signal is associated just with the steep decay of the response

<sup>10</sup>The situation with tail reconstruction is much simpler. The response of the medium exists in this case, too, but (since the causality principle works) it follows the reconstruction of the tail and so cannot distort it.

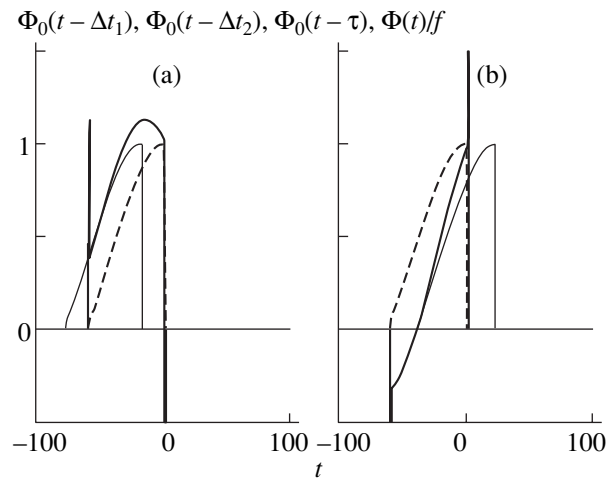


Fig. 7. Time dependence of the dipole signal with the cut leading and trailing edges at various points on the abscissa.  $x =$  (a) 10 and (b) 20. The notation is the same as in Fig. 3.

of the medium, which abruptly (within the time  $d/c$  after its occurrence) disappears instead of fading out as in a real dispersive medium. If the signal transmitted is cut at both ends, the reconstruction of the time dependence of the signal nose is accompanied by a loss of information about its tail. Of course, this does not happen if the trailing edge of the signal transmitted remains intact.

In practice, when signal transmission is strictly limited in time, the effects of nose reconstruction and tail reconstruction may lead to a situation where basically different signals are detected at different points of the space; moreover, the signals detected may even differ from that transmitted.

The effects considered reflect the well-known fact that, in any medium, there are two velocities of signal propagation, which radically differ in meaning and magnitude. These are the vacuum velocity of light, which is the velocity of signal discontinuities [1] and, hence, the rate of data transfer [1, 5, 6], and the group velocity, which is typical of the smooth envelope of a signal and may exceed, or be lower than, the vacuum velocity of light and even negative [4, 6, 8–11]. We emphasize that the vacuum velocity of light is the rate of data transfer (generally speaking, the propagation rate of any signal as a data carrier) in any medium and it is the vacuum velocity of light that obeys all the fundamental restrictions that follow from the causality principle and, in particular, from the restricted relativity theory (and are sometimes incorrectly imposed on the group velocity, which may be neither lower than the velocity of light nor positive).

In essence, we can treat the same phenomenon (the same curve) in two ways that do not contradict each other. In the first case (considering the group velocity as the “basic” one), we may suppose that the time dependence of a signal is approximately the same at various

points of the space but the signal may propagate with a slower-than-light velocity, the velocity of light, or a faster-than-light velocity. Its velocity may be even negative. If the time dependence of a signal is discontinuous, the signal is distorted in a specific way (its tail is reconstructed through a loss of information about its nose or vice versa) because of the difference between the propagation rate of the discontinuities and the group velocity.

In the second case (considering the vacuum velocity of light as basic), we assume that the velocity of a signal equals the vacuum velocity of light but the time dependence of the signal is distorted due to the difference between the group velocity and the vacuum velocity of light. Namely, the time dependence of the signal shifts in the interval between its sharp leading and trailing edges. Both approaches are equally justified, and the choice is a matter of convenience. For a (smooth) signal unlimited in time, the first approach seems preferable, while the second one is more convenient when a signal has abrupt leading and trailing edges.

### CONCLUSIONS

(1) In the general case, the delay time of a signal from a compact array of transmitters does not coincide with the optical or acoustic delay time of the signal and may significantly exceed, or be much shorter than, the latter. In particular, the delay time of the total signal may be negative. In this case, the maximum of the signal arrives at the observation point before it is transmitted by any transmitter in the array.

(2) Such behavior of the signal is consistent both with the concept that the vacuum velocity of light is a fundamental physical limit (when the signal delay time is shorter than the optical one) and with the causality principle (when the signal delay time is negative). The forward or backward shift of the time dependence of the total signal is caused by the forward or backward extrapolation of the signal time dependence. Such an extrapolation is a natural result of interference between several copies of the same signal. A by-product of the extrapolation is the reconstruction of the “cut” leading or trailing edge of a signal for which transmission was abruptly started or terminated.

(3) The same mechanism (interference-induced forward or backward extrapolation) gives rise to a faster-than-light or negative group velocity, i.e., underlies the nonanthropogenic prediction of a high-frequency signal in some dispersive media [8–11]. Therefore, physically, a faster-than-light or negative group velocity arises from the forward extrapolation of the time dependence of the signal detected. This extrapolation is naturally brought about as a result of interference between several copies of the same signal that are variously delayed and attenuated by the medium.

(4) In addition to the case when a high-frequency signal is transmitted in a dispersive medium, a similar extrapolation (with similar consequences) may also occur when a high-frequency or low-frequency multi-beam signal propagates in a nondispersive (inhomogeneous) medium.

### REFERENCES

1. L. D. Landau and E. M. Lifshitz, *Course of Theoretical Physics, Vol. 2: The Classical Theory of Fields* (Nauka, Moscow, 1988; Pergamon, Oxford, 1975).
2. M. B. Vinogradova, O. V. Rudenko, and A. P. Sukhorukov, *The Theory of Waves* (Nauka, Moscow, 1979) [in Russian].
3. M. A. Isakovich, *General Acoustics* (Nauka, Moscow, 1973) [in Russian].
4. N. S. Bukhman, *Opt. Spektrosk.* **96**, 687 (2004) [*Opt. Spectrosc.* **96**, 626 (2004)].
5. I. S. Gonorovskii, *Radio Engineering Circuits and Signals* (Radio i Svyaz', Moscow, 1986) [in Russian].
6. L. A. Vaĭnshteĭn, *Usp. Fiz. Nauk* **118**, 339 (1976) [*Sov. Phys. Usp.* **19**, 189 (1976)].
7. A. A. Amosov, Yu. A. Dubinskiĭ, and N. V. Kopchenova, *Computational Methods for Engineers* (Vysshaya Shkola, Moscow, 1994) [in Russian].
8. N. S. Bukhman, *Zh. Tekh. Fiz.* **72**, 136 (2002) [*Tech. Phys.* **47**, 132 (2002)].
9. N. S. Bukhman, *Kvantovaya Élektron. (Moscow)* **31**, 774 (2001).
10. N. S. Bukhman, *Pis'ma Zh. Tekh. Fiz.* **29** (18), 81 (2003) [*Tech. Phys. Lett.* **29**, 784 (2003)].
11. N. S. Bukhman, *Opt. Spektrosk.* **97**, 123 (2004) [*Opt. Spectrosc.* **97**, 114 (2004)].

*Translated by A. Pankratiev*

SHORT  
COMMUNICATIONS

## Two-Coordinate Diffusion of Optical Beams by an Acousto-optic Raman–Nath Modulator Based on a Paratellurite Crystal

S. N. Antonov

*Institute of Radio Engineering and Electronics, Russian Academy of Sciences (Fryazino Branch),  
pl. Vvedenskogo 1, Fryazino, Moscow Oblast, 141190 Russia*

*e-mail: olga-ant@yandex.ru*

Received February 18, 2004

**Abstract**—Acousto-optic Raman–Nath diffraction by a standing acoustic wave in a paratellurite crystal is investigated. An acoustic line is made in the form of a polished cube and serves as a high- $Q$  acoustic resonator. A slow shear wave is excited by a single piezoelectric transducer. Multiple lossless sound reflections lead to two-coordinate light diffusion. When the acoustic intensity introduced into the crystal is about  $2 \text{ W/cm}^2$  at a sound frequency of 7 MHz, there appears a diffraction pattern in the form of a homogeneous light spot with a solid angle of about 0.5 sr. An explanation for the features of the acousto-optic interaction is given. It is shown that this type of diffraction is helpful in designing acousto-optic two-coordinate diffusers of light beams. © 2005 Pleiades Publishing, Inc.

The overwhelming majority of acousto-optic (AO) devices are based on Bragg acousto-optic diffraction, which has a single diffraction order. At the same time, the Raman–Nath regime, characterized by several diffraction orders, is being little used [1]. This study investigates the feasibility of using Raman–Nath diffraction in acousto-optic diffusers of light.

In experiments, an optical radiation was diffracted by a slow shear acoustic wave traveling in a paratellurite ( $\text{TeO}_2$ ) single crystal that was placed in an AO cell. Among the rich variety of AO materials, this crystal has enjoyed the widest application, since it is characterized by a uniquely high AO figure of merit combined with good optical and acoustic properties and high processability. The efficiency of AO diffraction in this crystal is such that, for an interaction length on the order of a centimeter and an acoustic power of several tens of milliwatts, the index of phase modulation of light may reach  $2\pi$  (in other words, the efficiency approaches 100%). The experimental setup is schematically shown in Fig. 1. A light beam from single-mode semiconductor laser 1 (the wavelength is  $0.65 \mu\text{m}$ , the beam aperture is 0.7 mm) passes through AO modulator 2 with piezoelectric transducer 3. The light field distribution behind the modulator is viewed at the focal plane of lens 4 on screen 5. In the experiments, we used a  $\text{TeO}_2$  single crystal in the form of a cube measuring  $12 \times 12 \times 12 \text{ mm}$ . The faces of the crystal were optically finished, and their misalignment with respect to the  $[110]$ ,  $[1\bar{1}0]$ , and  $[001]$  directions was within  $5^\circ$ . The piezoelectric transducer  $7 \times 7 \text{ mm}$  in size was in acoustic contact with the  $(1\bar{1}0)$  face. Thus, the slow shear wave with a frequency of about 7 MHz was initially excited

along the  $[1\bar{1}0]$  direction and the displacement vector was parallel to the  $[110]$  direction. In all the experiments, the light was propagated along the  $[001]$  axis. As was mentioned above, the faces of the  $\text{TeO}_2$  crystal were parallel to each other with a high degree of accuracy, so that it might function as an high- $Q$  acoustic resonator. The mode spacing of the resonator was  $\Delta f = v/2L$ , where  $v$  is the sound velocity ( $0.617 \times 10^6 \text{ mm/s}$ ) and  $L$  is the spacing between the faces (12 mm). In our case,  $\Delta f \approx 26 \text{ kHz}$ . The quality factor of such an acoustic resonator was  $Q \approx 20$ . Thus, the diffraction intensity was maximal at resonant frequencies that were multiples of  $\Delta f$ .

Figure 2 demonstrates the diffraction pattern observed on the screen under the resonance condition for three different powers of the signal applied to the piezoelectric transducer: (a) 0.1, (b) 0.5, and (c) 0.8 W. It is seen that the pattern is two-coordinate in all cases, i.e., has diffraction orders both in the plane parallel to the direction of propagation of the initially excited acoustic wave and in the orthogonal plane. The angular

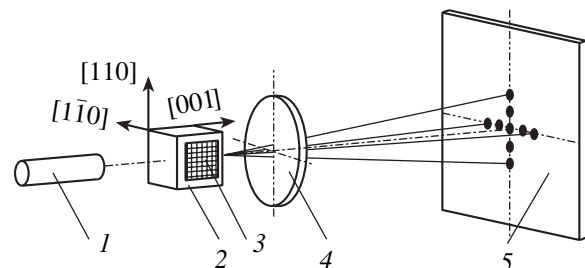
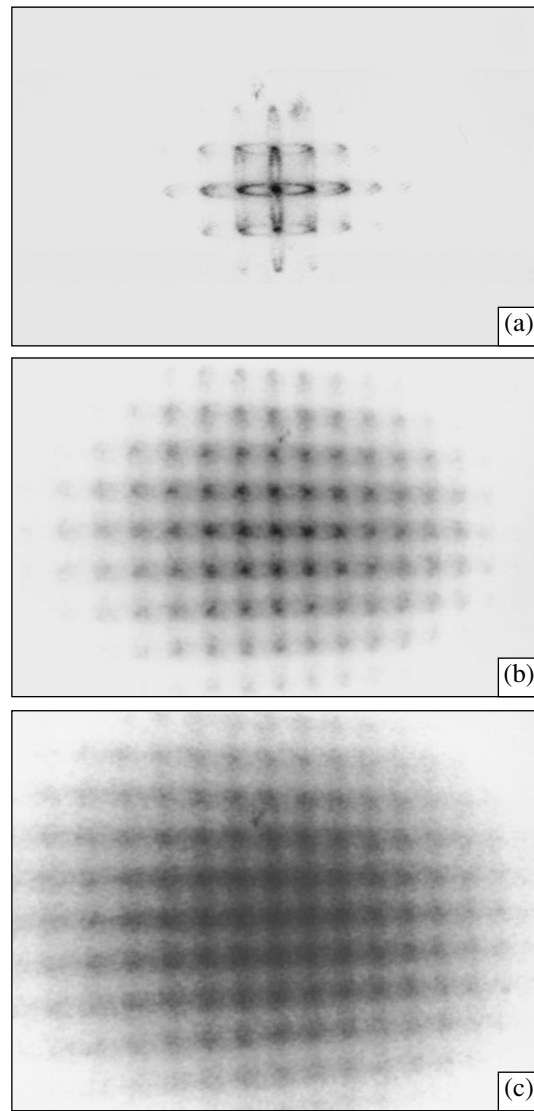


Fig. 1. Schematic of the experimental setup.

distance between the diffraction orders (in either plane) is  $\Delta\alpha = 0.42^\circ$ . As the acoustic wave power rises, the number of diffraction maxima increases and the maxima broaden, becoming diffuse. The most interesting and unexpected situation arises when the power reaches 1.5 W (the associated photograph is not presented) and the diffraction pattern transforms into a homogeneous light spot (having no visible internal structure) with a solid angle of about 0.5 sr. In this case, the sound intensity applied to the crystal was about  $2 \text{ W/cm}^2$  and the intensity of the standing wave in the crystal (along the  $[\bar{1}\bar{1}0]$  and  $[110]$  axes) was evaluated as  $20\text{--}30 \text{ W/cm}^2$ .

The pattern observed can be treated in terms of the following estimates. For low powers of the acoustical wave (Figs. 2a, 2b), the pattern in orthogonal diffraction planes is similar to a Raman–Nath diffraction pattern. In fact, for the given light and sound wavelengths and the dimensions of the piezoelectric transducer, we find that the dimensionless Klein–Cook parameter equals  $Q = 1.6$ , which allows us to identify this diffraction regime with Raman–Nath diffraction [1]. The appearance of the two-coordinate diffraction pattern is associated with the following features of the slow acoustic mode propagation in a  $\text{TeO}_2$  crystal. The first one is a small value of the acoustic absorption coefficient at the given frequency (about  $0.01 \text{ dB/cm}$ ) [2]. Consequently, the acoustic wave undergoes many lossless reflections. The second feature is considerable acoustic anisotropy [3], which causes the energy flux to diverge, with angle of divergence  $\Delta\theta$  significantly exceeding the initial diffraction divergence ( $\Delta\theta = 50\lambda/d$ , where  $\lambda$  is the sound wavelength and  $d$  is the aperture of the transducer along the  $[110]$  direction). In our experimental conditions,  $\Delta\theta \approx 34^\circ$ . Thus, acoustic waves propagating normally to the initial direction appear even after several reflections. Note that only the  $[\bar{1}\bar{1}0]$  and  $[110]$  directions are “resonant” and the sound intensity along them increases by the value of the acoustic  $Q$  factor: there appear two stable high-intensity orthogonal standing modes. The third reason is the fact that the acoustic and acousto-optic properties of the crystal in these two orthogonal crystallographic directions are identical. The diffraction orders diffuse, because each of them multiply interacts with a set of sound wavevectors that have different velocities.

Let us discuss the practical importance of the AO diffraction regime observed. In practice, optical engineers use diffusers that have either dull or holographic plates [4]. These plates broaden the directional diagram of light and remove the structure of the light sources’ image. They are widely used in projectors when the image of a filament must be transformed into a homogeneous light spot. Such an approach is also applied to eliminate speckles in the output radiation of fiber waveguides. It is clear that each such plate is fabricated with a certain angle of the scattering indicatrix.



**Fig. 2.** Diffraction field arising when the AO modulator is illuminated by the laser.

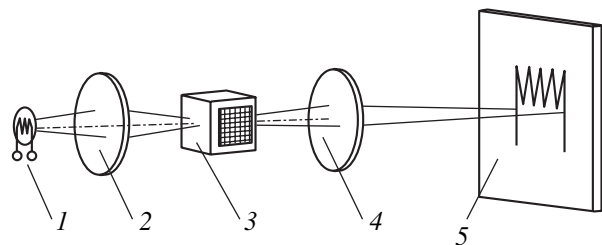


**Fig. 3.** Schematic of the projector.

Figure 3 demonstrates how a Raman–Nath AO diffuser can be used to eliminate the structure in the image of the projector lamp filament. Schematically, the projector consists of incandescent lamp 1, collimator 2, AO Raman–Nath modulator 3 (identical to that shown in

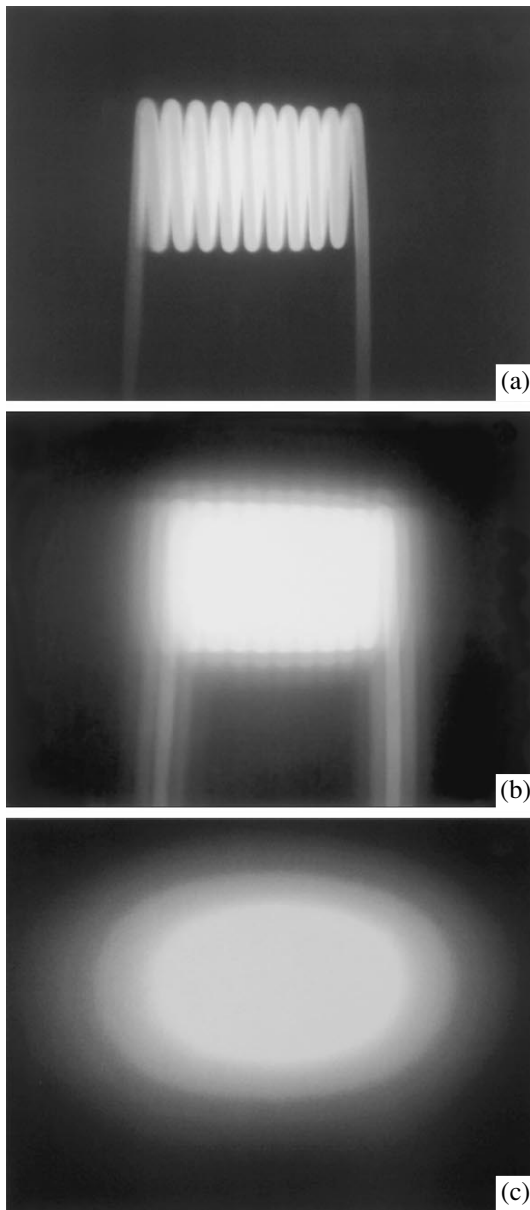


**Fig. 4.** Image of the filament.

Fig. 1), objective lens 4, and screen 5. Figure 4 shows the image of the filament for various powers of the signal applied to the piezoelectric transducer: (a) the signal is not applied, (b) the signal power equals 0.3 W, and (c) the signal power equals 1.5 W. It is well seen that the diffusion of the image is proportional to the increase in the sound power.

Thus, the AO diffraction regime investigated in this work may form the basis for designing light diffusers that radically differ from the conventional ones in that the former demonstrate the possibility of controlling the angle of scattering. This may be helpful in optimizing different types of images. In addition, there appears a possibility of rapidly controlling the scattering indicatrix. The rate of control depends on the sound velocity, the crystal size, and acoustic  $Q$ -factor. The time  $\tau$  it takes for the stationary diffraction field to form (or decay) once the excitation signal has been applied can be estimated as  $\tau \approx (L/v)Q$ . Under our experimental conditions, it was about 0.4 ms. It should also be noted that holographic diffusers exhibit light losses (from 10 to 15%) and impose limitations on the permissible intensity of incident light. In the above application, the AO modulator is evidently totally free of optical losses and the radiation resistance of  $\text{TeO}_2$  crystals is very high.

#### REFERENCES

1. L. N. Magdich and V. Ya. Molchanov, *Acoustooptic Devices and Their Applications* (Sov. Radio, Moscow, 1978; Gordon and Breach, New York, 1988).
2. S. N. Antonov, V. V. Proklov, and V. I. Mirgorodskii, *Akust. Zh.* **28**, 433 (1982) [*Sov. Phys. Acoust.* **28**, 257 (1982)].
3. V. P. Semenov, *Zh. Tekh. Fiz.* **51**, 2090 (1981) [*Sov. Phys. Tech. Phys.* **26**, 1219 (1981)].
4. *Edmund Industrial Optics* (Edmund Industrial Optics, Barrington, 2000).

*Translated by Yu. Vishnyakov*

---

SHORT  
COMMUNICATIONS

---

## Deformation of a Ferroelectric Smectic Film in an Electric Field

V. P. Romanov\* and S. V. Ul'yanov\*\*

\* *St. Petersburg State University, Universitetskaya nab. 7/9, St. Petersburg, 198904 Russia*  
*e-mail: v.romanov@pobox.spbu.ru*

\*\* *St. Petersburg Institute of Trade and Economics, ul. Novorossiiskaya 50, St. Petersburg, 194021 Russia*  
Received March 30, 2004

**Abstract**—Mechanisms of static deformation of a freely suspended ferroelectric smectic ( $C^*$ ) film in an external transverse electric field are analyzed. An equation for the shape of the film that includes the interaction of the applied field with the polarization vector and surface charges is derived in terms of the variational approach. The effect of deformation is shown to be of threshold character, which agrees with the experimental data.  
© 2005 Pleiades Publishing, Inc.

Liquid crystals, being intermediates between isotropic viscous liquids and crystalline solids, possess a number of intriguing properties [1, 2]. Of special interest are smectic liquid crystals. They feature not only orientation order but also an ordered arrangement of the centers of mass of molecules, which form a layered structure. Depending on the preferred orientation of molecules, which is specified by unit director vector  $\mathbf{n}$ , smectic liquid crystals can be subdivided into smectics  $A$ , where the director is aligned with normal  $\mathbf{N}$  to the planes of a layer, and smectics  $C$ , where vector  $\mathbf{n}$  makes angle  $\theta$  with the normal to the layer. If director  $\mathbf{n}$  in smectic  $C$  rotates in going from layer to layer with angle  $\theta$  remaining unchanged, we deal with smectic  $C^*$  [3].

Smectics may form macroscopic stable films containing from two layers to several hundred layers [3–5]. These films may be both freely suspended in a rigid frame and fixed on a substrate. The physical properties of thin-film (especially suspended) smectics are of particular interest, since they offer a unique possibility of studying a two-dimensional system (which is virtually impossible otherwise) and also are finding wide application, primarily in data displays.

External fields noticeably influence the equilibrium and dynamic properties of thin films. Ferroelectric smectics  $C^*$  [2, 6, 7], which have a constant dipole moment and are extremely sensitive to applied fields, are of special interest. The behavior of freely suspended ferroelectric smectic films in an electric field is being extensively studied both theoretically and experimentally [8–12]. It has been found that a variable electric field of different configuration leads to an electromechanical effect, i.e., causes the films to vibrate. The natural vibration spectra of the films and the vibration amplitude as a function of the applied field, film size,

and environmental conditions have been studied experimentally.

Theoretical analysis of these effects raises a number of issues, which have not been discussed in detail. First of all, we mean the excitation of transverse vibration in the film when it is placed in an electric field that is applied along its surface. The problem is that, when interacting with the spontaneous polarization vector, the field affects only the orientation of the director. To date, deformation of the film under the action of an external electric field has not been adequately explained on the quantitative basis. In an attempt to explain this effect qualitatively, Jakli [8] related the reorientation of the director in an external field to viscous stresses, which arise in so-called induced backward flows.

It was found [11] that a transverse electric field causes the film to arch but the shape of the film is other than spherical. This effect is akin to the Fredericksz effect [1, 2] and is of threshold character: the film starts deforming only if the electric field strength exceeds a critical value.

In this work, we analyze mechanisms of static deformation of the film subjected to an external electric field that is applied transversely to the film. It will be shown that reasons for the variable curvature of the film deformed can be found and the threshold field can be calculated in terms of a fairly general approach.

Consider a freely suspended thin film of ferroelectric smectic  $C^*$  placed in a uniform electric field that is applied normally to the surface of the film. Free energy  $F$  of deformation consists of the (i) Frank energy due to the nonuniform orientation of the director; (ii) elastic energy due to the deformation of the film; and (iii) energy of interaction of the applied electric film with the spontaneous polarization vector and surface

charges, which appear on the film in the presence of surrounding space charges. Eventually, we get [2, 3, 5]

$$F = \int d\mathbf{r}_\perp \left\{ \frac{1}{2} K_s (\nabla_\perp \mathbf{c})^2 + \frac{1}{2} K_b (\nabla_\perp \times \mathbf{c})^2 + \frac{1}{2} K_e (\Delta_\perp u)^2 + \alpha (\Delta_\perp u)^2 - \mathbf{P}_0 \cdot \mathbf{E} - \sigma u E \right\} \quad (1)$$

( $\Delta$  is the Laplacian). Here, it is assumed that thickness  $L$  of the film is so small that its internal structure can be ignored and the rotation of the director from layer to layer can be disregarded. In formula (1),

$$K_s = LK_{11} \sin^2 \theta, \quad (2)$$

$$K_b = L\bar{K} = L(K_{22} \sin^2 \theta \cos^2 \theta + K_{33} \sin^4 \theta).$$

Here,  $K_{ii}$  ( $i = 1, 2, 3$ ) are the Frank moduli;  $\mathbf{c}$  is the unit vector aligned with the projection of the director onto the plane of the film (the so-called  $\mathbf{c}$  director [3]);  $u$  is the displacement of the film along the  $z$  axis, which runs normally to the surface of the undeformed film (to

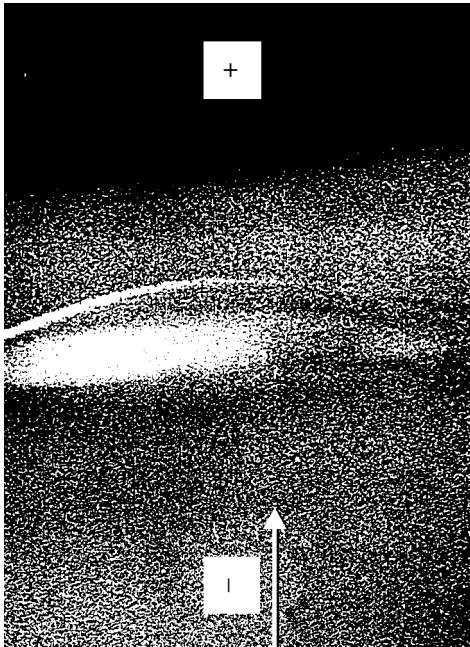
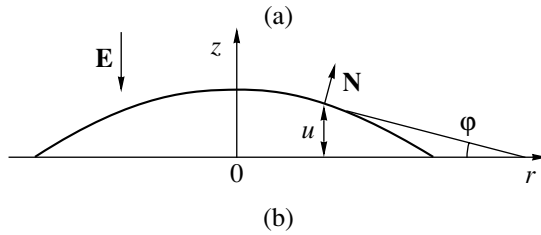


**Fig. 1.** (a) Mutual arrangement of electric field strength vector  $\mathbf{E}$ , displacement  $u$ , and coordinate system. (b) The profile of the ferroelectric smectic ( $C^*$ ) film in the uniform external electric field [11].

plane  $xy$ );  $K_e = LK$ , where  $K$  is the flex modulus of the film;  $\alpha$  is the surface tension coefficient;  $\mathbf{P}_0 = P_0 \mathbf{N} \times \mathbf{c}$  is the dipole moment per unit surface of the film ( $P_0$  is its absolute value);  $\mathbf{E}$  is the applied electric field strength; and  $\sigma$  is the surface charge density on the film. Vector  $\mathbf{P}_0$  is related to polarization vector  $\mathbf{P}$  as  $\mathbf{P}_0 = L\mathbf{P}$ .

If an external electric field is absent, the free energy of deformation in a flat film with the uniformly oriented director vanishes (takes a minimal value). In the presence of the field, the shape of the film and the distribution of the director orientation will change if these changes reduce the energy of deformation.

Consider a film fixed on a circular diaphragm of radius  $R$ . Owing to the axial symmetry of the problem, one can conclude that the value of  $|\mathbf{P}_0 \cdot \mathbf{E}|$  is maximal if the projection of vector  $\mathbf{P}_0$  onto plane  $xy$  is aligned with the radius of the diaphragm, which is occupied by the film. In this case, the  $\mathbf{c}$  director is oriented along the tangents to coaxial circles centered on the  $z$  axis and a disclination, the core radius  $a$  of which is comparable to the size of a molecule, arises at the center of the film [3, 13].

Further analysis is more convenient to perform in the cylindrical coordinate system. For the free energy of deformation, we have

$$F = 2\pi \int_a^R r dr \left\{ \frac{1}{2} K_b \frac{1}{r^2} + \frac{1}{2} K_e (\Delta_\perp u)^2 + \alpha \left( \frac{du}{dr} \right)^2 + P_0 E \frac{du}{dr} - \sigma u E \right\}. \quad (3)$$

Here, it is taken into account that, at low deformations of the film and, accordingly, at small angles  $\phi$  (see Fig. 1a), the following relationships hold:

$$-\mathbf{P}_0 \cdot \mathbf{E} = -P_0 E \sin \phi \approx -P_0 E \tan \phi \approx P_0 E \frac{du}{dr}.$$

Considering that, in thin films,  $K_e \sim 10^{-(10-11)} \text{erg}$ ,  $\alpha \approx 30 \text{ erg/cm}^2$ , and the characteristic length over which the shape of the film changes noticeable is  $R \sim 0.1 \text{ cm}$ , we can neglect the term  $(1/2)K_e(\Delta_\perp u)^2$  in formula (3), since it is much smaller than  $\alpha(du/dr)^2$ . In addition, we neglect the contribution of the disclination core to the free energy, since it is proportional to  $a^2$  and, hence, is much smaller than the contribution due to orientation elasticity [3, 13].

To find the shape of the film in an external field, we minimize free energy of deformation (3), taking into account that the film is fixed along the circumference of the diaphragm. Eventually, we arrive at the Euler-Lagrange equation

$$ru'' + u' + \frac{P_0 E}{2\alpha} + \frac{\sigma E}{2\alpha} r = 0 \quad (4)$$

with the boundary conditions

$$\begin{aligned} u(r=R) &= 0, \\ u'(r=a) + \frac{P_0 E}{2\alpha} &= 0. \end{aligned} \quad (5)$$

Integrating Eq. (4) yields

$$u = \frac{P_0 E}{2\alpha}(R-r) + \frac{\sigma E}{8\alpha}(R^2 - r^2) + \frac{a^2 \sigma E}{4\alpha} \ln \frac{r}{R}. \quad (6)$$

Figure 1b shows the deformed film profile obtained in [11]. At the edges of the film, its profile is nearly linear and the radius of curvature decreases toward the center. This profile is described well by expression (6).

Substituting (6) into (3), we find the free energy of the film deformed. Since the condition  $a \ll R$  is met, we have

$$F = \pi K_b \ln \frac{R}{a} - \frac{\pi E^2 R^2}{2\alpha} \left( \frac{1}{2} P_0^2 + \frac{1}{3} \sigma P_0 R + \frac{1}{16} \sigma^2 R^2 \right). \quad (7)$$

Formula (7) implies the existence of a threshold (critical) external field above which the free energy of deformation becomes negative and the deformed state of the film becomes energetically more favorable than its planar state. For the critical value of the field, we obtain

$$E_{\text{cr}} = \frac{2}{R} \sqrt{\frac{\bar{K} L \alpha \ln \frac{R}{a}}{P^2 L^2 + \frac{2}{3} \sigma R P L + \frac{1}{8} \sigma^2 R^2}}. \quad (8)$$

From this formula, it follows that, if the interaction of an external field both with surface charges and with the polarization vector is essential, the dependence of the critical field on thickness  $L$  and linear size  $R$  of the film is a complicated function. In the limiting case of a neutral system ( $\sigma = 0$ ), we have

$$E_{\text{cr}} = \frac{2}{R P} \sqrt{\frac{\bar{K} \alpha \ln \frac{R}{a}}{L}}. \quad (9)$$

In the other limiting case, when the effect of surface charges prevails,

$$E_{\text{cr}} = \frac{4\sqrt{2}}{\sigma R^2} \sqrt{\bar{K} L \alpha \ln \frac{R}{a}}. \quad (10)$$

It is worth noting that the dependences of the critical field on the film geometry are very different in these limiting cases.

In experiments with ferroelectric films placed in the corona field [11], the critical field was found to vary nearly as the square root of the film thickness. This is consistent with formula (10) and also with the conclusions drawn by the authors of [11], who argued that the deformation of the film in that experiment results from the interaction of the external field with surface charges.

## ACKNOWLEDGMENTS

This work was supported by the Russian Foundation for Basic Research (grant nos. 03-02-16173 and 02-02-16577).

## REFERENCES

1. P. G. de Gennes, *The Physics of Liquid Crystals* (Clarendon, Oxford, 1993; Mir, Moscow, 1977).
2. S. A. Pikin, *Structural Transformations in Liquid Crystals* (Nauka, Moscow, 1981) [in Russian].
3. P. G. de Gennes and J. Prost, *The Physics of Liquid Crystals*, 2nd ed. (Clarendon, Oxford, 1993; Mir, Moscow, 1982).
4. W. H. de Jeu, B. I. Ostrovskii, and A. N. Shalaginov, *Rev. Mod. Phys.* **75**, 181 (2003).
5. V. P. Romanov and S. V. Ul'yanov, *Usp. Fiz. Nauk* **173**, 941 (2003) [*Phys. Usp.* **46**, 915 (2003)].
6. L. M. Blinov, *Electro-Optical and Magneto-Optical Properties of Liquid Crystals* (Nauka, Moscow, 1978; Wiley, New York, 1983).
7. B. A. Strukov and A. P. Livanyuk, *The Physical Principles of Ferroelectric Phenomena in Crystals* (Nauka, Moscow, 1995; Springer, Berlin, 1998).
8. A. Jakli, L. Bata, A. Buka, *et al.*, *Ferroelectrics* **69**, 153 (1986).
9. S. V. Yablonskii, T. Oue, H. Nambu, *et al.*, *Appl. Phys. Lett.* **75**, 64 (1999).
10. S. V. Yablonskii, A. S. Mikhaïlov, K. Nakano, *et al.*, *Zh. Éksp. Teor. Fiz.* **120**, 109 (2001) [*JETP* **93**, 94 (2001)].
11. K. Yoshino, S. V. Yablonskii, J. Kyokane, *et al.*, *Jpn. J. Appl. Phys.* **42**, 1338 (2003).
12. S. V. Yablonskii, K. Nakano, M. Ozaki, *et al.*, *J. Appl. Phys.* **94**, 5206 (2003).
13. P. M. Chaikin and T. C. Lubensky, *Principles of Condensed Matter Physics* (Cambridge Univ. Press, Cambridge, 1995).

Translated by V. Isaakyan



---

**THEORETICAL  
AND MATHEMATICAL PHYSICS**

---

# Effect of Disorder on the Conductivity of Two-Phase Strongly Inhomogeneous Highly Filled Composites

**A. A. Snarskii\*, M. V. Shamonin\*\*, M. I. Zhenirovskyy\*, and R. Trautner\*\***

\* National Technical University of Ukraine, Kiev Polytechnical Institute,  
ul. Peremogi 37, Kiev, 03056 Ukraine

e-mail: phys@ln.com.ua

\*\* Fachberei Technische Hochschule, Regensburg, Germany

Received May 26, 2004

**Abstract**—The effect of the “stir” of a structure (small deviations from strict periodicity) on effective conductivity is considered. For determinate and random deviations, concentration and field dependences of the effective conductivity are found. Numerical experiments with determinate deviations are carried out for the cases of linear (with respect to the field) inclusions embedded in both a linear and nonlinear matrix. The numerical results are compared with the effective conductivity calculated analytically. © 2005 Pleiades Publishing, Inc.

## INTRODUCTION

We consider a two-phase composite with conductivities  $\sigma_1$  of the first (well-conducting) phase and  $\sigma_2$  of the second (poorly conducting) one. It is well known [1] that, when the concentration of the well-conducting phase increases, approaching percolation threshold  $p_c$ , the effective conductivity  $\sigma_e$  of the composite increases sharply. This increase is due to a continuous path (a so-called infinite cluster) that occurs in the well-conducting phase and closes the contacts.

In the vicinity of the percolation threshold, i.e., when the concentration of the well-conducting phase is close to  $p_c$ , the effective conductivity is an analogue to the order parameter in the theory of phase transitions of the second kind [1]. Similarly to the order parameter,  $\sigma_e$  universally depends on the closeness to the transition point  $\tau = (p - p_c)/p_c$  (i.e., is described by a scaling function) and its behavior is specified by few critical indices. Universality means that  $\sigma_e$  is independent of the realization of a random structure if the sample is sufficiently large. In particular, one may randomly shift each of the well-conducting inclusions in a poorly conducting matrix without changing  $\sigma_e$ . Figuratively, the system is stable against stir.

In a three-dimensional system, percolation usually occurs at  $p_c \approx 0.2$ , i.e., when the well-conducting phase is still small. Sometimes, there is a need for composites with a concentration of the well-conducting phase much higher than  $p_c$ , so-called highly filled composites [2]. In this case, the concentration of the well-conducting phase may approach a maximal value, since the inclusions of the well-conducting phase are closely packed. One can distinguish between two radically different kinds of packing: a purely random packing and a

packing with a periodical (or almost periodical) arrangement of the inclusions. The effective conductivity of randomly arranged inclusions is described well by a modification of the self-consistent field approximation introduced in [3] (see also [4]; a number of different approximations is also given in [5]), the effective medium approximation (EMA). Except in the neighborhood of the percolation threshold, where the methods of the percolation theory should be used, the EMA adequately fits a vast amount of experimental data [6]. However, this approximation takes no account of the arrangement of the inclusions and their interplay. As is known [5], the EMA reduces the problem of effective conductivity or, more specifically, the problem of current distribution in a medium with inclusions to the problem of current distribution in a resistance grating. For a high concentration of inclusions, i.e., when they are closely spaced and their interplay cannot be neglected, the EMA may introduce a significant error.

Let us consider the two-dimensional problem, i.e., circular inclusions arranged strictly periodically (Fig. 1). In real composites, this periodicity is violated. We are interested in the effect a small deviation of the structure from periodicity has on the effective conductivity. In Sec. 1.1, we consider a small deviation (stir) of the structure under determinate displacements of periodically arranged two-dimensional inclusions in the linear statement. In Sec. 1.2, the calculation results for the simplest displacements are compared with their theoretical description and the domain of applicability of our model is determined. In Sec. 2, random displacements are considered. In Sec. 3, the nonlinear problem (linear inclusions in a nonlinear matrix) is solved and the results are compared with direct calculations.

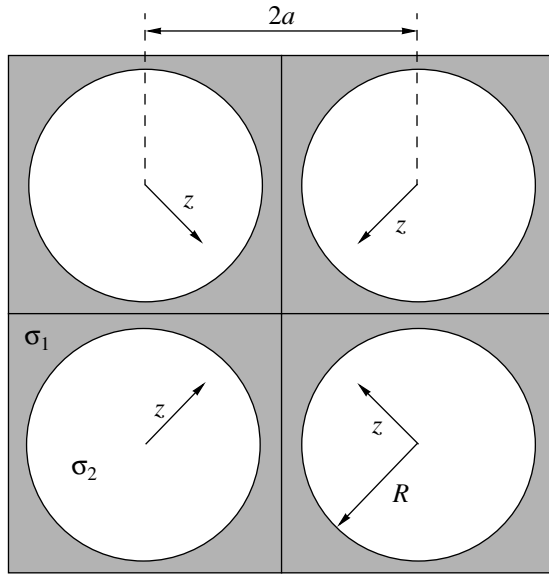


**Fig. 1.** Initial strictly periodical arrangement of the inclusions. Poorly conducting inclusions ( $\sigma_2$ ) in a well-conducting matrix ( $\sigma_1$ , gray color) are shown white. The arrows labeled by  $z$  indicate the direction of the simplest displacement in the numerical simulation.

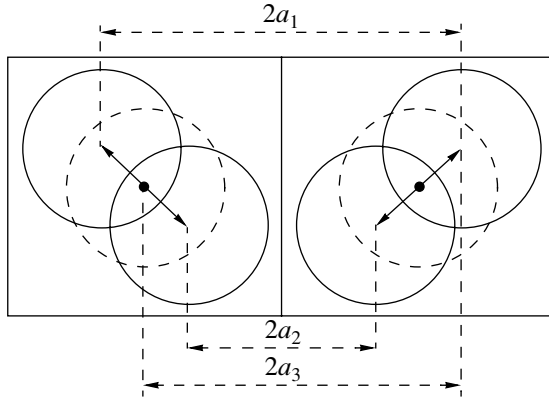


**Fig. 2.** Determinate disorder. Three types of displacements and, respectively, three types of effective values  $a_i$  are shown.

## 1. DISPLACEMENTS IN THE CASE OF A LINEAR (WITH RESPECT TO THE FIELD) MATRIX

**1.1. Determinate displacements.** For a strictly periodical arrangement of two-dimensional circular inclusions (circular cylinders), the solution of the effective conductivity problem is presented in [7]. For brevity, the well-conducting phase with conductivity  $\sigma_1$  will be referred to as the black phase and the poorly conducting phase with conductivity  $\sigma_2$  as the white phase. Let the structure consist of a black matrix with white circular inclusions. In the case of strict periodicity, the effective conductivity of such a structure  $\sigma_{WB}$  (sub-

script WB stands for “white in black”) has the form [7]

$$\sigma_{WB} = \sigma_1 \left( \alpha - \frac{\pi R^2}{4a^2} \right) \left( \alpha + \frac{\pi R^2}{4a^2} \right)^{-1}, \quad (1)$$

where  $R$  is the radius of the inclusions,  $2a$  is the size of a cell (Fig. 1),

$$\alpha = 1 - \frac{1}{3}(\eta R^4)^2 - \frac{1}{63}(\eta R^4)^4 - \frac{5}{9} \left( 1 + \frac{4}{5 \cdot 11 \cdot 13^2} \right) (\eta R^4)^6 - \dots,$$

$$\eta = K(1/\sqrt{2})^4 / (20a^4),$$

and  $K(1/\sqrt{2}) = 1.85407$  is the complete elliptic integral of the first kind with modulus  $1/\sqrt{2}$ .

Formula (1) is valid for  $0 \leq R \leq 0.95a$ . It also implies that  $\sigma_2 = 0$ . Note that the strictly periodical structure under consideration is equivalent to a grating of conductances  $g$  where

$$g(a) = \sigma_1 \left( \alpha - \frac{\pi R^2}{4a^2} \right) \left( \alpha + \frac{\pi R^2}{4a^2} \right)^{-1}. \quad (2)$$

Let us see what happens if strict periodicity is broken. Consider the first situation where strict periodicity is violated by introducing a “determinate” disorder; namely, we shift each of the inclusions of the white phase along the diagonal of a square cell by  $z$  in any direction (see Fig. 2) or keep it in place. If, in doing so, two inclusions move away from each other, the spacing between them increases and, accordingly, so does the “effective value” of  $a$ :

$$a_1 = a + \frac{z}{\sqrt{2}}, \quad g_1 = g(a_1). \quad (3)$$

If two inclusions come closer to each other, the spacing between them decreases:

$$a_2 = a - \frac{z}{\sqrt{2}}, \quad g_2 = g(a_2). \quad (4)$$

In the third case, one inclusion is shifted, while the other is left in place:

$$a_3 = a + \frac{z}{2\sqrt{2}}, \quad g_3 = g(a_3). \quad (5)$$

Let us restrict our analysis to the cases described above. Then, there are three types of the “effective value”  $a_i$  (see (3)–(5)) in our system, which determine  $\sigma_{WB}$ . Such a system is equivalent to a grating that consists of three types of conductances:  $g_1$ ,  $g_2$ , and  $g_3$ . A possible distribution of the conductances over the grating is shown in Fig. 3, which clarifies the way each of the inclusions has been shifted. Note that this arrangement of the inclusions is (i) periodical (with a period of

five grating cells) and (ii) isotropic. One can see in Fig. 3 that the concentrations of the conductances are  $p_1 = 0.2$  and  $p_2 = p_3 = 0.4$ . In the EMA, the effective conductivity  $\sigma_{WB}(p, z)$  of the grating that consists of conductances  $g_1, g_2$ , and  $g_3$  is given by

$$\sum_{i=1}^3 p_i \frac{\sigma_{WB}(p, z) - g_i}{\sigma_{WB}(p, z) + g_i} = 0. \quad (6)$$

Since the inclusions are impermeable, the displacement  $z$  of the center of a circular inclusion from the center of a cell is bounded by the value  $z_{\max}$ :

$$z \leq z_{\max} = \sqrt{2}(a - R). \quad (7)$$

Figure 4 plots the dependences of  $\ln(\sigma_{WB}(\tau, z))$  versus  $\ln(\tau)$  for various  $z$ . We are reminded that  $\tau = (p - p_c)/p_c$ , where  $p_c$  is the percolation threshold. In the case considered,  $p_c = 1 - \tau/4$ . It is evident that  $R(\tau) = 2a\sqrt{(1 - p_c(\tau + 1))/\pi}$ . One can see from Fig. 4 that displacement  $z$  does not change the slope of the curves, i.e., does not change the critical index. For

$$0.95a < R \leq a, \quad (8)$$

formula (1) is not valid. Therefore,  $z_{\max}$  must be subject to the condition  $z_{\max} = \sqrt{2}(a - R/0.95)$ , which is stronger than condition (7). Here, for example, the approximate solution

$$\sigma_{WB} = \sigma_1 \frac{1}{\pi} \sqrt{2 \frac{a - R}{R}} \quad (9)$$

may be used [8].

Expression (9) is written for the case  $R \rightarrow a$ , when the total resistance of the system is a sum of the resistances of narrow gaps between the inclusions. Here, the white phase is assumed to be nonconductive. The accuracy of expression (9) can be verified by directly comparing it with numerical calculations (see Fig. 5). As follows from Fig. 5, for concentrations  $p \leq 0.25$ , formula (1) fails, while formula (9) becomes valid. Then, instead of (2), we have

$$g(a) = \sigma_1 \frac{1}{\pi} \sqrt{2 \frac{a - R}{R}}. \quad (10)$$

An expression for effective conductivity  $\sigma_{WB}(p, z)$  in the case of well-conducting inclusions embedded in a poorly conducting matrix can be found in the same way (here, subscript BW stands for ‘‘black in white’’). Formula (2) is then replaced by

$$g(a) = \sigma_2 \left( \alpha - \frac{\pi R^2}{4a^2} \right) \left( \alpha + \frac{\pi R^2}{4a^2} \right)^{-1}, \quad (11)$$

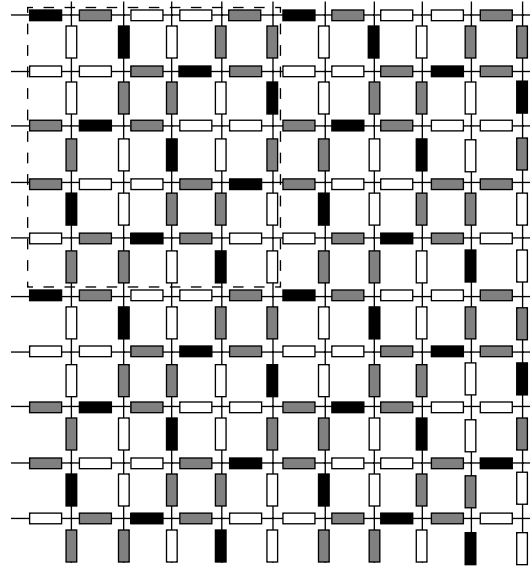


**Fig. 3.** Determinate displacements. Well-conducting inclusions (see (3)) and poorly conducting inclusions (see (4)) are colored black and white, respectively. The intermediate case (see (5)) is shown in gray. The dashed square is the period of this grating.

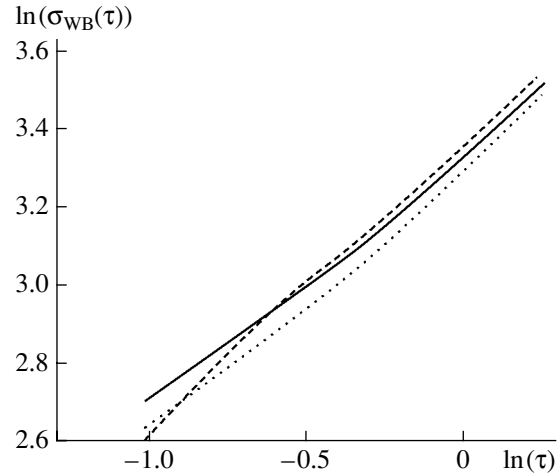


**Fig. 4.**  $\ln(\sigma_{WB}(\tau, z))$  vs.  $\ln(\tau)$  for different displacements  $z$  (the WB case). The dotted line,  $z = 0$  (the no-shift case); the continuous line,  $z = 0.02$ ; and the dashed line,  $z = 0.05$ .

and, instead of (10), we write [8]

$$g(a) = \frac{\pi \sigma_2}{\sqrt{2 \frac{a - R}{R}}}. \quad (12)$$

If the inclusions are shifted in the same way as in the WB case considered above, the effective conductivity problem reduces to a grating problem with the same values of  $a_i$  (see (3)–(5)) but with other concentrations ( $p_1 = p_3 = 0.4$  and  $p_2 = 0.2$ ).

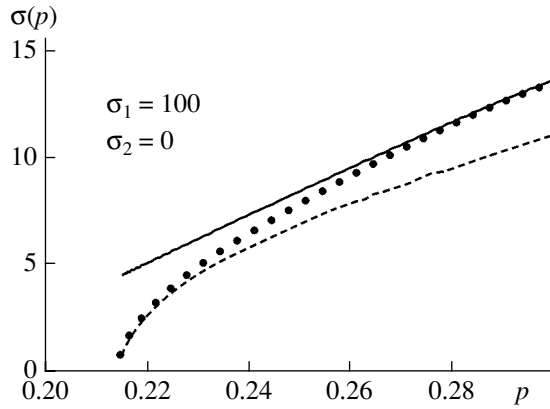


**Fig. 5.** Finding the domain of applicability of expressions (1) and (9) for the concentration dependence of the effective conductivity near percolation threshold  $p_c$ . The continuous curve, calculation by (1) (see also [7]); the dashed line, calculation by (9) (see also [8]); and the filled circles, the result of numerical calculation.

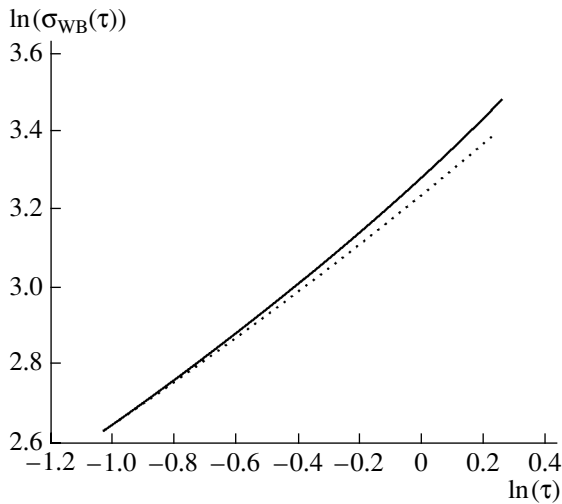


**Fig. 6.** Random displacements with uniformly distributed displacement amounts (the WB case). The dotted curve is calculated by (16), and the continuous curve corresponds to  $z = 0$  (the no-shift case).

### 1.2. Comparison with the numerical experiment.

To determine the domain of applicability of our grating model of resistances, which is stated by expressions (3)–(5) and (10)–(12), consider the simplest displacements. Let each of the inclusions in a  $4a \times 4a$  square be shifted by  $z$  toward its center (Fig. 1). On the one hand, such displacements can be exactly calculated in the framework of our model of resistances; on the other hand, they can be easily found by direct computation.

Here, we have conductances of only two types given by (3) and (4), where  $p_1 = p_2 = 0.5$ . In the WB case, our “black-and-white” grating with conductances  $g_1$  (white) and  $g_2$  (black) is equivalent to a “gray” grating

with conductance

$$\tilde{g}_{\text{WB}} = \frac{1}{2}(g_1 + g_2), \quad (13)$$

because here  $g_1$  and  $g_2$  are connected in parallel. Proceeding with the BW case in the same way, we get, instead of (13),

$$\tilde{g}_{\text{BW}} = 2 \frac{g_1 g_2}{g_1 + g_2}, \quad (14)$$

since  $g_1$  and  $g_2$  are now connected in series. Figure 8 suggests that the theoretical results are more consistent with the numerical calculations for the BW case (for details of numerical calculations, see the Appendix).

## 2. RANDOM DISPLACEMENTS IN THE CASE OF A LINEAR (WITH RESPECT TO THE FIELD) MATRIX

Now let us turn to the case when each of the inclusions is displaced randomly. For definiteness, consider the WB case. We suppose that, for such displacements,  $a$  equiprobably takes values from a certain interval  $a_{\min} \leq a \leq a_{\max}$ . In the case of white inclusions in a black matrix, the EMA applied to the model of resistances being used (the resistance of the system is concentrated in the gaps) yields

$$\int_{g_{\min}}^{g_{\max}} \frac{\sigma_{\text{WB}} - g}{\sigma_{\text{WB}} + g} S(g) dg = 0. \quad (15)$$

Here,  $S(g)dg = f(a)da$  and, according to the assumption that spacings  $a$  between the closest inclusions are uniformly distributed,  $f(a) = 1/(a_{\max} - a_{\min})$  for  $a_{\min} \leq a \leq a_{\max}$  and  $f(a) = 0$  outside this interval.

It is obvious that  $a_{\min} = R/0.95$ ,  $a_{\max} = 2a - R/0.95$ , and  $g_{\max(\min)}$  is related to  $a_{\max(\min)}$  in accordance with (2). Then, Eq. (15) can be recast as

$$\int_{a_{\min}}^{a_{\max}} \frac{\sigma_{\text{WB}} - g(a)}{\sigma_{\text{WB}} + g(a)} \frac{da}{a_{\max} - a_{\min}} = 0. \quad (16)$$

Figure 6 shows the results of calculations by formula (16). In this case, too, the critical index varies insignificantly compared with the no-shift case.

Now let us turn to the case  $0.95 < R \leq a$ , where an analytical solution can be obtained. In view of (10), instead of (16), we have

$$\int_{g_{\min}}^{g_{\max}} \frac{\sigma_{\text{WB}} - g}{\sigma_{\text{WB}} + g} g dg = 0, \quad (17)$$

where  $a_{\min} = R$ ,  $a_{\max} = 2a - R$ , and  $g_{\max(\min)}$  is related to  $a_{\max(\min)}$  by (9). Equation (17) yields the following non-

linear equation for  $\sigma_{\text{WB}}$ :

$$2(g_{\text{max}} - g_{\text{min}})\sigma_{\text{WB}} - \frac{1}{2}(g_{\text{max}}^2 - g_{\text{min}}^2) - 2\sigma_{\text{WB}}^2 \ln \frac{\sigma_{\text{WB}} + g_{\text{max}}}{\sigma_{\text{WB}} + g_{\text{min}}} = 0. \quad (18)$$

Solving Eq. (18), we obtain a dependence of  $\sigma_{\text{WB}}$  on  $g_{\text{max}}$  and  $g_{\text{min}}$ . If it is assumed that, at any random stir of the structure (i.e., at any displacement of the inclusions), the inclusions stay within their cells (i.e., the displacements are small), the value of  $g_{\text{max}}$  is given by

$$g_{\text{max}} = \frac{2\sigma_1}{\pi} \sqrt{\frac{a-R}{R}}. \quad (19)$$

Note that, for  $g_{\text{min}} = 0$ , i.e., in the case where some of the inclusions come into contact ( $a = a_{\text{min}} = R$ ) and cut off the current, Eq. (18) simplifies so that its solution can be written in analytic form:

$$\sigma_{\text{WB}} = Cg_{\text{max}} = C \frac{2\sigma_1}{\pi} \sqrt{\frac{a-R}{R}}, \quad (20)$$

where constant  $C = 0.616$  is the solution to the nonlinear equation

$$C \left( 1 - C \ln \frac{C+1}{C} \right) = \frac{1}{4}. \quad (21)$$

In the case  $g_{\text{min}} \neq 0$ , Eq. (18) cannot be solved analytically. One can immediately see from (20) that, for  $p$  close to  $p_c$ , we have  $\sigma_{\text{WB}} \sim (p - p_c)^{1/2}$ , which is also true for the no-shift case [7]. Note that all the systems considered above differ fundamentally in behavior from Swiss Cheese systems [9, 10]. In the latter, the resistance is also gained in ‘‘bottlenecks’’ between the inclusions but the inclusions are arranged chaotically. In particular, the system may contain inclusion-free domains of a size larger (or much larger) than two periods.

### 3. DISPLACEMENTS IN THE CASE OF A NONLINEAR (WITH RESPECT TO THE FIELD) MATRIX

Now let us turn to the case of a nonlinear matrix with conductivity  $\sigma_1(E)$  that contains circular inclusions with conductivity  $\sigma_2$ . Similarly to the linear case, we consider the two-dimensional problem. There are different types of nonlinearity, namely, strong nonlinearity, weak nonlinearity, etc. (see, for instance, [11–13]). In the absence of hysteresis, the problem of finding the effective conductivity is completely equivalent to the problem of determining the effective permeability, with the permeability of the ferromagnetic phase nontrivially and nonlinearly depending on the magnetic field. Since magnetic composites are widely used in practice and their properties are being intensively studied (see, for instance, [2]), it is interesting to

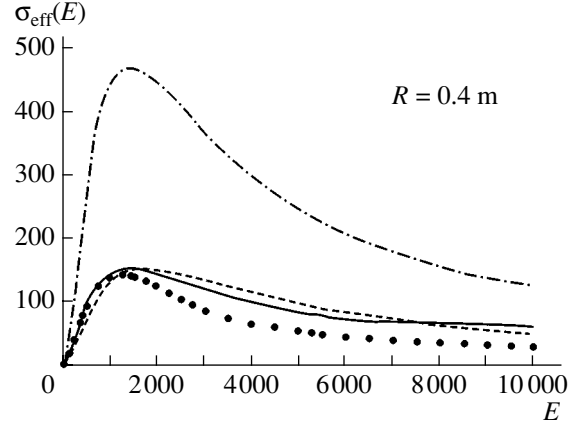


**Fig. 7.** Field dependences of the nonlinear-phase conductivity and effective conductivity. The dash-and-dot line, the nonlinear phase; the continuous curve, the effective conductivity calculated by the LL method [18, 19]; the dashed line, the effective conductivity calculated by the method presented in [20, 21]; and filled circles, the effective conductivity obtained by the direct numerical calculation.

consider the case of linear (with respect to the local field) inclusions embedded in a ferromagnetic matrix that features a negligibly small hysteresis loop. Following our notation, we denote magnetic field strength  $H$  by  $E$  and relative permeability  $\mu$  by  $\sigma$  ( $\mu$  does not contain the permeability of vacuum  $\mu_0$ ). The standard dependence of the permeability (for example, the permeability of steel) on  $H$  is demonstrated in Fig. 7. In our notation, it can be written as

$$\sigma_1(E) = 1 + 1.5 \times 10^6 \frac{\tanh(5 \times 10^{-4} E)}{E} - 2.5 \times 10^5 \frac{\tanh(3 \times 10^{-3} E)}{E}. \quad (22)$$

The permeability of the inclusions is  $\sigma_2 = 1$ . In such magnetic composites [14–17], complicated nonlinear dependences of the response of the whole sample to the applied magnetic field, as well as sharp concentration dependences of the effective coefficients that are related to their percolation behavior, are observed. We will outline approximate methods of finding the effective conductivity for a strictly periodical problem having a nonlinearity of type (22), since an exact solution to such a problem in the general case is absent.

First, consider the method of local linearization (LL method) [18, 19], which allows one to find an approximate analytical expression for the effective kinetic coefficients. According to this method, we have in our case

$$\sigma_{\text{eff}}(E) = \frac{\sigma_1(E)(\sigma_e(E) - \sigma_2) - \sigma_2(\sigma_e(E) - \sigma_{d1}(E))}{\sigma_{d1}(E) - \sigma_2}, \quad (23)$$

where  $\sigma_{d1}(E) = d(\sigma_1(E)E)/dE$  is the differential conductivity and  $\sigma_e(E)$  is a solution to a (geometrically) similar linear problem in which the real conductivities of the phases are replaced by differential ones [18, 19].

The case considered above is based on the exact solution to the linear problem [7]. From (1), we get

$$\sigma_e(R, E) = \sigma_{d1}(E) \frac{\alpha(R, E) - \frac{\pi R^2 \delta(E)}{4a^2}}{\alpha(R, E) + \frac{\pi R^2 \delta(E)}{4a^2}}, \quad (24)$$

where, in accordance with the approximate LL method, we have, similarly to the linear case (see also [7]),

$$\begin{aligned} \delta(E) &= (\sigma_{d1}(E) - \sigma_2)/(\sigma_{d1}(E) + \sigma_2), \\ \alpha &= 1 - \frac{1}{3}(\eta R^4)^2 \delta(E)^2 - \frac{1}{63}(\eta R^4)^4 \delta(E)^2 \\ &- \frac{5}{9} \left( \delta(E)^2 + \frac{4}{5 \times 11 \times 13^2} \right) (\eta R^4)^6 \delta(E)^2 - \dots \end{aligned}$$

Here, as above,  $R$  is the radius of an inclusion and  $2a$  is the size of a cell (Fig. 1).

Another approximate method was developed in [20, 21]. Although this method does not provide a result in analytical form (it implies the solution of a set of nonlinear equations, which, in the general case, can be solved only numerically), it gives a more accurate approximation in some cases [18, 19]. The basic assumption of this method is that the local field inside the inclusions is independent of the coordinates (this is valid only for ellipsoidal inclusions when the interaction between them can be neglected) and, accordingly, that the conductivity of the nonlinear phase,  $\sigma_1 = \sigma_1(E(\mathbf{r}))$  ( $\mathbf{r}$  is the radius vector), can be replaced by the coordinate-independent constant

$$\tilde{\sigma}_1 = \langle \sigma_1(E) \rangle_1, \quad (25)$$

where averaging is over the whole volume of the nonlinear phase,  $\langle \dots \rangle = (1/V_1) \int \dots dV$ .

Also, this method admits substitution, which, in our notation, has the form

$$\tilde{\sigma}_1 = \langle \sigma_1(E) \rangle_1 \rightarrow \sigma_1(\sqrt{\langle E^2 \rangle_1}). \quad (26)$$

In other words, a two-phase medium with coefficients  $\sigma_1(E(r))$  and  $\sigma_2 = 1$  (the second phase is linear) is replaced by a two-phase medium with  $\sigma_1(\sqrt{\langle E^2 \rangle_1})$  and  $\sigma_2$ , i.e., a medium in which local  $\sigma_1$  is independent of local field  $E = E(r)$ . For a given applied field  $\langle E \rangle$ , the entire first phase has the same value  $\sigma_1 = \tilde{\sigma}_1$  specified by  $\langle E^2 \rangle_1$ .

Thus, on the one hand, to determine  $\sigma_{\text{eff}}$  of a two-phase medium with phases  $\tilde{\sigma}_1$  and  $\sigma_2$ , any solution to the similar linear problem can be used, for instance, the

EMA [3, 4, 15, 16, 19] or expression (1). On the other hand, to determine  $\langle E^2 \rangle_1$ , one may use the equality  $\langle jE \rangle = \langle j \rangle \langle E \rangle$  (see, e.g., [22]), which implies that  $\sigma_{\text{eff}} \langle E \rangle = p \sigma_1 \langle E^2 \rangle_1 + (1-p) \sigma_2 \langle E^2 \rangle_2$ , where  $\langle \dots \rangle_{1,2}$  means averaging over the first or second phase, respectively, and  $p$  is the concentration of the first phase. Eventually, we have

$$\langle E^2 \rangle_1 = \frac{\langle E \rangle^2 \partial \sigma_{\text{eff}}}{p \partial \tilde{\sigma}_1}. \quad (27)$$

Substituting (1) where  $\tilde{\sigma}_1$  is used instead of  $\sigma_1$  into (27), we obtain a nonlinear equation for  $\langle E^2 \rangle_1$ . Determining  $\langle E^2 \rangle_1$  and substituting it into (1), we find  $\sigma_{\text{eff}}$  as a function of applied field  $\langle E \rangle$ , concentration, and parameters of the nonlinearity function.

In Fig. 7, the field dependences obtained by the methods described above are given together with the results of direct numerical calculations. One can see that both methods give satisfactory results up to the field at which  $\sigma_{\text{eff}}(E)$  reaches a maximum. At higher fields, both methods describe the behavior of  $\sigma_{\text{eff}}(E)$  only qualitatively. In this case, the method presented in [20–22] is less accurate than the LL method (and, moreover, requires a much more computer time than the latter). Therefore, we will use the LL method to estimate the effective conductivity in the presence of displacements.

Consider the displacements mentioned in Sect. 1.2. Since the inequality  $\sigma_1(E) \gg \sigma_2$  holds almost throughout the field range, we are dealing with poorly conducting inclusions in a well-conducting matrix (the WB case) and the linear model is described by formula (13). Finally, we have

$$\begin{aligned} &\sigma_{\text{eff}}(E, z) \\ &= \frac{\sigma_1(E)(\sigma_e(E, z) - \sigma_2) - \sigma_2(\sigma_e(E, z) - \sigma_{d1}(E))}{\sigma_{d1}(E) - \sigma_2}, \end{aligned} \quad (28)$$

where, according to (13),

$$\sigma_e(E, z) = 0.5(\sigma_{e1}(E, z) + \sigma_{e2}(E, z)),$$

$$\sigma_{ei}(E, z) = \sigma_{d1}(E) \frac{\alpha_i(E, z) - \frac{\pi R^2 \delta(E)}{4a_i(z)^2}}{\alpha_i(E, z) + \frac{\pi R^2 \delta(E)}{4a_i(z)^2}}, \quad (29)$$

$$\begin{aligned} \alpha_i(E, z) &= 1 - (0.333(\eta_i(z)R^4)^2 + 0.016(\eta_i(z)R^4)^4 \\ &+ 2.4 \times 10^{-4}(\eta_i(z)R^4)^6) \delta(E)^2 - 0.556(\eta_i(z)R^4)^6 \delta(E)^4, \end{aligned} \quad (30)$$

$\eta_i(z) = (1.85407/a_i(z))^4/20$ , and, in accordance with (3) and (4),

$$a_1(z) = a + z/\sqrt{2} \quad \text{and} \quad a_2(z) = a - z/\sqrt{2}.$$

In all these formulas,  $i = 1, 2$ .

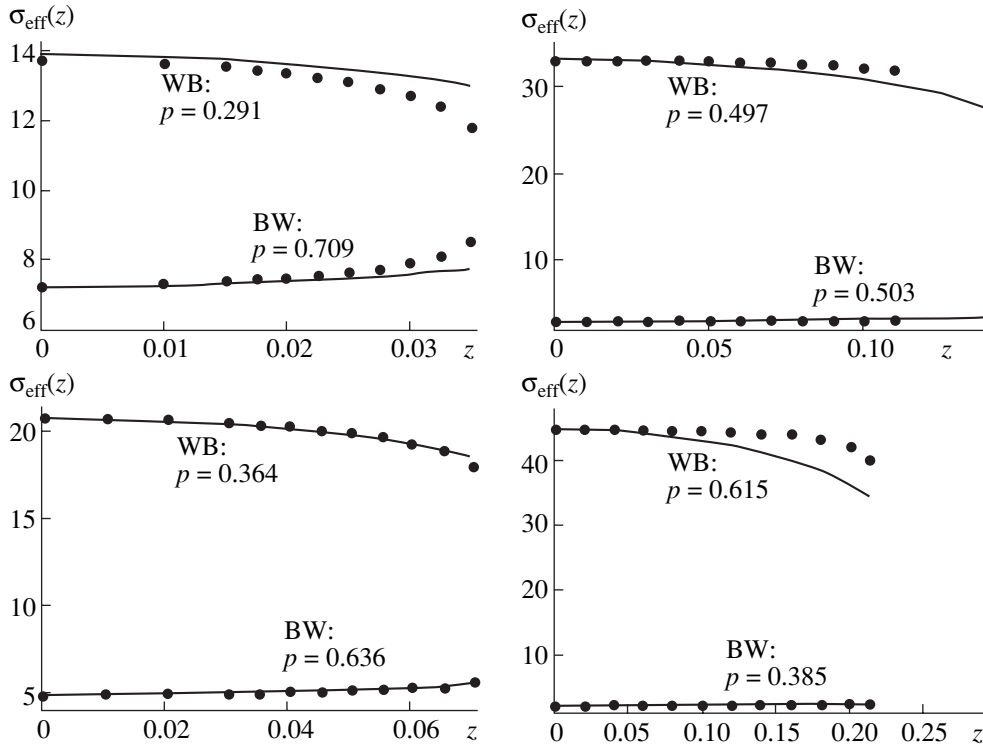


**Fig. 8.** Determination of the working interval of concentrations for poorly conducting inclusions in a well-conducting matrix (the WB case) and well-conducting inclusions in a poorly conducting matrix (the BW case) by comparing the calculations by formulas (13) and (14) with the direct numerical calculation. The continuous curve corresponds to the analytical calculation (formulas (13) and (14)), and the filled circles correspond to the numerical calculation.

## CONCLUSIONS

In the linear case, the weak disorder considered in this work does not violate the scaling dependence of the effective conductivity on the closeness to percolation threshold  $\tau$  (Figs. 4, 6; expression (20)). It should also be noted that, for random displacements and ultimate concentrations of inclusions (see (20)), the critical index is exactly equal to  $1/2$ , which agrees well with the no-shift case [7].

The nonlinear case is considered for only one type of nonlinearity, namely, for that typical of the permeability of a ferromagnet. The direct numerical experiment demonstrates that the approximate methods adequately describe the field and concentration dependences up to the field at which  $\sigma_{\text{eff}}(E)$  attains a maximum (Fig. 7).

## APPENDIX

The computational simulation was performed with the use of the OPERA-2D commercial software package (Vector Fields Co. [23]). This package employs the finite element method for the direct solution of the two-dimensional Maxwell equations. A graphical preprocessor allows one to represent two-dimensional objects in the form of polygons with edges of a given curvature and assign them the properties of relevant materials. An

automated grid generator partitions these polygons into elementary subdomains (finite elements). Within each of the finite elements, a solution is sought in the form of simple functions, e.g., polynomials. From symmetry considerations, it suffices to solve the Maxwell equations within a single elementary block. Such an elementary block is a  $2a \times 2a$ -square with a circular domain inside. The square and the circular domain consist of various materials, for instance, a nonlinear material and air. An applied field was specified by setting constant values of electric potential  $\phi$  (such that  $\Delta\phi = E_{\text{app}}2a$ ) on the opposite sides of the elementary block. These sides are equipotential surfaces, where the tangential component of the electric field vanishes. On two opposite sides of the block (that are parallel to the applied field), the normal component of the electric field was set equal to zero. The problem was solved by automatically refining the grid partitioning. The solution was assumed to be convergent if the difference between two successive solution steps was less than 0.1%. The processor time for a standard PC was varied from 1 min for random linear materials to 3 h for nonlinear models near the percolation threshold.

The results of numerical calculations are given in Fig. 8. The approximation considered (the “gray” grating) is adequate for black phase concentrations in the range  $0.2916 < p < 0.4970$ . This can be easily

explained: for  $p < 0.2916$ , formula (2) fails, while, for  $p > 0.497$ , the interaction between the inclusions, which is neglected in the above approximation, should be taken into account. For the BW case, black phase concentrations for which the model of a “gray” grating is valid fall into the range from 0.385 to 0.709 (see Fig. 8). Note that this range is wider than for the WB case.

#### ACKNOWLEDGMENTS

A. Snarskii is grateful to DAAD for the support of this study (grant no. A/02/16226).

M. Zhenirovskyy and R. Trautner thank Scheubeck-Jansen-Stiftung for the financial support.

#### REFERENCES

1. B. I. Shklovskii and A. L. Éfros, *Electronic Properties of Doped Semiconductors* (Nauka, Moscow, 1979; Springer-Verlag, New York, 1984).
2. T. J. Fiske, H. S. Gokturk, and D. M. Kalyon, Tech. Pap., Reg. Tech. Conf. Soc. Plast. Eng. **39**, 614 (1993).
3. D. A. Bruggeman, Ann. Phys. **24**, 636 (1935).
4. R. Landauer, J. Appl. Phys. **23**, 779 (1952).
5. M. I. Shvidler, *Statistical Hydrodynamics of Porous Media* (Nedra, Moscow, 1985) [in Russian].
6. *Proceedings of the 3rd International Conference on Electrical Transport and Optical Properties of Inhomogeneous Media*, Ed. by W. Mochan and R. Barrera; Physica A **207** (1994); *Proceedings of the 4th International Conference on Electrical Transport and Optical Properties of Inhomogeneous Media, 1996*, Ed. by A. N. Lagarkov and A. K. Sarychev; Physica A **241** (1997); *Proceedings of the 5th International Conference on Electrical Transport and Optical Properties of Inhomogeneous Media ETOPIM5, Hong Kong, 1999*, Ed. by P. M. Hui, P. Sheng, and L.-H. Tang; Physica B **279** (2000).
7. B. Ya. Balagurov and V. A. Kashin, Zh. Éksp. Teor. Fiz. **117**, 978 (2000) [JETP **90**, 850 (2000)].
8. J. B. Keller, J. Appl. Phys. **34**, 991 (1963).
9. B. I. Halperin and S. Feng, Phys. Rev. Lett. **54**, 2391 (1985).
10. S. Feng, B. I. Halperin, and P. N. Sen, Phys. Rev. B **35**, 197 (1987).
11. A. A. Snarskii and S. I. Buda, Élektrichestvo **2**, 67 (1988).
12. S. W. Kenkel and J. P. Straley, Phys. Rev. Lett. **49**, 767 (1982).
13. J. P. Straley and S. W. Kenkel, Phys. Rev. B **29**, 6299 (1984).
14. T. J. Fiske, H. S. Gokturk, and D. M. Kalyon, J. Mater. Sci. **32**, 5551 (1997).
15. V. V. Bakaev, A. A. Snarskii, and M. V. Shamonin, Zh. Tekh. Fiz. **71**, 84 (2001) [Tech. Phys. **46**, 1571 (2001)].
16. V. V. Bakaev, A. A. Snarskii, and M. V. Shamonin, Zh. Tekh. Fiz. **72**, 129 (2002) [Tech. Phys. **47**, 125 (2002)].
17. N. Shamonin, A. Snarskii, and M. Zhenirovskyy, NDT & E Int. **37**, 35 (2004).
18. A. A. Snarskii and M. I. Zhenirovskyy, J. Phys. B **322**, 84 (2002).
19. A. A. Snarskii, M. V. Shamonin, and M. I. Zhenirovskyy, Zh. Éksp. Teor. Fiz. **123** (2), 79 (2003) [JETP **96**, 66 (2003)].
20. P. M. Hui, Y. F. Woo, and W. M. V. Wan, J. Phys.: Condens. Matter **7**, L593 (1995).
21. P. M. Hui, P. Cheung, and Y. R. Kwong, Physica A **241**, 301 (1997).
22. A. M. Dykhne, Zh. Éksp. Teor. Fiz. **59**, 110 (1970) [Sov. Phys. JETP **32**, 63 (1970)].
23. <http://www.vectorfields.co.uk>.

*Translated by A. Pankratiev*



SHORT  
COMMUNICATIONS

## Simple Models of Hydrogen Adsorption on Germanium

S. Yu. Davydov

*Ioffe Physicotechnical Institute, Russian Academy of Sciences,  
Politekhnicheskaya ul. 26, St. Petersburg, 194021 Russia*

Received March 22, 2004

**Abstract**—The dependence of work function  $\Delta\phi$  on degree of coverage  $\Theta$  for the Ge(100) and Ge(111) surfaces determined in terms of simple models that include the dipole–dipole interaction of hydrogen adatoms. It is found that experimental dependence  $\Delta\phi(\Theta)$  for the Ge(111) surface can be explained by taking into account an increase in the adsorption bond length with  $\Theta$ . The charge of the adatoms as a function of  $\Theta$  is calculated, and the variation of the surface conductivity of the substrate is estimated. © 2005 Pleiades Publishing, Inc.

Although the modern theory of adsorption had been evolved from consideration of the model problem of hydrogen adsorption on metals [1], further efforts were concentrated largely on metal–metal and metal–semiconductor systems [2–4]. Gas adsorption has received much less attention. Such a situation is readily explained by the fact that an early problem of emission electronics was to minimize the work function of the system and simultaneously to heat the system to high temperatures. Metallic (or metal oxide) coatings, which reduce work function  $\phi$  by 1–3 eV, served this purpose as well as possible. Gas adsorption decreases  $\phi$  by only tenths of an electron volt. However, even such a minor decrease may considerably affect the surface conductivity of semiconductor substrates. It is this effect that resistive-type semiconductor gas sensors rely upon [5].

In this work, we consider simple models of atomic hydrogen adsorption on Ge(100) and Ge(111) surfaces, which was experimentally investigated in [6]. The measurements [6] showed that, in the H/Ge(100) system, the work function grows, the dependence  $\Delta\phi(\Theta)$  ( $\Theta = N/N_{ML}$ , where  $N$  and  $N_{ML}$  are the particle concentrations in an adlayer and monolayer, respectively) reaching a maximum at  $\Theta \approx 0.1$ . In the H/Ge(111) system, the value of  $\Delta\phi(\Theta)$  is negative at  $\Theta \leq 0.15$  (reaching a minimum at  $\Theta \approx 0.05$ ) and positive at  $\Theta > 0.15$ . According to the generally accepted concepts [2, 3], when hydrogen is adsorbed on the (100) surface, substrate electrons pass into adatoms. In the case of the (111) surface, adsorbed hydrogen donates electrons to the substrate at low coverages ( $\Theta \leq 0.15$ ) and picks up electrons at  $\Theta > 0.15$ . The change of sign of adatoms is inconsistent with the Anderson–Newns conventional model of adsorption [1, 7]. A model of adsorption for the Na/Cs system, where the change of sign of adatoms was also observed [9], was suggested in [8]. In this model, adsorption bond length  $a$  is assumed to depend on the coverage:

$$a = a_0(1 + \alpha\Theta), \quad (1)$$

where  $a_0$  is the adsorption bond length at zero coverage and  $\alpha$  is a dimensionless coefficient.

The extension of the adsorption bond is associated with the depolarization of adatoms as the coverage grows: positive charge  $Z$  of an adatom decreases, shell occupation number  $n = 1 - Z$  of the adatom rises, and shell radius  $a$  changes from a value close to ionic radius  $r_i$  to a value close to atomic radius  $r_a$ . This model will be used as the basis in the description of hydrogen atoms on Ge(111) [6].

According to the standard model of adsorption [7, 10], charge  $Z$  of an adatom is given by

$$Z(\Theta) = \frac{2}{\pi} \arctan \frac{\Omega - \xi\Theta^{3/2}Z(\Theta)}{\Gamma}, \quad (2)$$

where

$$\xi = 2e^2 a^2 N_{ML}^{3/2} A, \quad \Omega = \phi - I + \Delta, \quad \Delta = e^2/4a,$$

$\xi$  is the constant of dipole–dipole repulsion between adatoms,  $\Omega$  is the energy of the adatom quasi-level relative to the Fermi level of the substrate,  $A \approx 10$  is a dimensionless coefficient that weakly depends on the adatom lattice configuration,  $\Gamma$  is the half-width of the isolated adatom quasi-level,  $I$  is the energy of ionization of an adatom,  $\phi$  is the work function of germanium, and  $\Delta$  is the Coulomb shift of the adatom quasi-level (this shift arises when the electron of an adatom interacts with electrons of the substrate).

Adsorption-related change  $\Delta\phi$  in the work function is given by

$$\Delta\phi(\Theta) = -\Phi\Theta Z, \quad (3)$$

where

$$\Phi = 4\pi e^2 N_{ML} a.$$

Let  $\bar{\Theta}$  be the coverage meeting the condition  $\Delta\phi(\bar{\Theta}) = 0$ ; that is,  $\bar{\Theta} = 0.15$  for hydrogen adsorption on the (111) surface of germanium. We introduce vari-

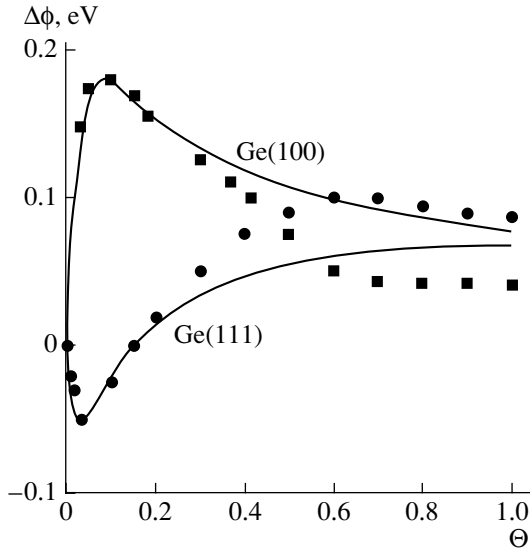


**Fig. 1.** Change  $\Delta\phi$  in the work function of the germanium surfaces vs. coverage  $\Theta$  by hydrogen atoms.

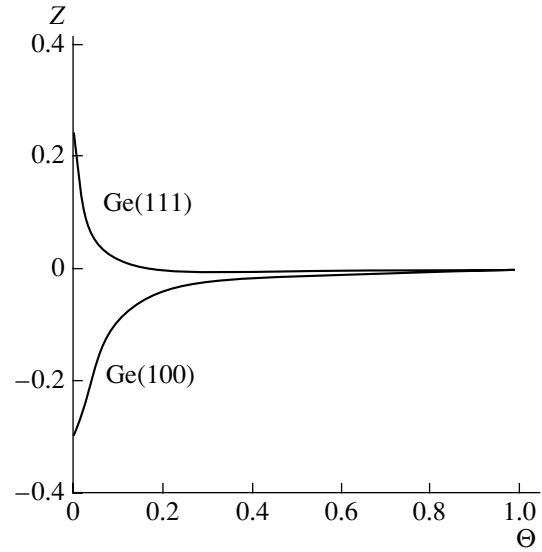


**Fig. 2.** Charge  $Z$  of a hydrogen adatom on the germanium surfaces vs. coverage  $\Theta$ .

able  $x = \Theta/\bar{\Theta}$  and put  $\bar{\xi} = \xi\bar{\Theta}^{3/2}$ ,  $\bar{\Phi} = \Phi\bar{\Theta}$ , and  $\bar{\alpha} = \alpha\bar{\Theta} = \Omega/(I - \phi)$ . Then, with regard to (1), we get, instead of (2) and (3),

$$Z = \frac{2}{\pi} \arctan \left[ \frac{\Omega_0(1-x)/(1+\bar{\alpha}x) - x^{3/2}\bar{\xi}Z(1+\bar{\alpha}x)^2}{\Gamma} \right],$$

$$\Delta\phi = -\bar{\Phi}_0x(1+\bar{\alpha}x)Z. \quad (4)$$

Here, subscript 0 indicates that the related energy parameter is calculated for  $a = a_0$ . If the charge is small, the first of expressions (4) can be recast as

$$Z \approx \frac{2\Omega_0(1-x)}{(1+\bar{\alpha}x)[\pi\Gamma + 2x^{3/2}\bar{\xi}_0(1+\bar{\alpha}x)^2]}. \quad (5)$$

To calculate the adsorption of hydrogen on Ge(111), we took the following values of the parameters:  $a_0 = 1.7 \text{ \AA}$ ,  $N_{ML} = 5.55 \times 10^{14} \text{ cm}^{-2}$ ,  $\bar{\Theta} = 0.15$ ,  $\xi_0 = 10.89 \text{ eV}$ ,  $\Phi_0 = 17.08 \text{ eV}$ ,  $\Omega_0 = 0.04 \text{ eV}$ ,  $\Gamma = 0.1 \text{ eV}$ , and  $\alpha = 0.43$ . The results of calculation of  $\Delta\phi(\Theta)$  and  $Z(\Theta)$  are shown in Figs. 1 and 2, respectively. Note that the scale in Fig. 2 shades the fine structure of the dependence  $Z(\Theta)$ : namely, charge  $Z$  first vanishes at  $\bar{\Theta}$ ; then takes a negative value, growing in magnitude up to  $\Theta = 0.3$  ( $Z(0.3) \approx -0.006$ ); and finally declines to  $Z \approx -0.003$  for a monolayer coating.

In the H/Ge(100) system, the dependence  $\Delta\phi(\bar{\Theta})$  does not change sign, remaining positive at any  $\Theta$ . Therefore, we can put  $\alpha = 0$  in this case and carry out the calculation by formula (2) for  $N_{ML} = 6.25 \times 10^{14} \text{ cm}^{-2}$ ,  $\xi = 10.89 \text{ eV}$ ,  $\Phi = 19.23 \text{ eV}$ ,  $\Omega = -0.053 \text{ eV}$ , and  $\Gamma = 0.1 \text{ eV}$ .

Comparison of the experimental and analytical values of the work function shows their good agreement for low coverages ( $\Theta = 0.2-0.3$  or less). At the same time, they diverge significantly when the coverage is high (close to a monolayer). The latter fact is not surprising, since the starting model [7, 10] is constructed just for small coverages. At high coverages, one must take into account not only dipole-dipole interaction but also exchange effects [3]. This can be done, for example, by considering the smearing of the quasi-level [11, 12]. However, we omit the case of high coverages, since the electronic state of an adlayer changes most considerably when the coverage is low.

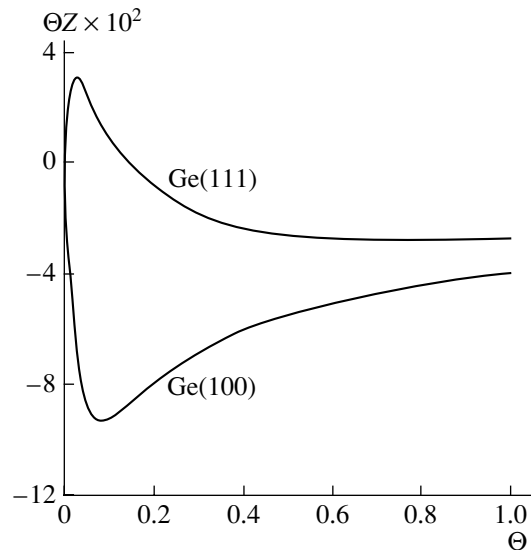


**Fig. 3.**  $\Theta$  dependence of the product  $|Z(\Theta)|\Theta$ , which varies in proportion to change  $\Delta\sigma$  in the surface conductivity.

Since hydrogen adsorbed on Ge(111) donates electrons to the substrate at  $\Theta \leq 0.15$  and accepts them at higher coverages, surface conductivity  $\sigma$  first increases relative to the conductivity of the uncovered surface and then drops. Figure 3 shows the  $\Theta$  dependence of product  $|Z(\Theta)|\Theta$ , which varies in proportion to change  $\Delta\sigma$  in the surface conductivity. Qualitatively, the calculation results fit the experimental data well [6].

It should be noted in conclusion that reasons for such different behavior of the hydrogen-coated Ge(100) and Ge(111) surface are still not clearly understood [6]. It is speculated that the hydrogen causes the  $2 \times 8$ -to- $1 \times 1$  surface reconstruction in the first case, while it removes the asymmetry of surface Ge–Ge dimers in the other. Our results obtained in terms of the simple models also suggest that the configuration of Ge(111) is much more sensitive to hydrogen adsorption than that of Ge(100).

#### REFERENCES

1. D. M. News, Phys. Rev. **178**, 1123 (1969).
2. L. A. Bol'shov, A. P. Napartovich, A. G. Naumovets, and A. G. Fedorus, Usp. Fiz. Nauk **122**, 125 (1977) [Sov. Phys. Usp. **20**, 432 (1977)].
3. O. M. Braun and V. K. Medvedev, Usp. Fiz. Nauk **157**, 631 (1989) [Sov. Phys. Usp. **32**, 328 (1989)].
4. L. A. Bol'shov and M. S. Veshchunov, Poverkhnost: Fiz. Khim. Mekh., No. 7, 5 (1989).
5. I. A. Myasnikov, V. Ya. Sukharev, L. Yu. Kupriyanov, and S. A. Zav'yalov, *Semiconductor Sensors for Physicochemical Research* (Nauka, Moscow, 1991) [in Russian].
6. L. Surnev and M. Tikhov, Surf. Sci. **138**, 40 (1984).
7. J. P. Muscat and D. M. News, J. Phys. C **7**, 2630 (1974).
8. S. Y. Davydov, Appl. Surf. Sci. **140**, 52 (1999).
9. F. Xu, G. Manico, F. Ascione, *et al.*, Phys. Rev. B **54**, 10401 (1996).
10. S. Yu. Davydov, Fiz. Tverd. Tela (Leningrad) **19**, 3376 (1977) [Sov. Phys. Solid State **19**, 1971 (1977)].
11. S. Yu. Davydov and I. V. Noskov, Pis'ma Zh. Tekh. Fiz. **27** (20), 1 (2001) [Tech. Phys. Lett. **27**, 844 (2001)].
12. S. Yu. Davydov and I. V. Noskov, Zh. Tekh. Fiz. **72** (11), 137 (2002) [Tech. Phys. **47**, 1481 (2002)].

*Translated by V. Isaakyan*

SHORT  
COMMUNICATIONS

# Spectroscopic Diagnostics of the Laser Erosion Plasma of an AgGaS<sub>2</sub> Polycrystalline Target

A. K. Shuaibov and M. P. Chuchman

Uzhhorod National University, vul. Pidgirna 46, Uzhhorod, 88000 Ukraine

e-mail: ishev@univ.uzhgorod.ua

Received October 28, 2003; in final form, March 19, 2004

**Abstract**—Results are presented from experimental studies of the radiation emitted from a plasma produced in vacuum after irradiating a polycrystalline target by 1.06- $\mu\text{m}$  laser radiation with an intensity of  $(3\text{--}5) \times 10^8 \text{ W/cm}^2$ . Plasma radiation from regions located at distances of 1 and 7 mm from the target is analyzed. It is shown that the main contribution to the plasma radiation in the 220–600 nm spectral range is made by transitions from the excited states of single-charged Ag<sup>+</sup> and S<sup>+</sup> ions. The atomic component of plasma radiation is represented by intense spectral lines corresponding to transitions from the Rydberg states of Ag and Ga atoms, whereas no resonance lines of these atoms are observed. © 2005 Pleiades Publishing, Inc.

## INTRODUCTION

Polycrystalline batch mixture of the AgGaS<sub>2</sub> compound is a promising material for the pulsed deposition of thin films used in solar batteries, optical filters, and nonlinear IR–visible light converters. The specific features of the laser processing of materials and pulsed laser deposition, as well as the influence of the matrix effect on the results of laser spectroscopy, stimulate interest in studying the laser erosion of multicomponent compounds and the expansion of the plasma produced [1–3]. Such a plasma can be studied using laser mass-spectrometry [4] and also emission spectroscopy [5], which is most efficient at small distances from the target.

In this paper, we present results from studying the radiation emitted from a laser erosion plasma produced by irradiating a massive AgGaS<sub>2</sub> polycrystalline target. Plasma radiation from regions located at distances of 1 and 7 mm from the target is analyzed. The irradiation conditions were close to those used to sputter materials when depositing thin films. The optical characteristics of silver and gallium laser plasmas were earlier studied in experiments with one-component Ag [6] and Ga [7, 8] targets. The diagnostic technique, apparatus, and experimental conditions were similar to those used previously by us in [6–8].

## RESULTS AND DISCUSSION

Figure 1 shows emission spectra of an AgGaS<sub>2</sub> laser plasma from two different regions located at distances of  $r = 1$  and 7 mm from the target. The identified spectral lines and the relative line intensities (with allowance for the spectral sensitivity  $k_\lambda$  of the measurement system) are presented in Tables 1 and 2. The emission spectrum of the multicomponent AgGaS<sub>2</sub> plasma is not

a superposition of the most intense spectral lines of the individual crystal constituents. Control experiments with a Ga target showed that the most intense spectral

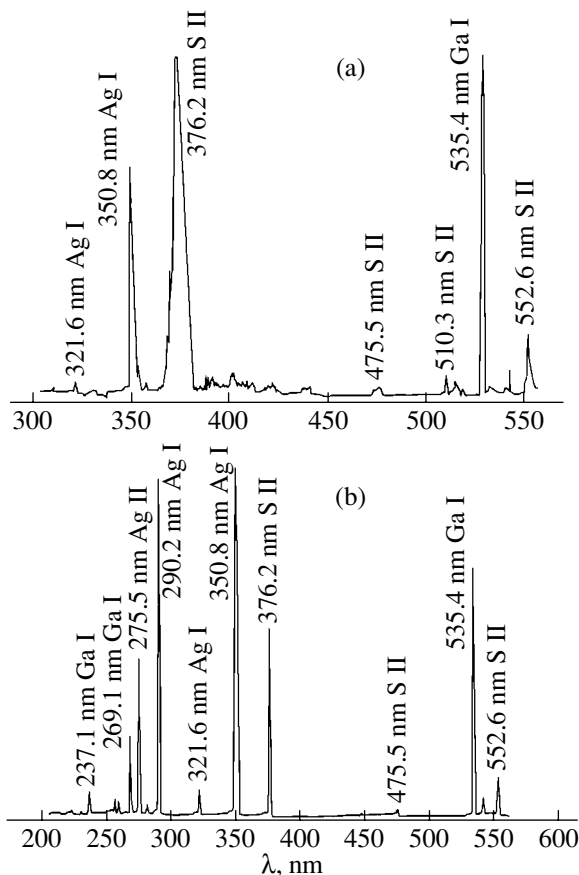


**Fig. 1.** Emission spectra of an AgGaS<sub>2</sub> laser plasma from two different regions located at distances of (a) 1 and (b) 7 mm from the target.

**Table 1.** Relative intensities of the spectral lines emitted from an AgGaS<sub>2</sub> laser erosion plasma at a distance of  $r = 1$  mm from the target

$\lambda$ , nm	Atom, ion	$E_{up}$ , eV	$I/k_\lambda$
321.6	Ag I	10.82	0.08
350.8	Ag I	7.2	1.24
376.2	S II	29.89	1.72
475.5	S II	27.8	0.10
535.4	Ga I	5.39	3.94
542.9	S II	26.26	0.29
552.6	S II	26.34	0.81
510.3	S II	26.5	0.20
386.1	S II	29.74	0.08
385.1	S II	29.72	0.08
389.2	S II	–	0.07
397.1	S II	29.72	0.10
405.9	S II	29.72	0.11
418.7	S II	30.76	0.07

**Table 2.** Relative intensities of the spectral lines emitted from an AgGaS<sub>2</sub> laser erosion plasma at a distance of  $r = 7$  mm from the target

$\lambda$ , nm	Atom, ion	$E_{up}$ , eV	$I/k_\lambda$
237.1	Ga I	5.32	0.22
256.4	Ag II	23.11	0.10
259.6	Ag II	23.14	0.08
269.1	Ga I	4.71	0.41
275.7	Ag II	23.14	0.78
281.6	Ag II	23.14	0.06
290.2	Ag II	22.58	1.68
321.6	Ag I	10.82	0.13
350.8	Ag I	7.2	1.72
376.2	S II	29.89	0.74
475.5	S II	27.8	0.06
535.4	Ga I	5.39	2.24
542.9	S II	26.26	0.19
552.6	S II	26.34	0.43

lines were the Ga I 403.3-, 294.4-, 417.3-, and 287.5-nm lines, whose total contribution to the emission intensity was about 90%. For silver plasma, the most intense spectral lines were the Ag I 328.1- and 338.3-nm resonance lines (39 and 26% of the total intensity, respectively). For sulfur targets, no laser plume was formed and only surface emission was observed. The emission spectrum of the multicomponent laser plasma did not contain the characteristic lines of the individual target constituents (the lines corresponding to transitions from the low energy states of Ag and Ga atoms). The emitting component of the laser plasma was mainly represented by SII and Ag II ions and by the Rydberg states of Ag I and Ga I. The emission spectrum recorded at a distance of 1 mm from the target contained a significant number of weak (at a level close to the detection limit of the apparatus) sulfur lines. In the spectral range of 370–380 nm, a series of intense unresolved spectral lines of sulfur ions was observed. At a distance of 7 mm from the target, the emission spectrum became a pure line spectrum. Weak sulfur lines disappeared, while the intensities of the remaining sulfur lines decreased. The intensities of gallium lines also decreased, whereas the intensities of atomic silver lines increased with distance from the target.

Taking into account the structure of the emission spectrum and the relationship between the ionization energies of the individual AgGaS<sub>2</sub> constituents,  $E_i(\text{S}) > E_i(\text{Ag}) > E_i(\text{Ga})$ , we may assert that the excitation of ions is not directly associated with the excitation and ionization of free atoms. The structure of the spectrum may be governed by chemical reactions in the laser

plume and specific mechanisms for molecular dissociation.

To interpret the results obtained, let us comparatively analyze the properties of the target material and the specific features of laser erosion.

Chemical bonds in an AgGaS<sub>2</sub> molecule are determined by the  $sp^3$  hybridization of the constituent atoms. The valence electrons are uniformly distributed among the constituents of an AgGaS<sub>2</sub> molecule, thus forming S<sup>2+</sup>, Ga<sup>1-</sup>, and Ag<sup>3-</sup> ions. This circumstance accounts for the high atomization energy. The absorption coefficient at a wavelength of 1.064  $\mu\text{m}$  ranges from 0.001 to 0.009  $\text{cm}^{-1}$ . The AgGaS<sub>2</sub> compound is characterized by the low density of free charge carriers, the width of the forbidden zone of  $E_g = 2.51\text{--}2.75$  eV, and the presence of  $p$ -type energy levels (0.11 and 0.72 eV) in the forbidden zone [9]. The energy structure of the target material is strongly deformed because of the use of a batch mixture.

When  $h\nu < E_g$ , the absorption coefficient is low and the bulk of energy required for laser erosion is deposited via inverse bremsstrahlung. The necessary amount of free electrons is produced via the multiphoton ionization of negative ions in the target. The absorbed radiation energy is transferred from electrons to molecules, thus heating the target material, rearranging chemical bonds, producing radicals, and delivering energy to the molecules that is sufficient for their escape from the target [10]. The photodestruction of the target is accompanied by the escape of electrons from the interaction region both inward the target and into vacuum; this, in turn, intensifies the surface erosion caused by the Coulomb interaction between ions, as well as between ions

and the electrons emitted into vacuum [11]. The specific properties of the target material stimulate photoheating and hamper the propagation of a thermal wave, whose velocity is anyway low (on the order of the speed of sound).

Our experimental results show the presence of gallium atoms in Rydberg states and the absence of gallium ions in the laser plume. Hence, we may suggest that the energy that has been deposited in the target via photoionization is spent on the escape of neutral molecules from the solid. This process is accompanied by the production of a large amount of sulfur ions since, in spite of the electron capture from silver atoms (which are easily ionized when within the solid structure), the electron density is not high enough to complete the electron shells of sulfur atoms. The above considerations point to the volume character of erosion, which proceeds through a direct solid–plasma phase transition.

The increase in the emission intensity of Ag atoms as the plasma plume expands can be explained by the intensification of thermal processes, which, taking into account the low dissociation energy of the silver-containing radicals, the high probability of the rearrangement of chemical bonds in ionized molecules and radicals, the high chemical activity of sulfur ions and ionized radicals, and the low chemical activity of gallium, provoke the production of silver ions and atoms. The contribution from dissociative recombination can be ignored because of the high atomization energy and the escape of electrons from the plasma. Most likely, dissociative recombination governs the composition of radicals.

In contrast to Ga atoms, the formation of the Rydberg states of sulfur ions and silver atoms is probably related to the absorption of laser radiation by all the valence electrons and even by the atomic core electrons, which do not take part in the formation of the molecular chemical bonds. The nonradiative relaxation of these states can also be one of the reasons for the destruction of the chemical structure of the target material. On the other hand, the low electron temperature and the collisionless character of plasma expansion (which are confirmed by the absence of low excited states) stimulate the recombination processes and the radiative decay of the highly excited states of atoms and single-charged ions. To gain a better insight into the above processes, it is necessary to perform additional mass-spectrometric studies of the plasma composition and to more accurately estimate the plasma parameters.

The most intense spectral lines from the laser erosion plasma are the Ag I 350.8-nm, Ga I 535.4-nm, Ag II 275.7-nm, Ag II 290.2-nm, S II 376.2-nm, and S II 552.6-nm lines. At  $r = 7$  mm, the bottlenecks of the recombination flow correspond to the 5.39-eV (Ga) and 10.82-eV (Ag) atomic levels and the 23.14-eV (Ag<sup>+</sup>) and 29.89-eV (S<sup>+</sup>) ionic levels. At  $r = 1$  mm, the bottlenecks of the recombination flow for the atomic compo-

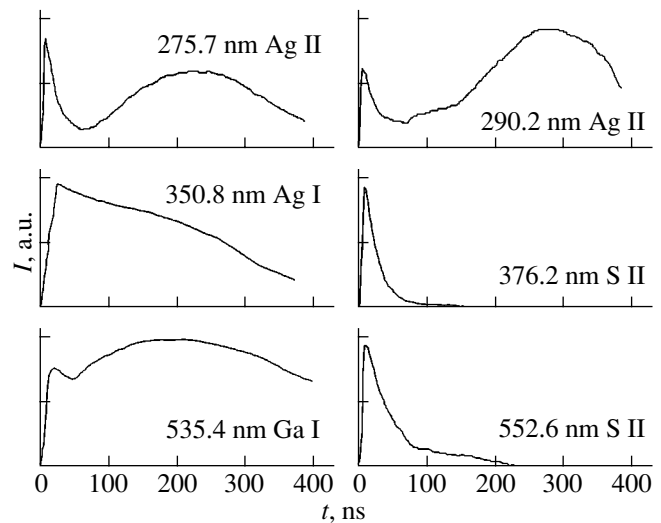


**Fig. 2.** Waveforms of the intensities of the most intense spectral lines emitted from an AgGaS<sub>2</sub> laser erosion plasma at a distance of 1 mm from the target.

nent are the same, while for the ion component, the bottleneck corresponds to the 30.76-eV level.

Figure 2 shows the waveforms of the line emission intensities from the expanding plasma. The spectral line intensities of argon and sulfur ions and argon and gallium atoms were recorded at a distance of 1 mm from the target. The emission intensities of the ion lines follow the shape of the laser pulse, whereas the line intensities corresponding to the radiative decay of the shifted excited states of silver and gallium continue to increase until the end of the laser pulse. Then (up to  $t = 60$ – $70$  ns), the spectral line intensities decrease (except for the Ag I line, which shows a specific behavior). From 70 to 150 ns, the emission intensity of sulfur ions decreases more slowly, whereas the emission intensity of the Ag II 290.2-nm spectral line shows a weakly pronounced maximum. After  $t = 150$  ns, the emission intensity of sulfur ions sharply decreases (the higher the excitation energy, the faster the decrease). The spectral line intensities of silver ions continue to increase up to  $t = 260$  ns and then begin to decrease. For low ion energy states, the second maximum of the emission intensity is much higher than the first one. The waveform of the intensity of the Ga I 535.4-nm spectral line resembles that of the Ag II spectral lines. The intensity of the Ag I 350.8-nm spectral line gradually decreases up to  $t = 260$  ns and then decays at a faster rate.

The excited states are produced in two stages. In view of the rapid expansion of the laser erosion plasma [12], these stages may be related to the dynamics of the plasma formation and expansion. In the first stage, photochemical erosion is dominant. The long tail in the waveform of the S II emission and the intermediate maximum in the waveform of the Ag II emission indicate that the erosion is stimulated by the radiation from the plasma itself. The second maximum in the wave-

form of the emission intensity shows that the erosion is significantly affected by thermal processes, which intensify the production of the low excited states of Ag II. In spite of the volume character of laser absorption, the two stages of plasma production can be caused by the increase in the absorption ability of the upper layer of the target material during its heating and by the explosive character of its expansion.

The recombination time estimated by the decay rate of the emission intensity from the highly excited sulfur and silver ions within the time interval of 30–70 ns amounts to 19 and 21 ns, respectively.

### CONCLUSIONS

The emitting component of the laser plasma is mainly represented by S II and Ag II ions and by the Rydberg states of Ag I and Ga I ions. The emission spectrum contains no atomic resonance lines. The most intense spectral lines are Ag I 350.8-nm, S II 376.2-nm, S II 552.6-nm, Ga I 535.4-nm, Ag II 275.7-nm, and Ag II 290.2-nm lines.

The specific features of the production of the excited states are related to the direct decomposition of the ionized AgGaS<sub>2</sub> molecules in the course of the direct solid–plasma phase transition induced by photochemical processes.

The bottlenecks of the recombination production of highly excited states of sulfur ions correspond to the 30.76-eV (for  $r = 1$  mm) and 29.89-eV (for  $r = 7$  mm) levels. For the atomic plasma component, the bottleneck corresponds to the shifted atomic levels of Ga and Ag and is independent of  $r$ . The recombination times of the S<sup>2+</sup> and Ag<sup>2+</sup> ions at a distance of 1 mm from the target are 19 and 21 ns, respectively.

The results obtained are of interest for optimizing the laser deposition of thin AgGaS<sub>2</sub> films and the laser spectral analysis of multicomponent compounds.

### REFERENCES

1. Hai-Xing Wang and Xi Chen, *J. Phys. D* **36**, 628 (2003).
2. M. Karas, M. Gluckmann, and J. Schafer, *J. Mass Spectrom.* **35**, 1 (2000).
3. E. Millon, O. Albert, J. C. Loulergue, *et al.*, *J. Appl. Phys.* **88**, 6937 (2000).
4. I. E. Kacher, I. I. Opachko, and M. Yu. Rigan, *Ukr. Fiz. Zh.* **34**, 1728 (1989).
5. A. K. Shuaibov, L. L. Shimon, and M. P. Chuchman, *Zh. Tekh. Fiz.* **71** (5), 85 (2001) [*Tech. Phys.* **46**, 590 (2001)].
6. A. K. Shuaibov, *Pis'ma Zh. Tekh. Fiz.* **27** (19), 1 (2001) [*Tech. Phys. Lett.* **27**, 801 (2001)].
7. A. K. Shuaibov, L. L. Shimon, A. J. Dashchenko, and M. P. Chuchman, *Uzhgorod Univ. Sci. Herald, Ser. Fiz.* **8** (Part 2), 348 (2000).
8. A. K. Shuaibov, L. L. Shimon, A. I. Dashchenko, *et al.*, *Fiz. Plazmy* **27**, 85 (2001) [*Plasma Phys. Rep.* **27**, 82 (2001)].
9. *Properties of Inorganic Compounds: A Handbook* (Khimiya, Leningrad, 1983).
10. N. B. Delone, *Interaction of Laser Radiation with Materials* (Nauka, Moscow, 1989) [in Russian].
11. S. S. Harilal, C. V. Bindhu, M. S. Tillack, *et al.*, *J. Phys. D* **35**, 2935 (2002).
12. O. K. Shuaibov, M. P. Chuchman, and L. L. Shimon, *Zh. Tekh. Fiz.* **73** (4), 77 (2003) [*Tech. Phys.* **48**, 455 (2003)].

*Translated by N. Ustinovskii*

**SHORT  
COMMUNICATIONS**

# Synthesis of Currents on a Disk Using a Directional Diagram

**S. I. Éminov**

*Ya. Mudryi State University, Nizhni Novgorod, 173003 Russia*

*e-mail: theorphy@novsu.ac.ru*

Received April 27, 2004

**Abstract**—The problem of synthesis of currents using a realizable or unrealizable directional diagram is solved. In the former case, the problem is solved analytically: the current is sought as a series in basis, with each of the basis functions satisfying the Meixner condition on an edge. If the diagram is unrealizable, the current is found from a solution to an integral equation with a small parameter. The solution to the integral equation also satisfies the Meixner condition on an edge. © 2005 Pleiades Publishing, Inc.

## 1. PROBLEM DEFINITION

Being fundamental, the problem of current synthesis has been considered by many authors. In [1, 2], the author suggested analytical methods for finding a current from a realizable directional diagram.

It was also suggested [3] that currents be found from an arbitrary directional diagram by solving an integral equation with a small parameter. Such a solution, however, may not satisfy the Meixner condition on an edge.

In this work, the author finds surface currents that satisfy the Meixner condition, using new approaches [4–6] and a set of functions including the Meixner condition on an edge [7].

## 2. BASIC INTEGRAL EQUATIONS OF SYNTHESIS

A relation between surface currents  $\mathbf{j}(j_r, j_\varphi)$  and directional diagram  $\mathbf{F}(F_\theta, F_\varphi)$  is described by a set of two integral equations [6]:

$$\iint_S [j_r(\mathbf{t}_\theta \cdot \mathbf{t}_r) + j_\varphi(\mathbf{t}_\theta \cdot \mathbf{t}_\varphi)] \exp(ikr' \cos \gamma) ds = F_\theta, \quad (1)$$

$$\iint_S [j_r(\mathbf{t}_\varphi \cdot \mathbf{t}_r) + j_\varphi(\mathbf{t}_\varphi \cdot \mathbf{t}_\varphi)] \exp(ikr' \cos \gamma) ds = F_\varphi. \quad (2)$$

Here,  $\mathbf{t}_\theta$ ,  $\mathbf{t}_\varphi$ , and  $\mathbf{t}_R$  are the unit vectors in the spherical coordinate system;  $\mathbf{t}_\varphi$  and  $\mathbf{t}_r$  are the unit vectors in the polar coordinate system on the surface of a circle;  $r'$  is the distance between the origin and an observation point on surface  $S$ ; and  $\gamma$  is the angle between the directions to the observation point and source point (the directions issue from the origin).

Equations (1) and (2) constitute a set of coupled integral equations in two variables. For simplicity, we will consider the case where the currents and diagram are  $\varphi$ -independent. Then, the set is split into two independent equations. After straightforward mathematical

transformations, the equation for radial currents will take the form

$$2\pi i \cos \theta \int_0^a j_r(r') J_1(kr' \sin \theta) r' dr' = F_\theta(\theta), \quad (3)$$

and that for azimuth currents,

$$2\pi i \sin \theta \int_0^a j_\varphi(r') J_1(kr' \sin \theta) r' dr' = F_\varphi(\theta). \quad (4)$$

Here,  $k$  is the wavenumber and  $J_1$  is the Bessel function.

## 3. THE ESSENCE OF THE SYNTHESIS PROBLEM

A solution to Eq. (3) is bound to give currents satisfying the Meixner condition,

$$j_r(r) \approx \sqrt{a^2 - r^2}, \quad r \rightarrow a,$$

and a solution to Eq. (4) must go to infinity by the law

$$j_\varphi(r) \approx \frac{1}{\sqrt{a^2 - r^2}}, \quad r \rightarrow a.$$

On the other hand, integral equations (3) and (4) have the same structure, but the coefficients multiplying the integral are different.

Making the change  $\sin \theta = x$  and carrying out straightforward transformations, we combine both equations to get

$$\int_0^1 j(t) J_1(akt) t dt = F(x), \quad (5)$$

where  $J_1$  is the Bessel function.

Equation (5) does not bear information on current and is insufficient for the current with desired behavior



on an edge be found. Additional information is therefore needed in order to solve the synthesis problem. Such information may be the specification of a functional space which the currents belong to. The current space, in its turn, can be determined by solving the analysis problem, i.e., via finding the currents induced by the primary field.

An integral or integro-differential equation of the analysis problem contain full information on the behavior of the current on an edge.

Finally, it should be noted that the current space is completely defined by the surface geometry and polarization. Therefore, the problem of antenna synthesis is essentially reduced to the problem of current space construction.

#### 4. CURRENT SPACES AND BASES

A current space is constructed using the operator of the analysis problem or, more strictly, its principal positive part. For the radial currents, this operator has the form

$$Aj_r = \int_0^{+\infty} J_1(ax\tau)\tau x^2 \int_0^1 j_r(t)J_1(axt)t dt dx; \quad (6)$$

for the azimuth currents,

$$Lj_\phi = \int_0^{+\infty} J_1(ax\tau)\tau \int_0^1 j_\phi(t)J_1(axt)t dt dx. \quad (7)$$

Operators  $A$  and  $L$  are positive. As spaces, we take the energy spaces of these operators,  $H_A$  and  $H_L$ . The scalar product and norm, e.g., in  $H_A$ , are given by the formulas

$$[u, v] = (Au, v), \quad [u]^2 = (Au, u), \quad (8)$$

where (...) means the scalar product in  $L_2[0, 1]$ .

In [7], sets of functions  $\varphi_n(t)$  and  $\psi_n(t)$ ,  $n = 1, 2, \dots$ , were suggested for which the Hankel transforms are given by

$$\tilde{\varphi}_n(x) = \int_0^1 \varphi_n(t)J_1(axt)t dt = \sqrt{4n+1} \frac{J_{2n+\frac{1}{2}}(ax)}{x^{\frac{3}{2}}}, \quad (9)$$

$$\tilde{\psi}_n(x) = \int_0^1 \psi_n(t)J_1(axt)t dt = \sqrt{4n+1} \frac{J_{2n-\frac{1}{2}}(ax)}{x^{\frac{1}{2}}}, \quad (10)$$

respectively.

On an edge, the former behave in the same way as the radial currents and the latter, as the azimuth currents. In other words, functions  $\varphi_n(t)$  and  $\psi_n(t)$  satisfy the Meixner condition on an edge. Moreover, these

functions turn out to be orthogonal to each other; namely,

$$(A\varphi_m, \varphi_n) = \sqrt{(4m+1)(4n+1)} \times \int_0^{+\infty} \frac{J_{2m+\frac{1}{2}}(ax)J_{2n+\frac{1}{2}}(ax)}{x} dx = \delta_{mn} = \begin{cases} 1, & m = n \\ 0, & m \neq n. \end{cases} \quad (11)$$

The integral in (11) is a tabulated integral [8]. Also, the following relationship holds:

$$(L\psi_m, \psi_n) = \delta_{mn}.$$

Thus, the set of functions  $\{\varphi_n\}_{n=1}^{+\infty}$  forms an orthonormalized basis of space  $H_A$  and the set of functions  $\{\psi_n\}_{n=1}^{+\infty}$  is a basis of space  $H_L$ .

#### 5. CURRENT SYNTHESIS FROM A REALIZABLE DIAGRAM AND CRITERION OF REALIZABILITY

Let us return to the synthesis equation

$$Kj = \int_0^1 j(t)J_1(axt)t dt = F(x), \quad 0 \leq x \leq 1. \quad (12)$$

If operator  $K$  (the left of (12)) maps space  $H_A$  into space  $L_2[0, 1]$ , it turns out to be completely continuous and, hence, noninvertible. If, however, this operator maps  $H_A$  into some space on a ray (i.e.,  $0 \leq x < +\infty$ ), it becomes invertible. Let us introduce Gilbert space  $H_1(0, +\infty)$  through the scalar product

$$(u, v)_1 = \int_0^{+\infty} u(x)\overline{v(x)}x^2 dx \quad (13)$$

and assume that the right of (12),  $F(x)$ , is an element of this space. Now we will find the diagrams meeting the basis functions  $\varphi_n$  of the currents. From (9), we have

$$\tilde{\varphi}_n(x) = K\varphi_n = \sqrt{4n+1} \frac{J_{2n+\frac{1}{2}}(ax)}{x^{\frac{3}{2}}}. \quad (14)$$

The diagrams found are orthogonal to each other. Operator  $K$  as an operator mapping space  $H_A$  into space  $H_1(0, +\infty)$  is isomorphic; in such mapping, the norm remains unchanged. Therefore, the map of  $H_A$  (mapped with operator  $\text{Im}K$ ) will be a closed set for such mapping. In this set, inverse operator  $K^{-1}$  is defined and bounded.

An arbitrary function  $F$  from a class of diagrams is now expanded in orthonormalized basis  $\tilde{\varphi}_n(x)$ ,

$$F(x) = \sum_{n=1}^{+\infty} C_n \tilde{\varphi}_n(x), \quad C_n = (F, \tilde{\varphi}_n)_1. \quad (15)$$

Directional diagrams are realizable if they, first, belong to space  $H_1(0, +\infty)$  and, second, meet the closeness equation

$$\|F\|_1^2 = \sum_{n=1}^{+\infty} |C_n|^2. \quad (16)$$

From expansion (15), we can immediately write the expansion for the current

$$j(t) = \sum_{n=1}^{+\infty} C_n \varphi_n(t). \quad (17)$$

The azimuth currents are synthesized in the same way. Here, operator  $K$  maps space  $H_L$  into space  $H_0(0, +\infty)$ , which is defined by the scalar product

$$(u, v)_0 = \int_0^{+\infty} u(x) \overline{v(x)} dx. \quad (18)$$

The maps of basis currents  $\psi_n$  (mapped with operator  $K$ ) form a closed set of realizable diagrams. It should be noted that, expanding a given realizable diagram in  $H_0(0, +\infty)$ ,

$$F(x) = \sum_{n=1}^{+\infty} C_n \tilde{\psi}_n(x), \quad C_n = (F, \tilde{\psi}_n)_0, \quad (19)$$

we find the currents

$$j(t) = \sum_{n=1}^{+\infty} C_n \psi_n(t), \quad (20)$$

realizing the given directional diagram.

### 6. CURRENT SYNTHESIS FROM AN ARBITRARY (NOT NECESSARILY REALIZABLE) DIAGRAM

If a diagram is unrealizable, it is necessary to find the currents that realize an approximate one and have the least norm. In [5, 6, 8], this problem was solved using equations with a small parameter. For the radial currents, the related equation has the form

$$Aj + K^*Kj = K^*F, \quad (21)$$

where

$$K^*F = \int_0^1 F(x) J_1(ax\tau) \tau dx,$$

$$K^*Kj = \int_0^1 J_1(ax\tau) \tau \int_0^1 j(t) J_1(ax\tau) t dt dx.$$

For the azimuth currents, the equation with a small parameter appears as

$$Lj + K^*Kj = K^*F. \quad (22)$$

Equations (21) and (22) only differ in their positive operators, which does not influence the structure of the equations. We will briefly discuss the theory of these equations, e.g., Eq. (21) and a method of approximate solution (for Eq. (22), the reasoning is the same).

Operator  $A$  is positive; therefore, it has a reciprocal,  $A^{-1}$ . Multiplying both sides of (21) by  $A^{-1}$  yields

$$j + A^{-1}K^*Kj = A^{-1}K^*F. \quad (23)$$

The operators on the left act in space  $H_A$ . The kernel of operator  $K^*K$  is smooth and infinitely often differentiable. With this in mind, one can easily check that operator  $A^{-1}K^*K$  is a completely continuous operator in  $H_A$ . Consequently, integral equation (23) is a Fredholm equation of the second kind.

Thus, Eq. (21) is equivalent to a Fredholm equation of the second kind. In addition, the left of (23) is a positive operator, since

$$[A^{-1}K^*Kj, j] = (K^*Kj, j) = (Kj, Kj).$$

Therefore, Eq. (23) has a unique solution. To find it, we expand the current in basis,

$$j(t) = \sum_{n=1}^N C_n \varphi_n(t), \quad (24)$$

substitute (24) into (23), and multiply both sides by  $\varphi_m(t)$  in space  $H_A$  ( $m$  runs from 1 to  $N$ ). Eventually, we arrive at the set of linear algebraic equations

$$C_n + \sum_{m=1}^N C_m K_{mn} = l_n, \quad 1 \leq n \leq N, \quad (25)$$

where

$$K_{mn} = \sqrt{(4n+1)(4m+1)} \int_0^1 \frac{J_{2n+\frac{1}{2}}(ax) J_{2m+\frac{1}{2}}(ax)}{x^3} dx,$$

$$l_n = \sqrt{(4n+1)} \int_0^1 F(x) \frac{J_{2n+\frac{1}{2}}(ax)}{x^{\frac{3}{2}}} dx.$$

Solving set (25) yields the coefficients of expansion of the current in basis. Knowing these coefficients, one can find the norm of the current and a directional dia-

gram of the currents. If necessary, the basis functions can be found using the Hankel transformation.

#### REFERENCES

1. S. I. Éminov, Zh. Vychisl. Mat. Mat. Fiz. **41**, 450 (2001).
2. S. I. Éminov, Zh. Tekh. Fiz. **71** (2), 82 (2001) [Tech. Phys. **46**, 212 (2001)].
3. L. D. Bakhrakh and S. D. Kremenetskiĭ, *Synthesis of Radiating Systems: The Theory and Computational Methods* (Sov. Radio, Moscow, 1974) [in Russian].
4. S. I. Éminov, Pis'ma Zh. Tekh. Fiz. **26** (14), 97 (2000) [Tech. Phys. Lett. **26**, 637 (2000)].
5. S. I. Éminov, Izv. Vyssh. Uchebn. Zaved. Radiofiz. **45**, 328 (2002).
6. S. I. Éminov, Antenny, No. 6 (61), 61 (2002).
7. R. F. Fikhmanas and P. Sh. Fridberg, Radiotekh. Élektron. (Moscow) **23**, 1625 (1978).
8. A. P. Prudnikov, Yu. A. Brychkov, and O. I. Marichev, *Integrals and Series, Vol. 3: More Special Functions* (Nauka, Moscow, 1986; Taylor & Francis, London, 1990).

*Translated by V. Isaakyan*

---

SHORT  
COMMUNICATIONS

---

# Modulation Instability of Electromagnetic Excitations for a Josephson Junction in a Finite-Thickness Slab

A. I. Lomtev

*Galkin Physicotechnical Institute, National Academy of Sciences of Ukraine, Donetsk, 83114 Ukraine*

*e-mail: lomtev@kinetic.ac.donetsk.ua*

Received April 28, 2004

**Abstract**—The modulation instability of finite-amplitude uniform plane waves oscillating with a Josephson frequency and experiencing a nonlinear frequency shift in a finite-thickness slab is studied in terms of the non-local electrodynamics of Josephson junction. A dispersion relation for the growth rate of small amplitude perturbation is derived. The domains of modulation instability for these waves are found. Modulation instability of the waves is shown to arise when the wavevectors of long-wave amplitude perturbations fall into the finite range  $0 < Q < Q_B(A, D, L)$ . In the range  $Q \geq Q_B(A, D, L)$ , the waves are stable. © 2005 Pleiades Publishing, Inc.

Modulation instability of waves in different nonlinear systems and media continues to be a subject of extensive research [1, 2]. It is known that a nonlinear wave may be contracted in both the transverse and longitudinal direction relative to the direction of its propagation. Light self-focusing predicted by Askar'yan [5] and instability such as wave partitioning into packets with subsequent self-contraction of the packets (Light-hill modulation instability [6]) are examples.

Modulation instability of electromagnetic waves in distributed Josephson junctions is related to the instability of solutions to the sine-Gordon equation. Being of undeniable fundamental interest, the phenomenon of modulation instability also offers a number of applications. Specifically, it may be applied for generation of chains of ultrashort optical pulses with a high repetition rate and development of new-generation logic.

In many cases, modulation instability is considered in terms of the nonlocal modifications of the sine-Gordon equation [7–18]. Since the problem geometries in the works cited are different, the equations of Josephson electrodynamics differ in the kernel of the differential operator that is responsible for the effect of spatially nonlocal coupling. However, in all of those works, the spatial nonlocality of the equations for the phase difference between the wave functions at the boundaries of the contact arises from the nonlocal coupling of the magnetic field at the interface and inside the superconductor. Such a reason for spatial nonlocality is common in the electrodynamics of Josephson junctions.

Modulation instability in terms of the spatially non-local electrodynamics of a Josephson junction between massive (thick) superconductors with  $d \gg \lambda$  (where  $d$  is the thickness of the superconductor and  $\lambda$  is the London penetration depth) was first considered in [7]. It was shown that the buildup of small amplitude and phase perturbations manifests the development of the modu-

lation instability of a constant (finite)-amplitude electromagnetic wave with a nonlinear frequency shift and linear mode dispersion. The stabilizing effect of spatial nonlocality on modulation instability was revealed. Abdullaev [19] studied the modulation instability of a plane nonlinear finite-amplitude wave oscillating with a Josephson frequency in the case of a Josephson junction between thick ( $d \gg \lambda$ ) superconductors. The modulation instability arose as a result of small amplitude perturbation buildup and led to the partitioning of the wave into packets. The modulation instability of dispersive electromagnetic waves propagating in a Josephson junction between thick superconductors ( $d \gg \lambda$ ) was discussed in [20]. A dispersion relation for the growth rate of small amplitude perturbations was derived, and the stabilizing effect of spatial nonlocality on the modulation instability at long wavelengths was revealed. It was demonstrated that there exists a possibility of controlling the domain of modulation instability using dispersion parameter  $k$  or  $\omega(k)$ , where  $k$  ( $\omega(k)$ ) is the wavevector (frequency) of the carrier wave in the linear approximation.

The other extreme case (a Josephson junction between thin,  $d \ll \lambda$ , two-dimensional or three-dimensional nonmagnetic or magnetic superconducting films) was studied in [21–23], where the modulation instability of finite-amplitude Josephson oscillations with a nonlinear frequency shift was caused by small amplitude perturbation buildup. The author [24] also considered the modulation instability of dispersive electromagnetic waves propagating in a Josephson junction between thin ( $d \ll \lambda$ ) superconducting films. For these waves, the stabilizing effect of spatial nonlocality on the modulation instability in the long-wavelength range was revealed. It was also demonstrated that there exists a possibility of controlling the domain of modulation instability using dispersion parameter  $k$

or  $\omega(k)$ , where  $k$  ( $\omega(k)$ ) is the wavevector (frequency) of the carrier wave in the linear approximation.

In view of the aforesaid, it seems topical to investigate the modulation instability of nonlinear electromagnetic excitations propagating in a Josephson junction in a finite-thickness slab for arbitrary ratio  $d/\lambda$ . Such a situation has not yet been analyzed.

A nonlinear system that may exhibit modulation instability is a Josephson junction in a finite-thickness superconducting slab with arbitrary ratio  $d/\lambda$ . In this case, the variation of phase difference  $\varphi(x, t)$  between the wave functions at the boundaries of the contact is described by the nonlinear integro-differential sine-Gordon equation with spatial nonlocality (provided that dissipation and the Meissner currents are neglected) [17]

$$\begin{aligned} \sin \varphi(x, t) + \frac{1}{\omega_J^2} \frac{\partial^2 \varphi(x, t)}{\partial t^2} \\ = \frac{\lambda_J^2}{\pi \lambda} \frac{\partial}{\partial x} \int_{-\infty}^{\infty} K(x-x') \frac{\partial \varphi(x', t)}{\partial x'} dx', \end{aligned} \quad (1)$$

where  $\omega_J$  and  $\lambda_J$  are the Josephson frequency and penetration depth, respectively, and kernel  $K(x)$  has the form

$$K(x) = K_0 \left( \frac{|x|}{\lambda} \right) + \frac{1}{d \lambda^2} \int_0^{\infty} \frac{dk J_0(kx)}{\kappa^3 [\kappa + k \coth(\kappa d)]}. \quad (2)$$

Here,  $K_0(|x|/\lambda)$  and  $J_0(kx)$  are the zeroth-order Macdonald and Bessel functions, respectively, and  $\kappa = (\lambda^{-2} + k^2)^{1/2}$ . In (2), the first term pertains to the case of contact between two thick superconductors ( $d \gg \lambda$ ) and is the kernel of the integral term that was first obtained in [7] and then used in [8]. In the case of contact between two thin ( $d \ll \lambda$ ) films,  $K(x)$  (i.e., the sum of the terms on the right of (2)) is the kernel of the integral term that was first studied in [9–11] and then rigorously derived in [12]. It is given by

$$K(x) = \frac{\lambda_{\text{eff}}}{\pi} \int_0^{\infty} dk \frac{1}{1 + 2k \lambda_{\text{eff}}} J_0(kx),$$

where  $\lambda_{\text{eff}} = \lambda^2/2d$  is the Pearl penetration depth.

In the linear approximation  $\sin \varphi(x, t) \approx \varphi(x, t)$ , a solution to Eq. (1) has the form of uniform Josephson oscillation of infinitely small amplitude  $a_0$ :

$$\varphi_0(t) = a_0 \exp(\pm i \omega_J t). \quad (3)$$

The nonlinearity of Eq. (1) results from the fact that the Josephson current through the contact harmonically depends on the phase difference between the wave functions at the contact's boundaries.

Assuming that  $\sin \varphi(x, t) \approx \varphi(x, t) - \varphi(x, t)^3/3!$  in Eq. (1), we will consider the evolution of small- (finite-) amplitude nonlinear waves of breather type oscillating

with Josephson frequency  $\omega_J$  in the contact. Let us represent the phase difference as

$$\begin{aligned} \varphi(x, t) = u(x, t) \exp(-i \omega_J t) + u^*(x, t) \exp(i \omega_J t), \\ |u(x, t)| \ll 1. \end{aligned} \quad (4)$$

We leave the lowest order of nonlinearity at fundamental frequency  $\omega_J$  in Eq. (1) and assume that amplitude  $u(x, t)$  is a function slowly varying in time, when the inequality  $|\partial^2 u(x, t)/\partial t^2| \ll 2\omega_J |\partial u(x, t)/\partial t|$  holds. Then, substituting field (4) into Eq. (1), we obtain a nonlinear nonlocal ‘‘Schrödinger equation’’ for amplitude  $u(x, t)$ :

$$\begin{aligned} i \frac{2}{\omega_J} \frac{\partial u(x, t)}{\partial t} + \frac{1}{2} |u(x, t)|^2 u(x, t) \\ + \frac{\lambda_J^2}{\pi \lambda} \frac{\partial}{\partial x} \int_{-\infty}^{\infty} K(x-x') \frac{\partial u(x', t)}{\partial x'} dx' = 0. \end{aligned} \quad (5)$$

This equation has an exact solution in the form of a uniform plane nonlinear wave of amplitude  $A$ ,

$$u_0(t) = A \exp(iA^2 \omega_J t/4), \quad A \ll 1. \quad (6)$$

Let us investigate the stability of this solution. The disintegration of wave (6) can be judged from the development of its small perturbations. We assume that a perturbation of small amplitude  $\psi(x, t)$  occurs randomly, so that

$$\begin{aligned} u(x, t) = [A + \psi(x, t)] \exp(iA^2 \omega_J t/4), \\ |\psi(x, t)| \ll A. \end{aligned} \quad (7)$$

For the small perturbation  $\psi(x, t)$ , Eq. (5) gives the linear equation

$$\begin{aligned} i \frac{2}{\omega_J} \frac{\partial \psi(x, t)}{\partial t} + \frac{1}{2} A^2 [\psi(x, t) + \psi^*(x, t)] \\ + \frac{\lambda_J^2}{\pi \lambda} \frac{\partial}{\partial x} \int_{-\infty}^{\infty} K(x-x') \frac{\partial \psi(x', t)}{\partial x'} dx' = 0. \end{aligned} \quad (8)$$

Representing  $\psi(x, t)$  in complex form,  $\psi(x, t) = v(x, t) + iw(x, t)$ , we arrive at a set of equations for its real and imaginary parts:

$$\begin{aligned} \frac{2}{\omega_J} \frac{\partial v(x, t)}{\partial t} + \frac{\lambda_J^2}{\pi \lambda} \frac{\partial}{\partial x} \int_{-\infty}^{\infty} K(x-x') \frac{\partial w(x', t)}{\partial x'} dx' = 0, \\ - \frac{2}{\omega_J} \frac{\partial w(x, t)}{\partial t} + A^2 v(x, t) \end{aligned} \quad (9)$$

$$+ \frac{\lambda_J^2}{\pi \lambda} \frac{\partial}{\partial x} \int_{-\infty}^{\infty} K(x-x') \frac{\partial v(x', t)}{\partial x'} dx' = 0.$$

For amplitude perturbations of type

$$\begin{aligned} v(x, t) &= V(Q, \Omega) \exp[i(Qx - \Omega t)], \\ w(x, t) &= W(Q, \Omega) \exp[i(Qx - \Omega t)] \end{aligned} \quad (10)$$

(arbitrary perturbations can be represented as a superposition of such perturbations), set of equations (9) yields the dispersion relation  $\tilde{\Omega} = \tilde{\Omega}(\tilde{Q})$  in the form

$$\tilde{\Omega}^2(\tilde{Q}) = 2^{-1} L \tilde{Q}^2 I(\tilde{Q}) [2L \tilde{Q}^2 I(\tilde{Q}) - A^2], \quad (11)$$

where  $I(\tilde{Q})$  is given by

$$\begin{aligned} I(\tilde{Q}) &= \frac{1}{\sqrt{1 + \tilde{Q}^2}} \\ &+ \frac{1}{\pi D} \int_0^{\infty} (1 + \tilde{Q}^2 \cosh^2 x)^{-3/2} [\sqrt{1 + \tilde{Q}^2 \cosh^2 x} \\ &+ \tilde{Q} \cosh x \coth(D \sqrt{1 + \tilde{Q}^2 \cosh^2 x})]^{-1} dx \end{aligned} \quad (12)$$

and  $\tilde{Q} = \lambda Q$ ,  $\tilde{\Omega} = \Omega/\omega_j$ ,  $L = \lambda_j^2/2\lambda^2$ , and  $D = d/\lambda$  are dimensionless quantities.

In view of expression (12) for the perturbation growth rate, dispersion relation (11) always has a positive solution  $\text{Im} \tilde{\Omega}(\tilde{Q}) > 0$  in the wavevector range  $0 < \tilde{Q} < \tilde{Q}_B$ . In this range, small amplitude perturbations (10) grow in time, giving rise to the modulation instability of the uniform plane nonlinear electromagnetic wave given by (6). In the range  $\tilde{Q} \geq \tilde{Q}_B$ ,  $\text{Im} \tilde{\Omega}(\tilde{Q}) \equiv 0$  and this wave is stable. Extreme wavevector  $\tilde{Q}_B$  is found from the equation

$$\tilde{Q}_B^2 I(\tilde{Q}_B) = \frac{A^2}{2L}. \quad (13)$$

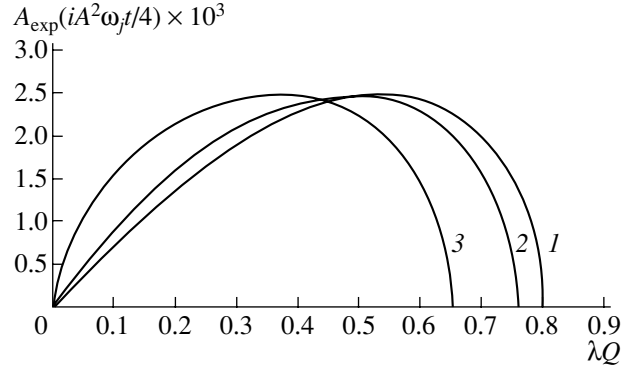
The maximal value of the perturbation growth rate, which equals

$$(\text{Im} \tilde{\Omega}(\tilde{Q}_m))_{\max} = \frac{A^2}{4} \quad (14)$$

is reached at wavevector  $\tilde{Q}_m$ , which is a root of the equation

$$\tilde{Q}_m^2 I(\tilde{Q}_m) = \frac{A^2}{4L}. \quad (15)$$

As the modulation instability develops, the uniform plane nonlinear wave oscillating with Josephson frequency  $\omega_j$  disintegrates into a chain of pulses (small-amplitude breathers), the pulse repetition rate of which depends on the modulation period  $L_0$  of the initial wave:  $L_0 = 2\pi/Q$ , where  $0 < Q < Q_B = \tilde{Q}_B/\lambda$ . Since phase perturbations are not considered in this paper, self-contraction of the wave packets is not observed.



Domains of modulation instability of the uniform plane nonlinear electromagnetic wave given by (6) for  $A = 10^{-1}$ ,  $L = 10^{-2}$ , and  $D = (1) 10^3$ , (2) 1, and (3)  $10^{-3}$ .

The figure shows the domains of modulation instability of the uniform plane nonlinear electromagnetic wave given by (6) for fixed amplitude  $A$  and parameter  $L$  and three values of  $D$ . It is seen that the domain of modulation instability shrinks as parameter  $D$  decreases.

Thus, it has been shown in this paper that the modulation instability of the uniform plane nonlinear electromagnetic wave given by (6) develops when long-wavelength amplitude perturbations fall into the wavevector range  $0 < Q < Q_B$ . For amplitude perturbations in the range  $Q \geq Q_B$ , this wave is stable.

In experiments, the modulation instability at arbitrary ratio  $d/\lambda$  can be observed in long Josephson junctions between finite-thickness superconductors when small- (finite-) amplitude waves oscillating with a Josephson frequency are excited in them.

## ACKNOWLEDGMENTS

The author thanks Yu.E. Kuzovlev for fruitful discussions, as well as Yu.V. Medvedev and I.B. Krasnyuk for support.

## REFERENCES

1. B. Hall, M. Lisak, D. Anderson, and V. E. Semenov, *Phys. Lett. A* **321**, 255 (2004).
2. Wen-cheng Xu, Shu-min Zhang, Wei-cheng Chen, *et al.*, *Opt. Commun.* **199**, 355 (2001).
3. V. I. Karpman, *Non-Linear Waves in Dispersive Media* (Nauka, Moscow, 1973; Pergamon, Oxford, 1975).
4. B. B. Kadomtsev, *Collective Phenomena in Plasma* (Nauka, Moscow, 1976) [in Russian].
5. G. A. Askar'yan, *Zh. Éksp. Teor. Fiz.* **42**, 1567 (1962) [*Sov. Phys. JETP* **15**, 1088 (1962)].
6. M. J. Lighthill, *J. Inst. Math. Appl.* **1**, 269 (1965).
7. Yu. M. Aliev, V. P. Silin, and S. A. Uryupin, *Sverkhprovodimost: Fiz. Khim. Tekh.* **5**, 228 (1992).
8. A. Gurevich, *Phys. Rev. B* **46**, 3187 (1992).

9. Yu. M. Ivanchenko and T. K. Soboleva, Pis'ma Zh. Éksp. Teor. Fiz. **51**, 100 (1990) [JETP Lett. **51**, 114 (1990)].
10. Yu. M. Ivanchenko and T. K. Soboleva, Phys. Lett. A **147**, 65 (1990).
11. Yu. M. Ivanchenko and T. K. Soboleva, Fiz. Tverd. Tela (Leningrad) **32**, 2029 (1990) [Sov. Phys. Solid State **32**, 1181 (1990)].
12. R. G. Mints and I. B. Snapiro, Phys. Rev. B **51**, 3054 (1995).
13. A. I. Lomtev, Pis'ma Zh. Éksp. Teor. Fiz. **69**, 132 (1999) [JETP Lett. **69**, 148 (1999)].
14. A. I. Lomtev, Fiz. Tverd. Tela (St. Petersburg) **42**, 16 (2000) [Phys. Solid State **42**, 15 (2000)].
15. A. I. Lomtev, Zh. Tekh. Fiz. **70** (9), 63 (2000) [Tech. Phys. **45**, 1159 (2000)].
16. I. O. Kulik and I. K. Yanson, *The Josephson Effect in Superconducting Tunnel Structures* (Nauka, Moscow, 1970).
17. Yu. V. Kuzovlev and A. I. Lomtev, Zh. Éksp. Teor. Fiz. **111**, 1803 (1997) [JETP **84**, 986 (1997)].
18. A. I. Lomtev, Zh. Éksp. Teor. Fiz. **113**, 1156 (1998) [JETP **86**, 1234 (1998)].
19. F. Kh. Abdullaev, Pis'ma Zh. Tekh. Fiz. **23** (2), 8 (1997) [Tech. Phys. Lett. **23**, 52 (1997)].
20. A. I. Lomtev, Pis'ma Zh. Tekh. Fiz. **30** (4), 6 (2004) [Tech. Phys. Lett. **30**, 131 (2004)].
21. A. I. Lomtev, Pis'ma Zh. Tekh. Fiz. **29** (8), 72 (2003) [Tech. Phys. Lett. **29**, 342 (2003)].
22. A. I. Lomtev, Fiz. Tverd. Tela (St. Petersburg) **45**, 1358 (2003) [Phys. Solid State **45**, 1423 (2003)].
23. A. I. Lomtev, Zh. Tekh. Fiz. **73** (11), 63 (2003) [Tech. Phys. **48**, 1424 (2003)].
24. A. I. Lomtev, Fiz. Tverd. Tela (St. Petersburg) **45**, 2131 (2003) [Phys. Solid State **45**, 2232 (2003)].

*Translated by V. Isaakyan*

SHORT  
COMMUNICATIONS

# Approximate Method of Solving the Problem of Diffraction of a Plane Electromagnetic Wave by a Thin Chiral Layer Covering a Perfectly Conducting Plane

A. A. Dolbichkin, V. A. Neganov, and O. V. Osipov

Samara State University, Samara, 443011 Russia

e-mail: neganov\_samara@mail333.com

Received April 28, 2004

**Abstract**—One-sided approximate impedance-type boundary conditions for a thin chiral layer placed on a perfectly conducting plane are derived. With these conditions, the problem of incidence of a plane electromagnetic wave on a chiral structure is solved. Approximate formulas for the coefficients of reflection of the fundamental and depolarized components are derived for the case of the perpendicular polarization of the electromagnetic wave (the electric field strength is normal to the plane of incidence). A comparison with an exact solution to the problem of diffraction by this chiral structure is made. © 2005 Pleiades Publishing, Inc.

Interest in interaction between electromagnetic waves and artificial composites that exhibit a spatial dispersion in the microwave range had sharply quickened by the end of the 20th century. Chiral media, which are simulated by arranging thin mirror-asymmetric conducting elements in a homogeneous magnetodielectric (or ferrite in a more general case), appear very promising in applications (such as low-reflection coatings in aircraft, as well as polarization- and frequency-selective filters in the microwave range).

In designing and simulating chiral media intended for the microwave range, conducting right- and left-handed wire helices are used most frequently. A chiral medium exhibits a considerable spatial dispersion if distance  $d$  between neighboring elements is comparable to the length  $\lambda$  of a microwave ( $d \sim \lambda$ ) and the size  $l$  of the helices is much smaller than the wavelength ( $l \ll \lambda$ ) (Fig. 1). In electrodynamics, such elements are called electromagnetic particles. A chiral medium is an artificial material consisting of electromagnetic particles of a mirror-asymmetric form (chiral elements) that are embedded in a homogeneous isotropic insulator.

Note that any chiral element may be viewed as a set of elementary electric and magnetic dipoles. For example, the rectilinear parts of the helices are scattering electric dipoles and the turns of the helices are magnetic dipoles. Accordingly, when an electromagnetic wave is incident on a conducting chiral element, the electric field of the wave will produce both an electric and a magnetic dipole moment. On the other hand, the magnetic field of the incident wave also induces both a magnetic and an electric dipole moment. Because of this, the material equations for a chiral medium relate the electric and magnetic induction vectors simultaneously

to the electric and magnetic field strengths. Therefore, the properties of a chiral medium are described using three material parameters: permittivity  $\epsilon$ ; permeability  $\mu$ ; and parameter of chirality  $\xi$ , which serves as a measure of the interplay between polarization and magnetization processes in the medium.

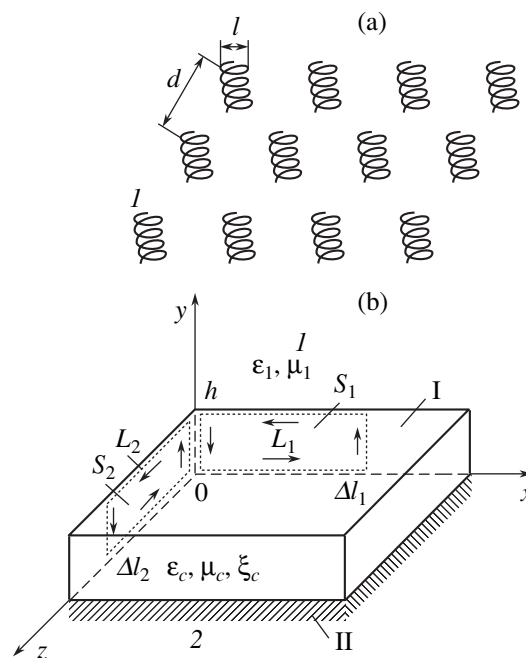


**Fig. 1.** On the derivation of one-sided approximate boundary conditions for a thin chiral layer covering a perfectly conducting plane. (a) Model of the chiral medium: (I) conducting helix; (b) geometry of the problem: (I) chiral layer and (II) perfect conductor.



Natural waves in a chiral medium are clockwise and counterclockwise polarized waves, which have different phase velocities. Therefore, linearly polarized electromagnetic waves cannot travel in a chiral medium. When they strike a chiral layer, the effect of depolarization occurs; that is, if the incident wave is, e.g., perpendicularly polarized, the reflected wave contains field components corresponding to orthogonal (parallel) polarization.

Reflection of electromagnetic waves from chiral layers was rigorously described in [1–3]. Tret'yakov [4] suggested an approximate approach to describing the reflecting properties of a chiral layer that is based on approximate boundary conditions (ABCs). Earlier, ABCs were derived for anisotropic films [5] and thin insulating layers with nonlinearity [6, 7]. However, the ABCs obtained in [4] do not allow for depolarization. Below, we derive other one-sided ABCs of the impedance type, which include the depolarization of a wave incident on a thin chiral layer covering a perfectly conducting plane.

### ONE-SIDED APPROXIMATE BOUNDARY CONDITIONS

Let us derive ABCs of the impedance type for a thin chiral layer covering a perfectly conducting plane. The geometry of the problem is shown in Fig. 1, where a thin chiral layer of thickness  $h$  covers a perfectly conducting plane.

A chiral medium is described by the material equations [1, 2]

$$\begin{aligned} \mathbf{D} &= \varepsilon_c \mathbf{E} - i\xi_c \mathbf{H}, \\ \mathbf{B} &= \mu_c \mathbf{H} + i\xi_c \mathbf{E}, \end{aligned} \quad (1)$$

where  $\varepsilon_c$  and  $\mu_c$  are the relative permittivity and relative permeability of the chiral medium, respectively;  $\xi_c$  is the parameter of chirality; and  $\mathbf{E}$ ,  $\mathbf{D}$ ,  $\mathbf{B}$ , and  $\mathbf{H}$  are the complex amplitudes of the respective electromagnetic field vectors. At  $\xi_c = 0$ , material equations (1) describe a homogeneous insulating medium. Note that Eqs. (1) are written in the Gaussian system of units.

To find ABCs, we will use the set of Maxwell equations in integral form:

$$\begin{aligned} \oint_L \mathbf{E} \cdot d\mathbf{l} &= -ik_0 \int_S \mathbf{B} \cdot d\mathbf{S}, \\ \oint_L \mathbf{H} \cdot d\mathbf{l} &= ik_0 \int_S \mathbf{D} \cdot d\mathbf{S}, \end{aligned} \quad (2)$$

where  $S$  is an arbitrary surface bounded by closed contour  $L$ ,  $d\mathbf{l} = \boldsymbol{\tau}_0 dl$ ,  $\boldsymbol{\tau}_0$  is the unit vector tangent to element  $dl$  of contour  $L$ ,  $d\mathbf{S} = \mathbf{n}_0 dS$ ,  $\mathbf{n}_0$  is the unit normal vector to element  $dS$  of surface  $S$ ,  $k_0 = \omega/c$ ,  $\omega$  is the electromagnetic wave frequency, and  $c$  is the speed of light.

Applying (2) to small contours  $L_1$  and  $L_2$  shown in Fig. 1 yields the following approximate relationships:

$$\begin{aligned} E_z^{(1)} \Delta l_2 - E_y|_{z=\Delta l_2} h + E_y|_{z=0} h &= -ik_0 \Delta l_2 h B_x, \\ E_y|_{x=\Delta l_1} h - E_x^{(1)} \Delta l_1 - E_y|_{x=0} h &= -ik_0 \Delta l_1 h B_z, \\ H_z^{(1)} \Delta l_2 - H_z^{(2)} \Delta l_2 - H_y|_{z=\Delta l_2} h - H_z^{(2)} \Delta l_2 \\ &+ H_y|_{z=0} h = ik_0 \Delta l_2 h D_x, \end{aligned} \quad (3)$$

$$H_x^{(2)} \Delta l_1 + H_y|_{x=\Delta l_1} h - H_x^{(1)} \Delta l_1 - H_y|_{x=0} h = ik_0 \Delta l_1 h D_z,$$

where superscripts 1 and 2 mean that the field is taken on the surfaces of isotropic regions 1 and 2 and components  $\mathbf{E}$  and  $\mathbf{H}$  without superscripts are defined at some points of surfaces  $S_1$  and  $S_2$  bounded by contours  $L_1$  and  $L_2$ , respectively.

When writing expressions (3), we used the theorem of mean. Namely, the integrals on the right of (2) were determined as follows: we assumed that the surface integral of a function defined on a certain planar figure equals the surface area of this figure times the integrand taken at some intermediate values of independent variables. For example,

$$\int_{S_1} \mathbf{B} \cdot d\mathbf{S} = B_z(\boldsymbol{\xi}) \Delta l_1 h,$$

where  $\Delta l_1 h$  is the surface area of the rectangle in plane  $z = 0$  that is bounded by contour  $L_1$  and  $\boldsymbol{\xi} = \{\xi_1, \xi_2, \xi_3 = 0\}$ , with  $\xi_1$  and  $\xi_2$  being some intermediate values of variables  $x$  and  $y$  (Fig. 1) inside contour  $L_1$ .

When calculating the integrals along contours  $L_1$  and  $L_2$  on the left of (2), we used, along with the theorem of mean, the boundary conditions for radial (tangential) components  $\mathbf{E}_\tau$  and  $\mathbf{H}_\tau$  on these contours at  $y = 0$  and  $y = h$ :

$$\begin{aligned} \mathbf{E}_\tau &= \mathbf{E}_\tau^{(1)}, \quad \mathbf{H}_\tau = \mathbf{H}_\tau^{(1)} \quad (y = h), \\ \mathbf{E}_\tau &= 0, \quad \mathbf{H}_\tau = \mathbf{H}_\tau^{(2)} \quad (y = 0). \end{aligned} \quad (4)$$

Vectors  $\mathbf{E}_\tau$  and  $\mathbf{H}_\tau$  in the chiral layer can be determined by means of the Lagrange linear interpolation using two points [7], namely, the values of the electromagnetic field components on its surface, i.e., at  $y = 0$  and  $y = h$ . Hereafter, we assume that, in (3), the field in the chiral layer is the field at its center (at  $y = h/2$ ). Lagrange interpolation in this case appears as

$$\mathbf{E}_\tau = \frac{\mathbf{E}_\tau^{(1)}}{2}, \quad \mathbf{H}_\tau = \frac{\mathbf{H}_\tau^{(1)} + \mathbf{H}_\tau^{(2)}}{2}. \quad (5)$$

It is apparent that expressions (5) apply only if the chiral layer is thin ( $k_0 h \sqrt{\varepsilon_c \mu_c} \ll 1$ ).

In view of the approximations of fields (5) and of material equations (1) in the limit  $\Delta l_1 \rightarrow 0$  and  $\Delta l_2 \rightarrow 0$ , expressions (3) can be recast as

$$\begin{aligned} -E_z^{(1)} + h \frac{\partial E_y}{\partial z} &= i \frac{k_0 h \mu_c}{2} (H_x^{(1)} + H_x^{(2)}) - \frac{k_0 h \xi_c}{2} E_x^{(1)}, \\ -E_x^{(1)} + h \frac{\partial E_y}{\partial x} &= -i \frac{k_0 h \mu_c}{2} (H_z^{(1)} + H_z^{(2)}) + \frac{k_0 h \xi_c}{2} E_z^{(1)}, \\ H_z^{(2)} - H_z^{(1)} + h \frac{\partial H_y}{\partial z} &= -\frac{k_0 h \epsilon_c}{2} E_x^{(1)} - \frac{k_0 h \xi_c}{2} (H_x^{(1)} + H_x^{(2)}), \\ H_x^{(2)} - H_x^{(1)} + h \frac{\partial H_y}{\partial x} &= i \frac{k_0 h \epsilon_c}{2} E_z^{(1)} + \frac{k_0 h \xi_c}{2} (H_z^{(1)} + H_z^{(2)}). \end{aligned} \quad (6)$$

The next step of deriving the ABCs is the elimination of normal-to-surface components  $E_y$  and  $H_y$  from (6) using the differential relations

$$\begin{aligned} E_y &= \frac{1}{k_0 n_c^2} \left[ -i \mu_c \frac{\partial H_x}{\partial z} + i \mu_c \frac{\partial H_z}{\partial x} - \xi_c \frac{\partial E_x}{\partial z} + \xi_c \frac{\partial E_z}{\partial x} \right], \\ H_y &= \frac{1}{k_0 n_c^2} \left[ -i \epsilon_c \frac{\partial E_z}{\partial x} + i \epsilon_c \frac{\partial E_x}{\partial z} - \xi_c \frac{\partial H_x}{\partial z} + \xi_c \frac{\partial H_z}{\partial x} \right], \end{aligned} \quad (7)$$

where  $n_c^2 = \epsilon_c \mu_c - \xi_c^2$ , which follow from the Maxwell equations and material equations (1) for a chiral medium.

With (7), it is easy to write the following boundary conditions of the impedance type (with the proviso that the field remains constant along the  $Oz$  axis,  $\partial/\partial z = 0$ ):

$$\begin{aligned} E_x^{(1)} &= i k_0 h \mu_c \left[ H_z^{(1)} + \frac{1}{k_0^2 n_c^2} \frac{\partial^2 H_z^{(1)}}{\partial x^2} \right] + \frac{\xi_c h}{k_0 n_c^2} \frac{\partial^2 E_z^{(1)}}{\partial x^2}, \\ E_z^{(1)} &= -i k_0 h \mu_c H_x^{(1)} + \frac{k_0 h \xi_c}{2} E_x^{(1)}. \end{aligned} \quad (8)$$

Relationships (8) will be called the one-sided ABCs (OSABCs) for a thin chiral layer placed on a perfectly conducting plane.

When deriving OSABCs (8), we left only the terms of the first order of smallness in parameter  $k_0 h \sqrt{\epsilon_c \mu_c}$ . It should be noted that our method makes it possible to obtain OSABCs of higher order of smallness in this parameter. Analysis shows, however, that there is little point in using second-order OSABCs for thin ( $k_0 h \sqrt{\epsilon_c \mu_c} \ll 1$ ) chiral layers.

Unlike the boundary conditions derived in [4], OSABCs (8) relate all the four tangential components of an electromagnetic field. In free space with a chiral layer, the  $E$ - and  $H$ -waves cannot therefore be indepen-

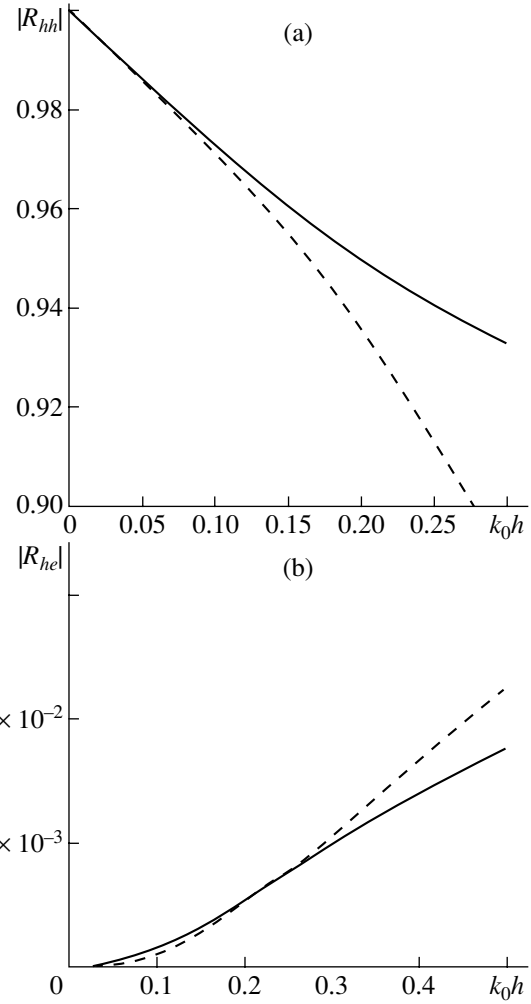


**Fig. 2.** (a)  $|R_{hh}|$  and (b)  $|R_{he}|$  vs. normalized thickness  $k_0 h$  of the chiral layer for the case of a plane perpendicularly polarized electromagnetic wave incident on the layer. The continuous curves, calculation by formulas (9); dashed curves, rigorous electrodynamic calculation [3].

dent. In addition, the OSABCs obtained in [4] are free of terms proportional to  $\xi_c$ , unlike formula (8).

#### REFLECTION OF A PLANE ELECTROMAGNETIC WAVE FROM A THIN CHIRAL LAYER PLACED ON A PERFECTLY CONDUCTING PLANE

With OSABCs (8), one can easily solve the problem of incidence of a plane electromagnetic wave on the structure shown in Fig. 1. Let us assume that the wave has perpendicular polarization (the electric field is normal to the plane of incidence) and strikes the chiral layer at an angle  $\theta$  ( $\theta$  is the angle between the direction of the wave and the normal to the plane of the layer). In this case, the coefficients of reflection of the fundamental component,  $R_{hh}$ , and depolarized component,  $R_{he}$ , are expressed as follows:

$$R_{hh} = \frac{(ik_0h\mu_c \cos \theta - 1)[ik_0h\mu_c \sin^2 \theta - n_c^2(\cos \theta + ik_0h\mu_c)] - k_0^2 h^2 \xi_c^2 \sin^2 \theta \cos \theta}{(ik_0h\mu_c \cos \theta + 1)[ik_0h\mu_c \sin^2 \theta - n_c^2(\cos \theta + ik_0h\mu_c)] + k_0^2 h^2 \xi_c^2 \sin^2 \theta \cos \theta}, \quad (9)$$

$$R_{he} = \frac{2ik_0^2 h^2 \mu_c \xi_c}{(ik_0h\mu_c \cos \theta + 1)[ik_0h\mu_c \sin^2 \theta - n_c^2(\cos \theta + ik_0h\mu_c)] + k_0^2 h^2 \xi_c^2 \sin^2 \theta \cos \theta}.$$

It is noteworthy here that, if the OSABCs from [4] are used, the depolarized wave does not reflect; that is,  $R_{he} = 0$ .

Figure 2 plots the absolute values of  $|R_{hh}|$  (the reflection coefficient for the fundamental mode) and  $|R_{he}|$  (the reflection coefficient for the depolarized mode) against normalized thickness  $k_0h$  of the chiral layer for the case when a plane perpendicularly polarized electromagnetic wave strikes the chiral layer at angle  $\theta = \pi/4$ . The following parameters of the chiral layer were taken in the calculations:  $\epsilon_c = 3.5 - 0.3i$ ,  $\mu_c = 2.2 - 0.3i$ , and  $\xi_c = 0.3$ . The continuous lines were obtained by formula (9); the dashed lines, by the rigorous electrodynamic calculation [3]. As follows from Fig. 2a, the OSABCs are applicable to sufficiently thin chiral layers:  $k_0h \lesssim 0.25$ . For thicker layers, the values of  $|R_{hh}|$  calculated by approximate formulas (9) exceed those obtained by the rigorous electrodynamic calculation.

In Fig. 2b (the reflection coefficient for the depolarized component), good agreement between the rigorous [3] and approximate (formulas (9)) calculations is observed for  $k_0h \lesssim 0.5$ . It is also seen that the reflection coefficient for the depolarized wave grows as normalized thickness  $k_0h$  of the chiral layer increases.

### CONCLUSIONS

The OSABCs derived in this work may be useful in simulating various reflecting structures that involve thin chiral layers, as well as in designing new-genera-

tion waveguides with chiral inclusions that are intended for operation at microwaves and extremely high-frequency waves. Our method of deriving OSABCs also makes it possible to obtain double-sided ABCs for a thin chiral layer located at the interface between magnetodielectric (or ferrite) media with different physical properties.

### REFERENCES

1. I. V. Lindell, A. H. Sihvola, S. A. Tretyakov, *et al.*, *Electromagnetic Waves in Chiral and Bi-Isotropic Media* (Artech House, London, 1994).
2. B. Z. Katsenelenbaum, E. N. Korshunova, A. N. Sivov, *et al.*, *Usp. Fiz. Nauk* **167**, 1201 (1997) [*Phys. Usp.* **40**, 1149 (1997)].
3. V. A. Neganov and O. V. Osipov, *Izv. Vyssh. Uchebn. Zaved. Radiofiz.* **42**, 870 (1999).
4. S. A. Tret'yakov, *Radiotekh. Élektron. (Moscow)* **39**, 184 (1994).
5. E. P. Kurushin and E. I. Nefedov, *Electrodynamics of Anisotropic Waveguide Structures* (Nauka, Moscow, 1983) [in Russian].
6. V. A. Neganov, E. I. Nefedov, and G. P. Yarovoï, *Strip-Slot Lines for Superhigh and Extremely High Frequencies* (Nauka, Moscow, 1996) [in Russian].
7. *Handbook of Mathematical Functions*, Ed. by M. Abramowitz and I. A. Stegun (Dover, New York, 1971; Nauka, Moscow, 1979).

*Translated by V. Isaakyan*

---

SHORT  
COMMUNICATIONS

---

## Effect of Synthesis Conditions on the Properties of Fe–Al–N Thin Films

A. S. Kamzin\*, S. A. Kamzin\*, F. Wei\*\*, and Z. Yang\*\*

\* Ioffe Physicotechnical Institute, Russian Academy of Sciences,  
ul. Politekhnikeskaya 26, St. Petersburg, 194021 Russia  
e-mail: kamzin@pop.ioffe.rssi.ru

\*\* Research Institute of Magnetic Materials, Lanzhou University, Lanzhou, 730000 China

Received April 28, 2004

**Abstract**—The magnetic properties, microstructure, and morphology of Fe–Al–N films that are deposited by reactive rf sputtering and synthesized *in situ*, *ex situ* (deposition followed by annealing), and by thermal crystallization of amorphous films are studied. The FeAlN films synthesized *ex situ* offer the highest soft-magnetic properties. The films produced by thermal crystallization offer the highest thermal stability. © 2005 Pleiades Publishing, Inc.

Increasing the data recording density in magnetic carriers requires materials with a high coercive force. High-quality recording on such carriers at 5000–7000 Oe is provided if the field strength in the gap of the recording head is equal to, or higher than, 2.0 T [1]. Under these conditions, saturation induction  $B_s$  in the core of the head must be no less than ~20 kG [2]. Nanostructured FeXN ( $X = \text{Ta, Hf, Nb, Zr, or Si}$ ) films satisfy these requirements (see, e.g., [3] and Refs. therein). Viala et al. [4] found that FeAlN films had high soft-magnetic properties. In this work, we study the effect of synthesis conditions on the properties of FeAlN films, which were (i) deposited on cooled substrates and then annealed (*ex situ* synthesis), (ii) synthesized during deposition (*in situ* synthesis), and (iii) deposited and then annealed in the amorphous state.

The films were deposited on glass substrates by rf magnetron sputtering. The target was an all-iron plate partially covered by aluminum foil. The Al content in the films deposited was controlled by varying the surface area covered by the Al foil. Nitrogen atoms modify the  $\alpha$ -Fe crystal lattice, making the FeXN films magnetically soft. The efficiency of this process, however, depends on the probability of nitrogen atoms chemically interacting with dopant  $X$  [4]. The third element, Al, readily interacts with nitrogen [5]. The Al content in the films was 2.5% and was strictly controlled in order to prevent the formation of nonmagnetic Al–N fractions [6]. The nitrogen concentration in the films was controlled by varying the nitrogen partial pressure in the Ar + N<sub>2</sub> gas mixture introduced into the sputtering chamber. The films were deposited under the following conditions: the pressure in the chamber was  $5 \times 10^{-7}$  Torr; the pressure of the Ar + N<sub>2</sub> mixture during sputtering,  $2 \times 10^{-3}$  Torr; the nitrogen partial pressure,

0–8%; the sputtering power density, 2.3 W/cm<sup>2</sup>; and the film deposition rate, 20–30 nm/min.

**Synthesis *ex situ*.** The study of the magnetic properties of the FeAlN compounds deposited on the cooled substrates at various partial pressures  $P(\text{N}_2)$  shows that the films synthesized at  $P(\text{N}_2) = 3\%$  offer the best soft-magnetic properties. As follows from X-ray diffraction analysis, the FeAlN films deposited at this pressure are anocrystalline. At  $P(\text{N}_2) < 3\%$ , X-ray diffraction patterns contain the well-resolved intense (110) line of the  $\alpha$ -Fe phase. As  $P(\text{N}_2)$  increases to 5%, this line becomes less intense and broadens. For the films deposited at  $P(\text{N}_2) \geq 5\%$ , this line of the  $\alpha$ -Fe phase diffuses and then disappears, which indicates that these compounds are amorphous. The number of N atoms incorporated into  $\alpha$ -Fe is likely to grow, and the films pass into the amorphous state.

During the *ex situ* synthesis, high residual stresses, giving rise to magnetoelastic anisotropy, which adversely affects the soft-magnetic properties of the films, were relieved by annealing in a vacuum furnace at a pressure of  $5 \times 10^{-5}$  Torr. Figure 1a shows the dependences of the saturation induction  $B_s$  and coercive force  $H_c$  of the FeAlN films on annealing temperature  $T_{\text{ann}}$ . The value of  $B_s$  is seen to be virtually independent of  $T_{\text{ann}}$ , whereas  $H_c$  increases weakly upon annealing at  $T_{\text{ann}} < 350^\circ\text{C}$  and appreciably at  $T_{\text{ann}} = 360^\circ\text{C}$ . The variation of  $H_c$  with annealing temperature agrees with the X-ray diffraction data. Annealing at  $T_{\text{ann}} < 350^\circ\text{C}$  has an insignificant effect on the X-ray diffraction patterns, while, at  $T_{\text{ann}} > 350^\circ\text{C}$ , the (110) line of the  $\alpha$ -Fe phase becomes higher and narrower, indicating an increase in the degree of crystallinity of  $\alpha$ -Fe grains. The annealing at  $T_{\text{ann}} > 350^\circ\text{C}$  also causes  $\alpha$ -Fe grains to grow, as demonstrated by atomic force microscopy (AFM) data. As

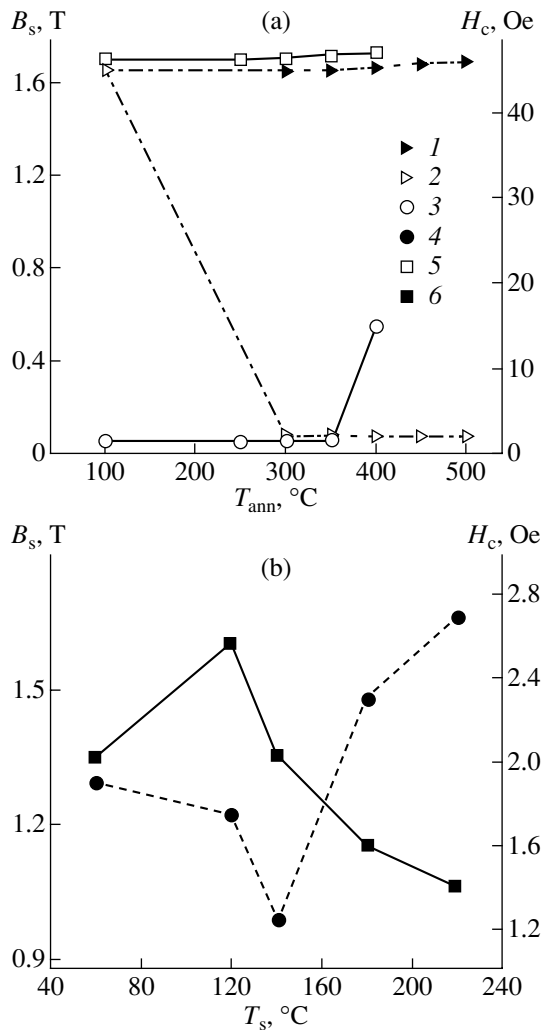


**Fig. 1.** (a) Dependences of  $B_s$  and  $H_c$  of the FeAlN films on annealing temperature  $T_{ann}$ : (1, 2) annealing of amorphous compounds and (3, 5) deposition on cooled substrates. (b) (4, 6)  $B_s$  and  $H_c$  of the FeAlN films vs. the substrate temperature  $T_s$ .

follows from these data, the size of  $\alpha$ -Fe grains is almost the same (10–20 nm) in the as-deposited films and those annealed at 200°C. This size is smaller than the length of ferromagnetic exchange interaction between the grains [2]. In AFM images, grain boundaries in the films annealed at 200°C are more distinct than in the as-deposited films. This finding can be explained by the enhanced crystallization of  $\alpha$ -Fe grains at relatively low annealing temperature (200°C). This process also contributes, along with residual stress relieving, to the improvement of the soft-magnetic properties of the FeAlN films. Annealing at 400°C facilitates the crystallization of grains with a size much larger than the length of exchange interactions, as a result of which the soft-magnetic properties of these films degrade.

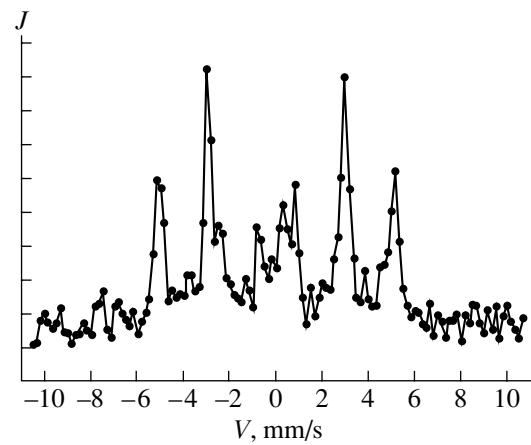


**Fig. 2.** Mössbauer spectrum of the FeAlN film annealed at 350°C that was taken by recording backscattered conversion and Auger electrons.

Figure 2 shows the Mössbauer spectrum of the FeAlN films annealed at 350°C that was obtained by recording backscattered conversion and Auger electrons. The spectrum consists of a Zeeman sextuplet with a linewidth of  $0.430 \pm 0.03$  mm/s, an effective magnetic field of  $326 \pm 1$  kOe on the iron atom nuclei, and a zero quadrupole split. The areas under the lines in the Zeeman sextuplet are in the ratio 3 : 4 : 1 : 1 : 4 : 3, indicating that the magnetic moments of iron atoms in the film are normal to the wavevector of gamma radiation, which runs normally to the film surface. Thus, the magnetic moments of iron ions lie in the film plane. In the range of the “zero” Doppler velocity of the Mössbauer source, the spectrum contains weak lines, which indicate the presence of a certain amount of paramagnetic iron. The parabolic background suggests that a small fraction of the amorphous phase is present in the films.

**Synthesis *in situ*.** Figure 1b plots  $B_s$  and  $H_c$  versus the substrate temperature  $T_s$  for the films synthesized *in situ*. The films deposited at  $T_s = 120$ °C have the highest values of  $B_s$ . This is explained by a low fraction of the  $\gamma$ -Fe<sub>4</sub>N phase, which decreases  $B_s$ , as follows from the X-ray diffraction data. The coercive force  $H_c$  of the films deposited at low  $T_s$  is higher than in those deposited at  $T_s = 120$ °C. This fact may be assigned to worse conditions for crystallization of  $\alpha$ -Fe grains at  $T_s < 120$ °C and the presence of high residual stresses. At  $T_s$  rises to 120°C, the degree of crystallinity of  $\alpha$ -Fe grains increases and the residual stresses are relieved. Taken together, these factors lead to a decrease in  $H_c$ . According to the X-ray diffraction data, high  $T_s$  facilitate the growth of the  $\gamma$ -Fe<sub>4</sub>N phase, specifically, on the faces of  $\alpha$ -Fe grains; correspondingly, exchange ferromagnetic coupling between  $\alpha$ -Fe grains weakens. The films synthesized at  $T_s = 150$ °C have the lowest value of  $H_c$ . The X-ray diffraction data show that the films deposited at

$T_s = 120^\circ\text{C}$  consist mainly of  $\alpha$ -Fe grains with a mean size smaller than 15 nm, whereas those deposited at the other substrate temperatures consist of the  $\alpha$ -Fe and  $\gamma$ -Fe<sub>4</sub>N phases. The films synthesized at  $T_s = 150^\circ\text{C}$  consist of nanocrystalline  $\alpha$ -Fe and a small amount of  $\gamma$ -Fe<sub>4</sub>N. In the films deposited at  $T_s > 150^\circ\text{C}$ , the fraction of the  $\gamma$ -Fe<sub>4</sub>N phase increases. These findings confirm the assumption [7] that a small amount of the  $\gamma$ -Fe<sub>4</sub>N phase present in FeAlN films raises their soft-magnetic properties.

**Synthesis by annealing of amorphous compounds.** Amorphous FeAlN films were deposited under the conditions described above with the difference that the substrate was rotated at a constant velocity during sputtering. The axis of rotation was offset from the center of the round target, making the deposition intermittent. The X-ray diffraction patterns of the films thus deposited had no lines associated with the crystalline structure, thereby indicating that the films are amorphous. Then, they were annealed in a vacuum furnace.

The dependences of the saturation induction  $B_s$  and coercive force  $H_c$  of the films on annealing temperature  $T_{\text{ann}}$  are shown in Fig. 1a. When the annealing temperature increases, coercive force  $H_c$  decreases sharply and reaches a minimum in the range  $300 < T_{\text{ann}} < 350^\circ\text{C}$ , whereas  $B_s$  remains virtually unchanged. The decrease in  $H_c$  can be explained by the formation of nanocrystalline  $\alpha$ -Fe particles, ferromagnetic exchange interaction between which substantially suppresses local crystalline magnetic anisotropy. A further increase in  $T_{\text{ann}}$  does not change the values of  $B_s$  and  $H_c$ . The X-ray diffraction patterns of the heat-treated films contain the (110) line of the  $\alpha$ -Fe phase. Its intensity remains almost constant with increasing  $T_{\text{ann}}$ , which indicates that neither the size of  $\alpha$ -Fe grains nor the fraction of  $\alpha$ -Fe changes in these films. However, the annealing does not result in complete crystallization of the films; therefore, they consist of the nanocrystalline  $\alpha$ -Fe and amorphous phases, as demonstrated by the Mössbauer spectroscopy data. The crystallization of  $\alpha$ -Fe grains starts at low  $T_{\text{ann}}$  and is completed at  $300$ – $350^\circ\text{C}$ . One may assume that atoms in the amorphous film are randomly distributed and those atoms that have similar properties combine first. Therefore,  $\alpha$ -Fe nanoparticles crystallize in the first place from the amorphous matrix at low annealing temperatures. Then, Al–N compounds form around the  $\alpha$ -Fe grains, suppressing their further growth.

The table summarizes the magnetic and structural characteristics of the films synthesized by the three methods. It is seen that the films produced *ex situ* have the highest saturation induction and the lowest coercive force. These films consist mainly of  $\alpha$ -Fe nanocrystals with a mean size smaller than the length of ferromagnetic exchange interaction between them. As a result, local effective crystalline magnetic anisotropy in the films is low and their soft-magnetic properties are

improved. The lattice expansion in these films approaches a critical value of 0.28%, which is further evidence for their good soft-magnetic properties [8].

	<i>Ex situ</i>	<i>In situ</i>	Crystallization from amorphous state
Phase composition	$\alpha$ -Fe	$\alpha$ -Fe + $\gamma$ -Fe <sub>4</sub> N	$\alpha$ -Fe + amorphous matrix
Grain size $D$ , nm	10–15	9–12	
Lattice expansion, %	0.19–0.37	From 0.23 to 0.14	
$B_s$ , T	1.8	1.58	1.65
$H_c$ , Oe	1.2	1.8	2.5

improved. The lattice expansion in these films approaches a critical value of 0.28%, which is further evidence for their good soft-magnetic properties [8].

In the FeAlN films synthesized *in situ*, the saturation induction is lower than in those produced *ex situ*, possibly because of the formation of the  $\gamma$ -Fe<sub>4</sub>N phase (where the saturation induction is lower than in  $\alpha$ -Fe). The precipitation of  $\gamma$ -Fe<sub>4</sub>N on  $\alpha$ -Fe grains decreases the ferromagnetic exchange interaction between them, and the coercive force of these films is higher than in the films synthesized *ex situ*, although the grains in the former are smaller. In addition, the expansion of the  $\alpha$ -Fe lattice is far from the related critical value.

Thus, our experiments show that, among the FeAlN films synthesized by different methods, those synthesized *ex situ* offer the highest soft-magnetic properties.

#### ACKNOWLEDGMENTS

This work was supported by the Russian Foundation for Basic Research (grant no. 02-02-39006) and the National Science Foundation of China.

#### REFERENCES

1. L. T. Romankiw, J. Magn. Soc. Jpn. **24**, 1 (2001).
2. K. H. J. Buschow, *Handbook of Magnetic Materials* (Elsevier Science, Amsterdam, 1997), Vol. 10, p. 433.
3. D. Zheng, Y. Ma, D. Wu, *et al.*, Phys. Status Solidi A **193**, 61 (2002).
4. B. Viala, M. K. Minor, and J. A. Barnard, J. Appl. Phys. **80**, 3941 (1996).
5. R. D. Pehkle and F. Elliot, Trans. AIME **218**, 1088 (1960).
6. D. J. Rogers, S. Wang, D. R. Laoghlín, and M. H. Kryder, IEEE Trans. Magn. **28**, 2419 (1992).
7. S. Wang and M. H. Kryder, J. Appl. Phys. **67**, 5134 (1990).
8. M. Takahashi, T. Shimatsu, and H. Shoji, in *Proceedings of the 6th International Conference on Ferrites, Kyoto, 1992*, p. 1483.

*Translated by K. Shakhlevich*

---

SHORT  
COMMUNICATIONS

---

# Influence of the Reversible Adsorption of Methyl Alcohol on Magnetization Reversal in Ferromagnets

V. E. Zubov, A. D. Kudakov, N. L. Levshin, and T. S. Fedulova

*Moscow State University, Vorob'evy gory, Moscow, 119992 Russia*

*e-mail: kudakov@magn.ru*

Received April 28, 2004

**Abstract**—A change in the dynamics of  $180^\circ$  domain walls on the surface of a soft amorphous ferromagnet in methyl alcohol atmosphere is established by means of a magneto-optic method. A reversible decrease in the relaxation frequency of the domain walls near the surface in the presence of methyl alcohol admolecules is observed. This effect is related to the magnetic defects resulting from methyl alcohol adsorption on the ferromagnet surface, which proceeds through hydrogen bonding. Based on earlier data for the influence of the reversible adsorption of water molecules on the domain wall dynamics in ferromagnets, it is concluded that reversible adsorption through the mechanism of hydrogen bond formation considerably affects the domain wall dynamics in soft ferromagnets. © 2005 Pleiades Publishing, Inc.

## INTRODUCTION

Previously, we established that the room-temperature reversible adsorption of water molecules on the surface of a soft amorphous ferromagnet leads to an increase in the effective drag factor of the domain walls near the surface [1]. As a result of water adsorption, the amplitude of domain wall oscillations at the surface abruptly drops as the magnetization reversal frequency exceeds 10 kHz, while the oscillation amplitude inside the material remains nearly constant. This observation is quite unexpected, since eddy currents in ferromagnetic metals are bound to cause the inverse effect according to the theory developed in a number of works (see, e.g., [2]). Indeed, since the density of the eddy currents induced by the wall motion near the surface is lower than in the bulk, their drag effect in the bulk is expected to be stronger than at the surface. The unexpectedness of this phenomenon lies in the fact that weak (and reversible at room temperature) water adsorption, which touches upon only a few surface layers of a ferromagnet, affects the domain wall dynamics more severely than the eddy currents penetrating incomparably deeper into the sample. It is known that the adsorption of water molecules on real surfaces proceeds through the formation of hydrogen bonds [3] and is an intermediate between physical and chemical adsorption in bond strength. A strong influence of adsorption associated with hydrogen bonding on the domain wall dynamics could be confirmed by observing the same effect with other molecules that are

adsorbed by the same mechanism, e.g., molecules of alcohols [4]. In this study, we investigate the influence of the methyl alcohol reversible adsorption on the domain wall dynamics in an amorphous ferromagnet. Molecules of methyl alcohol and water are close in size but form hydrogen bonds in different amounts.

## EXPERIMENTAL

Amorphous ferromagnetic iron-based alloy sheets of composition  $\text{Fe}_{76.5}\text{Cu}_1\text{Nb}_3\text{Si}_{13.5}\text{B}_6$  used as samples were subjected to special thermal treatment in order to improve the homogeneity and magnetic softness [5]. The sheets were 25–30  $\mu\text{m}$  thick, 0.55 mm wide, and from 15 to 20 mm long.

The surface properties of the domain wall were studied with the help of a magneto-optic micromagnetometer configured with a vacuum cell into which test samples were placed and with a gas-supply system that delivers various gases to the cell [1]. The adsorbate pressure in the cell could be varied from the atmospheric value to  $10^{-3}$  Pa. We detected the equatorial magneto-optic Kerr effect, which arose when the magnetization of a  $1 \mu\text{m}^2$ -area of the sample changed under illumination. The slit of a photoelectric multiplier scanned the sample perpendicularly to its longer side. Magnetization reversal was induced by an external magnetic field applied parallel to the longer side of the

sample. The field amplitude was 300 A/m, and the frequency was varied from 30 Hz to 20 kHz.

We studied the frequency dependences of the wall oscillation amplitude  $\Delta$  on the amorphous ferromagnet surface. Dependence  $\Delta(f)$  was characterized by relaxation frequency  $f_r$ , which was determined for  $\Delta(f=f_r) = 0.7\Delta_0$ , where  $\Delta_0$  is the value of  $\Delta$  at  $f \rightarrow 0$ .

The experiment was carried out on the real surface, i.e., after the sample had been exposed to air. Once the cell with the sample has been evacuated, the surface of the sample exhibits a thin oxide film covered by hydroxyl groups, as well as by water molecules coordination-bonded to the surface. The evacuation was followed by inflow of methyl alcohol vapors.

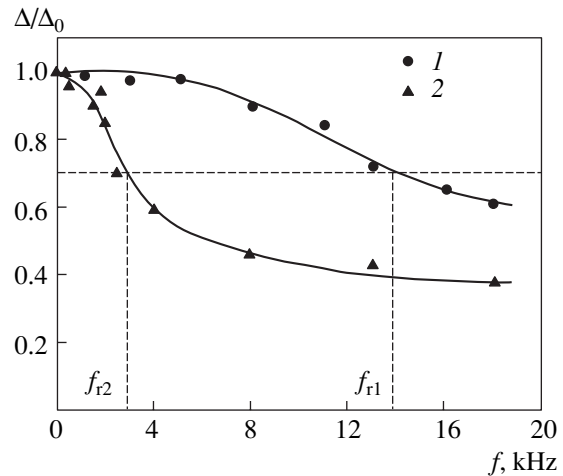
In the bulk of the structure, the domain wall oscillations were studied by the induction method. For this purpose, a measuring coil was wound on the sample. The signal from the coil is proportional to the magnetization of the sample, which, in turn, is proportional to the displacement of the wall in the bulk.

## RESULTS AND DISCUSSION

The magneto-optic study of the domain wall dynamics in the amorphous sheets indicates that the methyl alcohol adsorption decreases the domain wall relaxation frequency at the surface, whereas the wall oscillation amplitude in the bulk remains constant throughout the frequency range considered. The relaxation frequency at the surface in a vacuum was found to be 13.5 kHz. The presence of the methyl alcohol vapor at a pressure of 10 kPa diminishes the relaxation frequency to 2.6 kHz, i.e., more than fivefold (see figure). After repeat evacuation, the relaxation frequency takes its initial value, which gives evidence for the reversibility of the effect.

The results obtained are in qualitative agreement with the data reported in [1, 6]. In those studies, water adsorption on the surface of iron whiskers and iron-based amorphous sheets led to a reversible decrease in the relaxation frequency at the surface. This decrease was attributed to surface magnetic defects arising when the water molecule adsorption proceeds via hydrogen bonding. The qualitative agreement between the results cited and our data suggests that water and methyl alcohol, when adsorbed on the surface, have a similar effect on the magnetic properties of ferromagnets.

In detail, the mechanism underlying the influence of the methyl alcohol reversible adsorption on the domain wall dynamics appears as follows. Upon evacuation, the water molecules adsorbed by the hydrogen-bonding mechanism and partially those coordination-bonded to the surface are desorbed. This follows from the change in the charge state of the oxide surface after evacuation [7]. Note that neither the adsorption nor the desorption of the molecules that produce hydrogen and van der Waals bonds change the charge state of the surface oxide. When entering into the measuring cell, methyl



Domain wall oscillation amplitude at the sample surface vs. the magnetic field frequency (1) in a vacuum and (2) in the presence of methyl alcohol adsorbed.

alcohol is first adsorbed on the centers that are left by the coordination-bonded water molecules and then generates hydrogen bonds to the surface. Thus, methanol molecules substitute for both some of the coordination-bonded and weakly sorbed water molecules. The reversible change in the relaxation frequency is explained by the adsorption/desorption of these weakly sorbed molecules of methanol. In contrast to an admolecule of water, which can, without branching of the molecular chains, attach two molecules adsorbed by the hydrogen-bonding mechanism, a molecule of methyl alcohol can attach only one molecule adsorbed via this mechanism [4]. When adsorbed, methyl alcohol and water produce a similar effect on the domain wall dynamics, but the decrease in the relaxation frequency is more appreciable in the former case. The latter circumstance contradicts the assumption that the rate of magnetic defect generation increases with bunching of weakly sorbed molecules and, therefore, seems surprising. Such a behavior calls for additional experimental investigation.

Note in conclusion that the results of this study, in combination with the earlier data on water adsorption, show that the domain wall dynamics in soft ferromagnets is appreciably affected by the reversible adsorption of gases with the formation of hydrogen bonds.

## ACKNOWLEDGMENTS

This study was supported by the Russian Foundation for Basic Research (grant no. 02-02-16627).



## REFERENCES

1. V. E. Zubov, A. D. Kudakov, N. L. Levshin, *et al.*, *Vestn. Mosk. Univ., Ser. 3: Fiz., Astron.*, No. 2, 52 (2002).
2. B. N. Filippov and A. P. Tankeev, *Dynamic Effects in Ferromagnets with a Domain Structure* (Nauka, Moscow, 1987) [in Russian].
3. V. F. Kiselev and O. V. Krylov, in *Absorption Processes on Semiconductor and Dielectric Surfaces*, Vol. 32: *Series in Chemical Physics* (Springer, Berlin, 1987), p. 237.
4. N. D. Sokolov, *Usp. Fiz. Nauk* **57**, 205 (1955).
5. Yu. N. Starobudtsev, L. D. Son, V. S. Tsepelev, *et al.*, *Rasplavy* **4**, 76 (1992).
6. V. E. Zubov, A. D. Kudakov, N. L. Levshin, *et al.*, *J. Magn. Magn. Mater.* **140–144**, 1985 (1995).
7. V. F. Kiselev, S. N. Kozlov, and N. L. Kevshin, *Phys. Status Solidi A* **66**, 93 (1981).

*Translated by A. Sidorova*

**SHORT  
COMMUNICATIONS**

# Vortex Properties of a Photon Flux in a Dielectric Waveguide

**I. V. Dzedolik**

*Vernadsky National University, pr. Vernadskogo 4, Simferopol, 95007 Ukraine*

*e-mail: dzedolik@crimea.edu*

Received February 6, 2004

**Abstract**—It is shown theoretically and experimentally that the photon flux energy in a dielectric waveguide depends on the mode composition of the field and the ratio between the numbers of photons with left- and right-handed helicity. © 2005 Pleiades Publishing, Inc.

The vortex properties of an electromagnetic field that propagates in both free space and a medium have recently attracted considerable attention [1–8]. This interest is stimulated by advances in the technology of capture and transport of insulating microparticles by a vortex electromagnetic field, in designing optical-vortex-based transducers of physical quantities, and in nanotechnologies using single vortices and vortex lattices [6]. Of special interest in this field is transport of a vortex electromagnetic field in dielectric waveguides, specifically, in optical fibers [2–5, 7, 8].

For electromagnetic vortices, energy circulation, i.e., the precession of the Poynting vector about the longitudinal axis of the waveguide, is typical [4, 5, 7]. In this case, as obviously follows from electrodynamic considerations, the angular momentum of a dielectric waveguide–electromagnetic field system is distributed among the waveguide and vortex field, the distribution being dependent on the field excitation conditions and waveguide parameters. In this situation, the field gives up a part of its energy to the waveguide. In terms of quantum theory, an electromagnetic vortex is formed by photons that possess some net angular momentum about the longitudinal axis. In other words, the photon flux energy in a dielectric waveguide is bound to depend on the ratio between the numbers of photons with left- and right-handed helicity, as well as on the mode composition of the field. This work is aimed at theoretically (in terms of quantum optics) and experimentally studying the relationship between the energy, polarization, and mode composition of an electromagnetic field transmitted through the waveguide; i.e., we study the vortex properties of radiation in a dielectric waveguide, specifically, in a low-mode graded-index optical waveguide.

Consider a monochromatic field propagating in a circular dielectric waveguide in the linear regime. For a quiescent (stationary) insulating medium without free charges and currents, one can use the Hamilton gage of potentials:  $\Phi = 0$  [9, p. 16; 10, p. 76]. The field equation

then appears as [8]

$$\nabla^2 \mathbf{A} - \frac{\varepsilon}{c^2} \frac{\partial^2 \mathbf{A}}{\partial t^2} = \nabla(\nabla \mathbf{A}), \quad (1)$$

where  $\varepsilon = \varepsilon(r)$  is the radial-coordinate-dependent permittivity of the waveguide. Since the problem is axisymmetric, a solution to Eq. (1) will be sought in the form  $\mathbf{A} = \mathbf{F}(r)\exp[i(\omega t - \beta z + kl\varphi)]$ , where  $k = \pm 1$  and  $l = 0, 1, 2, \dots$ . As boundary conditions, we take the continuity of the tangential components of the electric field,  $E_{\varphi, z} = -\partial A_{\varphi, z}/\partial t$ , and magnetic field,  $B_{\varphi, z} = (\nabla \times \mathbf{A})_{\varphi, z}$ , on the lateral surface of the waveguide (of radius  $r_0$ ). Functions  $\mathbf{F}$  are polynomials depending on the profile of  $\varepsilon$ , and propagation constants  $\beta_l$  of waveguide modes satisfy a characteristic equation following from the boundary conditions at  $r = r_0$ .

Let us expand the field inside the waveguide in clockwise and counterclockwise polarized modes ( $k = \pm 1$ ):

$$\mathbf{A} = \frac{\sqrt{\pi c}}{\sqrt{V}} \sum_{j, l, k} \mathbf{I}_j F_j(R) \{ a_{jlk}(t) \exp[i(\beta_l z - kl\varphi)] + a_{jlk}^*(t) \exp[-i(\beta_l z - kl\varphi)] \}, \quad (2)$$

where amplitudes  $a_{jlk}(t)$  vary as  $\exp(-i\omega t)$  ( $j = r, \varphi, z$ ) and  $V$  is the volume occupied by the field. To make use of the quantum theory, we transform the variables so that the field equation can be written in the form of the Hamilton equations by introducing the generalized coordinates and momenta [11, p. 20]:

$$Q_{jlk} = \frac{1}{2}(a_{jlk} + a_{jlk}^*), \quad P_{jlk} = \frac{\omega}{2i}(a_{jlk} - a_{jlk}^*). \quad (3)$$

In coordinates (3), vector potential (2) takes the form

$$\mathbf{A} = \frac{\sqrt{4\pi c}}{\sqrt{V}} \sum_{j, l, k} \mathbf{I}_j F_j(A_{jlk} \cos \phi_{lk} - \omega^{-1} P_{jlk} \sin \phi_{lk}), \quad (4)$$

where  $\phi_{lk} = \beta_l z - kl\varphi$ .

Next, we will find the Hamiltonian of the system, using an expression for the energy of a monochromatic electromagnetic field in an insulating nonmagnetic medium:

$$\tilde{E}_L = \frac{1}{8\pi} \int dV (\epsilon \mathbf{E}^2 + \mathbf{B}^2). \quad (5)$$

Substituting the expressions for the electric field,  $\mathbf{E} = -\partial \mathbf{A}/c\partial t$ , and magnetic field,  $\mathbf{B} = \nabla \times \mathbf{A}$ , into (5), we integrate this expression over a finite volume that is a cylinder of radius  $r_0$  and length  $\Lambda$ , which equals the distance between the nearest field minima). Now, we replace canonic variables  $P_{jlk}$  and  $Q_{jlk}$  by operators obeying the law of commutation  $[\hat{P}_{jlk}, \hat{Q}_{jlk}] = -i\hbar\delta_{jj'}$ , transform the expression for the energy into Hamiltonian  $\tilde{E}_L \sim \hat{H}_L$ , and introduce the annihilation and birth operators

$$\begin{aligned} a_{jlk} &= \frac{1}{\sqrt{2\hbar\omega}} (\omega \hat{Q}_{jlk} + i\hat{P}_{jlk}), \\ a_{jlk}^+ &= \frac{1}{\sqrt{2\hbar\omega}} (\omega \hat{Q}_{jlk} - i\hat{P}_{jlk}) \end{aligned} \quad (6)$$

obeying the law of commutation  $[a_g, a_{g'}^+] = \delta_{gg'}$ .

Then, the Hamiltonian takes the form

$$\begin{aligned} \hat{H}_L &= \hbar\omega \sum_l \sum_{k=\pm 1} \left[ \frac{1}{2} \sum_{j=1,2,3} q_{jl} (a_{jlk} a_{jlk}^+ + a_{jlk}^+ a_{jlk}) \right. \\ &\quad \left. + klq_{4l} (a_{zlk} a_{\phi lk}^+ + a_{zlk}^+ a_{\phi lk}) \right], \end{aligned} \quad (7)$$

where

$$q_{1l} = \int_0^1 dRR \left[ \epsilon(R) + \frac{c^2}{r_0^2 \omega^2} \left( r_0^2 \beta_l^2 + \frac{l^2}{R^2} \right) \right] F_{rl}^2,$$

$$j = (r \equiv 1, \phi \equiv 2, z \equiv 3),$$

$$q_{2l} = \int_0^1 dRR \left[ \left( \epsilon(R) + \frac{c^2}{\omega^2} \beta_l^2 \right) F_{\phi l}^2 + \frac{c^2}{r_0^2 \omega^2} \left( \frac{dF_{\phi l}}{dR} + \frac{1}{R} F_{\phi l} \right)^2 \right],$$

$$q_{3l} = \int_0^1 dRR \left[ \left( \epsilon(R) + \frac{c^2}{r_0^2 \omega^2} \frac{l^2}{R^2} \right) F_{zl}^2 + \frac{c^2}{r_0^2 \omega^2} \left( \frac{dF_{zl}}{dR} \right)^2 \right],$$

$$q_{4l} = \frac{c^2 \beta_l^2}{r_0 \omega^2} \int_0^1 dRR F_{zl} F_{\phi l}, \quad R = r/r_0.$$

The energy of the system is expressed through num-

bers  $N_{jlk}$  of photons in the field mode:

$$\begin{aligned} \tilde{E}_L &= \hbar\omega \sum_l \sum_{k=\pm 1} \left[ \sum_{j=1,2,3} q_{jl} \left( N_{jlk} + \frac{1}{2} \right) \right. \\ &\quad \left. + klq_{4l} (\sqrt{N_{zlk}(N_{\phi lk} + 1)} + \sqrt{N_{\phi lk}(N_{zlk} + 1)}) \right]. \end{aligned} \quad (8)$$

If the number of photons with tight-handed helicity ( $k = 1$ ) equals the number of photons with left-handed helicity ( $k = -1$ ) in a linearly polarized mode, the terms multiplied by coefficient  $q_4$  in (8) disappear upon summation over  $k$ . Otherwise, when the field is a superposition of circularly polarized modes with  $l \neq 0$ , the terms with  $q_4$  do not cancel each other and field energy (8) depends on the ratio between numbers  $N_{\phi lk}$  and  $N_{zlk}$  of photons with left- and right-handed helicity in a relevant mode. This effect may be treated as the dependence of the energy of the system on the ‘‘spin-orbit interaction’’ of the electromagnetic field in the waveguide, provided that, in the case of mode superposition, the field orbital moment (characterized by subscript  $l$  of the mode) is other than zero and the spin of the photons characterizes the polarization of the mode [1, 5].

A classical interpretation of this effect can be given if a mode with subscript  $l > 0$  is assigned a ray (normal to the wave front at a given point) that propagates along a left- or right-handed helix when reflecting from the walls of the waveguide. If the sense of polarization of the circularly polarized mode coincides with the sense of the helical trajectory of the ray, the energy of the field grows and vice versa. In other words, the asymmetry that is observed in the polarization dependence of the radiation energy transmitted through the cylindrical system arises upon exciting the waveguide.

Alternatively, this effect can be explained in classical terms either by invoking the idea of stable and unstable optical vortices generated in the waveguide, which transfer different angular momenta, or by considering the evolution of the angular momentum of radiation as a result of waveguide mode interference [2, 3, 5].

The ratio of the energies of the system for linearly and circularly polarized modes ( $\tilde{E}_{Ll}$  and  $\tilde{E}_{Cl}$ , respectively),

$$\begin{aligned} \frac{\tilde{E}_{Ll}}{\tilde{E}_{Cl}} &= \sum_{j=1,2,3} q_{jl} \left( N_{jl} + \frac{1}{2} \right) \left\{ \sum_{j=1,2,3} q_{jl} \left( N_{jlk} + \frac{1}{2} \right) \right. \\ &\quad \left. + klq_{4l} (\sqrt{N_{zlk}(N_{\phi lk} + 1)} + \sqrt{N_{\phi lk}(N_{zlk} + 1)}) \right\}^{-1} \end{aligned}$$

depends on the numbers of photons in the mode components (here, the number of photons in the linearly

polarized mode equals the number of photons in the circularly polarized mode:  $N_{j_l+} + N_{j_l-} = N_{j_l}$ ; i.e.,  $\tilde{E}_{Ll}/\tilde{E}_{Cl}$  is greater or smaller than unity according to the sense of the related circularly polarized mode ( $k = \pm 1$ ).

Straightforward analysis makes it possible to reveal a relationship between the angular momentum and energy of the field in an insulating medium. For a circularly polarized mode propagating along the  $z$  axis, the angular momentum of the photon flux is  $L_z = N_C \hbar$ , where  $N_C = \tilde{E}_C/\hbar\omega$  is the number of photons. On the other hand, the work per unit time that is done on a classical electron in a given atom by the electromagnetic wave field is given by

$$\frac{d\tilde{E}_C}{dt} = -e(\mathbf{E} \cdot \mathbf{v}),$$

where  $\mathbf{v} = \omega \mathbf{r}$  is the rotation velocity of the electron and  $\mathbf{r}$  is the wave-field-induced displacement of the electron relative to the center of rotation. The rotational moment of the electron,  $\mathbf{M} = -[\mathbf{r} \times (e\mathbf{E})]$ , equals the time derivative of the angular momentum:  $\frac{d\mathbf{L}}{dt} = \mathbf{M}$ . Comparing

the equations for the work and angular momentum, we arrive at a relationship between the longitudinal component of the angular momentum and the energy of the circularly polarized wave:  $\frac{dL_z}{dt} = \frac{1}{\omega} \frac{d\tilde{E}_C}{dt}$  or  $dL_z =$

$\frac{1}{\omega} d\tilde{E}_C$ . The linearly polarized wave propagating along the  $z$  axis does not transfer the angular momentum: the average angular momentum of this wave is zero, since it results from interference between the clockwise and counterclockwise polarized modes that have the same number of photons.

To verify this effect in practice, we performed a simple experiment (see Fig. 1). Linearly polarized radiation from laser  $L$  ( $\lambda = 0.632 \mu\text{m}$ ) was incident on a quarter-wave crystal plate. With the plate oriented appropriately, the radiation took either circular or linear polarization. Microscope objective  $MO$  excited either the fundamental mode ( $l = 0$ ) or higher modes ( $l = 1, 2, \dots$ ) in low-mode graded-index optical fiber  $F$  (Fig. 2). The mode composition of the radiation was determined through the field distribution behind the  $\lambda/4$  plate and at the exit end face of the fiber with a CCD camera and a monitor. The radiation transmitted through the fiber was directed to photodiode  $PD$ , which was connected to digital voltmeter  $V$ . The readings of the voltmeter for both polarizations were processed by methods of the theory of errors.

For the fundamental mode ( $l = 0$ ), the ratio of the voltmeter readings for the linear and circular polarization of the radiation was equal to unity within an experimental error ( $\tilde{E}_{L0}/\tilde{E}_{C0} = 1.027 \pm 0.067$ ), while for a combination of higher modes ( $l = 1, 2, \dots$ ), this ratio

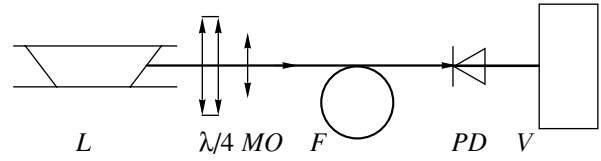


**Fig. 1.** Experimental scheme.  $L$ , He-Ne laser ( $\lambda = 0.632 \mu\text{m}$ ).  $\lambda/4$ , crystal plate;  $MO$ , microscope objective;  $F$ , optical fiber;  $PD$ , photodiode; and  $V$  digital voltmeter.

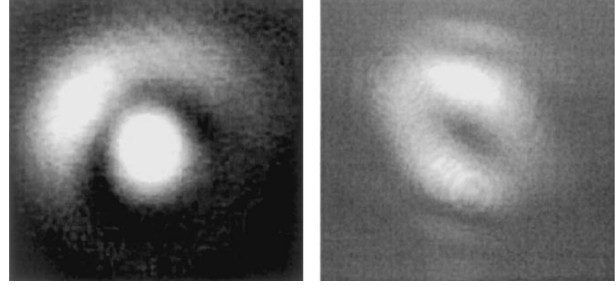


**Fig. 2.** Fundamental mode (on the left) and a superposition of higher modes (on the right) in the graded-index fiber. The radiation from the fiber cladding is seen around the spot of the fundamental mode.

was higher than unity ( $\tilde{E}_{Ll}/\tilde{E}_{Cl} = 0.893 \pm 0.053$  with a relative error of 6.5% and a confidence interval of 95%). In the latter case, the modes with  $k = 1$  were excited.

Let us analyze the effect of nonlinear processes on the propagation of the radiation along the dielectric waveguide with regard to the nonlinear response of an insulating medium (fused quartz) which the optical fiber is made of. In this case, the equations for the field and energy must contain nonlinear terms [8]:

$$\nabla^2 \mathbf{A} - \frac{\epsilon}{c^2} \frac{\partial^2 \mathbf{A}}{\partial t^2} = \nabla(\nabla \mathbf{A}) + \frac{\alpha_3}{c^4} \frac{\partial}{\partial t} \left( \frac{\partial \mathbf{A}}{\partial t} \right)^3, \quad (9)$$

$$\tilde{E}_{NL} = \frac{1}{8\pi} \int_V dV \left( \epsilon \mathbf{E}^2 + \frac{\alpha_3}{2} \mathbf{E}^4 + \mathbf{B}^2 \right), \quad (10)$$

where  $\alpha_3 = 4\pi\chi_3$  is the dielectric susceptibility of the medium that is a cubic function of the field [12].

Assuming that the linear response of the medium is weak, i.e., affects the mode structure insignificantly, we represent the Hamiltonian in the form  $\hat{H} = \hat{H}_L + \hat{H}_{NL}$ , where  $\hat{H}_L$  has the form of (7) and

$$\begin{aligned} \hat{H}_{NL} = & 8(\hbar\omega)^2 \sum_l \sum_{k=\pm 1} \tilde{q}_l \\ & \times \left[ \sum_j \sum_{j'} (a_{jlk} a_{j'lk} a_{j'l k}^+ a_{j'l k}^+ + a_{j'l k}^+ a_{j'l k}^+ a_{j'lk} a_{j'lk}) \right. \\ & \left. + a_{jlk} a_{j'l k}^+ a_{j'l k} a_{j'l k}^+ + a_{j'l k}^+ a_{j'l k}^+ a_{j'lk} a_{j'lk} \right] \end{aligned} \quad (11)$$

$$+ a_{jlk} a_{jlk}^+ a_{jlk} a_{jlk}^+ + a_{jlk} a_{jlk}^+ a_{jlk} a_{jlk}^+ \Big].$$

Here,  $\tilde{q}_l = \alpha_3 \int_0^1 dR R (\sum_j F_l^2)^2$ . In the nonlinear case, the energy of the system is  $\tilde{E} = \tilde{E}_L + \tilde{E}_{NL}$ , where linear term  $\tilde{E}_L$  is given by (8) and nonlinear term  $\tilde{E}_{NL}$  is found from (11) in the form

$$\tilde{E}_{NL} = 48(\hbar\omega)^2 \times \sum_l \sum_{k=\pm 1} \tilde{q}_l \left\{ \sum_{j,j'} \left[ N_{jlk} \left( N_{jlk} + \frac{1}{2} \right) + \frac{1}{2} N_{jlk} \right] + 2 \right\}. \quad (12)$$

From (12), it follows that the nonlinear contribution to the energy of the field does not depend on photon helicity  $k$  (in the given approximation).

Thus, the energy of an electromagnetic field propagating in a circular dielectric waveguide depends on the ratio between the numbers of photons with left- and right-handed helicity, i.e., on the mode composition and mode polarization. If the waveguide is excited by a circularly polarized radiation, the energy of the field in the waveguide may be both higher and lower than this energy in the case of excitation by a linearly polarized radiation. In the latter case, the circularly polarized field gives up the angular momentum to the waveguide. Weak nonlinear effects in the waveguide do not introduce the polarization dependence of the radiation energy. Based on the energy effect considered in this work, waveguide sensors of physical quantities can be designed.

## REFERENCES

1. V. S. Liberman and V. Ya. Zel'dovich, Phys. Rev. A **45**, 5199 (1992).
2. A. V. Volyar and T. A. Fadeeva, Pis'ma Zh. Tekh. Fiz. **22** (8), 57 (1996) [Tech. Phys. Lett. **22**, 330 (1996)].
3. A. V. Volyar and T. A. Fadeeva, Pis'ma Zh. Tekh. Fiz. **22** (17), 69 (1996) [Tech. Phys. Lett. **22**, 719 (1996)].
4. A. V. Volyar, V. Z. Zhilaitis, and V. G. Shvedov, Opt. Spektrosk. **86**, 664 (1999) [Opt. Spectrosc. **86**, 593 (1999)].
5. C. N. Alexeyev, M. S. Soskin, and A. V. Volyar, Semicond. Phys. Quantum Electron. Optoelectron. **3**, 500 (2000).
6. M. S. Soskin and M. V. Vasnetsov, in *Singular Optics*, Vol. 42: *Progress in Optics*, Ed. by E. Wolf (Elsevier Science, 2001), pp. 219–276.
7. I. V. Dzedolik, Pis'ma Zh. Tekh. Fiz. **29** (5), 43 (2003) [Tech. Phys. Lett. **29**, 194 (2003)].
8. I. V. Dzedolik, Pis'ma Zh. Tekh. Fiz. **29** (17), 16 (2003) [Tech. Phys. Lett. **29**, 708 (2003)].
9. L. D. Faddeev and A. A. Slavnov, *Gauge Fields: Introduction to Quantum Theory* (Nauka, Moscow, 1988; Addison-Wesley, Redwood, 1990).
10. L. D. Landau and E. M. Lifshitz, *Course of Theoretical Physics*, Vol. 2: *The Classical Theory of Fields* (Nauka, Moscow, 1988; Pergamon, Oxford, 1975).
11. V. B. Berestetskii, E. M. Lifshitz, and L. P. Pitaevskii, *Course of Theoretical Physics*, Vol. 4: *Quantum Electrodynamics* (Nauka, Moscow, 1989; Pergamon, New York, 1982).
12. S. A. Akhmanov, V. A. Vysloukh, and A. S. Chirkin, *The Optics of Femtosecond Laser Pulses* (Nauka, Moscow, 1988) [in Russian].

Translated by V. Isaakyan

## SHORT COMMUNICATIONS

# Hydrogen Adsorption on Silicon

S. Yu. Davydov

*Ioffe Physicotechnical Institute, Russian Academy of Sciences,  
Politekhnicheskaya ul. 26, St. Petersburg, 194021 Russia*

Received June 16, 2004

**Abstract**—Change  $\Delta\phi(\Theta)$  in work function versus surface coverage  $\Theta$  for the Si(100) surface is determined in terms of a model that includes not only the dipole–dipole interaction of hydrogen adatoms but also an elongation of the adsorption length with increasing  $\Theta$ . The charge of the adatoms as a function of  $\Theta$  is calculated, and the variation of the surface conductivity of the substrate is estimated. © 2005 Pleiades Publishing, Inc.

Until recently, theoretical investigation of gas adsorption has received little attention. In [1], models of atomic hydrogen adsorption on germanium were suggested. It turned out that the experimental data for hydrogen adsorption on Ge(111) [2] can be described adequately if the Anderson–Newns standard model [3, 4] assumes the dependence of adsorption bond length  $a$  on degree of coverage  $\Theta = N/N_{ML}$  (where  $N$  and  $N_{ML}$  are the particle concentrations in an adlayer and monolayer, respectively):

$$a = a_0(1 + \alpha\Theta), \quad (1)$$

where  $a_0$  is the adsorption bond length at zero coverage and  $\alpha$  is a dimensionless coefficient.

In the H/Ge(111) system, the value of  $\Delta\phi(\Theta)$  is negative at small  $\Theta$  (charge  $Z$  of an adatom is positive), vanishes at  $\Theta = 0.15$ , and then becomes positive (the adatom takes a negative charge) and grows. In going from  $Z > 0$  to  $Z = 0$ , shell occupation number  $n = 1 - Z$  of the adatom rises and shell radius  $a$  increases from a value close to ionic radius  $r_i$  to a value close to atomic radius  $r_a$ . Below, we will analyze the experimental data for the H/Ge(100) system [5].

For hydrogen adsorption on Si(100), the dependence  $\Delta\phi(\Theta)$  is in a sense inverse to this dependence for Ge(100): the work function of the system does not change up to  $\bar{\Theta} \approx 0.1$  (that is,  $\Delta\phi(\Theta) = 0$ ) and then, at  $\Theta > \bar{\Theta}$ , function  $\Delta\phi(\Theta)$  becomes negative.<sup>1</sup> Generally speaking, it is unclear why the work function of the H/Ge(100) system remains constant in the coverage interval (0, 0.1). Conversely, the work function of adsorption systems (such as metal-on-metal [4], metal-on-semiconductor [6], and gas-on-semiconductor [2, 7] systems) usually varies most significantly in this range, according to observations. Moreover, it was shown [5] that, when a submonolayer germanium film is applied

on the silicon substrate (i.e., in the H/Ge/Si(100) system), there appears a range of coverages (0,  $\Theta^*$ ) where  $\Delta\phi(\Theta)$  is positive and reaches a maximum at  $\Theta \approx 0.05$ . As the adatom concentration grows,  $\Theta^*$  increases. This allows us to expect a positive correction to the work function in the coverage interval (0, 0.1) for the uncovered Si(100) surface too. Subsequently, we will proceed from this assumption.

As was shown in [1], charge  $Z$  of an adatom and change  $\Delta\phi$  in the work function can be calculated with regard to dipole–dipole interaction in an adsorbed layer as follows:

$$Z = \frac{2}{\pi} \arctan \left[ \frac{\Omega_0(1-x)/(1+\bar{\alpha}x) - x^{3/2}\bar{\xi}_0 Z(1+\bar{\alpha}x)^2}{\Gamma} \right],$$

$$\Delta\phi = -\bar{\Phi}_0 x(1+\bar{\alpha}x)Z, \quad (2)$$

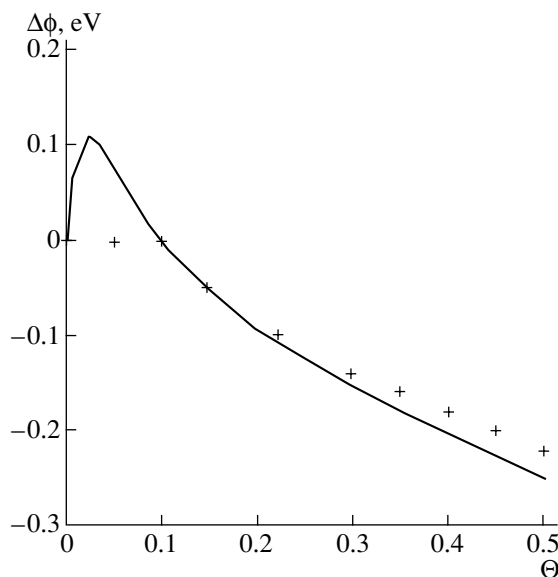


**Fig. 1.** Change  $\Delta\phi$  in the work function of the silicon surface vs. coverage  $\Theta$  by hydrogen atoms.

<sup>1</sup> When analyzing the data in [5], we assume that an exposure of 10L corresponds to  $\theta = 0.1$ . It is also assumed for simplicity that the coverage is a linear function of exposure.

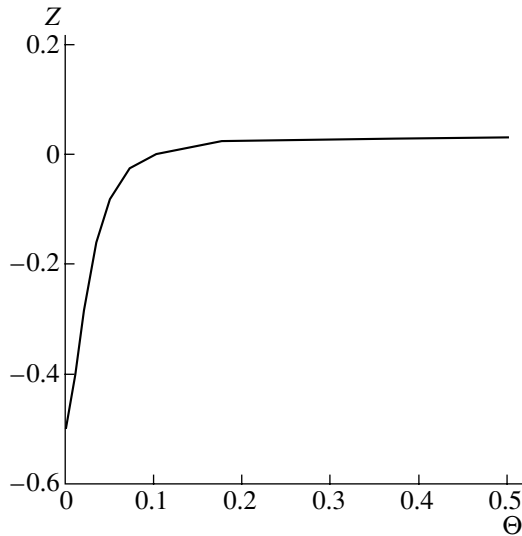


**Fig. 2.** Charge  $Z$  of a hydrogen adatom on the silicon surface vs. coverage  $\Theta$ .

where

$$z = \frac{\Theta}{\bar{\Theta}}, \quad \bar{\xi}_0 = \xi_0 \bar{\Theta}^{3/2}, \quad \bar{\Phi}_0 = \Phi_0 \bar{\Theta},$$

$$\bar{\alpha} = \alpha \bar{\Theta} = \frac{\Omega_0}{I - \phi}, \quad \xi_0 = 2e^2 a_0^2 N_{ML}^{3/2} A, \quad (3)$$

$$\Omega_0 = \phi - I + \Delta_0, \quad \Delta_0 = \frac{e^2}{4a_0}, \quad \alpha = \frac{\Omega_0}{I - \phi}.$$

Here,  $\Omega_0$  is the energy of the adatom quasi-level relative to the Fermi level of the substrate,  $\xi_0$  is the constant of dipole–dipole repulsion between adatoms,  $A \sim 10$  is a dimensionless coefficient that weakly depends on the adatom lattice configuration,  $\Gamma$  is the half-width of the isolated adatom quasi-level,  $I$  is the energy of ionization of the adatom,  $\phi$  is the work function of silicon, and  $\Delta_0$  is the Coulomb shift of the adatom quasi-level (this shift arises when the electron of an adatom interacts with electrons of the substrate).

To calculate the adsorption, we took the following values of the parameters:  $a_0 = 1.5 \text{ \AA}$ ,  $N_{ML} = 6.78 \times 10^{-14} \text{ cm}^{-2}$ ,  $\bar{\Theta} = 0.1$ ,  $\xi_0 = 11.44 \text{ eV}$ ,  $\Phi_0 = 18.4 \text{ eV}$ ,  $\Omega_0 = -0.1 \text{ eV}$ ,  $\Gamma = 0.1 \text{ eV}$ ,  $\Delta_0 = 2.4 \text{ eV}$ , and  $\alpha = -0.1$ . Note that here  $\alpha < 0$ ; that is, the adsorption bond shortens and the adatom quasi-level shifts upward, passing from its initial position under the Fermi level ( $\Omega_0 \equiv \Omega(\Theta = 0) < 0$ ) to a position above the Fermi level ( $\Omega(\Theta) = \Omega_0 - \Delta_0[\alpha\Theta/(1 + \alpha\Theta)]$ ).

The analytical dependence  $\Delta\phi(\Theta)$  is given in Fig. 1. Good agreement with the experimental data is observed for coverages between 0.1 and 0.3. A slight discrepancy at  $\Theta > 0.3$  is related to the neglect of exchange processes, which cause adatom depolarization [4]. Figure 2

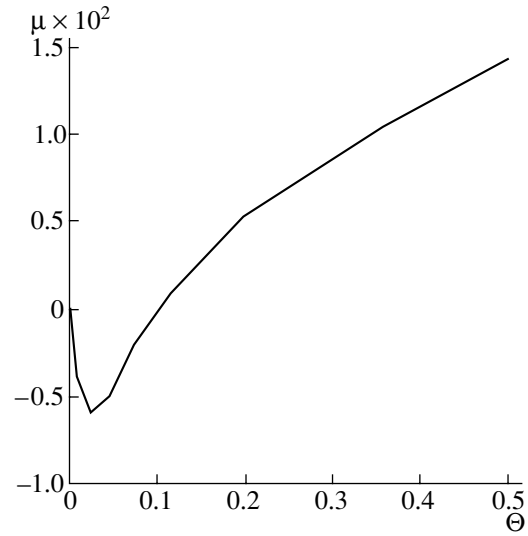


**Fig. 3.**  $\Theta$  dependence of product  $\mu \equiv |Z(\Theta)|\Theta$ , which varies in proportion to relative change  $\Delta\sigma/\sigma_0$  in the surface conductivity.

shows the variation of charge  $Z$  with  $\Theta$ . Note that the scale in Fig. 2 shades the fine structure of the dependence  $Z(\Theta)$ : namely, charge  $Z$  first vanishes at  $\bar{\Theta}$ ; then takes a positive value, growing in magnitude up to  $\Theta = 0.4$  ( $Z(0.4) \approx 0.029$ ); and finally declines slowly.

Since hydrogen accepts the electrons of the substrate at  $\Theta \leq 0.1$  and donates them at higher coverages, surface conductivity  $\sigma$  first declines relative to the conductivity of the uncovered surface and then exceeds it. Figure 3 shows the  $\Theta$  dependence of product  $\mu \equiv |Z(\Theta)|\Theta$ , which varies in proportion to relative change  $\Delta\sigma/\sigma_0$  in the surface conductivity, where  $\sigma_0$  is the conductivity of the uncovered Si(100) surface.

Thus, the simple model adopted in this work, which was initially proposed for sodium atom adsorption on cesium [8], can also be applied to hydrogen adsorption on germanium and silicon.

## REFERENCES

1. S. Yu. Davydov, *Zh. Tekh. Fiz.* **75**, 112 (2005) [*Tech. Phys.* **50**, 110 (2005)].
2. L. Surnev and M. Tikhov, *Surf. Sci.* **138**, 40 (1984).
3. *Theory of Chemisorption*, Ed. by J. R. Smith (Springer-Verlag, Berlin, 1980; Mir, Moscow, 1983).
4. O. M. Braun and V. K. Medvedev, *Usp. Fiz. Nauk* **157**, 631 (1989) [*Sov. Phys. Usp.* **32**, 328 (1989)].
5. G. Boishin and L. Surnev, *Surf. Sci.* **345**, 64 (1996).
6. *Physics and Chemistry of Alkali Metal Adsorption*, Ed. by H. P. Bonzel, A. M. Bradshaw, and G. Ertl (Elsevier, Amsterdam, 1989).
7. V. E. Heinrich and V. E. Cox, *The Surface Science of Metal Oxides* (Cambridge Univ. Press, Cambridge, 1994).
8. S. Y. Davydov, *Appl. Surf. Sci.* **140**, 52 (1999).

*Translated by V. Isaakyan*

---

GASES  
AND LIQUIDS

---

## On the Time Evolution of the Surface Shape of a Charged Viscous Liquid Drop Deformed at Zero Time

A. N. Zharov and A. I. Grigor'ev

Yaroslavl State University, Sovetskaya ul. 14, Yaroslavl, 150000 Russia

e-mail: grig@uniyar.ac.ru

Received May 14, 2004

**Abstract**—The problem of capillary oscillations of the equilibrium spherical shape of a charged viscous incompressible liquid drop is solved in an approximation linear in amplitude of the initial deformation that is represented by a finite sum of axisymmetric modes. In this approximation, the shape of the drop as a function of time, as well as the velocity and pressure fields of the liquid in it, may be represented by infinite series in roots of the dispersion relation and by finite sums in numbers of the initially excited modes. In the cases of low, moderate, and high viscosity, the infinite series in roots of the dispersion relation can be asymptotically correctly replaced by a finite number of terms to find compact analytical expressions that are convenient for further analysis. These expressions can be used for finding higher order approximations in amplitude of the initial deformation. © 2005 Pleiades Publishing, Inc.

(1) Capillary oscillation and stability of a charged incompressible liquid drop are of both scientific and applied interest [1–3]. Therefore, this problem was repeatedly solved in the linear and nonlinear statements. However, up to now the analytical calculations of nonlinear oscillations of a charged drop have been made only in the ideal liquid approximation [4–9], and nonlinear analysis of viscous drops has been performed only by numerical methods [10, 11]. The attempt [12] to asymptotically calculate nonlinear oscillations of an arbitrary-viscosity drop [12] resulted in very awkward expressions at the final stage, which are hardly amenable to conventional methods of mathematical analysis. It seems, however, that the difficulties faced in [12] may be avoided in the limits of extremely high and negligible viscosity. In this work, we solve the problem of time evolution of the shape of a charged viscous liquid drop that is deformed at the zero time in an approximation linear in oscillation amplitude and find asymptotic solutions in the limits of high and low viscosity. In the previous studies of linear oscillations of a charged viscous liquid drop, which were carried out in terms of the linear theory, the basic result was the derivation of the dispersion relation, based on which one can judge the oscillation modes and stability of the drop [1, 13, 14]. Initial conditions were not included in the statement of the problem. As applied to the time evolution of the shape of an oscillating drop, these studies were reduced to deriving asymptotic expressions for the damping decrements. In this work, we suggest a qualitatively different approach to linear analysis of the oscillations of a viscous liquid drop. Our approach is, in essence, the

linear stage of solving the problem of nonlinear oscillations of a viscous drop.

(2) Let a spherical drop of a perfectly conducting incompressible viscous liquid with density  $\rho$ , kinematic viscosity  $\nu$ , and surface tension coefficient  $\sigma$  bear electric charge  $Q$ . The radius of the drop is  $r_0$ . Denote the liquid velocity field in the drop as  $\mathbf{U}(r, \vartheta, t)$ ; the pressure field as  $P(r, \vartheta, t)$ ; and the electric field potentials in the vicinity of the drop and on its surface as  $\phi(r, \vartheta, t)$  and  $\phi_s(t)$ , respectively. In spherical coordinate system  $(r, \vartheta, \varphi)$ , an equation for the surface of the drop, which executes axisymmetric oscillations at any time instant  $t$ , can be written in the form

$$F(r, \vartheta, t) = r - r_0 - \xi(\vartheta, t), \quad (1)$$

with the initial condition

$$t = 0: \xi = \varepsilon \sum_{m \in \Omega} h_m P_m(\mu), \quad \mu \equiv \cos \vartheta. \quad (2)$$

Here,  $\varepsilon$  is a small parameter characterizing the initial perturbation amplitude,  $P_m(\mu)$  is the Legendre polynomial of the  $m$ th order,  $\Omega$  is the set of indices of initially excited modes, and  $h_m$  are constants taking into account the partial contributions of an  $m$ th mode to the initial shape of the drop ( $\sum_{m \in \Omega} h_m = O(1)$ ).

Mathematically, the problem of oscillations of a charged conducting incompressible viscous liquid drop whose shape is defined by (1) and (2) is stated as



[13, 14]

$$\partial_t \mathbf{U} + (\mathbf{U} \cdot \nabla) \mathbf{U} = -\frac{1}{\rho} \text{grad} p + \nu \Delta \mathbf{U}; \quad \text{div} \mathbf{U} = 0;$$

$$\Delta \phi = 0;$$

$$t = 0: \mathbf{U} = 0;$$

$$r \rightarrow 0: \mathbf{U} < \infty;$$

$$r \rightarrow +\infty: \nabla \phi \rightarrow 0;$$

$$r = r_0 + \xi(\vartheta, t): \phi = \phi_s(t); \quad \partial_t F + (\mathbf{U} \cdot \nabla) F = 0;$$

$$\boldsymbol{\tau} \cdot (\mathbf{n} \cdot \nabla) \mathbf{U} + \mathbf{n} \cdot (\boldsymbol{\tau} \cdot \nabla) \mathbf{U} = 0;$$

$$-p + 2\rho \nu \mathbf{n} \cdot (\mathbf{n} \cdot \nabla) \mathbf{U} - p_Q + p_\sigma = 0;$$

$$\int_S \mathbf{n} \cdot \nabla \phi dS = -4\pi Q;$$

$$S = \{r, \vartheta, \phi | r = r_0 + \xi; 0 \leq \vartheta \leq \pi; 0 \leq \phi \leq 2\pi\};$$

$$\int_V r^2 \sin \vartheta dr d\vartheta d\phi = \frac{4\pi}{3} r_0^3;$$

$$V = \{r, \vartheta, \phi | 0 \leq r \leq r_0 + \xi; 0 \leq \vartheta \leq \pi; 0 \leq \phi \leq 2\pi\};$$

$$\int_V \mathbf{r} r^2 \sin \vartheta dr d\vartheta d\phi = 0.$$

Here, symbol  $\partial_t$  means a partial derivative with respect to variable  $t$ ;  $\mathbf{n}$  and  $\boldsymbol{\tau}$  are the unit vectors normal and tangent to the surface of the drop, respectively;

$$p_Q = \frac{1}{8\pi} (\nabla \phi)^2, \quad p_\sigma = \sigma (\nabla \cdot \mathbf{n})$$

are the pressures of surface tension forces and forces due to the electric field of the self-charge of the drop; and  $\Delta$  is the Laplacian.

(3) Since the set of equations written above is nonlinear, we expand all the desired quantities in small parameter  $\varepsilon$  to find its solution by the direct expansion method [15]:

$$\xi(\vartheta, t) = \varepsilon \xi^{(1)}(\vartheta, t) + O(\varepsilon^2);$$

$$\mathbf{U}(r, \vartheta, t) =$$

$$\varepsilon U_r^{(1)}(r, \vartheta, t) \mathbf{e}_r + \varepsilon U_\vartheta^{(1)}(r, \vartheta, t) \mathbf{e}_\vartheta + O(\varepsilon^2);$$

$$p(r, \vartheta, t) = p^{(0)}(r, \vartheta, t) + \varepsilon p^{(1)}(r, \vartheta, t) + O(\varepsilon^2);$$

$$\phi(r, \vartheta, t) = \phi^{(0)}(r, t) + \varepsilon \phi^{(1)}(r, \vartheta, t) + O(\varepsilon^2);$$

$$\phi_s(t) = \phi_s^{(0)}(t) + \varepsilon \phi_s^{(1)}(t) + O(\varepsilon^2).$$

(i) Substituting these expansions into the basic set of equations and equating the coefficients multiplying the zeroth power of the small parameter to each other, we

obtain a set of equations of the zeroth order of smallness:

$$\Delta \phi^{(0)} = 0;$$

$$r \rightarrow +\infty: \nabla \phi^{(0)} \rightarrow 0;$$

$$r = r_0: \int_{-1}^1 r_0^2 \partial_r \phi^{(0)} d(\cos \vartheta) = -2Q; \quad \phi^{(0)} = \phi_s^{(0)}(t);$$

$$-p^{(0)} - p_Q^{(0)} + p_\sigma^{(0)} = 0.$$

Solving it, we find

$$\phi^{(0)} = \frac{Q}{r}; \quad \phi_s^{(0)} = \frac{Q}{r_0}; \quad p^{(0)} + \frac{Q^2}{8\pi r_0^4} = \frac{2\sigma}{r_0}. \quad (3)$$

(ii) Separating out the terms involving the small parameter in the first power and taking into account the vector identity [16]

$$\Delta \mathbf{U} = \text{grad}(\text{div} \mathbf{U}) - \text{curl}(\text{curl} \mathbf{U}),$$

we arrive at the first-order problem

$$\partial_t U_r^{(1)} = -\frac{1}{\rho} \partial_r p^{(1)} + \nu \left( \frac{1}{r^2} \partial_{\vartheta\vartheta} U_r^{(1)} + \frac{\cot(\vartheta)}{r^2} \partial_\vartheta U_r^{(1)} - \frac{1}{r} \partial_{r\vartheta} U_\vartheta^{(1)} - \frac{\cot(\vartheta)}{r} \partial_r U_\vartheta^{(1)} - \frac{1}{r^2} \partial_\vartheta U_\vartheta^{(1)} - \frac{\cot(\vartheta)}{r^2} U_\vartheta^{(1)} \right);$$

$$\partial_t U_\vartheta^{(1)} = -\frac{1}{\rho r} \partial_\vartheta p^{(1)} + \nu \left( \partial_{rr} U_\vartheta^{(1)} + \frac{2}{r} \partial_r U_\vartheta^{(1)} - \frac{1}{r} \partial_{r\vartheta} U_r^{(1)} \right);$$

$$\partial_r U_r^{(1)} + \frac{2}{r} U_r^{(1)} + \frac{1}{r} \partial_\vartheta U_\vartheta^{(1)} + \frac{\cot(\vartheta)}{r} U_\vartheta^{(1)} = 0; \quad \Delta \phi^{(1)} = 0;$$

$$t = 0: \xi^{(1)} = \varepsilon \sum_{m \in \Omega} h_m P_m(\mu); \quad \mathbf{U}^{(1)} = 0;$$

$$r \rightarrow 0: \mathbf{U}^{(1)} < \infty; \quad r \rightarrow +\infty: \nabla \phi^{(1)} \rightarrow 0; \quad (4)$$

$$r = r_0: \partial_t \xi^{(1)} = U_r^{(1)}; \quad \partial_r U_\vartheta^{(1)} + \frac{1}{r} \partial_\vartheta U_r^{(1)} - \frac{1}{r} U_\vartheta^{(1)} = 0;$$

$$-p^{(1)} + 2\rho \nu \partial_r U_r^{(1)} - \frac{1}{4\pi} \partial_r \phi^{(0)} (\partial_r \phi^{(1)} + \xi^{(1)} \partial_{rr} \phi^{(0)})$$

$$- \frac{\sigma}{r_0^2} (2 + \Delta_\Omega) \xi^{(1)} = 0;$$

$$\int_{-1}^1 (r_0 \partial_r \phi^{(1)} + \xi^{(1)} (r_0 \partial_{rr} \phi^{(0)} + 2\partial_r \phi^{(0)})) d(\mu) = 0;$$

$$\phi^{(1)} + \xi^{(1)} \partial_r \phi^{(0)} = \phi_s^{(1)}(t);$$

$$\int_{-1}^1 \xi^{(1)} d(\mu) = 0; \quad \int_{-1}^1 \xi^{(1)} P_1(\mu) d(\mu) = 0,$$

where  $\Delta_\Omega$  is the angular part of the Laplacian.

(4) Now we apply the Laplace transformation to set (4), that is, turn from the functions to their Laplace transforms [17]:

$$F(S) = \int_0^{+\infty} f(t) \exp(-St) dt; \quad f = U_r^{(1)}; \quad f = U_\vartheta^{(1)};$$

$$f = p^{(1)}; \quad f = \xi^{(1)}; \quad f = \phi^{(1)}; \quad f = \phi_S^{(1)}$$

and expand the Laplace images in an infinite set of Legendre polynomials:

$$U_r^{(1)}(r, \vartheta, S) = \sum_{n=0}^{+\infty} U_{rn}^{(1)}(r, S) P_n(\mu);$$

$$U_\vartheta^{(1)}(r, \vartheta, S) = \sum_{n=0}^{+\infty} U_{\vartheta n}^{(1)}(r, S) \partial_\vartheta P_n(\mu);$$

$$\xi^{(1)}(\vartheta, S) = \sum_{n=0}^{+\infty} \xi_n^{(1)}(S) P_n(\mu); \quad (5)$$

$$\phi^{(1)}(r, \vartheta, S) = \sum_{n=0}^{+\infty} \phi_n^{(1)}(r, S) P_n(\mu);$$

$$p^{(1)}(r, \vartheta, S) = \sum_{n=0}^{+\infty} p_n^{(1)}(r, S) P_n(\mu).$$

As a result, set (4) takes the form

$$S U_{rn}^{(1)}(r, S) = -\frac{1}{\rho} \partial_r p_n^{(1)}(r, S) + \nu n(n+1)$$

$$\times \left( \frac{1}{r} \partial_r U_{\vartheta n}^{(1)}(r, S) + \frac{1}{r^2} U_{\vartheta n}^{(1)}(r, S) - \frac{1}{r^2} U_{rn}^{(1)}(r, S) \right); \quad (6)$$

$$S U_{\vartheta n}^{(1)}(r, S) = -\frac{1}{\rho r} p_n^{(1)}(r, S) + \nu \left( \partial_{rr} U_{\vartheta n}^{(1)}(r, S) \right.$$

$$\left. + \frac{2}{r} \partial_r U_{\vartheta n}^{(1)}(r, S) - \frac{1}{r} \partial_r U_{rn}^{(1)}(r, S) \right); \quad (7)$$

$$\partial_r U_{rn}^{(1)}(r, S) + \frac{2}{r} U_{rn}^{(1)}(r, S) - \frac{n(n+1)}{r} U_{\vartheta n}^{(1)}(r, S) = 0; \quad (8)$$

$$r \rightarrow 0: U_{rn}^{(1)}(r, S) < \infty; \quad U_{\vartheta n}^{(1)}(r, S) < \infty; \quad (9)$$

$$r = r_0: S \xi_n^{(1)}(S) - h_n = U_{rn}^{(1)}; \quad (10)$$

$$\partial_r U_{\vartheta n}^{(1)}(r, S) + \frac{1}{r} U_{rn}^{(1)}(r, S) - \frac{1}{r} U_{\vartheta n}^{(1)}(r, S) = 0; \quad (11)$$

$$-p_n^{(1)}(r, S) + 2\rho\nu \partial_r U_{rn}^{(1)}(r, S) - \frac{1}{4\pi} \partial_r \phi^{(0)}(\partial_r \phi_n^{(1)}(r, S))$$

$$+ \xi_n^{(1)}(S) \partial_{rr} \phi^{(0)} + \frac{\sigma}{r_0^2} (n+2)(n-1) \xi_n^{(1)}(S) = 0; \quad (12)$$

$$\int_{-1}^{+1} \sum_{n=0}^{+\infty} \xi_n^{(1)}(S) P_n(\mu) d(\mu) = 0; \quad (13)$$

$$\int_{-1}^{+1} \sum_{n=0}^{+\infty} \xi_n^{(1)}(S) P_n(\mu) P_1(\mu) d(\mu) = 0;$$

$$\partial_{rr} \phi_n^{(1)}(r, S) + \frac{2}{r} \partial_r \phi_n^{(1)}(r, S) - n(n+1) \phi_n^{(1)}(r, S) = 0; \quad (14)$$

$$r \rightarrow +\infty: \partial_r \phi_n^{(1)}(r, S) \rightarrow 0; \quad \phi_n^{(1)}(r, S) \rightarrow 0; \quad (15)$$

$$r = r_0: \int_{-1}^{+1} \sum_{n=0}^{+\infty} (r_0 \partial_r \phi_n^{(1)}(r, S) + \xi_n^{(1)}(S) (r_0 \partial_{rr} \phi^{(0)}$$

$$+ 2\partial_r \phi^{(0)}) P_n(\mu) d(\mu) = 0; \quad (16)$$

$$\phi_n^{(1)}(r, S) + \xi_n^{(1)}(S) \partial_r \phi^{(0)} = \phi_S^{(1)}(S) \delta_{n0}, \quad (17)$$

where  $\delta_{n0}$  is the Kronecker symbol.

We start to solve set (6)–(17) from the solution of Eqs. (13), which, subject to the orthogonality conditions for the Legendre polynomials, yield  $\xi_0^{(1)}(S) = \xi_1^{(1)}(S) = 0$ . With these conditions and zeroth-order solutions (3), it is easy to find a solution to set of equations (14)–(17) in the form

$$\phi_S^{(1)}(S) = 0; \quad \phi_n^{(1)}(r, S) = \frac{Q}{r_0^2} \left( \frac{r_0}{r} \right)^{n+1} \xi_n^{(1)}(S). \quad (18)$$

To find the liquid velocity and pressure fields in the drop, we express  $U_{\vartheta n}^{(1)}(r, S)$  appearing in continuity equation (8) as

$$U_{\vartheta n}^{(1)}(r, S) = \frac{r}{n(n+1)} \left( \partial_r U_{rn}^{(1)}(r, S) + \frac{2}{r} U_{rn}^{(1)}(r, S) \right), \quad (19)$$

and  $p_n^{(1)}(r, S)$  from Eq. (7) as

$$p_n^{(1)}(r, S) = -S\rho r U_{\vartheta n}^{(1)}(r, S) + \rho\nu r \left( \partial_{rr} U_{\vartheta n}^{(1)}(r, S) \right.$$

$$\left. + \frac{2}{r} \partial_r U_{\vartheta n}^{(1)}(r, S) - \frac{1}{r} \partial_r U_{rn}^{(1)}(r, S) \right). \quad (20)$$

With expressions (19) and (20) substituted into (6), (6) takes the form [18]

$$\left(\partial_{rr} + \frac{4}{r}\partial_r - \frac{(n-1)(n+2)}{r^2}\right) \times \left(\partial_{rr} + \frac{4}{r}\partial_r - \frac{(n-1)(n+2)}{r^2} - \frac{S}{v}\right) U_{rn}^{(1)}(r, S) = 0. \quad (21)$$

A solution to Eq. (21) that satisfies boundedness condition (9) has the form

$$U_{rn}^{(1)}(r, S) = A_n(S)r^{n-1} + B_n(S)\frac{1}{r}j_n\left(\sqrt{\frac{S}{v}}r\right), \quad (22)$$

where  $A_n(S)$  and  $B_n(S)$  are arbitrary constants and  $j_n$  is the  $n$ th-order modified spherical Bessel function of the first kind.

Substituting (22) into (19) and (20), we find  $U_{\partial n}^{(1)}(r, S)$  and  $p_n^{(1)}(r, S)$ :

$$U_{\partial n}^{(1)}(r, S) = \frac{1}{n(n+1)}\left(A_n(S)(n+1)r^{n-1} + B_n(S)\frac{1}{r}j_n\left(\sqrt{\frac{S}{v}}r\right) + B_n(S)\partial_r j_n\left(\sqrt{\frac{S}{v}}r\right)\right); \quad (23)$$

$$p_n^{(1)}(r, S) = -A_n(S)\frac{S\rho}{n}r^n. \quad (24)$$

Now we substitute (3), (18), and (22)–(24) into Eqs. (10)–(12) to obtain a set of three equations from which dependences  $A_n(S)$ ,  $B_n(S)$ , and  $\xi_n^{(1)}(S)$  can be found:

$$r_0(S\xi_n^{(1)}(S) - h_n) = A_n(S)r_0^n + B_n(S)j_n(\chi);$$

$$2A_n(S)(n-1)(n+1)r_0^n + B_n(S)((n-1)(n+2)j_n(\chi) + \chi^2\partial_{\chi\chi}j_n(\chi)) = 0; \quad (25)$$

$$\omega_n^2 r_0^3 \xi_n^{(1)}(S) + A_n(S)r_0^n(2n\nu(n-1) + r_0^2 S)$$

$$+ 2n\nu B_n(S)(\chi\partial_{\chi}j_n(\chi) - j_n(\chi)) = 0;$$

$$\chi = \sqrt{\frac{S}{v}}r_0; \quad \omega_n^2 = \frac{\sigma}{\rho r_0^3}n(n-1)\left(n+2 - \frac{Q^2}{4\pi\sigma r_0^3}\right).$$

Applying the recurrence relations for the modified spherical Bessel functions [19]

$$\partial_{\chi}j_n(\chi) = j_{n+1}(\chi) + \frac{n}{\chi}j_n(\chi);$$

$$\partial_{\chi}j_n(\chi) = j_{n-1}(\chi) - \frac{n+1}{\chi}j_n(\chi);$$

$$\partial_{\chi\chi}j_n(\chi) = \left(1 + \frac{n(n-1)}{\chi^2}\right)j_n(\chi) - \frac{2}{\chi}j_{n+1}(\chi);$$

we find functions  $\xi_n^{(1)}(S)$ ,  $A_n(S)$ , and  $B_n(S)$  from set (25). Substituting them into expressions (22)–(24) yields

$$\xi_n^{(1)}(S) = \left(S + 2(n-1)(2n+1)\frac{\nu}{r_0^2} + 2(n-1)^2(n+1)\right.$$

$$\left.\times \frac{\nu}{r_0^2}\left(1 - \frac{\chi}{2} \frac{j_n(\chi)}{j_{n+1}(\chi)}\right)^{-1}\right) \frac{h_n}{D_n(S)};$$

$$U_{rn}^{(1)}(r, S) = \left(\left(2(n^2-1) + \frac{r_0^2 S}{\nu}\right) \frac{1}{2\chi} \frac{j_n(\chi)}{j_{n+1}(\chi)} - 1\right)$$

$$\times \left(1 - \frac{\chi}{2} \frac{j_n(\chi)}{j_{n+1}(\chi)}\right)^{-1} \frac{\omega_n^2 h_n}{D_n(S)} \left(\frac{r}{r_0}\right)^{n-1} + 2(n^2-1)$$

$$\times \left(1 - \frac{2j_{n+1}(\chi)}{\chi j_n(\chi)}\right)^{-1} \frac{\omega_n^2 \nu}{r_0 S j_n(\chi) D_n(S)} \frac{h_n}{r} j_n\left(\sqrt{\frac{S}{v}}r\right);$$

$$U_{\partial n}^{(1)}(r, S) = \left(\left(2(n^2-1) + \frac{r_0^2 S}{\nu}\right) \frac{1}{2\chi} \frac{j_n(\chi)}{j_{n+1}(\chi)} - 1\right)$$

$$\times \left(1 - \frac{\chi}{2} \frac{j_n(\chi)}{j_{n+1}(\chi)}\right)^{-1} \frac{\omega_n^2 h_n}{n D_n(S)} \left(\frac{r}{r_0}\right)^{n-1}$$

$$+ 2(n-1)\left(1 - \frac{2j_{n+1}(\chi)}{\chi j_n(\chi)}\right)^{-1} \frac{\omega_n^2 \nu}{r_0 S j_n(\chi) n D_n(S)}$$

$$\times \left(\frac{n+1}{r} j_n\left(\sqrt{\frac{S}{v}}r\right) + \frac{\sqrt{S}}{\sqrt{v}} j_{n+1}\left(\sqrt{\frac{S}{v}}r\right)\right);$$

$$p_n^{(1)}(r, S) = -\left(\left(2(n^2-1) + \frac{r_0^2 S}{\nu}\right) \frac{1}{2\chi} \frac{j_n(\chi)}{j_{n+1}(\chi)} - 1\right)$$

$$\times \left(1 - \frac{\chi}{2} \frac{j_n(\chi)}{j_{n+1}(\chi)}\right)^{-1} \frac{S\rho\omega_n^2 h_n r^n}{n D_n(S) r_0^{n-1}};$$

$$D_n(S) = S^2 + 2(n-1)(2n+1)\frac{S\nu}{r_0^2} \quad (26)$$

$$+ 2(n-1)^2(n+1)\frac{S\nu}{r_0^2}\left(1 - \frac{\chi}{2} \frac{j_n(\chi)}{j_{n+1}(\chi)}\right)^{-1} + \omega_n^2.$$

It is seen that expressions (26) have singular points whose positions are defined by the condition  $D_n(S_n^{(k)}) = 0$ .

The equation  $D_n(S_n^{(k)}) = 0$  is the dispersion relation of the problem, which has an infinite number of solutions.

In each of these solutions, function  $(1/D_n(S_n^{(k)}))$  has a first-order pole. In addition, each of expressions (26)

tends to zero at  $S \rightarrow \infty$ . Then, we can replace the integral taken along straight line  $\text{Re}S = \gamma$  in the inverse Laplace transformation

$$f(t) = \frac{1}{2\pi i} \int_{\gamma - i\infty}^{\gamma + i\infty} F(S) \exp(St) dS$$

by the circulation integral taken along a contour enclosing the whole left-hand part of the complex plane and then apply the residue theorem to this integral. Eventually, the inversion formula takes the form

$$f(t) = \sum_{k=1}^{+\infty} \text{Res}[F(S) \exp(St), S_k]. \quad (27)$$

Substituting (26) into (5) and using inversion formula (27) along with the initial conditions, we find expressions for the deviation of the shape of the drop from the equilibrium sphere and for the velocity and pressure fields of the liquid flow in the drop:

$$\begin{aligned} \xi^{(1)}(\vartheta, t) &= \sum_{n \in \Omega} \xi_n^{(1)}(t) h_n P_n(\mu); \\ U_r^{(1)}(r, \vartheta, t) &= \sum_{n \in \Omega} U_{rn}^{(1)}(r, t) h_n P_n(\mu); \\ U_{\vartheta}^{(1)}(r, \vartheta, t) &= \sum_{n \in \Omega} U_{\vartheta n}^{(1)}(r, t) h_n \partial_{\vartheta} P_n(\mu); \\ p_n^{(1)}(r, \vartheta, t) &= \sum_{n \in \Omega} p_n^{(1)}(r, t) h_n P_n(\mu); \end{aligned} \quad (28)$$

where

$$\begin{aligned} \xi_n^{(1)}(t) &= \sum_{k=1}^{+\infty} a_{\xi}(S_n^{(k)}) \exp(S_n^{(k)} t); \\ U_{rn}^{(1)}(r, t) &= \sum_{k=1}^{+\infty} \left( a(S_n^{(k)}) \left( \frac{r}{r_0} \right)^{n-1} + b(S_n^{(k)}) \frac{1}{r} \frac{j_n(\eta_n^{(k)} r)}{j_n(\eta_n^{(k)} r_0)} \right) \exp(S_n^{(k)} t); \\ U_{\vartheta n}^{(1)}(r, t) &= \sum_{k=1}^{+\infty} \left( a(S_n^{(k)}) \left( \frac{r}{r_0} \right)^{n-1} + b(S_n^{(k)}) \left( \frac{1}{r} \frac{j_n(\eta_n^{(k)} r)}{j_n(\eta_n^{(k)} r_0)} \right. \right. \\ &\quad \left. \left. + \frac{\eta_n^{(k)}}{n+1} \frac{j_{n+1}(\eta_n^{(k)} r)}{j_n(\eta_n^{(k)} r_0)} \right) \right) \frac{\exp(S_n^{(k)} t)}{n}; \\ \eta_n^{(k)} &\equiv \sqrt{S_n^{(k)} v^{-1}}; \end{aligned}$$

$$p_n^{(1)}(r, t) = -\rho r_0 \sum_{k=1}^{+\infty} a(S_n^{(k)}) S_n^{(k)} \left( \frac{r}{r_0} \right)^n \frac{\exp(S_n^{(k)} t)}{n}; \quad (29)$$

$$a_{\xi}(S_n^{(k)}) = \left( S_n^{(k)} + 2(n-1)(2n+1) \frac{v}{r_0^2} \right.$$

$$\left. + 2(n-1)^2(n+1) \frac{v}{r_0^2} \left( 1 - \frac{\chi}{2} \frac{j_n(\chi)}{j_{n+1}(\chi)} \right)^{-1} \right) \frac{1}{\partial_S D_n(S_n^{(k)})};$$

$$\begin{aligned} a(S_n^{(k)}) &= \left( \left( 2(n^2 - 1) + \frac{r_0^2 S_n^{(k)}}{v} \right) \frac{1}{2\chi} \frac{j_n(\chi)}{j_{n+1}(\chi)} - 1 \right) \\ &\quad \times \left( 1 - \frac{\chi}{2} \frac{j_n(\chi)}{j_{n+1}(\chi)} \right)^{-1} \frac{\omega_n^2}{\partial_S D_n(S_n^{(k)})}; \end{aligned}$$

$$b(S_n^{(k)}) = 2(n^2 - 1) \left( 1 - \frac{2}{\chi} \frac{j_{n+1}(\chi)}{j_n(\chi)} \right)^{-1} \frac{\omega_n^2 v}{r_0 S_n^{(k)} \partial_S D_n(S_n^{(k)})};$$

$$\partial_S D_n(S_n^{(k)}) = 2S_n^{(k)} + 2(n-1)(2n+1) \frac{v}{r_0^2}$$

$$+ (n-1)^2(n+1) \frac{v}{r_0^2} \left( 2 + \frac{(2n+1)\chi}{2} \frac{j_n(\chi)}{j_{n+1}(\chi)} \right.$$

$$\left. + \frac{\chi^2}{2} \left( 1 - \left( \frac{j_n(\chi)}{j_{n+1}(\chi)} \right)^2 \right) \right) \left( 1 - \frac{\chi}{2} \frac{j_n(\chi)}{j_{n+1}(\chi)} \right)^{-2}.$$

Note that, in expressions (29), which define coefficients  $\xi_n^{(1)}(t)$ ,  $U_{rn}^{(1)}(r, t)$ ,  $U_{\vartheta n}^{(1)}(r, t)$ , and  $p_n^{(1)}(r, t)$  of expansions (28), summation is over the infinite set of the roots of the equation  $D_n(S_n^{(k)}) = 0$ .

(5) Let us consider the case when the viscosity of the liquid is so low that the argument of the modified spherical Bessel function becomes sufficiently large for the asymptotic expansion [19]

$$\begin{aligned} j_n(\chi) &= \frac{\exp(\chi)}{2\chi} \left( 1 - \frac{n(n+1)}{2\chi} \right. \\ &\quad \left. + \frac{n(n^2-1)(n+2)}{8\chi^2} + O\left(\frac{1}{\chi^3}\right) \right); \quad \chi \rightarrow \infty \end{aligned} \quad (30)$$

be valid.

In the expressions for  $a_{\xi}(S_n^{(k)})$ ,  $a(S_n^{(k)})$ ,  $b(S_n^{(k)})$ , and  $D_n(S_n^{(k)})$ , we leave the first two terms in series (30):

$$\begin{aligned} a_{\xi}(S_n^{(k)}) &= \left( S_n^{(k)} + 2(n-1)(2n+1) \frac{v}{r_0^2} + O(v^{3/2}) \right) \\ &\quad \times \frac{1}{\partial_S D_n(S_n^{(k)})}; \end{aligned}$$

$$a(S_n^{(k)}) = -\left(1 + 2(n^2 - 1)\frac{\nu}{r_0^2 S_n^{(k)}} + O(\nu^{2/3})\right) \frac{\omega_n^2}{\partial_S D_n(S_n^{(k)})};$$

$$b(S_n^{(k)}) = \left(2(n^2 - 1)\frac{\nu}{r_0^2 S_n^{(k)}} + O(\nu^{2/3})\right) \frac{\omega_n^2}{\partial_S D_n(S_n^{(k)})}; \quad (31)$$

$$D_n(S_n^{(k)}) = (S_n^{(k)})^2 + 2(n-1)(2n+1)\frac{S_n^{(k)}\nu}{r_0^2} + \omega_n^2 + O(\nu^{3/2}).$$

As follows from (31), the dispersion relation  $D_n(S_n^{(k)}) = 0$  in the low viscosity approximation has only two complex conjugate roots  $S_n^+ = -\delta_n + i\omega_n$  and  $S_n^- = -\delta_n - i\omega_n$ , where  $\delta_n = (n-1)(2n+1)\nu/r_0^2$ . Therefore, the infinite sums in expressions (29) can be replaced by the sum of two values  $S_n^{(1)} = S_n^+$  and  $S_n^{(2)} = S_n^-$ . Coefficients (29) then simplify to

$$\xi_n^{(1)}(t) = \left(\cos(\omega_n t) + \frac{\delta_n}{\omega_n} \sin(\omega_n t)\right) \exp(-\delta_n t);$$

$$U_{rn}^{(1)}(r, t) = -\left(\frac{r}{r_0}\right)^{n-1} \left(\omega_n \sin(\omega_n t) - 2(n^2 - 1)\frac{\nu}{r_0^2} \cos(\omega_n t)\right)$$

$$\times \exp(-\delta_n t) - (n^2 - 1)\frac{\nu}{r_0 r} \left( \frac{j_n(\sqrt{S_n^-} r)}{j_n(\sqrt{S_n^-} r_0)} \exp(-i\omega_n t) + \frac{j_n(\sqrt{S_n^+} r)}{j_n(\sqrt{S_n^+} r_0)} \exp(i\omega_n t) \right) \exp(-\delta_n t);$$

$$U_{\partial n}^{(1)}(r, t) = -\frac{\exp(-\delta_n t)}{n} \left\{ \left(\frac{r}{r_0}\right)^{n-1} \left(\omega_n \sin(\omega_n t) - 2(n^2 - 1)\right) \right.$$

$$\times \frac{\nu}{r_0^2} \cos(\omega_n t) \left. + (n^2 - 1)\frac{\nu}{r_0 r} \left( \frac{j_n(\sqrt{S_n^-} r)}{j_n(\sqrt{S_n^-} r_0)} \exp(-i\omega_n t) \right. \right.$$

$$\left. + \frac{j_n(\sqrt{S_n^+} r)}{j_n(\sqrt{S_n^+} r_0)} \exp(i\omega_n t) \right) + (n-1)\frac{\sqrt{\omega_n} \sqrt{\nu}}{r_0}$$

$$\times \left( \frac{j_{n+1}(\sqrt{S_n^-} r)}{j_n(\sqrt{S_n^-} r_0)} \sqrt{-i} \exp(-i\omega_n t) + \frac{j_{n+1}(\sqrt{S_n^+} r)}{j_n(\sqrt{S_n^+} r_0)} \right.$$

$$\left. \times \sqrt{i} \exp(i\omega_n t) \right) + 2(n-1)\frac{\nu}{r_0^2} \left( \frac{j_{n+1}(\sqrt{S_n^-} r)}{j_n(\sqrt{S_n^-} r_0)} \right.$$

$$\left. \times \exp(-i\omega_n t) + \frac{j_{n+1}(\sqrt{S_n^+} r)}{j_n(\sqrt{S_n^+} r_0)} \exp(i\omega_n t) \right) \left. \right\}; \quad (32)$$

$$p_n^{(1)}(r, t) = \rho \omega_n^2 r_0 \left(\frac{r}{r_0}\right)^n \frac{\exp(-\delta_n t)}{n} \times \left( \cos(\omega_n t) + \frac{(n-1)\nu}{\omega_n r_0^2} \sin(\omega_n t) \right).$$

In the above expressions, the ratios of the spherical cylindrical functions are left instead of being replaced according to (30). This is because the arguments of the spherical cylindrical functions in the numerators of (32) are small at the center of the drop ( $r \rightarrow 0$ ), so that asymptotic expansion (30) fails.

Note that, when the viscosity tends to zero, expressions (32) transform into the well-known expressions for an ideal liquid:

$$\xi_n^{(1)}(t) = \cos(\omega_n t); \quad p_n^{(1)}(r, t) = \frac{\rho \omega_n^2 r_0}{n} \left(\frac{r}{r_0}\right)^n \cos(\omega_n t);$$

$$U_{rn}^{(1)}(r, t) = -\left(\frac{r}{r_0}\right)^{n-1} \omega_n \sin(\omega_n t);$$

$$U_{\partial n}^{(1)}(r, t) = -\left(\frac{r}{r_0}\right)^{n-1} \frac{\omega_n}{n} \sin(\omega_n t).$$

(6) Consider now a moderate-viscosity liquid such that argument  $\chi$  in the expansion [19]

$$j_n(\chi) = \frac{\chi^n}{(2n+1)!!} \left( 1 + \frac{\chi^2}{1! \times 2^1 \times (2n+3)} + \frac{\chi^4}{2! \times 2^2 \times (2n+3)(2n+5)} + \dots \right) \quad (33)$$

of the modified spherical cylindrical function is sufficiently small for each subsequent term of the series in the parentheses to be smaller than the preceding one and the condition  $\text{Re}\chi^2 < 0$  to be fulfilled. The latter condition means that the series becomes alternating-sign and only a few of its initial terms may be left. At the same time, the viscosity is assumed to be such that the periodical oscillations of the drop persist.

Leaving the first two terms in (33), we find expressions for coefficients  $a_\xi(S_n^{(k)})$ ,  $a(S_n^{(k)})$ , and  $b(S_n^{(k)})$  and for  $D_n(S_n^{(k)})$  in the form

$$a_\xi(S_n^{(k)}) = \left( \frac{3(4n^3 + 8n^2 + 6n + 3)}{(2n+1)^2(2n+5)} S_n^{(k)} + \frac{2(n-1)(2n^2 + 4n + 3)\nu}{2n+1} \frac{\nu}{r_0^2} + O\left(\frac{1}{\nu}\right) \right) \frac{1}{\partial_S D_n(S_n^{(k)})};$$

$$a(S_n^{(k)}) = -\left( \frac{8n^3 + 24n^2 + 22n + 9}{(2n+1)^2(2n+5)} \right)$$

$$\begin{aligned}
 & + \frac{2(n^2 - 1)(2n + 3)}{2n + 1} \frac{\nu}{S_n^{(k)} r_0^2} + O\left(\frac{1}{\nu}\right) \frac{\omega_n^2}{\partial_S D_n(S_n^{(k)})}; \\
 b(S_n^{(k)}) = & - \frac{2(n^2 - 1)}{2n + 1} \left( \frac{2}{(2n + 1)(2n + 5)} - (2n + 3) \frac{\nu}{r_0^2 S_n^{(k)}} \right) \\
 & + O\left(\frac{1}{\nu}\right) \frac{r_0 \omega_n^2}{\partial_S D_n(S_n^{(k)})}; \\
 D_n(S_n^{(k)}) = & \frac{3(4n^3 + 8n^2 + 6n + 3)}{(2n + 1)^2 (2n + 5)} (S_n^{(k)})^2 \\
 & + \frac{2(n - 1)(2n^2 + 4n + 3) S_n^{(k)} \nu}{2n + 1} + \omega_n^2 + O\left(\frac{1}{\nu}\right).
 \end{aligned} \tag{34}$$

From expression (34), it readily follows that the dispersion relation  $D_n(S_n^{(k)}) = 0$  in the case of a moderate-viscosity liquid has only two complex conjugate roots, as for a low-viscosity liquid:

$$\begin{aligned}
 S_n^+ & = -\delta_n + i\gamma_n; \quad S_n^- = -\delta_n - i\gamma_n; \\
 \gamma_n & = \alpha_n \frac{\nu}{r_0^2} \sqrt{\beta_n \frac{r_0^4 \omega_n^2}{\nu^2} - 1}; \quad \delta_n = \alpha_n \frac{\nu}{r_0^2}; \\
 \alpha_n & = \frac{(2n + 1)(2n + 5)(n - 1)(2n^2 + 4n + 3)}{3(4n^3 + 8n^2 + 6n + 3)}; \\
 \beta_n & = \frac{3(4n^3 + 8n^2 + 6n + 3)}{(2n + 5)(n - 1)^2 (2n^2 + 4n + 3)}.
 \end{aligned} \tag{35}$$

Therefore, in expressions (29), we will have, instead of the infinite sum, the sum of two values  $S_n^{(1)} = S_n^+$  and  $S_n^{(2)} = S_n^-$ . Taking into account this and expansions (33) and (34), it is easy to derive asymptotic expressions for the deviation of the surface shape of the drop from the equilibrium sphere and for the liquid velocity and pressure fields in the drop:

$$\xi_n^{(1)}(t) = \exp(-\delta_n t) \left( \cos(\gamma_n t) + \frac{\alpha_n \nu}{r_0^2 \gamma_n} \sin(\gamma_n t) \right);$$

$$\begin{aligned}
 & U_{rn}^{(1)}(r, t) \\
 & = \frac{\alpha_n \omega_n^2}{\gamma_n r_0^2} \frac{n + 1}{2n^2 + 4n + 3} \left( \frac{r}{r_0} \right)^{n-1} \left( r^2 - \frac{n(n + 2)}{n^2 - 1} r_0^2 \right) \\
 & \quad \times \exp(-\delta_n t) \sin(\gamma_n t);
 \end{aligned}$$

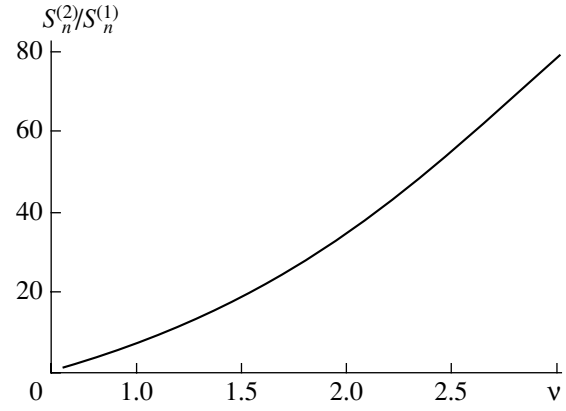


**Fig. 1.** Ratio between the second,  $S_n^{(2)}$ , and first,  $S_n^{(1)}$ , roots of the dispersion relation  $D_n(S_n^{(k)}) = 0$  as a function of dimensionless liquid viscosity  $\nu$  in the high-viscosity range, where the periodic motions in the liquid disappear at  $W = 1$  and  $n = 2$ .

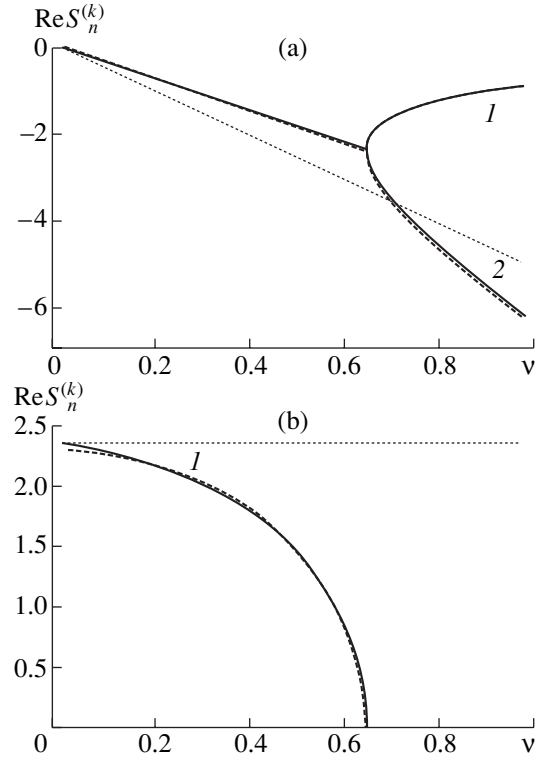


**Fig. 2.** (a) Real,  $\text{Re}(S_n^{(k)})$ , and (b) imaginary,  $\text{Im}(S_n^{(k)})$ , components of the roots of the dispersion relation  $D_n(S_n^{(k)}) = 0$  vs. dimensionless liquid viscosity  $\nu$  for  $W = 1$ ,  $n = 2$ , and different  $k$ . The numbers by the curves mean root number  $k$ . The solid line depicts the exact solution; the dotted line, low-viscosity approximation; and the dashed line, moderate-viscosity approximation.

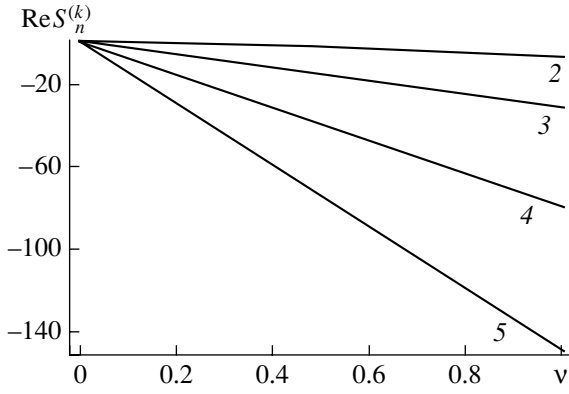


**Fig. 3.** Real components  $\text{Re}(S_n^{(k)})$  of the roots of the dispersion relation  $D_n(S_n^{(k)})=0$  vs. dimensionless liquid viscosity  $v$  for  $W=1$ ,  $n=2$ , and different  $k$ . The numbers by the curves coincide with root number  $k$ .

$$\begin{aligned}
 U_{\vartheta n}^{(1)}(r, t) &= \frac{\alpha_n \omega_n^2}{\gamma_n r_0^2} \frac{n+3}{(2n^2+4n+3)n} \left(\frac{r}{r_0}\right)^{n-1} \\
 &\times \left(r^2 - \frac{n(n+2)}{(n-1)(n+3)} r_0^2\right) \exp(-\delta_n t) \sin(\gamma_n t); \\
 p_n^{(1)}(r, t) &= \frac{\rho \omega_n^2 r_0}{\gamma_n} \frac{8n^3+24n^2+22n+9}{3n(4n^3+8n^2+6n+3)} \left(\frac{r}{r_0}\right)^n \\
 &\times \exp(-\delta_n t) \left( \frac{(4n+3)(8n^4+28n^3+34n^2+20n+9)}{(2n^2+4n+3)(8n^3+24n^2+22n+9)} \right. \\
 &\quad \left. \times \delta_n \sin(\gamma_n t) + \gamma_n \cos(\gamma_n t) \right).
 \end{aligned} \tag{36}$$

(7) Finally, consider a high-viscosity liquid (such that  $v^2/(r_0^4 \omega_n^2) \gg \beta_n$ ), where the periodic flows of the liquid disappear and the drop can execute only aperiodic motions. Using expansion (33), as in the previous case, one can find that two roots  $S_n^+$  and  $S_n^-$  of the dispersion relation are given by

$$S_n^+ = -\frac{2n+1}{2(n-1)(2n^2+4n+3)} \frac{r_0^2 \omega_n^2}{v}; \quad S_n^- \cong -2\alpha \frac{v}{r_0^2}$$

and obey the inequality  $|S_n^-| \gg |S_n^+|$  in a wide viscosity range (Fig. 1). When constructing an asymptotic solution in such a situation, one may leave only root  $S_n^+$ , which decreases with increasing viscosity. In this case, expressions (36) take the form

$$\begin{aligned}
 \xi_n^{(1)}(t) &= \exp(S_n^+ t); \\
 p_n^{(1)}(r, t) &= \rho \omega_n^2 r_0 \frac{(n+1)(2n+3)}{n(2n^2+4n+3)} \left(\frac{r}{r_0}\right)^n \exp(S_n^+ t);
 \end{aligned}$$

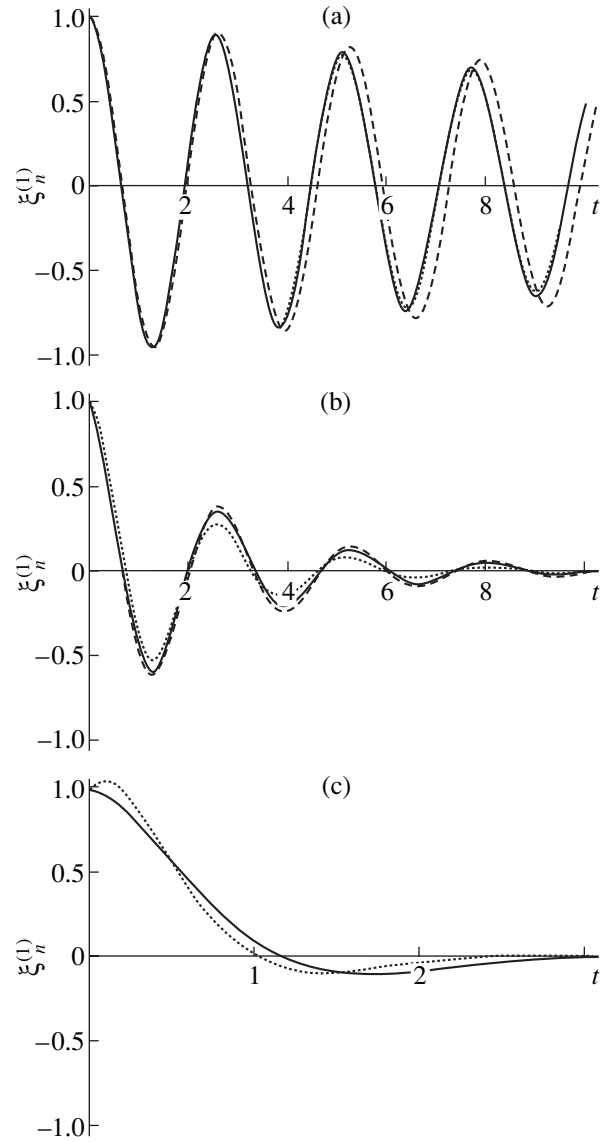


**Fig. 4.** Dimensionless coefficient  $\xi_n^{(1)}$  as a function of dimensionless time  $t$  at  $W=1$  and  $n=2$ . The solid line, exact solution; dotted line, low-viscosity approximation; and dashed line, moderate-viscosity approximation.  $v =$  (a) 0.01, (b) 0.1, and (c) 0.4. When coinciding with the solid one, the dotted or dashed line becomes indistinguishable.

$$\begin{aligned}
 U_{rn}^{(1)}(r, t) &= \frac{\omega_n^2}{2v} \frac{n+1}{2n^2+4n+3} \left(\frac{r}{r_0}\right)^{n-1} \\
 &\times \left(r^2 - \frac{n(n+2)}{n^2-1} r_0^2\right) \exp(S_n^+ t); \\
 U_{\vartheta n}^{(1)}(r, t) &= \frac{\omega_n^2}{2v} \frac{n+3}{(2n^2+4n+3)n} \left(\frac{r}{r_0}\right)^{n-1} \\
 &\times \left(r^2 - \frac{n(n+2)}{(n-1)(n+3)} r_0^2\right) \exp(S_n^+ t).
 \end{aligned} \tag{37}$$

Dimensionless roots  $S_n^{(k)}$  of the dispersion relation  $D_n(S_n^{(k)}) = 0$  and coefficients  $a_\xi(S_n^{(k)})$ ,  $a(S_n^{(k)})$ , and  $b(S_n^{(k)})$  calculated for  $n = 2$ ,  $W = 1$ , and different dimensionless viscosity  $\nu$

$k$	$S_n^{(k)}$	$a_\xi(S_n^{(k)})$	$a(S_n^{(k)})$	$b(S_n^{(k)})$
$\nu = 0.01$				
1	$-0.04721 + 2.44660i$	$0.50072 - 0.00936i$	$0.03201 + 1.22244i$	$-0.03274 + 0.00305i$
2	$-0.04721 - 2.44660i$	$0.50072 + 0.00936i$	$0.03201 - 1.22244i$	$-0.03274 - 0.00305i$
3	$-0.28228$	$-0.00061$	$0.01319$	$-0.01301$
4	$-0.78440$	$-0.00039$	$0.00350$	$-0.00319$
5	$-1.47743$	$-0.00024$	$0.00164$	$-0.00129$
6	$-2.36657$	$-0.00012$	$0.00083$	$-0.00055$
7	$-3.45262$	$-0.00005$	$0.00041$	$-0.00024$
8	$-4.73585$	$-0.00002$	$0.00020$	$-0.00011$
9	$-6.21638$		$0.00010$	$-0.00005$
10	$-7.89426$		$0.00005$	$-0.00003$
11	$-9.76952$		$0.00003$	$-0.00001$
12	$-11.84215$		$0.00002$	
$\nu = 0.1$				
1	$-0.39951 + 2.36952i$	$0.50799 - 0.07524i$	$0.36731 + 1.12760i$	$-0.39198 + 0.10615i$
2	$-0.39951 - 2.36952i$	$0.50799 + 0.07524i$	$0.36731 - 1.12760i$	$-0.39198 - 0.10615i$
3	$-2.91160$	$-0.01548$	$0.09730$	$-0.05222$
4	$-7.87661$	$-0.00045$	$0.00671$	$-0.00317$
5	$-14.78764$	$-0.00003$	$0.00099$	$-0.00048$
6	$-23.67140$		$0.00023$	$-0.00011$
7	$-34.52866$		$0.00007$	$-0.00004$
8	$-47.35961$		$0.00003$	$-0.00001$
9	$-62.16433$		$0.00001$	
$\nu = 1$				
1	$-0.90254$	$1.16747$	$8.81096$	$-9.86465$
2	$-6.21851$	$-0.16697$	$-0.43380$	$1.47210$
3	$-29.93916$	$-0.00050$	$0.02192$	$-0.00703$
4	$-78.80501$		$0.00078$	$-0.00035$
5	$-147.88167$		$0.00010$	$-0.00005$
6	$-236.71521$		$0.00002$	$-0.00001$

Note that expressions (37) are in good agreement with exact solution (29) only at those time instants when the inequality  $|S_n^-|t \gg 1$  is valid. For small times, when the value of  $|S_n^-|t$  is comparable to unity, the solutions for velocity field components  $(U_{rn}^{(1)}(r, t)$ , and  $U_{\vartheta n}^{(1)}(r, t))$  differ drastically from their true values and (37) is inapplicable.

(8) To perform numerical analysis of the solution to the problem of capillary oscillations of a charged axisymmetric viscous drop, we turn to dimensionless variables for convenience, putting  $\rho = \sigma = r_0 = 1$ . Then, all the physical quantities involved in the problem will be expressed in terms of their characteristic scales. Namely, quantities  $r_0$ ,  $\rho$ ,  $\sqrt{\rho r_0^3 / \sigma}$ ,  $\sqrt{\sigma / \rho r_0^3}$ ,  $\sqrt{\sigma / \rho r_0}$ ,  $\sigma / r_0$ , and  $\sqrt{\delta r_0 / \rho}$  will serve as the scales of length, density, frequency, pressure, and kinematic viscosity.



We assume that the radius of drops varies from  $r_0 = 10^{-4}$  to  $10^{-1}$  cm. The surface tension coefficient and the density of liquids equal, on average,  $\sigma = 50$  dyn/cm and  $\rho = 1$  g/cm<sup>3</sup>. For these values of the physical parameters, the characteristic scales are as follows: time,  $5 \times 10^{-7}$ – $10^{-3}$  s; frequency,  $2 \times 10^2$ – $10^7$  s<sup>-1</sup>; liquid velocity, 20–700 cm/s; liquid pressure,  $5 \times 10^2$ – $5 \times 10^5$  dyn/cm; and viscosity,  $7 \times 10^{-2}$ – $2$  cm<sup>2</sup>/s.

In terms of the dimensionless variables, the physical quantities of the problem will depend on parameter  $W = Q^2/(4\pi)$ , which characterizes the stability of the drop against its self-charge [1]; dimensionless kinematic viscosity  $\nu$  of the liquid; small parameter  $\varepsilon$ ; set  $\Omega$  of the indices of initially excited modes; and constants  $h_n$  ( $n \in \Omega$ ), which take into account the contribution of an  $n$ th mode to the formation of the initial shape of the drop.

The numerical analysis of the exact dispersion relation  $D_n(S_n^{(k)}) = 0$  (see (26)) carried out in terms of the dimensionless variables indicates that this equation has the infinite number of roots. For low and moderate viscosity  $\nu$  at  $W < 4$ , there are two complex conjugate roots  $S_n^{(1)}$  and  $S_n^{(2)}$  with a negative real part. Their imaginary part  $\text{Im}(S_n^{(2)}) = -\text{Im}(S_n^{(1)})$  defines the oscillation frequency of the drop (see expression (29)); their real part  $\text{Re}(S_n^{(1)}) = \text{Re}(S_n^{(2)})$ , the damping decrement. The rest of the roots,  $S_n^{(k)}$ , of the equation  $D_n(S_n^{(k)}) = 0$  ( $k \geq 3$ ) are negative real numbers and specify the damping decrements.

As the viscosity grows, the real parts of the roots  $S_n^{(1)}$  and  $S_n^{(2)}$  increase in magnitude, while the imaginary parts decrease until the aperiodic motion is totally suppressed at  $\nu \approx 0.65$  (Fig. 2). At  $\nu > 0.65$ , roots  $S_n^{(1)}$  and  $S_n^{(2)}$  become negative real numbers. One of them asymptotically decreases in magnitude, tending to the abscise axis with increasing  $\nu$  (Fig. 2), and the other grows in absolute value, asymptotically tending to linearly grow with increasing viscosity (Figs. 2, 3). Roots  $S_n^{(k)}$  with higher superscripts  $k$  diminish rapidly by the linear law as the viscosity increases (Fig. 2).

Figure 2b allows for discrimination between the cases of low, moderate, and high viscosity. At  $\nu > 0.1$ , the difference between the exact solution of the dispersion relation and the solution obtained in the moderate-viscosity approximation is very small (on the order of the linewidth). At  $\nu < 0.05$ , the oscillation frequency of the viscous drop is approximated well by the low-viscosity approximation, while the moderate-viscosity approximation gives a conservative value of the frequency in the limit  $\nu \rightarrow 0$ . The high-viscosity approximation is naturally adequate at  $\nu > 0.65$ , where the periodic solutions disappear.

Numerical calculations (see the table) show that, as number  $k$  of the root of the dispersion relation  $D_n(S_n^{(k)}) = 0$  increases, coefficients  $a_\xi(S_n^{(k)})$ ,  $a(S_n^{(k)})$ , and  $b(S_n^{(k)})$ , which are responsible for the shape of an oscillating drop, as well as for the velocity and pressure field in it (see (28), (29)), rapidly tend to zero, the rate of decrease depending on the viscosity.

It should also be noted that, according to (29), coefficients  $a_\xi(S_n^{(k)})$ ,  $a(S_n^{(k)})$ , and  $b(S_n^{(k)})$  exponentially decrease with time, the damping decrements (which are equal to  $\text{Re}(S_n^{(k)})$ ) increasing rapidly with  $k$  (see the table). Therefore, the high- $k$  terms of series (29) tend to zero very rapidly with time, so that the terms corresponding to the first two roots of the equation  $D_n(S_n^{(k)}) = 0$ , i.e., those with the smallest damping increments, become of decisive significance. Eventually, we observe good agreement between exact expressions (28) and the asymptotic approximations for the low-viscosity (expression (32)) and moderate-viscosity (expression (36)) cases (Fig. 4).

The moderate-viscosity approximation, which leads to well-solvable inhomogeneous problems in the second and third order of smallness in initial deformation amplitude, seems to be the most appropriate for further nonlinear analysis.

## CONCLUSIONS

We considered the time evolution of capillary oscillations of a charged viscous incompressible conducting liquid drop in the first order of smallness in initial deformation amplitude. The analysis showed that infinite summation over the roots of the dispersion relation in the expressions for the shape of the drop and for the velocity and pressure fields in it may be replaced by the sum of the first two terms. The analytical solutions thus obtained are compact enough that finding of higher order solutions becomes topical. In other words, one can tackle the yet unsolved problem of nonlinear oscillations of a charged viscous liquid drop.

## ACKNOWLEDGMENTS

This work was supported by the President of the Russian Federation (grant no. MK-2946-2004-1) and the Russian Foundation for Basic Research (grant no. 03-01-00760).

## REFERENCES

1. A. I. Grigor'ev and S. O. Shiryayeva, *Izv. Ross. Akad. Nauk, Mekh. Zhidk. Gaza*, No. 3, 3 (1994).
2. A. I. Grigor'ev, *Zh. Tekh. Fiz.* **70** (5), 22 (2000) [*Tech. Phys.* **45**, 543 (2000)].
3. D. F. Belonozhko and A. I. Grigor'ev, *Élektrokhim. Obrab. Met.*, No. 4, 17 (2000).

4. J. A. Tsamopolous and R. A. Brown, *J. Fluid Mech.* **127**, 519 (1983).
5. S. O. Shiryayeva, *Izv. Ross. Akad. Nauk, Mekh. Zhidk. Gaza*, No. 3, 173 (2001).
6. S. O. Shiryayeva, *Zh. Tekh. Fiz.* **72** (4), 15 (2002) [*Tech. Phys.* **47**, 389 (2002)].
7. S. O. Shiryayeva, *Zh. Tekh. Fiz.* **73** (2), 19 (2003) [*Tech. Phys.* **48**, 152 (2003)].
8. A. N. Zharov, A. I. Grigor'ev, and S. O. Shiryayeva, *Pis'ma Zh. Tekh. Fiz.* **29** (9), 75 (2003) [*Tech. Phys. Lett.* **29**, 388 (2003)].
9. A. N. Zharov, S. O. Shiryayeva, and A. I. Grigor'ev, *Zh. Tekh. Fiz.* **73** (12), 9 (2003) [*Tech. Phys.* **48**, 1511 (2003)].
10. J. A. Basaran, *J. Fluid Mech.* **241**, 169 (1992).
11. E. Becker, W. J. Hiller, and T. A. Kowalewski, *J. Fluid Mech.* **258**, 191 (1994).
12. S. O. Shiryayeva, D. F. Belonozhko, V. B. Svetovoï, and A. I. Grigor'ev, Preprint No. 1, IMI RAN (Institute of Microelectronics and Informatics, Russian Academy of Sciences, Yaroslavl, 2001).
13. A. I. Grigor'ev and A. E. Lazaryants, *Zh. Vychisl. Mat. Mat. Fiz.* **32**, 929 (1992).
14. S. O. Shiryayeva, A. E. Lazaryants, A. I. Grigor'ev, *et al.*, Preprint No. 27, IMI RAN (Institute of Microelectronics, Russian Academy of Sciences, Yaroslavl, 1994).
15. A.-H. Nayfeh, *Perturbation Methods* (Wiley, New York, 1973; Mir, Moscow, 1976).
16. G. A. Korn and T. M. Korn, *Mathematical Handbook for Scientists and Engineers* (McGraw-Hill, New York, 1968; Nauka, Moscow, 1984).
17. V. A. Ditkin and A. P. Prudnikov, *Integral Transforms and Operational Calculus* (Vysshaya Shkola, Moscow, 1975; Pergamon, Oxford, 1966).
18. G. A. Levacheva, E. A. Manykin, and P. P. Poluéktov, *Izv. Akad. Nauk SSSR, Mekh. Zhidk. Gaza*, No. 2, 17 (1985).
19. M. Abramovitz and I. A. Stegun, *Handbook of Mathematical Functions* (Dover, New York, 1971; Nauka, Moscow, 1979).

*Translated by N. Mende*

## GAS DISCHARGES, PLASMA

# Theory of the Interaction of High-Power Short Laser Pulses with Plasmas

I. N. Kosarev

*All-Russia Research Institute of Experimental Physics, Russian Federal Nuclear Center,  
Sarov, Nizhni Novgorod Oblast, 607190 Russia*

*e-mail: kosarev@vniief.ru*

Received April 12, 2004

**Abstract**—A theory of the interaction of short laser pulses with plasmas is constructed based on the previously developed kinetic theory of a tenuous plasma. The generation of fast electrons by a relativistically strong femtosecond laser pulse in a plasma with a nearly critical density is investigated. The results obtained agree with the results from particle-in-cell simulations and with the experimental data. © 2005 Pleiades Publishing, Inc.

### INTRODUCTION

State-of-the-art tera- and petawatt lasers [1] have made it possible to produce radiation pulses with intensities of  $10^{18}$ – $10^{21}$  W/cm<sup>2</sup>. In the interaction of such an intense laser pulse with a gaseous or a solid-state target, the target material is transformed into a plasma (the plasma can also be created by a lower power prepulse). Laser-produced plasmas are subject to parametric instabilities [2–6], which lead to the excitation of plasma waves. Under the action of the laser field, the plasma parameters oscillate. As in a mechanical oscillatory system, such oscillations can give rise to a parametric resonance, due to which the self-field of the oscillations increases with time. The turbulent field of the plasma waves accelerates electrons by a mechanism analogous to the Fermi acceleration mechanism [7]. At such high laser intensities, the electrons can also be efficiently accelerated by ponderomotive forces [8].

A substantial portion of the laser pulse energy (30–50%) is converted into the energy of the fast electron beam. This is confirmed by particle-in-cell (PIC) simulations [9, 10] and experimental data [11]. Intense beams of fast electrons are planned to be used for the rapid ignition of fusion targets [12] and also as a source of gamma photons generated by the electron bremsstrahlung [13].

A theory of the interaction of short laser pulses with plasmas will be formulated in the next section on the basis of the previously developed kinetic theory of a tenuous plasma [14]. In what follows, the correlations occurring in the plasma will be ignored, i.e., the plasma kinetics will be treated in the collisionless approximation.

### FORMULATION OF THE THEORY OF THE INTERACTION OF SHORT LASER PULSES WITH PLASMAS

In the present study, it is proposed to describe the behavior of the plasma distribution function on short time scales (less than the plasma relaxation time) by the propagator obtained in my earlier paper [14]. The plasma kinetics on sufficiently long time scales was investigated by repeatedly applying the propagator. For a classical (nondegenerate) plasma consisting of the particles of two species, *a* and *b*, the propagator for the density matrix  $\rho_a(\mathbf{r}, \mathbf{r}', t)$  in the self-consistent field approximation has the form

$$\begin{aligned}
 K_a(2, 1) = & \exp \left\{ (i/\hbar) \int_{t_1}^{t_2} dt \left( -m_a c^2 \sqrt{1 - \frac{\mathbf{v}_a^2(t)}{c^2}} \right. \right. \\
 & \left. \left. + m_a c^2 \sqrt{1 - \frac{\mathbf{v}_a'^2(t)}{c^2}} \right) + n_a V_{aa}^{st} + n_b V_{ba}^{st} \right\} \\
 & \times \exp \left\{ (i/\hbar) \int_{t_1}^{t_2} dt \left( \frac{Z_a e}{c} \mathbf{A}(t) \mathbf{v}_a(t) - \frac{Z_a e}{c} \mathbf{A}(t) \mathbf{v}_a'(t) \right) \right\} \\
 & \times \left( \frac{m_a}{2\pi\hbar(t_2 - t_1)} \right)^3, \quad (1) \\
 V_{ba}^{st} = & \int d\mathbf{p} d\mathbf{R} f_b(\mathbf{R}, \mathbf{p}, t)
 \end{aligned}$$

$$\times \left[ \exp \left\{ -\frac{i}{\hbar} \int_{t_1}^{t_2} dt (U_{ba}(\mathbf{R} - \mathbf{v}(t_2 - t) - \mathbf{r}_a(t)) - U_{ba}(\mathbf{R} - \mathbf{v}(t_2 - t) - \mathbf{r}'_a(t))) \right\} - 1 \right].$$

Here,  $\mathbf{v}_a$  and  $\mathbf{r}_a$  are the velocity of a particle of species  $a$  and its position vector,  $U_{aa}$  and  $U_{ab}$  are the particle interaction energies,  $\mathbf{R}_i$  is the position vector of the scattering center,  $\mathbf{A}$  is the vector potential of the external field acting on a particle, and  $n_a$  and  $Z_a$  are the mean density of the particles of species  $a$  and their charge.

Propagator (1) describes the plasma dynamics on time scales shorter than the relaxation time of the distribution function.

In analyzing the plasma kinetics, it is convenient to pass over to the difference variable  $\Delta\mathbf{r} = \mathbf{R} - \mathbf{R}'$  (where  $\mathbf{r} = (\mathbf{R} + \mathbf{R}')/2$ ) and accordingly to the density matrix  $\rho(\mathbf{r} + \Delta\mathbf{r}/2, \mathbf{r} - \Delta\mathbf{r}/2)$ . In terms of this variable, the density matrix is related to the distribution function by the relationship

$$f(\mathbf{r}, \mathbf{p}) = \frac{V}{(2\pi\hbar)^3} \int d\Delta\mathbf{r} \rho(\mathbf{r}, \Delta\mathbf{r}) \exp\left(-i\frac{\Delta\mathbf{r} \cdot \mathbf{p}}{\hbar}\right), \quad (2)$$

$$\rho(\mathbf{r}, \Delta\mathbf{r}) = \frac{1}{V} \int d\mathbf{p} f(\mathbf{r}, \mathbf{p}) \exp\left(i\frac{\Delta\mathbf{r} \cdot \mathbf{p}}{\hbar}\right),$$

where  $V$  is the plasma volume.

In the problem under investigation, the quantum effects are unimportant; consequently, the action of the particle,

$$S_a[\mathbf{r}(t), \Delta\mathbf{r}(t)] = \frac{\hbar}{i} \ln \left( \frac{m_a}{2\pi\hbar(t_2 - t_1)} \right)^{-3} K_a(2, 1)$$

(see Eq. (1)), can be expanded in powers of the small difference  $\Delta\mathbf{r}(t)$ . Since the contribution of the zero-order term in the expansion is zero, the expansion is equivalent to taking the nonrelativistic limit. The action can be described by a nonrelativistic expression; in this case, however, the relationship between the velocity and the momentum remains relativistic, just as it is in the standard kinetic theory (in the self-consistent field approximation) [15]. In this approximation, the propagator for the particles of species  $a$  in a classical (nondegenerate) plasma has the form

$$K_a(2, 1) = \left( \frac{m_a}{2\pi\hbar(t_2 - t_1)} \right)^3 \exp \left\{ \frac{i}{\hbar} (S_0 + \Delta S_p) + \Delta S_{st} \right\}, \quad (3)$$

where the action  $S_0$  for a particle in a linearly polarized laser field (typical of high-power lasers) is given by the following expression, in which the field nonuniformity is taken into account parametrically:

$$S_0 = \frac{m_a}{t_2 - t_1} (\mathbf{r}_2 - \mathbf{r}_1) (\Delta\mathbf{r}_2 - \Delta\mathbf{r}_1) - \frac{Z_a e}{\omega c (t_2 - t_1)} \int_{\varphi_1}^{\varphi_2} \mathbf{A} d\varphi$$

$$+ \frac{Z_a e}{\omega c (t_2 - t_1)} \frac{\mathbf{r}_2 - \mathbf{r}_1}{(t_2 - t_1)} \left( - \int_{\varphi_1 - \Delta\varphi_1}^{\varphi_2 + \Delta\varphi_1} \mathbf{A} d\varphi + \int_{\varphi_2 - \Delta\varphi_2}^{\varphi_1 + \Delta\varphi_2} \mathbf{A} d\varphi \right) \quad (4)$$

$$- \frac{Z_a^2 e^2}{\omega^2 m_a (t_2 - t_1)} \int_{\varphi_1}^{\varphi_2} \mathbf{A} d\varphi \left( - \int_{\varphi_1 - \Delta\varphi_1}^{\varphi_1 + \Delta\varphi_1} \mathbf{A} d\varphi + \int_{\varphi_2 - \Delta\varphi_2}^{\varphi_2 + \Delta\varphi_2} \mathbf{A} d\varphi \right)$$

$$+ \frac{Z_a^2 e^2}{2\omega m_a c^2} \left( - \int_{\varphi_1 - \Delta\varphi_1}^{\varphi_1 + \Delta\varphi_1} \mathbf{A}^2 d\varphi + \int_{\varphi_2 - \Delta\varphi_2}^{\varphi_2 + \Delta\varphi_2} \mathbf{A}^2 d\varphi \right).$$

Here,  $\mathbf{A} = \mathbf{A}_0(\mathbf{r}_1, \varphi/\omega) \sin \varphi$  is the vector potential of the laser field,  $\mathbf{r}_1 \perp \mathbf{k}$ ;  $\varphi_{1,2} = \omega t_{1,2} - \mathbf{k} \cdot \mathbf{r}_{1,2}$ ;  $\Delta\varphi_{1,2} = -\mathbf{k} \Delta\mathbf{r}/2$ ;  $\omega$  is the laser field frequency;  $\mathbf{k}$  is the wave vector; and  $\Delta S_p$  is the contribution to the action that comes from the ponderomotive forces associated with the nonuniformity of the laser field amplitude  $A_0$ .

The ponderomotive forces are accounted for in terms of perturbation theory. This approach is valid on sufficiently small time scales on which the displacement of the particle is small in comparison to the characteristic spatial scale of the laser field amplitude  $A_0$ :

$$\Delta S_p = -\frac{Z_a^2 e^2}{4m_a c^2} \nabla A_0^2 \int_{t_1}^{t_2} \Delta\mathbf{r}_a dt. \quad (5)$$

Here,  $\Delta\mathbf{r}_a$  is the trajectory of a particle in a uniform laser field, the boundary conditions being  $\Delta\mathbf{r}_a(t_1) = \Delta\mathbf{r}_1$  and  $\Delta\mathbf{r}_a(t_2) = \Delta\mathbf{r}_2$ . The contribution to the action that comes from the interaction between particles,  $\Delta S_{st}$ , is also calculated in terms of perturbation theory and is given by the formulas

$$\text{Im}\{\Delta S_{st}\} = \pi \sum_b n_b v_p$$

$$\times \int d\mathbf{p}_b f_{1Z}(\mathbf{p}_b, t_1) \int_{t_1}^{t_2} dt \frac{Z_a(\mathbf{r}_1) e^2 c^2 [\Delta\mathbf{r}_{a \perp \mathbf{v}_b}(t)]^2}{\hbar \mathbf{v}_b \Delta\mathbf{r}_a(t)}, \quad (6)$$

$$f_{1Z}(\mathbf{p}_b, t_1) = \int d\mathbf{r} f(\mathbf{r}, \mathbf{p}_b, t_1) Z_b(\mathbf{r});$$

$$\text{Re}\{\Delta S_{st}\} = -\pi \sum_b n_b$$

$$\times \int d\mathbf{p}_b f_{2Z}(\mathbf{p}_b, t_1) \int_{t_1}^{t_2} dt \frac{Z_a^2(\mathbf{r}_1) e^4}{\hbar v_b} [\Delta \mathbf{r}_{a \perp v_b}(t)]^2, \quad (7)$$

$$f_{2Z}(\mathbf{p}_b, t_1) = \int d\mathbf{r} f(\mathbf{r}, \mathbf{p}_b, t_1) Z_b^2(\mathbf{r}),$$

where  $Z_b$ ,  $\mathbf{p}_b$ ,  $\mathbf{v}_b$ , and  $n_b$  are the charge, momentum, velocity, and mean density of the plasma particles of species  $b$ , respectively. The collisional volume was calculated using the following expression for the potential energy of the interaction between particles [14]:

$$U_{bd}(\mathbf{r}_b - \mathbf{r}_a) = Z_a Z_b e^2 \left( 1 - \frac{\dot{\mathbf{r}}_a \mathbf{v}_b}{c^2} \right) \times \frac{1}{\sqrt{(\mathbf{r}_a - \mathbf{r}_b)^2 \left( 1 - \frac{\dot{\mathbf{r}}_a^2}{c^2} \right) + \frac{[(\mathbf{r}_a - \mathbf{r}_b) \dot{\mathbf{r}}_a]^2}{c^2}}}, \quad (8)$$

where account is taken of both the scalar and the vector potentials of the field that a particle of species  $b$  (moving at constant velocity) exerts on a test particle of species  $a$ .

In deriving formulas (6) and (7), we took into account the fact that the laser frequency is low in comparison to the characteristic (Weisskopf) rate at which the collisional volume  $V_{ba}^{st}$  varies. In the case under consideration, this rate is equal to the ratio of the characteristic velocity to the largest of the two characteristic scale lengths—the Landau length and the de Broglie wavelength. It should be noted that the imaginary part of the collisional volume describes the shift of the momentum distribution function of particles of species  $a$  and is determined by the vector potentials of the fields of perturbing particles. The real part of the collisional volume describes the broadening of the momentum distribution function of particles of species  $a$  and is determined by the scalar potentials of the fields of perturbing particles.

The evolution of prescribed initial distribution functions of the plasma particles can be analyzed by repeatedly applying propagators (3)–(7). The statistically averaged plasma fields and scattered electromagnetic fields can be determined from the distribution functions of the plasma particles [15]. The Fourier components of the intensities of the longitudinal and transverse electric fields have the form

$$(\mathbf{E}_{\parallel} \mathbf{E}_{\parallel})_{\omega, \mathbf{k}} = \frac{\sum_a \frac{4\pi e^2 n_a}{k^2} \int 2\pi \delta(\omega - \mathbf{k}\mathbf{v}) f_{2Z}(\mathbf{p}) d\mathbf{p}}{|\epsilon_{\parallel}(\omega, \mathbf{k})|^2},$$

$$(\mathbf{E}_{\perp} \mathbf{E}_{\perp})_{\omega, \mathbf{k}}$$

$$= \frac{\sum_a \frac{4\pi e^2 n_a}{k^2} \int 2\pi \delta(\omega - \mathbf{k}\mathbf{v}) (\mathbf{k} \times \mathbf{v})^2 f_{2Z}(\mathbf{p}) d\mathbf{p}}{|\omega^2 \epsilon_{\perp}(\omega, \mathbf{k}) - c^2 k^2|^2}, \quad (9)$$

$$(\mathbf{H}, \mathbf{H})_{\omega, \mathbf{k}} = (\mathbf{E}_{\perp} \mathbf{E}_{\perp})_{\omega, \mathbf{k}}, \quad \mathbf{E}_{\parallel} \parallel \mathbf{k}, \quad \mathbf{E}_{\perp} \perp \mathbf{k}.$$

The longitudinal and transverse dielectric functions of the plasma are given by the expressions

$$\epsilon_{\parallel}(\omega, \mathbf{k}) = 1 + \sum_a \frac{4\pi e^2 n_a}{k^2 \omega} \int \frac{(\mathbf{k}\mathbf{v}) \mathbf{k} \partial f_{2Z}(\mathbf{p}) / \partial \mathbf{p}}{\omega - \mathbf{k}\mathbf{v} + i0} d\mathbf{p}, \quad (10)$$

$$\epsilon_{\perp}(\omega, \mathbf{k}) = 1 + \sum_a \frac{4\pi e^2 n_a}{k^2 \omega} \int \frac{((\mathbf{k} \times \mathbf{v}) \times \mathbf{k}) \partial f_{2Z}(\mathbf{p}) / \partial \mathbf{p}}{\omega - \mathbf{k}\mathbf{v} + i0} d\mathbf{p}.$$

It is also necessary to calculate the mean charges of the particles (ions). In the case of a short (femtosecond) laser pulse, the charge of an ion at a given point is governed by the laser electric field [16], provided that the laser field at this point is increasing. When the laser field at this point is decreasing, the ion charge does not change. This model of the ion charge kinetics results from the over-barrier nature of the ionization of ions by the laser field and from the short time of the interaction of a femtosecond laser pulse with a target. In the general case in which the ionization is not of the over-barrier nature, the mean ion charges are determined from the charge kinetic equations.

The laser field amplitude  $E(t)$  and the ion charge  $Z$  are related by the Bethe formula (in atomic units) [17]

$$E(t) = \frac{I_{Z-1}^2}{4Z}, \quad (11)$$

where  $I_{Z-1}$  is the ionization energy of an ion with the charge  $Z-1$ .

When the plasma electric field differs substantially from the laser field in vacuum, the electric field amplitude in formula (11) should be replaced with the plasma field amplitude calculated from Fourier components (9).

For over-barrier ionization by a linearly polarized laser field, Krainov [18] obtained the following estimate for the electron velocity distribution function:

$$f_0(v_{\parallel}, v_{\perp}) \sim Ai^2 \left\{ \frac{2I_{Z-1} + v_{\parallel}^2 \gamma^2 / 3 + v_{\perp}^2}{(2E)^{2/3}} \right\}, \quad \mathbf{v}_{\perp} \parallel \mathbf{E}, \quad (12)$$

where  $Ai(x)$  is the Airy function and  $\gamma = \omega \sqrt{2I_{Z-1}} / E$  is the Keldysh parameter (in atomic units).

In the case of tunneling and multiphoton ionization by a relativistic laser field, the expressions for the electron velocity distribution function were obtained by Hafizi *et al.* [19].

### GENERATION OF HOT ELECTRONS BY A RELATIVISTIC FEMTOSECOND LASER PULSE

In the field of the laser pulse, the electron executes oscillatory motion. For  $I\lambda^2 \geq 10^{18} \text{ W/cm}^2 \mu\text{m}^2$  (where  $\lambda$  is the laser wavelength), the electron oscillatory velocity is close to the speed of light. Here, we are considering a linearly polarized laser pulse with the envelop

$$A_{0,x} = A_0 \exp(-(t-z/c)^2/\tau^2) \quad (13)$$

$$\times \exp(-(x^2+y^2)/\sigma^2),$$

where the  $z$  axis is directed along the wave vector of the laser pulse and the  $x$  axis is directed along the polarization axis. The electron density distribution has the form

$$n_c(z) = n_{cr} \exp(z/L), \quad 0 < z < z_{\max}, \quad (14)$$

where  $n_{cr} = \pi m_e c^2 / e^2 \lambda^2$  is the critical density above which a nonrelativistic electromagnetic wave cannot propagate in the plasma.

This density distribution is established as a result of the ablation of a solid-state target by a laser prepulse. In this case, the plasma is heated to a temperature of about 1 keV.

In formulas (6) and (7), it is convenient to switch to a purely coordinate representation of the quantities in accordance with relationships (2). All the integrals in formulas (6) and (7) were calculated by the multidimensional stationary-phase method [20]. These integrals belong to the type of integral of a rapidly oscillating function because we are dealing with a classical (non-degenerate) plasma.

First, we performed calculations for a hydrogen plasma. The laser pulse parameters and the degree to which the plasma is inhomogeneous were chosen to be the same as those in [21], specifically,  $\tau = 150$  fs,  $\sigma = 6\lambda$ , and  $L = 30\lambda$  (the laser wavelength being  $\lambda = 1 \mu\text{m}$ ). The length of the computation region was somewhat smaller:  $z_{\max} = 40\lambda$ . The calculations were performed for the maximum laser intensities of  $I_0 = 10^{18}$ ,  $10^{19}$ , and  $10^{20} \text{ W/cm}^2$ . The electron distribution functions over the  $z$  component of the momentum are shown in Figs. 1–3. It is in this direction that the electrons are predominantly accelerated. The calculated results agree with those obtained by Pukhov *et al.* [21]. In fact, for a laser intensity of  $I_0 = 10^{18} \text{ W/cm}^2$ , fast electrons are heated to a temperature of about  $T_h \sim 0.8 \text{ MeV}$ ; for an intensity of  $I_0 = 10^{19} \text{ W/cm}^2$ , electrons in the energy range below 12.5 MeV are heated to about  $T_h \approx 4.5 \text{ MeV}$  (in the energy range below 50 MeV, the mean electron temperature is about  $T_h \approx 8 \text{ MeV}$ ); and, for an intensity of  $I_0 = 10^{20} \text{ W/cm}^2$ , electrons in the energy range above 25 MeV are heated to about  $T_h \approx 15 \text{ MeV}$ . In [21], the temperatures of fast electrons in these three cases lie in the ranges 0.5–1.2, 3–8, and 9–16 MeV,

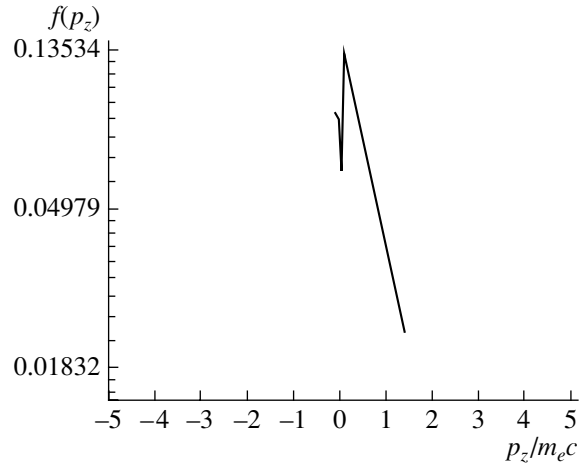


**Fig. 1.** Electron distribution function over the  $z$  component of the momentum for  $I_0 = 10^{18} \text{ W/cm}^2$ .

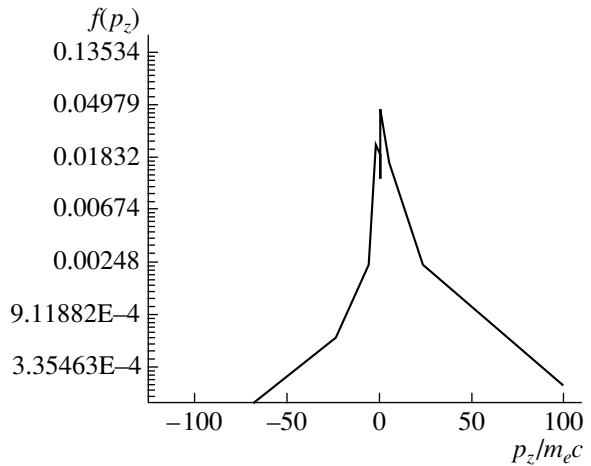


**Fig. 2.** The same as in Fig. 1, but for  $I_0 = 10^{19} \text{ W/cm}^2$ .

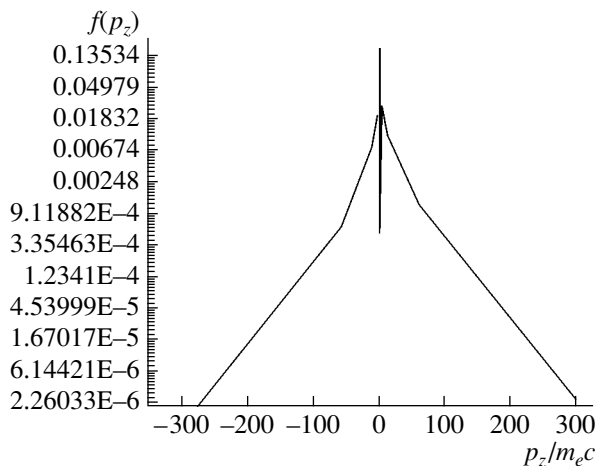


**Fig. 3.** The same as in Fig. 1, but for  $I_0 = 10^{20} \text{ W/cm}^2$ .

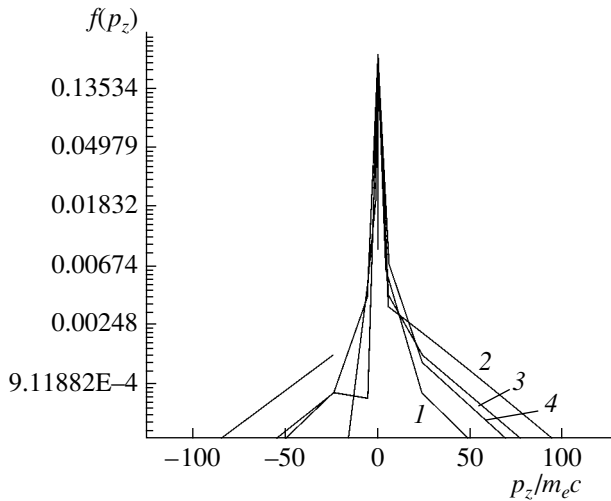


**Fig. 4.** Electron distribution function over the  $z$  component of the momentum for  $I_0 = 10^{19}$  W/cm<sup>2</sup> at four subsequent times: (1) 45, (2) 46, (3) 47, and (4) 48 $T$  (where  $T$  is the laser field period, the initial time being  $t_0 = 50T$ ).

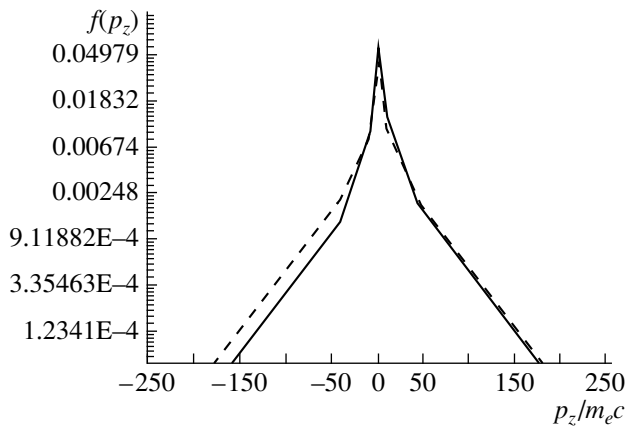


**Fig. 5.** Electron distribution function over the  $z$  component of the momentum in a plasma with multicharged gold ions for  $I_0 = 10^{20}$  W/cm<sup>2</sup> (solid curve) and  $I_0 = 3 \times 10^{20}$  W/cm<sup>2</sup> (dashed curve).

respectively. In Figs. 2 and 3, we can clearly see the presence of electrons accelerated in the opposite direction. This occurs because of the onset of the Weibel instability of the anisotropic momentum distribution of the plasma electrons [22]. In addition, thermal electrons are heated to temperatures of about 10 keV due to anomalous conductivity.

In order to gain a better insight into the electron heating mechanism, let us consider how the electron distribution over the  $z$  component of the momentum changes on shorter time scales on which a steady-state distribution has not yet been established. Figure 4 shows the electron distribution function at four subsequent times for a laser intensity of  $I_0 = 10^{19}$  W/cm<sup>2</sup>. We can see that the distribution function exhibits irregular

temporal behavior, which is associated with the turbulent pulsations of the plasma electric field. Hence, the electrons are predominantly accelerated by these pulsations through a mechanism analogous to the Fermi acceleration mechanism [7]. It can be concluded that the electron acceleration is not dominated by the mechanism associated with the mechanical resonance between the electron oscillations in the laser field and the betatron oscillations in quasi-steady magnetic and electric fields [21].

It can be seen from Figs. 2–4 that the momentum distribution of hot electrons is two-temperature in character. This can be explained by the combined action of the ponderomotive force and the turbulent plasma field: the ponderomotive force accelerates the tail electrons that have already been accelerated by the plasma field.

We also performed calculations for a plasma with multicharged gold ions and for two maximum laser intensities,  $I_0 = 10^{20}$  and  $3 \times 10^{20}$  W/cm<sup>2</sup>. According to Bethe formula (11), such intense laser fields are capable of ionizing gold atoms to ions with charge numbers of up to  $Z_i = 50$ . This charge is approximately equal to the equilibrium charge at characteristic temperatures of 300–500 eV and at the critical plasma density. The values of the parameters in formulas (13) and (14) were chosen to be as follows:  $\tau = 150$  fs,  $\sigma = 9\lambda$ ,  $L = 20\lambda$  (the laser wavelength being  $\lambda = 1$   $\mu$ m), and  $z_{\max} = 60\lambda$ . The calculated results are illustrated in Fig. 5. In the energy range from 10 to 25 MeV, the electrons are heated to a temperature of about  $T_h \approx 10$  MeV; this temperature agrees with the estimate  $T_h \sim 4 \pm 1$  MeV, which was obtained experimentally in [11]. As in the case of a hydrogen plasma, the electrons are accelerated by turbulent pulsations of the plasma electric field. Thermal electrons are heated to temperatures of about 10 keV due to anomalous plasma conductivity. All the above calculations were performed on a personal computer.

## CONCLUSIONS

An analytic expression for the propagator describing the evolution of a classical Coulomb plasma in the field of a short laser pulse on time scales less than the relaxation time has been derived and used to investigate the generation of fast electrons by a relativistically strong femtosecond laser pulse in a plasma with a nearly critical density. This approach makes it possible to simulate the three-dimensional dynamics of a plasma with actual ions on a personal computer.

The momentum distributions of hot electrons that have been obtained in this study agree with the results from PIC simulations and with the experimental data. The main mechanism for electron heating is associated with plasma turbulence. The momentum distribution of hot electrons is two-temperature in character; this can be explained by the combined action of the ponderomotive force and the turbulent plasma field. The fast elec-

trons produced in the plasma are heated to temperatures of about 10 keV due to anomalous conductivity.

## REFERENCES

1. P. G. Kryukov, *Kvantovaya Élektron. (Moscow)* **31**, 95 (2001).
2. V. P. Silin, *Parametric Action of High-Power Radiation on Plasma* (Nauka, Moscow, 1973) [in Russian].
3. W. L. Kruer, *The Physics of Laser-Plasma Interaction* (Addison-Wesley, New York, 1988).
4. B. Quesnel *et al.*, *Phys. Rev. Lett.* **78**, 2132 (1997).
5. Z.-M. Sheng, K. Mita, Y. Sentoku, and K. Nishihara, *Phys. Rev. E* **61**, 4362 (2000).
6. Z.-M. Sheng, K. Nishihara, T. Honda, *et al.*, *Phys. Rev. E* **64**, 066 409 (2001).
7. V. N. Tsytovich, *Theory of Turbulent Plasma* (Atomizdat, Moscow, 1971; Plenum, New York, 1974).
8. Y. I. Salamin and C. H. Keitel, *Phys. Rev. Lett.* **88**, 095005 (2002).
9. G. A. Askar'yan, S. V. Bulanov, F. Pegoraro, and A. M. Pukhov, *Pis'ma Zh. Éksp. Teor. Fiz.* **60**, 240 (1994) [*JETP Lett.* **60**, 251 (1994)].
10. A. Pukhov and J. Meyer-ter-Vehn, *Phys. Rev. Lett.* **76**, 3975 (1996).
11. S. P. Hatchett *et al.*, *Phys. Plasmas* **7**, 2076 (2000).
12. M. Tabak, J. Hammer, M. E. Glinsky, *et al.*, *Phys. Plasmas* **1**, 1626 (1994).
13. S. Karch, D. Habbs, T. Schaetz, *et al.*, *Laser Part. Beams* **17**, 565 (1999).
14. I. N. Kosarev, *Zh. Tekh. Fiz.* **74** (4), 133 (2004) [*Tech. Phys.* **49**, 509 (2004)].
15. Yu. L. Klimontovich, *Kinetic Theory of Nonideal Gases and Nonideal Plasmas* (Nauka, Moscow, 1975; Pergamon, Oxford, 1982).
16. V. P. Krainov and A. S. Roshupkin, *Phys. Rev. A* **64**, 063204 (2001).
17. H. A. Bethe and E. E. Salpeter, *Quantum Mechanics of One- and Two-Electron Atoms*, 2nd ed. (Rosetta, New York, 1977).
18. V. P. Krainov, *J. Opt. Soc. Am. B* **14**, 425 (1997).
19. B. Hafizi, P. Sprangle, J. R. Penano, and D. F. Gordon, *Phys. Rev. E* **67**, 056407 (2003).
20. M. V. Fedoryuk, *Asymptotics: Integrals and Series* (Nauka, Moscow, 1987) [in Russian].
21. A. Pukhov, Z.-M. Sheng, and J. Meyer-ter-Vehn, *Phys. Plasmas* **6**, 2847 (1999).
22. E. S. Weibel, *Phys. Rev. Lett.* **2**, 83 (1959).

*Translated by O. Khadin*



# Line Vortices in a Three-Dimensional Ordered Josephson Medium

M. A. Zelikman

St. Petersburg State Polytechnical University,  
ul. Politekhnikeskaya 29, St. Petersburg, 195251 Russia

Received May 20, 2004

**Abstract**—Two equilibrium configurations of a line vortex in a three-dimensional ordered Josephson medium are considered: (i) the vortex core is at the center of a cell and (ii) the vortex core is on a contact. Infinite systems of equations describing these configurations are derived. In going to a finite system, the currents far away from the center are neglected. A new technique for solving the finite system of equations is suggested. It does not require smallness of phase discontinuities at all vortex cells and, therefore, can be applied for any values of pinning parameter  $I$  down to zero. The structures and energies of both equilibrium states for isolated line vortices are calculated for any  $I$  from the range considered. For  $I > 0.3$ , a vortex can be thought of as fitting a square of  $5 \times 5$  cells. For lower  $I$ , the vortex energy can be expressed as a sum of the energies of the small discrete core and the quasi-continuous outside. The core energy is comparable to the energy of the outside and is a major contributor to the vortex energy when  $I$  is not too small. For any  $I$ , the energy of the vortex centered on the contact is higher than the energy of the configuration centered at the center of the cell. © 2005 Pleiades Publishing, Inc.

## INTRODUCTION

One very important problem in the physics of high-temperature superconductors (HTSCs) is analysis of the structure, motion, and pinning of the vortices arising in a sample exposed to a magnetic field. The behavior of vortices has been the subject of extensive investigation [1–7]. One-dimensional vortices in a long Josephson contact were analyzed in [3, 4]. However, in the works cited, the vortex was assumed to arise in the space with the continuous phase distribution, while its pinning was caused by interaction with discrete pinning centers. Actually, the Josephson medium is a cellular structure and, taken alone, causes pinning, which depends on the energy necessary for the vortex center to be displaced from one cell to another.

The vortex behavior in a linear chain of SQUIDS was analyzed in [5]. However, in that work, the two-dimensional case is considered: the magnetic field of a separate loop is taken into account only in the magnetic flux penetrating this loop. In the three-dimensional case, a vortex is represented by a set of coaxial “solenoids”; therefore, the magnetic flux through a loop is produced not only by the loop itself but also by other, including distant, current-carrying parts. In this case, as the critical current of the contact decreases, the vortex size grows. In other words, the number of loops contributing to the magnetic flux through the central cell of the vortex increases, which compensates for the decreased contribution to the magnetic flux from each of the loops. The author derived [6, 7] a set of equations of fluxoid quantization in the cells for a three-dimensional ordered Josephson medium and, based on these

equations, studied the structure of possible screening, laminar, and vortical current states in detail.

In [8], the equilibrium configurations of a laminar (planar) vortex in a three-dimensional ordered Josephson medium were calculated and the dependences of the pinning energy of a planar vortex, as well as of its magnetic and Josephson energies, on the critical current of a Josephson contact were constructed. The aim of this paper is to perform a similar study for the case of a line vortex in a three-dimensional Josephson medium. This problem is of great practical interest, since most HTSCs feature just such vorticity. Also, the author suggests a new technique for analysis of the line vortex structure. This technique, unlike that used in [6], does not require smallness of phase discontinuities at central cells of a vortex, allowing one to extend the applicability of the model to the range of low pinning parameters.

## ANALYSIS OF THE STRUCTURE AND ENERGY OF A LINE VORTEX

Let us consider a model representing a cubic lattice with a period  $a$  that consists of superconducting wires of diameter  $\delta$ . Every link of the lattice contains a small Josephson contact, all the contacts having the same value of critical current  $J_c$ . The current distribution is assumed to be planar; i.e., the currents are identically distributed in all parallel planes that run perpendicularly to the vortex axis and are spaced  $a$  apart. Such a simple model allows us to judge the structure of the vortices, as well as their pinning and dynamics. The

predictions of this model are qualitatively valid for more complicated configurations.

Let us consider the possibility of an isolated self-sustaining line vortex existing far away from the sample boundary in the absence of an external magnetic field. As follows from symmetry considerations, the equilibrium configurations of such a vortex are as follows: (i) the vortex core is at the center of a cell, (ii) the vortex core is on one of the contacts, and (iii) the vortex core is at an intersection between the wires. However, detailed analysis shows that the last-listed case has no solution.

Among the two remaining equilibrium configurations, the one with a lower energy is stable. The stability of the higher energy state calls for further investigation. This issue was considered at length in [9], where the stability of the equilibrium states of a planar vortex in a three-dimensional Josephson medium was touched upon. It was shown that the higher energy state is not necessarily unstable. Correct stability analysis has to be based on studying the quadratic form that describes the current configuration energy. For low values of the pinning parameter, the higher energy state of the planar vortex turns out to be quasi-stable.

Since the stability of line vortices also needs further investigations, the author, contrary to [6], will not use the inadequate terms *stable* and *unstable* as applied to a line vortex. The two main vortex configurations will be designated by superscripts *a* and *b* instead of *s* (stable) and *u* (unstable).

Consider both equilibrium configurations of a line vortex in greater detail.

**The vortex core is at the center of a cell (configuration *a*).** The cross section of a part of such a vortex by the plane perpendicular to the vortex axis is shown in Fig. 1. The vortex is axisymmetric and has four planes of symmetry (the vertical, horizontal, and two diagonal planes passing through the center of the lower left-hand cell in Fig. 1). On this basis, the entire cross section of the vortex can be constructed. In each of the cells, the condition of fluxoid quantization is fulfilled:

$$2\pi\Phi_m/\Phi_0 + \sum_k \varphi_k^{(m)} = 2\pi K_m, \quad (1)$$

where  $\sum_k \varphi_k^{(m)}$  is the sum of phase discontinuities at the Josephson elements in an *m*th cell,  $\Phi_m$  is the total magnetic flux through the *m*th cell,  $\Phi_0$  is a fluxoid quantum (fluxon), and  $K_m$  is an integer equal to one for the central cell (with current  $i_0$ ) of the vortex and zero for other cells.

Josephson currents  $J_k = J_c \sin \varphi_k$  decrease with distance from the vortex core, with the rate of decrease rising as critical current  $J_c$  increases. We shall consider only configurations such that  $\varphi_k \ll 1$ ; i.e.,  $\sin \varphi_k \approx \varphi_k$  for all  $\varphi_k$  except for the highest values of the phase discontinuity,  $\varphi_0$ , and  $\varphi_1$  in the cells nearest to the center

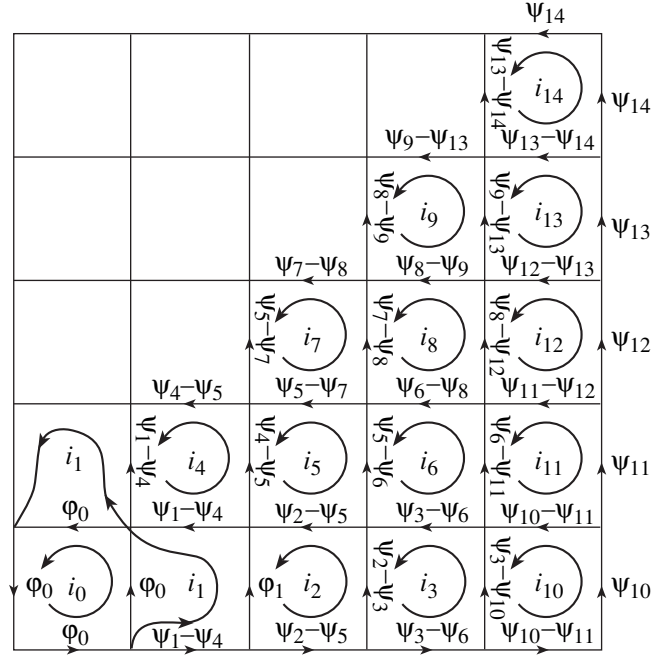


**Fig. 1.** Distribution of the currents and phase discontinuities over the contacts for vortex configuration *a* in the plane perpendicular to its axis.  $i_m$  and  $\psi_m$  are, respectively, the loop current in an *m*th loop and the corresponding loop phase discontinuity. Phase discontinuity  $\psi_m$  is shown above each of the contacts. Discontinuities  $\varphi_0$  and  $\varphi_1$  are not regarded as small. The cell with  $i_0$  has one fluxon of flux  $\Phi_0$ ; the other cells contain no fluxons.

(Fig. 1). The validity of this assumption will be corroborated by the results obtained (the technique suggested in this paper allows for, unlike the one used in [6], any values of  $\varphi_0$  and  $\varphi_1$  and, thereby, makes it possible to extend the domain of its applicability). In this case, it is convenient to deal with loop currents in the cells instead of writing the conditions of current balance at the sites. Let loop current  $i_m = J_c \psi_m$  flow in each cell  $m$  ( $m \neq 0$ ), where  $\psi_m$  is the “loop” phase discontinuity. Then, phase discontinuities  $\varphi_k$  (except for  $\varphi_0$  and  $\varphi_1$ ) at the contacts are defined as the differences between the corresponding “loop” values (Fig. 1). The magnetic flux through an *m*th cell can be written in the form [6]

$$\Phi_m = \mu_0 S/a \left( i_m + b \sum_k J_k^{(m)} \right) \quad (m \neq 0), \quad (2a)$$

$$\Phi_m|_{m=0} = \mu_0 S/a (i_0 + i_1 + 4b i_0) \quad (m = 0), \quad (2b)$$

where  $b$  is the coefficient of field nonuniformity [6] due to the discrete current distribution along the vortex axis,  $\sum_k J_k^{(m)}$  is the algebraic sum of the contacts currents in the *m*th cell, and  $S$  is the surface area of the cell.

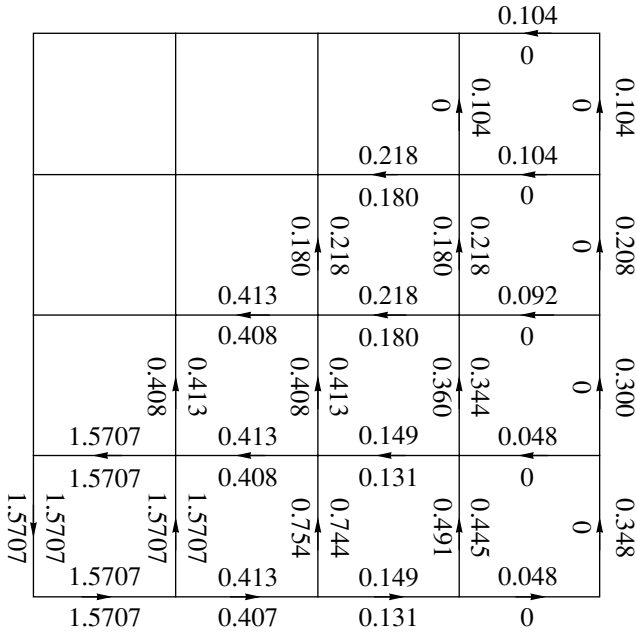


**Fig. 2.** Distribution of the phase discontinuities in vortex configuration  $a$  at  $I = 10^{-4}$ . The upper figures correspond to the calculations the  $7 \times 7$  square; the lower ones, for the  $5 \times 5$  square.

For a wire of thickness  $\delta \ll a$ , parameter  $b$  is given by

$$b = -\frac{1}{2\pi} \ln\left(2 \sinh \frac{\pi\delta}{a}\right).$$

For simplicity, we shall consider the case  $Ib \ll 1$ , where  $I$  is the pinning parameter given by Eq. (4). We note that such a consideration is also valid for a structure formed by superconducting filaments glued together along their length, so that the glued surfaces of the filaments may be viewed as long Josephson contacts in this case. The cross section of the structure has to have the form of a square lattice, but the cells may not be square; the filaments may have, in particular, a circular cross section.

Substituting Eq. (2) into Eq. (1) and assuming that  $i_0 = J_c \sin \varphi_0$  and that loop currents  $i_m = J_c \psi_m$  for  $m \neq 0$  and 1, we arrive (for  $Ib \ll 1$ ) at a set of equations of fluxoid quantization ( $m$  is the number of a cell, Fig. 1):

$$\begin{aligned} I \sin \varphi_0 + 4\varphi_0 + I\psi_1 &= 2\pi \quad (m=0), \\ (I+2)\psi_1 - 2\psi_4 + \varphi_1 - \varphi_0 &= 0 \quad (m=1), \\ (I+4)\psi_4 - 2\psi_1 - 2\psi_5 &= 0 \quad (m=4), \\ (I+3)\psi_2 - \varphi_1 - 2\psi_5 - \psi_3 &= 0 \quad (m=2), \\ (I+4)\psi_5 - \psi_2 - \psi_4 - \psi_6 - \psi_7 &= 0 \quad (m=5), \\ (I+4)\psi_7 - 2\psi_5 - 2\psi_8 &= 0 \text{ etc., } (m=7), \\ \sin \varphi_1 &= \psi_1 - \psi_2, \end{aligned} \quad (3)$$

where

$$I \equiv 2\pi\mu_0 J_c a / \Phi_0. \quad (4)$$

The last equation in (3) is obtained under the additional condition  $J_c \sin \varphi_1 = i_1 - i_2$  imposed on the current at the contact with  $\varphi_1$  ( $\varphi_1$  is not regarded small).

For such a configuration, the Josephson,  $E_J^a$ , and magnetic,  $E_H^a$ , energies per unit vortex length are given by

$$E_J^a = \frac{E_c}{a} \sum_k (1 - \cos \varphi_k) = E_0 I \sum_k (1 - \cos \varphi_k), \quad (5)$$

$$\begin{aligned} E_H^a &= \sum_m \frac{B_m^2}{2\mu_0} V_m = \frac{I^2}{2} E_0 \left[ (\sin \varphi_0 + \sin \varphi_1 + \psi_2)^2 \right. \\ &\quad \left. + 4(\sin \varphi_1 + \psi_2)^2 + 4(8) \sum_{m \neq 0,1} \psi_m^2 \right]. \end{aligned} \quad (6)$$

Here,  $E_c = \Phi_0 J_c / 2\pi$  is the energy of a Josephson contact,  $B_m^2 / 2\mu_0$  is the magnetic energy density in an  $m$ th cell,  $V_m$  is the relevant volume, and  $E_0 = \Phi_0^2 / 4\pi\mu_0 a^2$  is the normalizing factor.

In (5) (subscript  $k$ ), summation is over the Josephson contacts; in (6) (subscript  $m$ ), over the cells with regard to vortex symmetry (which leads to a factor of four for the cells lying in the central column and central row and to a factor of eight for the other cells).

It can be shown that set (3) may be obtained from the extremum conditions for the vortex total energy (the sums in (5) and (6)). In other words, a solution to system (3) corresponds to the maximal, minimal, or saddle value of the energy.

One may pass from infinite system (3) to a finite one by neglecting the currents distant from the center (Fig. 1). The size of the square necessary for calculations must be such that the phase discontinuities at the contacts close to the center vary insignificantly as the size of the square increases.

The set of equations was solved by expressing all  $\psi_m$  through  $\varphi_0$  and  $\varphi_1$  appearing in the linear equations of set (3) and substituting them into the first and last equations of (3). As a result, we obtain the set of two nonlinear equations

$$\varphi_1 = (2\pi - I \sin \varphi_0 - A(I)\varphi_0) / B(I), \quad (7a)$$

$$\varphi_0 = (\sin \varphi_1 - C(I)\varphi_1) / D(I), \quad (7b)$$

where  $A$ ,  $B$ ,  $C$ , and  $D$  are the polynomials in  $I$ .

Curves (7a) and (7b) have one point of intersection. The values  $\varphi_0$  and  $\varphi_1$  corresponding to this intersection are determined by a numerical method. Knowing  $\varphi_0$  and  $\varphi_1$ , we can determine all  $\psi_m$ .

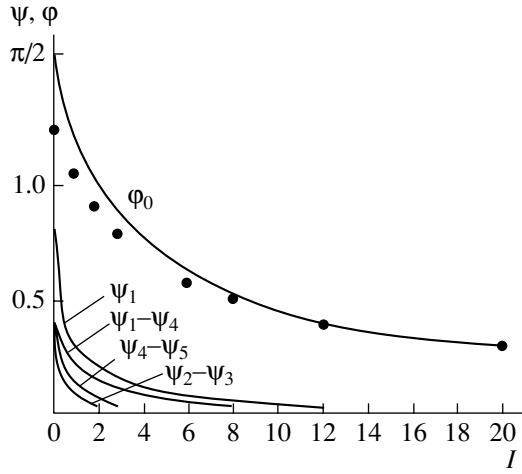


**Fig. 3.** Results of calculation of the phase discontinuity for several contacts nearest to the center that have the maximal currents (configuration *a*). The solid lines, the exact solutions to set (3); the symbols,  $\phi_0$  and  $\phi_1$  calculated by asymptotic formulas (8).

The analytic distribution of the phase discontinuity over the contacts is shown in Fig. 2 for  $I = 10^{-4}$ . In the calculation, we used  $5 \times 5$  (7 equations) and  $7 \times 7$  (11 equations) squares; i.e., we took two and three rows of cells on each of the sides away from the central cell. In going from the smaller square (lower figures) to the larger (upper figures), the values of  $\phi_k$  at the contacts near the center change insignificantly. The transition from  $7 \times 7$  to  $9 \times 9$  would cause even less change. This leads us to conclude that a  $7 \times 7$  square would suffice to calculate the vortex core structure no matter how small  $I$ .

The results obtained show that, unlike planar vortices, whose width tends to infinity with decreasing  $I$  [8], a line vortex has a core several cells in size for any  $I$ . Phase discontinuities and, hence, contact currents in the core of a line vortex are much higher than in the rest part of the vortex. Figuratively, a planar vortex “smears” with decreasing  $I$ , while a line vortex always has a rigid “pimple” several cells in size. It should be emphasized that the case at hand is the vortex structure: the currents decrease with decreasing  $J_c$  if it is  $J_c$  that is responsible for a decrease in  $I$ . If  $I$  decreases with a decrease in lattice spacing  $a$ , the vortex core diameter decreases but the currents remain unchanged and the vortex energy even increases according to Eq. (5).

It is noteworthy that all the currents in the cells occupying the major diagonals are the same:  $\psi_1 - \psi_4 = \psi_4 - \psi_5$ ,  $\psi_5 - \psi_7 = \psi_7 - \psi_8$ , etc.

The  $I$  dependences of the phase discontinuity that were calculated for several maximal-current contacts nearest to the vortex core (Fig. 1) are shown in Fig. 3. As is seen from Figs. 2 and 3, the condition under

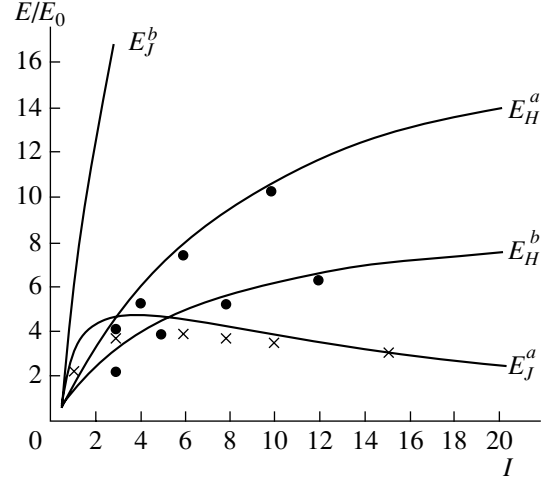


**Fig. 4.** Josephson and magnetic energies as a function of  $I$  in configurations *a* and *b*. The crosses, the calculation of  $E_J^a$ ; the dots,  $E_H^a$  and  $E_H^b$  found from asymptotic formulas (9) and (27).

which the calculations are valid ( $\sin_k \approx \phi_k$  for  $k \neq 0$  and 1) is met for any  $I$  down to  $I = 0$ .

As to the vortex energy, calculations by Eqs. (5) and (6) are correct only for values of  $I$  such that the vortex entirely fits the square considered. The typical vortex size is  $a/\sqrt{I}$ . Therefore, for the  $7 \times 7$  square, Eqs. (5) and (6) are applicable for  $I > 0.25$ , as follows from the fact that, for these values of  $I$ , the energy changes insignificantly in going from the  $5 \times 5$  to  $7 \times 7$  square. However, the mere fact of the minor change in the energy is not a sufficient condition that the energy calculations are valid. As the square size increases, an extra outer “ring” of cells starts contributing to the total energy, and the smallness of this addition does not mean that the total contribution from such rings extending to infinity will be small too. At low  $I$ , the outside of the vortex will be the basic contributor to the vortex energy. Figure 4 plots the Josephson,  $E_J$ , and magnetic,  $E_H^a$ , energies versus  $I$  for  $I > 0.25$ .

For high values of  $I (\geq 2\pi)$ , it follows from set (3) that  $\phi_0, \phi_1 \ll 1$ . Then, Eqs. (3), (5), and (6) yield

$$\tilde{\phi}_0^a = \frac{2\pi}{I+5}; \quad \tilde{\phi}_1^a = \frac{\tilde{\phi}_0^a}{I+3}, \quad (8)$$

$$\tilde{E}_J^a = E_0 \left( \frac{4\pi}{I+5} \right)^2 I, \quad \tilde{E}_H^a = 2E_0 \left[ \frac{\pi I(I+3)}{(I+2)(I+5)} \right]^2. \quad (9)$$

Figures 3 and 4 also present the asymptotic values of  $\tilde{\phi}_0^a$ ,  $\tilde{E}_J^a$ , and  $\tilde{E}_H^a$  that follow from (8) and (9).

At small  $I$ , our approach does not allow for direct calculations of the vortex energy, since an appreciable part of the energy is outside of the square. Let us sup-

**Table 1**

$I$	$10^{-4}$	$10^{-3}$	$10^{-2}$	0.1
$E_J/E_0I$ from (5)	8.63	8.60	8.37	6.75
$E_H/E_0I^2$ from (6)	13.56	13.50	12.8	8.32
$(E_J + E_H)/E_0I$	8.63	8.60	8.50	7.58
$E/E_0I$ from (14)	10.1	6.5	2.9	–

pose that the coordinate dependence of  $\phi$  is quasi-continuous in the outside. Magnetic field  $H$  is there given by [7]

$$\mathbf{H} + \frac{a^2}{I} \text{curlcurl} \mathbf{H} = \mathbf{A} \delta(\mathbf{r}). \quad (10)$$

In the range  $a \ll r \ll a/\sqrt{I}$ , the solution to Eq. (10) has the form [10]

$$H = \frac{\Phi_0 I}{2\pi\mu_0 a^2} \ln \frac{a}{r\sqrt{I}}, \quad |\text{curl} H| = \frac{\Phi_0 I}{2\pi\mu_0 a^2 r}. \quad (11)$$

If the contribution from the core is neglected, the total energy of such a vortex is given by [10]

$$E = E_0 \frac{\pi}{2} I \ln \frac{1}{I}. \quad (12)$$

Equation (12) determines the energy of the vortex without considering its core. The addition due to the core is also of interest. In the case of Abrikosov vortices in a continuous medium, taking into account the core energy leads to the expression [10]

$$E = E_0 \frac{\pi}{2} I \left( \ln \frac{1}{I} + 0.1 \right). \quad (13)$$

In the case of a discrete medium, which is considered in this paper, calculations of the vortex core energy may be performed using the above technique. Let us assume that the continuous approach is valid at  $r > 4a$ , i.e., beyond the  $7 \times 7$  square. Then, instead of (12), the energy of the outside is given by

$$E = E_0 \frac{\pi}{2} I \ln \frac{1}{16I}. \quad (14)$$

calculated by Eq. (14) in units of  $IE_0$ , as well as the magnetic (in  $I^2 E_0$ ), Josephson, and total energies of the  $7 \times 7$  square (Eqs. (5), (6)). These data suggest that, unlike Abrikosov vortices in a continuous medium, in which case the core energy may be neglected at small  $I$ , in the core energy in a discrete medium is comparable to the energy of the outer part and even becomes a major contributor to the vortex energy if  $I$  is not too small.

It is worth noting that, at small  $I$ , the Josephson energy of the vortex core, which is proportional to  $I$ , is much higher than the magnetic energy, which varies as  $I^2$ .

The expression for the total vortex energy with regard to the core can approximately be written in the form

$$E = E_0 I \left( \frac{\pi}{2} \ln \frac{1}{16I} + 8.63 \right) = E_0 \frac{\pi}{2} I \left( \ln \frac{1}{I} + 2.77 \right). \quad (15)$$

If it is assumed that the continuous approach is also valid at distances closer to the center, we come to a formula similar to Eq. (15) where the constant in the parentheses equals 2.70 for a  $5 \times 5$  square, 2.68 for a  $3 \times 3$  square, and 2.55 for a  $1 \times 1$  square. The proximity of the constant values confirms the validity of the approach suggested.

Equation (15) applies at small  $I$ , i.e., until the total energy in Table 1 remains almost constant. This condition fails starting from  $I = 0.1$ . Thus, Eq. (15) is a correct estimator of the vortex energy at very small  $I$ , while Eqs. (5) and (6) are valid for  $I > 0.25$ . For intermediate  $I$ , the vortex energy in a continuous medium can be found from the (more exact than (12)) expression [10]

$$E = E_0 \pi I K_0(4\sqrt{I}), \quad (16)$$

where  $K_0$  is the zero-order Bessel function of imaginary argument (Hankel function).

It is assumed in Eq. (16) that the continuous approach is valid for  $r > 4a$ . Then, the total vortex energy with regard to the core can be approximated as

$$E = E_0 I \pi (K_0(4\sqrt{I}) + \varepsilon), \quad (17)$$

where  $\varepsilon = E_\Sigma/\pi I E_0$  and  $E_\Sigma$  is the sum of the energies calculated by (5) and (6).

For  $I = 0.25$ , we have  $\varepsilon = 2.1$  and  $K_0(2) \approx 0.1$ ; for  $I = 0.1$ ,  $\varepsilon = 2.4$  and  $K_0(1.265) \approx 0.3$ . The fact that the first term in the parentheses in Eq. (17) is much smaller than the second one and can be neglected quantitatively confirms the above assumption that the vortex fits a  $7 \times 7$  square at  $I > 0.25$ . This result can be extended, with a certain error, to smaller (but not too small) values of  $I$ .

**The vortex center is at the contact (configuration b).** Such a vortex has two planes of symmetry (the lower horizontal plane and the vertical plane in the middle of the left-hand column in Fig. 5). All the vortex cross sections can be constructed on this basis. It follows from symmetry consideration that the phase discontinuity is equal to  $\pi$  at the central contact and to zero at all other contacts in the same row (Fig. 5). Calculations will show that the phase discontinuities at all the contacts, except for  $\phi_1$ ,  $\phi_2$ ,  $\phi_3$ , and  $\phi_4$ , may be regarded small ( $\sin \phi_k \approx \phi_k$ ) for any  $I$ . As in the previous section, we introduce loop currents  $i_m = J_c \psi_m$  at  $m \neq 0$ . This allows us to automatically satisfy the conditions of current balance at all the sites except for the upper right-hand site of the cell with  $m = 0$ . At this site, the balance condition has the form

$$\psi_3 - \phi_1 + \sin \phi_1 - \sin \phi_2 = 0. \quad (18)$$

At  $b = 0$ , we get a set of equations of fluxoid quantization in the cells ( $m$  is the number of a cell in Fig. 5) that is similar to (3):

$$I \sin \varphi_2 = \pi - 2\varphi_2 - \varphi_1 - I\psi_1 \quad (m = 0),$$

$$(I + 1)\psi_1 - \psi_4 + \varphi_4 - \varphi_2 = 0 \quad (m = 1),$$

$$(I + 2)\psi_{10} - 2\psi_4 + \varphi_3 - \varphi_1 = 0 \quad (m = 10),$$

$$(I + 4)\psi_4 - \psi_1 - \psi_5 - \psi_{10} - \psi_{12} = 0 \quad (m = 4), \text{ etc.}$$

These equations should be complemented by the conditions  $J_c \sin \varphi_3 = i_{10} - i_{11}$  and  $J_c \sin \varphi_4 = i_1 - i_2$  for the currents in the contact with  $\varphi_3$  and  $\varphi_4$  (these values are not regarded as small):

$$\sin \varphi_3 = \psi_{10} - \psi_{11}, \quad (20)$$

$$\sin \varphi_4 = \psi_1 - \psi_2. \quad (21)$$

The transition from this infinite set of equations to a finite one is accomplished in the same way as above, i.e., by neglecting the currents distant from the center.

Unlike set (3), set (18)–(21) cannot be reduced to a set of two nonlinear equations, which can be solved numerically. Therefore, here we apply the method of successive approximations. To this end, we represent  $\varphi_3$ ,  $\varphi_4$ , and their sine functions in the form  $\varphi_3 = \varphi_3^0 + \delta_3$ ,  $\varphi_4 = \varphi_4^0 + \delta_4$ ,  $\sin \varphi_3 = \sin \varphi_3^0 + \cos \varphi_3^0 \delta_3$ , and  $\sin \varphi_4 = \sin \varphi_4^0 + \cos \varphi_4^0 \delta_4$ . The values of  $\varphi_3^0$  and  $\varphi_4^0$  are assumed to be known (and equal to zero at the first iteration), while  $\delta_3$  and  $\delta_4$  are new variables (instead of  $\varphi_3$  and  $\varphi_4$ ) in respect to which the system is linear.

Now, let us express all  $\psi_m$ , as well as  $\delta_3$  and  $\delta_4$ , through  $\varphi_1$  and  $\varphi_2$  using the linear equations of the system (these are Eq. (20), Eq. (21), and all of Eqs. (19) minus the first one). Substituting them into the first equation of set (19) and into Eq. (18), we arrive at the following set of nonlinear equations:

$$\varphi_2 = [\pi - I \sin \varphi_1 - E(I)\varphi_1 - D(I)]/F(I), \quad (22)$$

$$\varphi_1 = [\pi - I \sin \varphi_2 - G(I)\varphi_1 - H(I)]/M(I), \quad (23)$$

where  $E, D, F, G, H$ , and  $M$  are fractional rational functions of  $I$ .

The values of  $\varphi_2$  and  $\varphi_1$  corresponding to the only point of intersection between curves (22) and (23) can be calculated numerically. Knowing  $\varphi_2$  and  $\varphi_1$ , we then find  $\delta_3$ ,  $\delta_4$ , and all  $\psi_m$ . For the next iteration, we take new values of  $\varphi_3^0$  and  $\varphi_4^0$  (that result by adding the obtained values of  $\delta_3$  and  $\delta_4$  to their previous values) and solve the set again. The iteration procedure converges, i.e., every next iteration step gives  $\delta_3$  and  $\delta_4$  several orders of magnitude smaller than their previous values. In this way, the initial set of equations can be solved with any accuracy in several steps only.

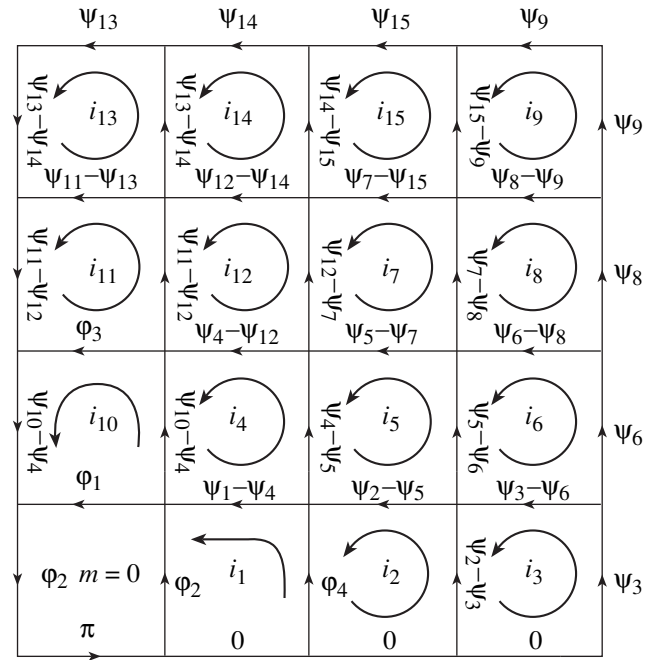


**Fig. 5.** Distribution of the currents and phase discontinuities over the contacts for configuration  $b$ . Discontinuities  $\varphi_1$ ,  $\varphi_2$ ,  $\varphi_3$ , and  $\varphi_4$  are not regarded as small. The cell with  $m = 0$  has one fluxon of  $\Phi_0$ ; the other cells contain no fluxons.

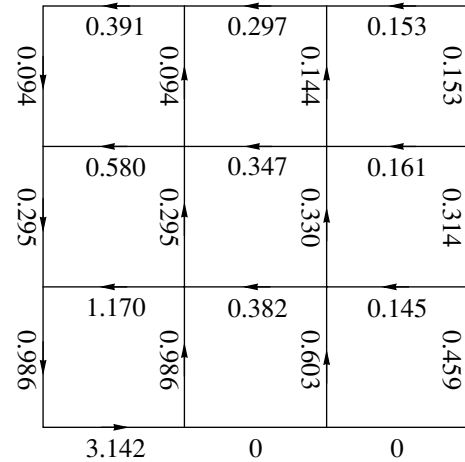


**Fig. 6.** Distribution of the phase discontinuities in vortex configuration  $b$  at  $I = 10^{-4}$ .

Figure 6 demonstrates the phase discontinuity distributions over the vortex contacts that were calculated for  $I = 10^{-4}$ . In the calculations, a  $6 \times 5$  rectangle (12 equations) was used; i.e., we took two cells on each of the sides of two central cells. The  $I$  dependences of the phase discontinuities that were constructed for several (nearest to the vortex core) contacts with the maximal currents (Fig. 5) are shown in Fig. 7. It is seen from Fig. 6 and 7 that the calculations are valid ( $\sin \varphi_k \approx \varphi_k$  at  $k \neq 1, 2, 3, 4$ ) any  $I$  down to  $I = 0$ .

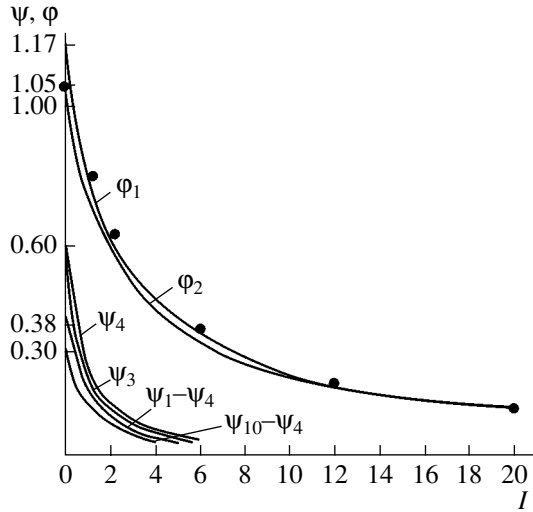


**Fig. 7.** Phase discontinuities calculated for several contacts with the maximal currents for configuration  $b$ . The dots show  $\phi_1$  and  $\phi_2$  calculated by asymptotic formulas (27).

Reasoning similar to that behind the calculation of the vortex energy in configuration  $a$  can be applied to find the vortex energy in configuration  $b$ . The difference lies in that, in the latter case, we employ the  $6 \times 5$  rectangle (or a square of  $5 \times 5$  cells in the symmetric case). Therefore, the following energy estimators give the vortex total energy (with the energy of its outside neglected) at  $I > 0.3$ :

$$E_J^b = E_0 I \left[ 2 + \sum_k (1 - \cos \phi_k) \right], \quad (24)$$

$$E_H^b = I^2 E_0 \left[ (\sin \phi_2 + \psi_1)^2 + \sum_{m \neq 0} \psi_m^2 \right]. \quad (25)$$

To confirm the validity of (24) and (25), we will make use of an analogue to Eq. (17), substituting  $K_0(4\sqrt{I})$  for  $K_0(3\sqrt{I})$ , since the vortex outside corresponds to  $r > 3a$ :

$$E = E_0 I \pi (K_0(3\sqrt{I}) + \varepsilon). \quad (26)$$

Here,  $\varepsilon = E_\Sigma / \pi I E_0$ ,  $E_\Sigma$  is the sum of the energies calculated by (24) and (25) for the configuration depicted in Fig. 5 where the upper row of cells is lacking (in such a

way, we obtain a  $5 \times 5$  square). For  $I = 0.25$ , we have  $\varepsilon = 2.15$  and  $K_0(1.5) \approx 0.2$ ; for  $I = 0.3$ ,  $\varepsilon = 2.08$  and  $K_0(1.65) \approx 0.13$ .

The  $I$  dependences of  $E_J^b$  and  $E_H^b$  that were calculated by (24) and (25) for  $I > 0.3$  are shown in Fig. 4. The asymptotic values of the phase discontinuities in the central cell and of the energies for configuration  $b$  at  $I \gg 2\pi$  are given by

$$\begin{aligned} \tilde{\phi}_1^b \approx \tilde{\phi}_2^b &\approx \frac{\pi}{I+3}, & \tilde{E}_J^b &\approx E_0 \left[ 4I + \frac{6\pi^2 I}{(I+3)^2} \right], \\ \tilde{E}_H^b &\approx E_0 \left( \frac{\pi I}{I+3} \right)^2. \end{aligned} \quad (27)$$

Figures 4 and 7 also show the values calculated by (27).

Table 2 lists the magnetic energy in units of  $I^2 E_0$  (formula (25)), Josephson energy in units of  $IE_0$  (Eq. (24)), total energy of the  $6 \times 5$  rectangle, and total energy of the  $5 \times 5$  square (the upper row of cells is omitted).

For small values of  $I$ , the vortex total energy with regard to the core can be approximated as

$$E = E_0 I \left( \frac{\pi}{2} \ln \frac{1}{9I} + 7.90 \right) = E_0 \frac{\pi}{2} I \left( \ln \frac{1}{I} + 2.81 \right). \quad (28)$$

Thus, the core energy and, hence, the vortex total energy in configuration  $b$  are somewhat higher than those in configuration  $a$ . The same relationship is also true for higher values of  $I$ . However, based on this fact alone, one cannot conclude that configuration  $b$  is unstable and is certain to change to configuration  $a$ . It was already noted that the configuration with the least possible energy is always stable, while the stability of the higher energy configuration calls for further investigation. This issue was discussed in terms of stability analysis as applied to planar vortices [9].

Knowing the vortex energy  $E$ , one can find the critical value of external magnetic field  $H_{c1}$  at which vortices arise. The Gibbs thermodynamic potential of a volume unit of the sample placed in external magnetic field  $H_e$  is equal to

$$G = NE - BH_e/2 = 0.5B(H_{c1} - H_e), \quad (29)$$

where  $N$  is the number of vortices per  $1 \text{ m}^2$  (i.e.,  $B = \Phi/S = N\Phi_0$ ) and

$$H_{c1} = 2E/\Phi_0. \quad (30)$$

For  $H_e < H_{c1}$ , potential  $G$  grows with  $B$ ; i.e.,  $G$  is minimal at  $B = 0$  (the complete Meissner effect). For  $H_e > H_{c1}$ ,  $G$  decreases with increasing  $B$ ; i.e., the formation of such vortices becomes energetically favorable.

**Table 2**

$I$	$10^{-4}$	$10^{-3}$	$10^{-2}$	0.1
$E_J/E_0 I$ from (24)	8.14	8.12	8.06	6.85
$E_H/E_0 I^2$ from (25)	8.48	8.45	7.98	6.01
$(E_J + E_H)/E_0 I$ ( $6 \times 5$ )	8.14	8.13	8.06	7.45
$(E_J + E_H)/E_0 I$ ( $5 \times 5$ )	7.90	7.89	7.76	6.72

## CONCLUSIONS

Two equilibrium configurations of a line vortex in a three-dimensional ordered Josephson medium were considered: (i) the vortex core is at the center of a cell and (ii) the vortex core is at one of the contacts. Infinite sets of equations describing these configurations are derived. In going to a finite system, the currents far away from the center are neglected. The size of the square necessary for the calculations must be such that the phase discontinuities at the contacts close to the center vary insignificantly as the size of the square increases.

A new technique for solving the finite set of equations is suggested. Contrary to the one used earlier [6], this technique does not require the smallness of phase discontinuities at all vortex cells and, therefore, can be applied for any values of pinning parameter  $I$  down to zero. One of the configurations has two large phase discontinuities, and the other has four; therefore, a special iteration procedure was applied.

The structures and energies of both equilibrium configurations for isolated line vortices were calculated for any  $I$  from the range considered. Unlike planar vortices, whose width tends to infinity with decreasing  $I$ , a line vortex has a core several cells in size at any values of  $I$ . In the core of a line vortex, the phase discontinuities and, hence, the contact currents are much higher than in its rest part. For  $I > 0.3$ , a vortex can be viewed as fitting a square of  $5 \times 5$  cells. For lower  $I$ , the vortex energy can be expressed as a sum of the energies of the geometrically small discrete core and the quasi-continuous outside. However, unlike Abrikosov vortices in a con-

tinuous medium, where the core energy may be neglected at small  $I$ , the core energy in a discrete medium is comparable to the energy of the outside and even becomes a major contributor to the vortex energy when  $I$  is not too small.

For any  $I$ , the energy of the vortex centered at the contact is higher than that of the vortex centered at the center of the cell.

## REFERENCES

1. K.-H. Müller, J. C. Macfarlane, and R. Driver, *Physica C* **158**, 69 (1989).
2. M. S. Rzchowski, S. P. Benz, M. Tinkham, and C. J. Lobb, *Phys. Rev. B* **42**, 2041 (1990).
3. Y. S. Kivshar and B. A. Malomed, *Rev. Mod. Phys.* **61**, 763 (1989).
4. V. V. Bryksin and S. N. Dorogovtsev, *Zh. Éksp. Teor. Fiz.* **102**, 1025 (1992) [*Sov. Phys. JETP* **75**, 558 (1992)].
5. F. Parodi and R. Vaccarone, *Physica C* **173**, 56 (1991).
6. M. A. Zelikman, *Supercond. Sci. Technol.* **10**, 469 (1997).
7. M. A. Zelikman, *Supercond. Sci. Technol.* **10**, 795 (1997).
8. M. A. Zelikman, *Zh. Tekh. Fiz.* **72** (7), 28 (2002) [*Tech. Phys.* **47**, 821 (2002)].
9. M. A. Zelikman, *Zh. Tekh. Fiz.* **74** (9), 55 (2004) [*Tech. Phys.* **49**, 1158 (2004)].
10. P. G. de Gennes, *Superconductivity of Metals and Alloys* (Benjamin, New York, 1966; Mir, Moscow, 1968).

*Translated by M. Astrov*



## Infrared Quenching of Electroluminescence in ZnS : Mn Thin-Film Electroluminescent Structures

N. T. Gurin and D. V. Ryabov

Ulyanovsk State University, Ulyanovsk, 432970 Russia

e-mail: ido@ulsu.ru

Received February 26, 2004

**Abstract**—Electroluminescence from thin-film electroluminescent devices is found to be quenched after IR irradiation of the devices in the interval between exciting voltage pulses. The IR irradiation decreases the emission intensity in the spectral range 530–540 nm, while increasing it between 640 and 690 nm. These effects are explained by IR-induced charge exchange between the deep centers due to  $V_S^{2+}$  and  $V_S^+$  sulfur vacancies, an increase in the concentration of the latter vacancies, and the redistribution of the channels of impact excitation of  $Mn^{2+}$  and  $V_S^+$  centers in favor of  $V_S^+$  centers. The cross section and rate of impact excitation of  $V_S^+$  centers, the photoexcitation cross section for  $V_S^{2+}$  centers, the IR radiation absorption coefficient, the internal quantum efficiency of electroluminescence, and the probability of radiative relaxation of  $Mn^{2+}$  centers, as well as the electron multiplication factor in the phosphor layer, are evaluated. © 2005 Pleiades Publishing, Inc.

The currently available data on the effect of infrared (IR) irradiation on the electroluminescence properties of powdered zinc sulfide phosphors exhibiting recombination electroluminescence suggest the presence of an absorption band in the IR range [1]. This stems from the fact that pulsed IR irradiation of the samples causes a decrease in the emission wave amplitude in a part of this range, i.e., quenches the electroluminescence.

In thin-film electroluminescence devices (TFELDs) exhibiting in-center luminescence, pulsed IR irradiation applied between exciting voltage pulses raises the amplitude of a current pulse passing through the phosphor layer during the action of these voltage pulses [2, 3]. Earlier [4], we showed that IR irradiation under these conditions quenches electroluminescence in TFELDs and changes the intensity of certain bands in their emission spectrum. Also, it was found that electroluminescence spectra taken of ac ZnS : Mn TFELDs in the continuous excitation mode cannot be related to the kinetics of current passage through the phosphor layer and to the variation of the instantaneous brightness, because such spectra typically show the average TFELD brightness [5].

The aim of this work is to study the electroluminescence spectra, as well as the electrical and optical performance, of TFELDs subjected to pulsed IR irradiation between exciting voltage pulses. The spectra were recorded in different parts of the brightness wave that correspond to different excitation levels under the conditions when adjacent brightness waves did not overlap and the interval between exciting voltage pulses was

long enough for the space charge in the phosphor layer to be neutralized.

To elucidate the effect of IR irradiation on the electroluminescent spectra in various parts of the brightness wave, we experimented with a TFELD based on the layered MISIM structure. Here, M refers to the 0.2- $\mu\text{m}$ -thick bottom transparent  $\text{SnO}_2$  electrode deposited on a glass substrate and to the 0.15- $\mu\text{m}$ -thick top nontransparent aluminum electrode with a diameter of 1.5 mm; S, to the 0.48- $\mu\text{m}$ -thick ZnS : Mn (0.5 wt% of Mn) phosphor layer; and I, to the  $\text{ZrO}_2\text{:Y}_2\text{O}_3$  (13 wt% of  $\text{Y}_2\text{O}_3$ ) insulating layers. The phosphor layer was applied by vacuum evaporation in the quasi-closed volume on the substrate heated to 250°C and then annealed at 250°C for 1 h. The nontransparent electrode was also applied by vacuum deposition, while the insulating layers were deposited by electron-beam evaporation. The resistivity of the insulating layers was  $\sim 10^{13} \Omega \text{ cm}$ , and the ac breakdown field (the frequency was varied between 10 Hz and 1 kHz) was  $(3.2\text{--}3.6) \times 10^6 \text{ V/cm}$ . The leakage current in these layers was two to three orders of magnitude lower than the current passing through the phosphor layer at the maximal operating voltage of the TFELD.

The experimental study of brightness waves in the TFELD, i.e., recording the dependence of instantaneous brightness  $I_\lambda$  on time  $t$  at given wavelength  $\lambda$ , was performed under conditions when the TFELD was excited by alternating-sign triangular voltage pulses  $V(t)$ . The excitation mode was either continuous (the voltage frequency was 20 Hz) or pulsed (a two-period train of pulses with a repetition rate of 20 Hz). In the

first half-period, either the positive or negative voltage half-wave was applied to the top electrode (the +Al and -Al modes, respectively). Interval  $T_s$  between the trains was 1, 50, or 100 s. Current  $I_e(t)$  through the TFELD was measured by using a 10-k $\Omega$  resistor connected in series with the TFELD. The voltage drop across the resistor was no more than 0.5% of  $V(t)$ . To increase the recording sensitivity, the TFELD emission corresponding to the first brightness wave was first transmitted through an MUM-2 monochromator (with a wavelength inaccuracy of 0.5 nm, linear dispersion of 4.8 nm/mm, and slit width of 3 mm) and then measured by means of an FÉU-79 photoelectron multiplier. The measurements were performed in the wavelength range from 400 to 750 nm with a 5-nm step. Exciting voltage  $V(t)$ , current  $I_e(t)$  through the TFELD, total brightness wave  $L(t)$ , and brightness waves  $L_\lambda(t)$  at certain wavelength  $\lambda$  were recorded with an S9-16 dual-trace storage oscilloscope interfaced with a PC. Such a configuration provides the measurement and storage of 2048 points for a given discretization period and 256 levels of amplitude digitization in either channel. Mathematical processing of the results and graphing were carried out using the Maple V Release 4 Version 4.00b and GRAPHER Version 1.06 2-D Graphing System application packages. The experimental dependences were approximated using the TableCurve2D v2.03 program. The time dependence  $F_p(t)$  of the mean field strength in the phosphor layer, as well as the dependences of current  $I_p(t)$  and charge  $Q_p(t)$  passing through the phosphor layer in the luminescence mode, was taken by the method reported in [6, 7]. The capacitance of the insulating layers,  $C_i = 730$  pF, and that of the phosphor layer,  $C_p = 275$  pF, were measured by an E7-14 immitance meter with regard to the sizes of the TFELD. The average luminescent brightness of the TFELD was determined using a YaRM-3 luminance meter.

As in [3], difference  $\Delta Q_p(t)$  between the charges transferred through the phosphor layer with and without IR irradiation was determined via difference  $\Delta I_p(t)$  in the corresponding currents:

$$\Delta Q(t) = \int_0^t \Delta I_p(t) dt. \quad (1)$$

The TFELD was IR-excited from the side of the substrate (in both the continuous and pulsed mode) by using two AL107B light-emitting diodes with an emission band maximum at wavelength of  $\lambda_m = 950$  nm, FWHM  $\Delta\lambda_0 = 25$  nm, total power  $P \approx 12$  mW, and total photon flux density  $\Phi \approx 3 \times 10^{15}$  mm $^{-2}$  s $^{-1}$ . The parameters listed above were obtained by statistically averaging over five series of emission spectrum measurements.

The average brightness at certain wavelengths  $\lambda$ , as well as in portions I, II, III, and IV of the brightness wave (the portions were selected as described in [5];

namely, portion I corresponds to the initial fast increase of current  $I_p(t)$  through the phosphor layer; in portions II and III,  $I_p(t)$  increases slowly; and in portion IV, current  $I_p(t)$  and the brightness decay once the pulses of exciting voltage  $V(t)$  have reached a maximum (Fig. 1)) were determined from the Talbot's law for an intermittent radiation source:

$$L_n = \frac{1}{t_1 - t_2} \int_{t_1}^{t_2} L_\lambda(t) dt, \quad (2)$$

where  $t_1$  and  $t_2$  are the time extremities for portions I, II, III, and IV of the brightness wave (Figs. 1a, 1b).

The dependences  $L_n(\lambda)$  ( $n = I, II, III, \text{ and } IV$ ) specify the emission spectrum in each of the portions. The total (net) emission spectrum, which is the sum of partial spectra  $L_n(\lambda)$ , was determined by the formula

$$L(\lambda) = \sum_n L_n(\lambda). \quad (3)$$

The instantaneous value of internal quantum efficiency  $\eta_{\text{int}}(t)$  was found as the ratio of  $L(t)$  to  $I_p(t)$  [8].

The basic results of the study are as follows. In the continuous mode of TFELD excitation, no influence of the IR irradiation on current  $I_p(t)$ , brightness waves  $L(t)$  and  $L_\lambda(t)$ , or the emission spectrum was detected within the experimental error. In the pulse excitation mode, the above dependences remained unchanged during the action of exciting voltage pulses.

However, in the interval between the pulses, we observed, as in [3], an increase in currents  $I_e(t)$  and  $I_p(t)$  ( $\Delta I_e(t)$  and  $\Delta I_p(t)$ , respectively; Figs. 1a, 1b, and 1d) and increase  $\Delta Q_p(t)$  in charge  $Q_p(t)$  (Fig. 1e). Also, we found the variations of (i) brightness waves  $L_\lambda(t)$  (Figs. 1a and 1b), (ii) total brightness wave  $\Delta L(t)$  (Fig. 1d), (iii) internal quantum yield  $\eta_{\text{int}}(t)$  (Fig. 1f), (iv) the emission spectra in portions I–IV of the brightness wave, and (v) the total emission spectrum taken during the first half-period of the exciting voltage pulse following the interval in both ( $\pm$ Al) modes (Figs. 2, 3). In addition, we noticed the decrease in brightness wave amplitudes  $L_\lambda(t)$ , in particular, near the basic maximum of emission from Mn $^{2+}$  centers at  $\lambda_m = 585$  nm (Figs. 1a and 1b) and in total brightness wave amplitude  $L(t) - \Delta L(t)$  in Fig. 1d. The decrease in  $L(t)$ ,  $L_\lambda(t)$ , and  $\eta_{\text{int}}(t)$  was the most pronounced in portions I and II of the brightness wave, i.e., where the irradiation-induced increases in the current and charge ( $\Delta I_p(t)$  and  $\Delta Q_p(t)$ ) passing through the phosphor layer are the highest (Figs. 1d–1f), as well as where the time dependence of field strength  $F_p(t)$  starts deviating (portion I) and deviates significantly (portion II) from a straight line (Fig. 1c). Other observations are as follows. The intensity of the basic electroluminescence peak ( $\approx 585$  nm) in portions I–III and of the total spectrum taken in the -Al mode (Figs. 2a–2c, and 2e), as well as the spectra in

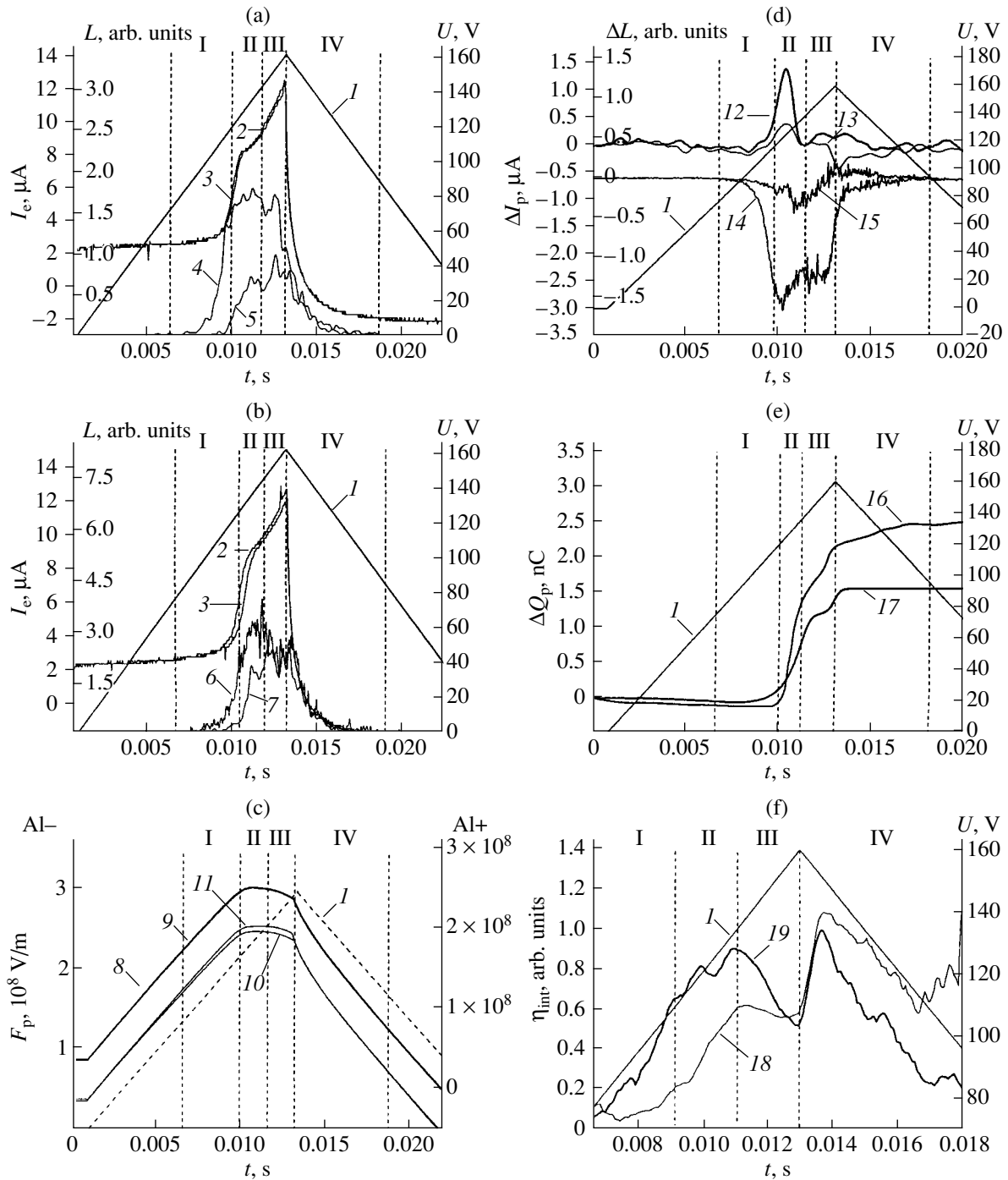


**Fig. 1.** (1)  $U(t)$ , (2, 3)  $I_e(t)$ , (4–7)  $L_\lambda(t)$  at  $\lambda = 585$  nm, (8–11)  $F_p(t)$ , (12, 13)  $\Delta I_p$ , (14, 15)  $\Delta L(t)$ , (16, 17)  $\Delta Q_p(t)$ , and (18, 19)  $\eta_{\text{int}}(t)$ ; (2, 4, 6, 8, 10, 19) without IR irradiation and (3, 5, 9, 11, 18) with IR irradiation in the interval between exciting voltage pulses. (a) (8, 9, 13, 15, 17) +Al mode and (b, f) (10, 12, 14, 16) –Al mode.  $T_s = 100$  s.

portions I–IV and the total spectrum that were taken in the +Al mode (Figs. 3a–3e), decreased by a factor of 1.1–2.6. In particular, the maximum of the total spectrum decreased  $\approx 1.5$  and  $\approx 2.1$  times in the –Al and +Al modes, respectively, and the basic emission peak in portion IV increased by a factor of  $\approx 1.7$  in the –Al

regime (Fig. 2d) with the simultaneous growth of internal quantum yield  $\eta_{\text{int}}(t)$  (Fig. 1f). Finally, we note (i) the attenuation of the emission intensity in the range 530–540 nm and the enhancement of the intensity in the partial spectra (portions I and IV of the brightness wave) and in the total spectrum between 640 and

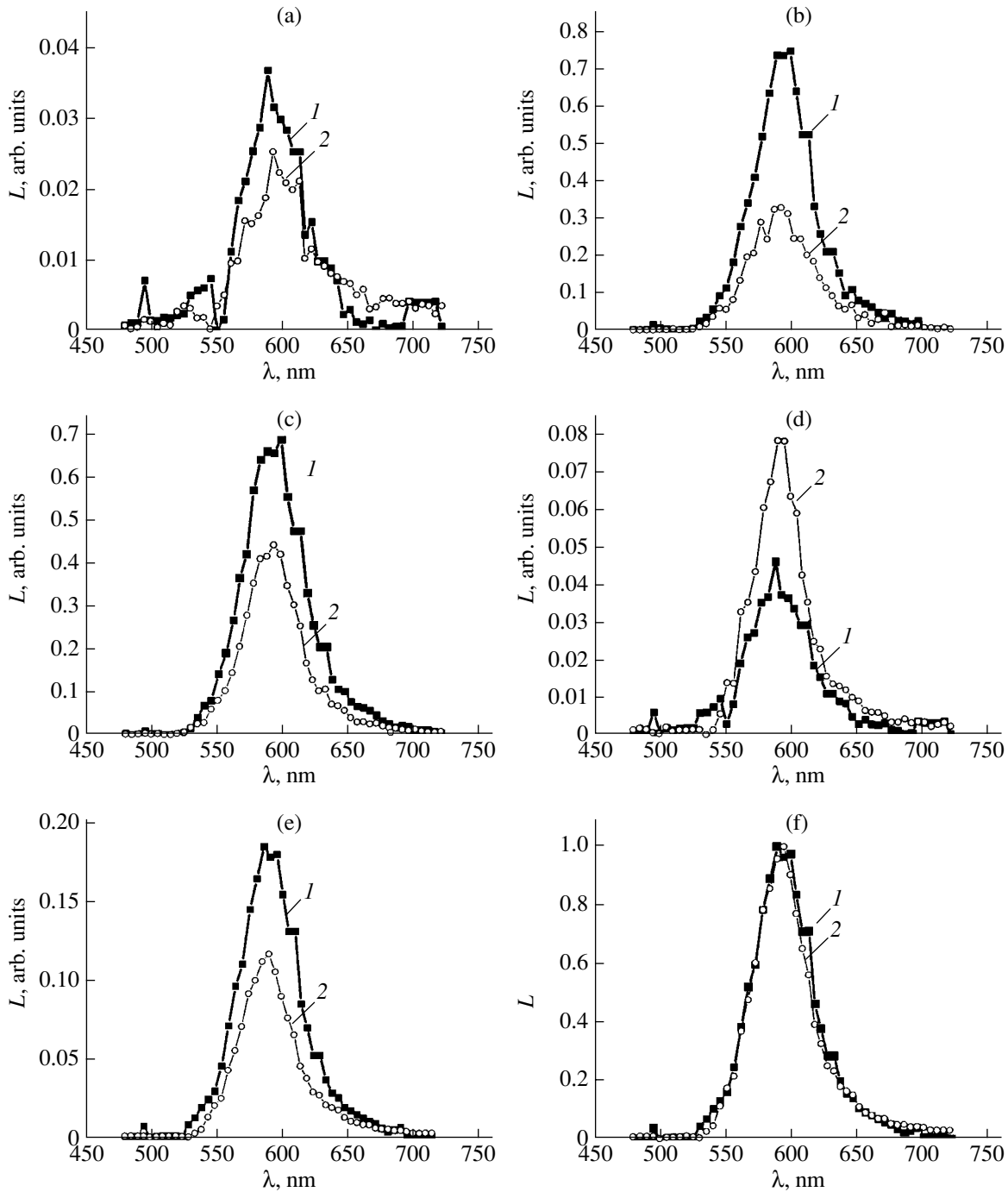


**Fig. 2.** Electroluminescence spectra recorded (1) without and (2) with the IR irradiation in the  $-Al$  mode: (a) portion I, (b) portion II, (c) portion III, and (d) portion IV of the brightness wave; (e) total electroluminescence spectra and (f) total electroluminescence spectra normalized to their maxima.  $T_s = 100$  s.

690 nm in the  $-Al$  regime (Figs. 2a and 2d); (ii) the attenuation of the emission intensity in the range 530–540 nm for partial spectrum I in the  $+Al$  regime (Fig. 3a); (iii) the attenuation of the peak intensity at  $\approx 495$  nm in partial spectra I–IV and in the total spectrum in the  $-Al$  mode (Figs. 2a–2f); and (iv) the shift of the long-wave side of the electroluminescence spectra

toward shorter wavelengths: the total spectrum experiences a moderate shift in the  $-Al$  mode (Fig. 2f), while the total spectrum and partial spectra I and IV shift more appreciably in the  $+Al$  mode (Figs. 3a, 3d, and 3f).

All the changes become more pronounced as the interval between exciting voltage pulses (during which the IR irradiation is accomplished) expands.

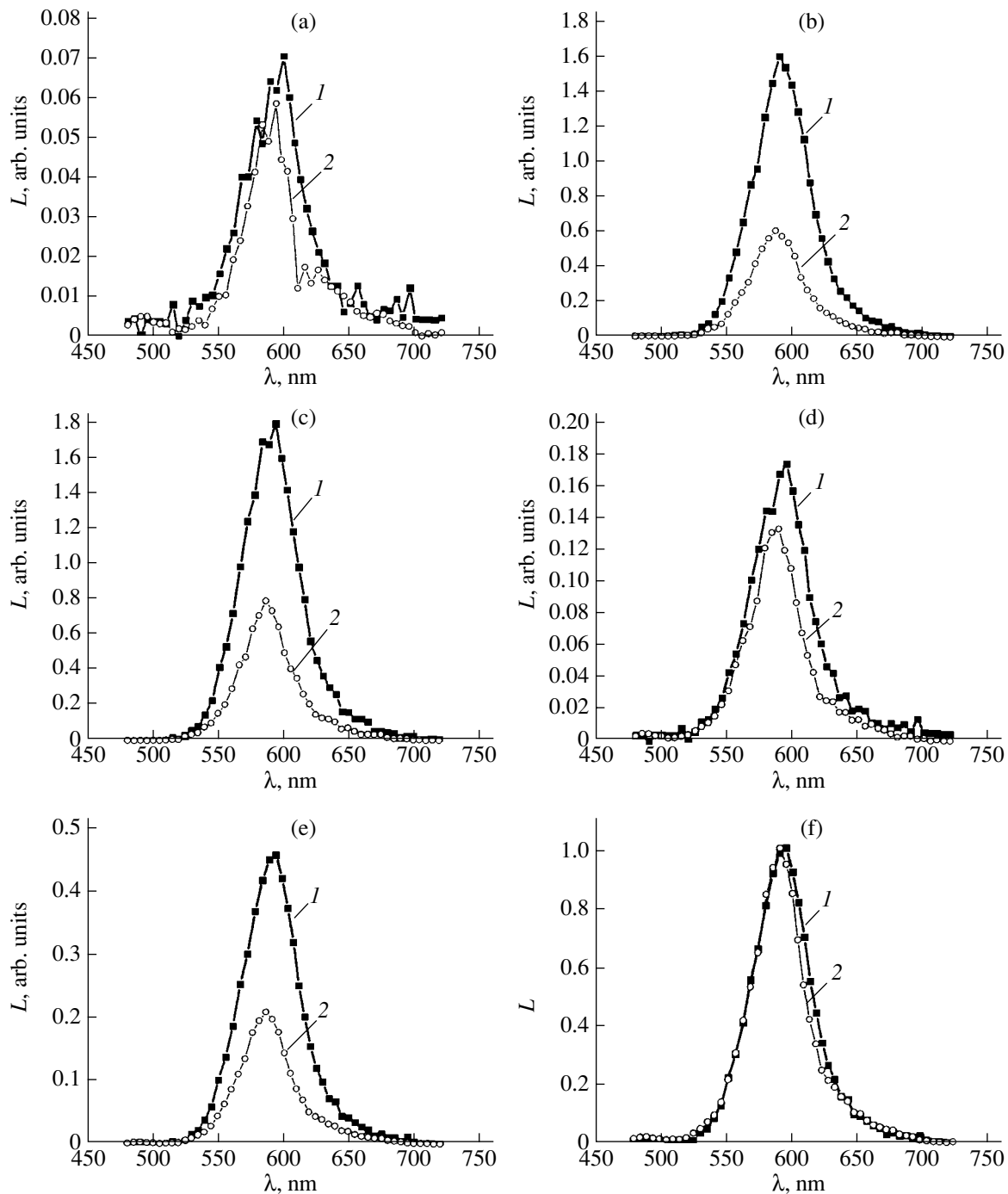


**Fig. 3.** Electroluminescence spectra recorded (1) without and (2) with the IR irradiation in the +Al mode: (a–f) the same as in Fig. 2.

The above results can be explained as follows. When TFELD is in the active mode and the applied voltage exceeds a threshold value, the electrons tunnel-emitted from the surface states near the cathodic side of the insulator–phosphor interface (Fig. 4) are ballistically accelerated, causing impact ionization of shallow donor levels ( $\text{Mn}^{2+}$ -related luminescent centers, which substitute for zinc ions at the sites of the ZnS lattice,

and deep centers due to zinc vacancies  $V_{\text{Zn}}^{2-}$  and sulfur vacancies  $V_{\text{S}}^{+}$ ) with the formation of the positive space charge in the anode region of the phosphor layer. In the cathode region, free electrons are trapped by deep centers  $V_{\text{S}}^{2+}$  and  $V_{\text{S}}^{+}$ , which lie  $\approx 1.3$  and  $\leq 1.9$  eV above the valence band top, respectively, and create the negative space charge, thereby neutralizing the positive

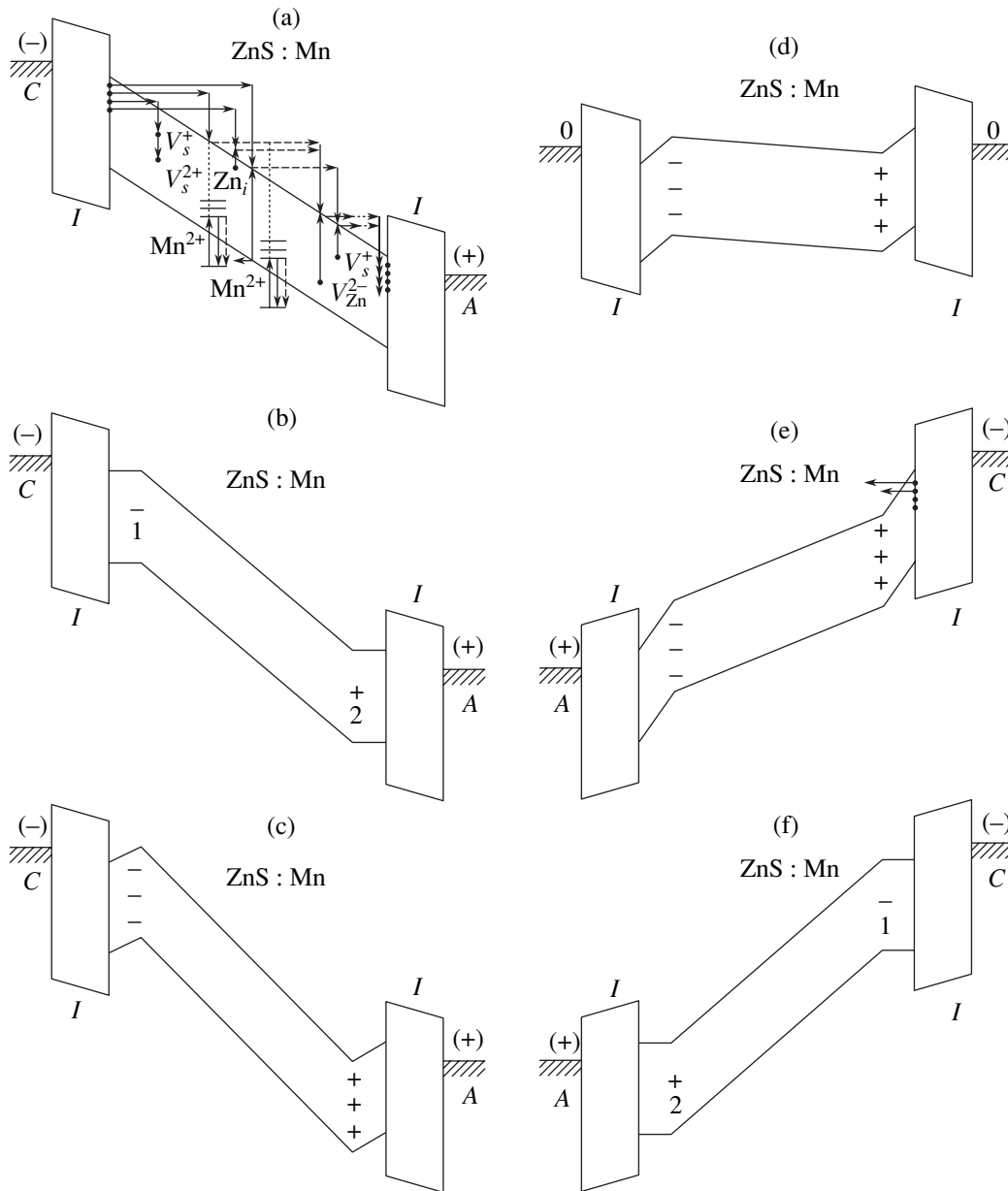


**Fig. 4.** Processes triggering electroluminescence in the ZnS : Mn-based TFELD: (a–c) The first half-period,  $T/2$ , and (d–f) the second half-period of exciting voltage  $V(t)$ . (a, e) The threshold voltage is exceeded, (b) formation of space charges at  $t < T/4$ , (c)  $t = T/4$ , (d)  $t = T/2$ , and (f) formation of space charges at  $t < 3T/4$ . I, insulator; C, cathode; A, anode; 1, negative space charge; and 2, positive space charge.

space charge produced earlier (Fig. 4a–4c, 4e, 4f). The neutralization takes place in the interval between two sequential operating cycles of the TFELD, the degree of neutralization increasing with interval duration [2, 3]. The irradiation by IR photons of appropriate energy in the interval generates additional sulfur vacancies  $V_S^+$ , since the electrons being released from the valence band under the action of the IR radiation are trapped by  $V_S^{2+}$  centers. As a result, the positive space charge, field strength in the cathode region, and tunnel-

emission current (portion I) (Fig. 1d) decrease in the next operating cycle (Fig. 4e). As applied voltage  $V(t)$  and, hence, field strength  $F_p(t)$  rise, currents  $I_e(t)$  and  $I_p(t)$  (portions I and II) start exceeding their values in the absence of the irradiation (Figs. 1a, 1b, and 1d) because of the ionization of the extra sulfur vacancies  $V_S^+$  in the phosphor layer. Differences  $\Delta I_p(t)$  and  $\Delta Q_p(t)$  in both ( $\pm A$ ) modes reflect the nonuniform distribution of structural defects in the phosphor layer [2, 3]. According to [5, 9–11], the electroluminescence spectrum of the TFELD is related to in-center emission

from  $\text{Mn}^{2+}$  and consists of the bands with maxima at  $\lambda_m = 557, 578, 600, 616,$  and  $635\text{--}637$  nm. These maxima are due to the different positions of  $\text{Mn}^{2+}$  ions in the real ZnS lattice and, possibly, to the formation of the  $\alpha$ -MnS phase ( $\lambda_m = 635$  nm [10, 11]). The spectrum may also contain a band with a maximum at  $\lambda_m = 606\text{--}610$  nm, which is related to the complexes formed by  $\text{Mn}^{2+}$  ions and sulfur vacancies  $V_S$  [12–14].

The emission observed in the interval 530–540 nm in the absence of the IR irradiation (Figs. 2 and 3) may be attributed to the recombination arising when free electrons are trapped by deep centers that are doubly ionized sulfur vacancies  $V_S^{2+}$  lying 1.3 eV above the valence band top [5, 12, 15]. The fact that this emission is more intense in the –Al mode is explained by technological reasons. As was noted, a part of the ZnS : Mn layer that is adjacent to the upper electrode is sulfur-depleted. As a result, under equilibrium conditions, the concentration of sulfur vacancies in this region exceeds that in the lower part of the ZnS layer [2, 3]. The decay of this emission in portion I of the brightness wave and in the total spectrum in the –Al mode (Fig. 2a, 2e, and 2f) after the irradiation is explained by a decrease in the concentration of  $V_S^{2+}$  centers and an increase in the concentration of  $V_S^+$  centers when the electrons being released from the valence band are trapped by the former. Because of this, the recombination emission band at 640–690 nm observed in portion I in the –Al regime (Figs. 2a and 2d) becomes more intense. This band is produced by electron transitions from the conduction band (or from shallow donor levels, such as  $\text{Zn}_i^0$  centers lying 0.10–0.12 eV below the conduction band bottom [2, 3, 12]) to the  $V_S^+$  level lying  $\geq 1.9$  eV below the conduction band bottom.

The emission band with a maximum at  $\lambda_m = 490\text{--}495$  nm (Figs. 2, 3a, 3d–3f) is probably caused by the recombination emission from donor–acceptor pairs related to sulfur vacancies  $V_S^{2+}$ . The quenching of this luminescent band after the IR irradiation, which is observed in all the spectra taken in the –Al regime, and its appearance in the spectra in portions I and IV that were taken in the +Al mode may be related to the non-uniform distribution of structural defects across the phosphor layer (specifically, to the enrichment of the upper part of this layer by sulfur vacancies, as discussed earlier). Upon the irradiation, the concentration of sulfur vacancies  $V_S^{2+}$  and, hence, the donor–acceptor pairs drops.

The attenuation of these emission bands is much less pronounced in the spectra taken in portions II and III of the brightness wave (Figs. 2 and 3), because here the intensity of the in-center emission from  $\text{Mn}^{2+}$  ions significantly grows.

The decrease in the basic emission band peak after the IR irradiation, which is observed in portion IV of the brightness wave in the –Al mode (Figs. 2d–2f), and in internal quantum yield  $\eta_{\text{int}}(t)$  in the same portion (Fig. 1f) may be caused by the resonance absorption of the radiation at  $\lambda_m = 530$  nm by  $\text{Mn}^{2+}$  ions [16] in the vicinity of sulfur vacancies  $V_S^{2+}$  in the upper part of the phosphor layer, where field strength  $F_p(t)$  decreases (Fig. 1c) and the impact ionization of  $\text{Mn}^{2+}$  centers ceases. This weakens the emission band at  $\approx 530$  nm in portion IV and also in the total spectrum (Figs. 2d–2f).

The shift of the long-wave side of the electroluminescence spectra toward shorter waves (Figs. 2f, 3a, 3d, 3f) is probably due to a decrease in the concentration of the complexes formed by  $\text{Mn}^{2+}$  ions and sulfur vacancies (which are responsible for the band with  $\lambda_m = 606\text{--}610$  nm [12–14]). This decrease reflects the change in the charge state of the sulfur vacancies, as described before. This shift is more apparent in the +Al mode, because the concentration of sulfur vacancies and  $\text{Mn}^{2+}$  centers near the top Al electrode is higher in this case [2, 3]. It can thus be concluded that  $\text{Mn}^{2+}$  ions and  $V_S^{2+}$  sulfur vacancies do form these complex centers, since the IR irradiation diminishes the concentration of  $V_S^{2+}$  centers.

The fact that the IR irradiation does not influence the electroluminescence spectra recorded in the continuous excitation mode and during the action of exciting voltage pulses in the pulsed mode is explained by the small thickness of the phosphor layer and by the short interval between the voltage pulses ( $< 10$  ms). Because of this, the concentration of additional deep centers  $V_S^+$  remains insignificant for the IR photon flux density used in the experiments [3].

The IR quenching of the basic electroluminescence peak is probably related to the redistribution of the channels via which the impact excitation of  $\text{Mn}^{2+}$  luminescence centers and deep centers related to the sulfur,  $V_S^+$ , and zinc,  $V_{\text{Zn}}^{2-}$ , vacancies takes place [4]. This supposition is supported by the decay of brightness wave  $L_\lambda(t)$  at  $\lambda = 585$  nm (Figs. 1a and 1b) and of total brightness wave  $\Delta L(t)$  (Fig. 1d), which is accompanied by the simultaneous increase in current  $\Delta I_p(t)$  and charge  $\Delta Q_p(t)$  (Figs. 1d and 1e), as well as by the decrease in internal quantum yield  $\eta_{\text{int}}(t)$  (Fig. 1f). If the charge in portions I–III increases by  $\Delta Q_p = (1.5\text{--}2.1) \times 10^{-9}$  C (Fig. 1e) and the depth of the positive space charge layer and the surface area of the THELD are taken to be  $d = 0.2$   $\mu\text{m}$  and  $S_e = 2$   $\text{mm}^2$ , respectively, the concentration of  $V_S^+$  centers (and, hence, the equilibrium concentration of  $V_S^{2+}$  centers) increases by  $\Delta N_{V_S} = (2.3\text{--}3.2) \times 10^{16}$   $\text{cm}^{-3}$ , which is in agreement with the early results

[3]. Since the equilibrium concentration of  $V_S^+$  vacancies is estimated as  $N_{V_S} = (3-4) \times 10^{16} \text{ cm}^{-3}$  [3], the IR irradiation may “skew” the distribution of impact ionizations of  $V_S^+$  and  $Mn^{2+}$  centers by a factor of 1.5–2.1 (depending on whether the +Al or –Al mode is used) in favor of  $V_S^+$  centers. This statement holds even if one ignores the fact that the ionization potential of  $V_S^+$  centers ( $\approx 1.9 \text{ eV}$ ) is lower than that of the  $Mn^{2+}$  centers (2.4–2.5 eV) (accordingly, the effective thickness of the phosphor layer where the ionization of  $V_S^+$  centers occurs increases as compared with  $Mn^{2+}$  centers) and that the impact excitation cross section of  $V_S^+$  centers is larger than that of  $Mn^+$  centers.

Let us consider the relationship between the concentrations of  $V_S^+$  and  $Mn^{2+}$  centers in greater detail. Under the assumption that the TFELD radiation is monochromatic and omnidirectional during half-period  $T/2$  of voltage  $V(t)$ , the number of  $Mn^{2+}$  centers that are excited by impact ionization and relax via emission of photons can be expressed as [6]

$$N_r^* = \frac{AL_e T}{2K_0}, \quad (4)$$

where  $A = (\pi S_e)/(h\nu f_\lambda)$ ,  $h\nu$  is the photon energy,  $f_\lambda$  is the luminous efficiency,  $L_e$  is the average brightness of TFELD emission during half-period  $T/2$  of exciting voltage  $V(t)$ , and  $K_0$  is the coefficient of emission extraction from the TFELD.

For  $h\nu = 2.12 \text{ eV}$  ( $\lambda_m = 585 \text{ nm}$ ),  $f_\lambda = 510 \text{ lm/W}$ ,  $K_0 = 0.2$ ,  $T = 0.05 \text{ s}$ ,  $S_e = 2 \text{ mm}^2$  (the measurements were carried out without IR irradiation in the continuous excitation mode at a frequency of 20 Hz), and  $L_e = 5 \text{ cd/m}^2$ , we obtain  $N_r^* = 2.7 \times 10^{10}$ . This value corresponds to the concentration of luminescent centers  $N^* = (3.4-4.5) \times 10^{16} \text{ cm}^{-3}$  when the effective thickness of the phosphor layer, where the impact excitation of  $Mn^{2+}$  centers occurs, is equal to  $d_{pe} = 0.3-0.4 \text{ }\mu\text{m}$ . This concentration is even smaller than the total equilibrium concentration of  $V_S^+$  and  $V_{Zn}^{2-}$  centers,  $(6.2-7.7) \times 10^{16} \text{ cm}^{-3}$  [3], the impact ionization of which generates the positive space charge. This concentration of deep ionized centers responsible for the formation of the positive space charge agrees completely with the values determined previously, such as  $10^{16}-10^{17} \text{ cm}^{-3}$  [17] and  $(4.8-9.0) \times 10^{16} \text{ cm}^{-3}$  [18], as well as with the equilibrium concentration of  $V_S^+$  and  $V_{Zn}^{2-}$  centers in ZnS [15]. Thus, the irradiation-induced increase in the concentration of  $V_S^+$  centers by  $\Delta N_{V_S} = (2.3-3.2) \times 10^{16} \text{ cm}^{-3}$

does have a noticeable effect on the distribution of the channels of impact excitation of the luminescent centers and the centers associated with intrinsic structural defects.

Charge  $Q_p$  transferred through the phosphor layer during the half-period of exciting voltage  $V(t)$  was determined by the technique described in [3] and was found to be  $\sim 2.7 \times 10^{-8} \text{ C}$ . This value is consistent with the number of charge carriers (electrons, since their mobility in ZnS is 28 times the mobility of holes [3]),  $n_p = 17 \times 10^{10}$ . On the one hand, this indicates that the concentration of free electrons is sufficient for the impact ionization of  $Mn^{2+}$  luminescence centers and centers due to zinc and sulfur vacancies to occur. On the other hand, under the above assumption that the TFELD radiation is monochromatic and omnidirectional during the half-period of voltage  $V(t)$ , the internal quantum yield of the TFELD can be determined as follows [19]:

$$\eta_{\text{unt}} = \frac{N_r^*}{n_p}. \quad (5)$$

For the values for  $N_r^*$  and  $n_p$  given before, formula (5) yields  $\eta_{\text{int}} = 0.16$ . This testifies that only each sixth electron passing through the phosphor layer is capable of exciting  $Mn^{2+}$  centers that emit when relaxing. The rest of the total number  $n_p$  of electrons participates in the impact excitation of  $Mn^{2+}$  centers that feature non-radiative relaxation and of the deep centers, mostly sulfur,  $V_S^+$ , and zinc,  $V_{Zn}^{2-}$ , vacancies. The fact is supported by the data reported in [20], where the distribution of hot electrons in ZnS was found to decrease abruptly at energies of 2.64–2.82 eV (the ionization energy for  $V_{Zn}^{2-}$  is 2.6–2.8 eV [3]).

Now we will estimate total number  $N_\Sigma^*$  of excited  $Mn^{2+}$  centers and probability  $P_r$  of their radiative relaxation:

$$N_\Sigma^* = \frac{N_r^*}{P_r}. \quad (6)$$

Internal quantum yield  $\eta_{\text{int}}$  is related to  $P_r$  and number  $N_1$  of  $Mn^{2+}$  centers ionized by one electron having passed through the phosphor layer as

$$\eta_{\text{int}} = N_1 P_r, \quad (7)$$

where

$$N_1 = d_{pe} \sigma N, \quad (8)$$

$\sigma$  is the impact excitation cross section for  $Mn^{2+}$  centers ( $\sigma = 2 \times 10^{-16} \text{ cm}^2$  [21]) and  $N$  is their concentration in the phosphor layer (at a doping level of 0.5 wt%,  $N = 2 \times 10^{20} \text{ cm}^{-3}$  [17]).



Taking  $\eta_{\text{int}} = 0.16$ ,  $d_{\text{pe}} = 0.3\text{--}0.4 \mu\text{m}$ ,  $N^* = 2.7 \times 10^{10}$ , we find from (6)–(8) that  $N_{\Sigma}^* = (20\text{--}27) \times 10^{10}$ . This value exceeds the number of electrons passing through the phosphor layer ( $n_p = 17 \times 10^{10}$ ), indicating that expression (8) is inapplicable, since the value of  $N_1$  is limited by number  $n_{p0}$  of electrons emitted from the surface states at the cathodic side of the insulator–phosphor interface during the half-period of voltage  $V(t)$  and by number  $N_V$  of deep centers  $V_S^+$  and  $V_{Zn}^{2-}$ . Then, assuming that all  $V_S^+$  and  $V_{Zn}^{2-}$  centers are excited by impact ionization, as follows from the dependences  $\Delta I_p(t)$  and  $\Delta Q_p(t)$  (Figs. 1d and 1e), we can conclude that total number  $N_{\Sigma}^*$  of  $\text{Mn}^{2+}$  centers excited obeys the inequality

$$N_{\Sigma}^* \leq n_p - N_V. \quad (9)$$

In view of the above values of  $n_p$  and  $N^*$ , the total number of  $V_S^+$  and  $V_{Zn}^{2-}$  centers corresponding to their equilibrium concentration in the phosphor layer ( $(6.2\text{--}7.7) \times 10^{16} \text{cm}^{-3}$  [3]), and the value of  $N_V = (4.8\text{--}6.4) \times 10^{10}$ , we find that  $N_{\Sigma}^* \leq (10.6\text{--}12.2) \times 10^{10}$ . In this case, (6) yields  $P_r \geq 0.22\text{--}0.25$ , which is close to the estimate  $P_r = 0.4$  [21]. It should be noted that the values of  $N_{\Sigma}^*$ ,  $N_r^*$ , and  $\eta_{\text{int}}$  can be increased 2.0–2.5 times by merely using exciting voltage  $V(t)$  with a higher rate of rise [22], since, in this case, currents  $I_e(t)$  and  $I_p(t)$  (and, hence,  $n_{p0}$ ) will grow [7, 22]. Another way of increasing these values several times is to shrink the nonemitting cathode region of the phosphor layer and to increase  $d_{\text{pe}}$ . Thickness  $d_{\text{pe}}$  is made larger in advanced TFELDs prepared by atomic layer epitaxy [21], where  $N_{\Sigma}^*$  is higher for the same concentration  $N$  of  $\text{Mn}^{2+}$  centers in the phosphor layer.

If it is taken into account that the impact excitation of  $\text{Mn}^{2+}$  centers does not generate extra free carriers, factor  $M$  of electron multiplication in the ZnS layer may be expressed as follows:

$$M = \frac{n_p}{n_{p0}}. \quad (10)$$

Since number  $m$  of ionization events per electron leaving the high field region is

$$m = 1 - \frac{1}{M}, \quad (11)$$

the total number of ionization events causing electron multiplication will be  $mn_p$ . On the other hand, if we assume that basically electron multiplication is the result of ionization of all deep centers  $V_S^+$  and  $V_{Zn}^{2-}$ , the

total number of which is  $N_V$ , the values of  $m$  and  $M$  are then given by

$$m = \frac{N_V}{n_p}, \quad M = \frac{n_p}{n_p - N_V}. \quad (12)$$

For the above values of  $N_V$  and  $n_p$ , we have  $m = 0.28\text{--}0.38$  and  $M = 1.4\text{--}1.6$ . This value of  $M$  agrees well with  $M = 1.4\text{--}1.8$  obtained in [23] for “thin” TFELDs ( $d_p = 230 \text{nm}$ ), which are produced by atomic layer epitaxy and have the smallest thickness of the nonemitting near-cathode region (about 20 nm [21]), where free electrons are accelerated to the ionization energy of  $\text{Mn}^{2+}$  centers, as compared to TFELDs obtained by other techniques (up to 200 nm [21]). The values of  $M$  found by Shin *et al.* [23] ( $M = 1.4\text{--}1.8$ ) are somewhat smaller than those obtained by the same authors for thicker TFELD samples ( $M = 2.1\text{--}4.0$ ) and than  $M$  obtained in [24] ( $M = 3.9$ ).

Having found  $M$ , we can now evaluate the number of electrons tunnel-injected through a barrier at the cathodic side of the insulator–phosphor interface during the half-period of exciting voltage  $V(t)$ :

$$n_{p0} = \frac{n_p}{M} = (10.6\text{--}12.1) \times 10^{10}. \quad (13)$$

With regard to the surface area of the TFELD,  $S_e = 2 \text{mm}^2$ , we find the surface density of states responsible for electron tunneling,  $(5.3\text{--}6.0) \times 10^{12} \text{cm}^{-2}$ . This value is in good agreement with the available data [21].

Using  $m$  and  $d_{\text{pe}}$  found above ( $d_{\text{pe}} = 0.3\text{--}0.4 \mu\text{m}$ ) and assuming that the field in the region of ionization is uniform, we estimate the rate  $\alpha$  of impact ionization as

$$\alpha = \frac{m}{d_{\text{pe}}} = (0.7\text{--}1.3) \times 10^4 \text{cm}^{-1}. \quad (14)$$

From these data, one can determine the cross section  $\sigma_{V_S}$  of impact excitation of  $V_S^+$  centers. Assuming that all  $V_S^+$  centers are ionized during the half-period of exciting voltage  $V(t)$  and taking into account that, at  $N_{V_S} < n_{p0}$ , the number of  $V_S^+$  centers excited by an electron passing through the phosphor layer is  $N_{V_S}^1$ , we estimate  $\sigma_{V_S}$  by (8) as follows:

$$\sigma_{V_S} = \frac{N_{V_S}^1}{d_{\text{pe}} N_{V_S}}. \quad (15)$$

At  $d_{\text{pe}} = 0.3\text{--}0.4 \mu\text{m}$ ,  $N_{V_S}^1 \leq 1$ ,  $N_{V_S} = (3\text{--}4) \times 10^{16} \text{cm}^{-3}$ , we find that  $\sigma_{V_S} \leq (0.6\text{--}1.1) \times 10^{-12} \text{cm}^2$ , which is typical of centers of attraction [25] and is much larger than the cross section of impact excitation of neutral  $\text{Mn}^{2+}$  centers ( $\approx 2 \times 10^{-16} \text{cm}^2$ ).

The parameters estimated above allow us to evaluate the cross section  $\sigma_\phi$  of absorption of an IR photon by a  $V_S^{2+}$  center (i.e., the cross section of hole photogeneration from  $V_S^{2+}$  centers in the valence band). According to [25],

$$\sigma_\phi = \frac{\alpha_\phi}{\Delta N_{V_S}^\phi}, \quad (16)$$

where  $\alpha_\phi$  is the coefficient of absorption of IR radiation and  $\Delta N_{V_S}^\phi$  is the concentration of photogenerated  $V_S^+$  centers.

Assuming that the reflection of the IR radiation from and the absorption of the radiation in the other layers and substrate of the TFELD structure are negligible and also assuming that the radiation is absorbed in the phosphor layer (by  $V_S^{2+}$  centers) by the exponential law, we can write  $\alpha_\phi$  in the form

$$\alpha_\phi = \frac{1}{d} \ln \frac{n_{\phi 0}}{n_{\phi d}} = \frac{1}{d} \ln \frac{\Phi T_S}{(\Phi T_S - \Delta N_{V_S}^\phi d)}, \quad (17)$$

where  $d$  is the thickness of the positive space charge layer,  $n_{\phi 0} = \Phi S_e T_S$  is the number of IR photons incident on the TFELD surface, and  $n_{\phi d} = \Phi T_S S_e - N_{V_S}^\phi S_e d$  is the number of IR photons having passed through the phosphor layer without absorption.

Substituting  $d = 0.2 \mu\text{m}$ ,  $\Phi = 3 \times 10^{15} \text{ mm}^{-2} \text{ s}^{-1}$ ,  $T = 100 \text{ s}$ , and  $\Delta N_{V_S}^\phi = (2.3\text{--}3.2) \times 10^{16} \text{ cm}^{-3}$  into (16) and (17), we get  $\alpha_\phi = (7.5\text{--}10.5) \times 10^{-4} \text{ cm}^{-1}$  and  $\sigma_\phi = 3.3 \times 10^{-20} \text{ cm}^2$ .

Thus, we can conclude that the quenching of electroluminescence in ZnS : Mn-based TFELDs is observed when the channels of impact excitation of deep  $V_S^+$  centers in the energy gap of ZnS : Mn become more efficient than those of impact ionization of  $\text{Mn}^{2+}$  luminescent centers. The concentration of  $V_S^+$  centers rises when the device is exposed to the IR radiation in the interval between exciting voltage pulses. The change in the electroluminescence spectra substantiates the mechanism explaining the effect of IR irradiation on TFELD characteristics and validates the energy levels of sulfur vacancies  $V_S^{2+}$  and  $V_S^+$  (which were found to be 1.3 eV above the valence band top and 1.9 eV below the conduction band bottom, respectively). The emission band with a peak at 490–495 nm probably results from radiative recombination of donor–acceptor pairs related to sulfur vacancies  $V_S^{2+}$ . We experimentally evaluated a number of the parameters of the deep centers associated with intrinsic defects in the phosphor layer. These are the cross section of impact excitation of

$V_S^+$  centers,  $\sigma_{V_S} \leq (0.6\text{--}1.1) \times 10^{-12} \text{ cm}^2$ ; the rate of impact ionization of these centers,  $\alpha = (0.7\text{--}1.3) \times 10^4 \text{ cm}^{-1}$ ; the cross section of photoexcitation of  $V_S^{2+}$  centers,  $\sigma_\phi \approx 3.3 \times 10^{-20} \text{ cm}^2$ ; and the coefficient of absorption of IR radiation,  $\alpha_\phi \approx (7.5\text{--}10.5) \times 10^{-4} \text{ cm}^{-1}$ . Also, we estimated the internal quantum yield of electroluminescence,  $\eta_{\text{int}} \sim 0.16$ ; the probability of radiative relaxation of excited  $\text{Mn}^{2+}$  centers,  $P_r \geq (0.22\text{--}0.25)$ ; and the multiplication factor of electrons in the phosphor layer,  $M = 1.4\text{--}1.6$ . The data obtained indicate, among other things, that the efficiency of electroluminescence from ZnS : Mn-based TFELDs, which is caused by impact excitation of  $\text{Mn}^{2+}$  luminescent centers, depends on the internal quantum yield and may be appreciably limited by the competing process of impact excitation of the deep centers due to intrinsic defects (that is, sulfur and zinc vacancies) in the phosphor layer structure.

#### ACKNOWLEDGMENTS

This work was supported by a grant of the President of the Russian Federation (grant no. NSh-1482.2003.8).

#### REFERENCES

1. A. N. Georgobiani and Yu. G. Penzin, *Lyuminestsitsiya*, 321 (1963).
2. N. T. Gurin, A. V. Shlyapin, O. Yu. Sabitov, and D. V. Ryabov, *Pis'ma Zh. Tekh. Fiz.* **29** (4), 14 (2003) [*Tech. Phys. Lett.* **29**, 134 (2003)].
3. N. T. Gurin, A. V. Shlyapin, O. Yu. Sabitov, and D. V. Ryabov, *Zh. Tekh. Fiz.* **73** (4), 30 (2003) [*Tech. Phys.* **48**, 469 (2003)].
4. N. T. Gurin and D. V. Ryabov, *Pis'ma Zh. Tekh. Fiz.* **30** (9), 88 (2004) [*Tech. Phys. Lett.* **30**, 392 (2004)].
5. N. T. Gurin, A. V. Shlyapin, and O. Yu. Sabitov, *Pis'ma Zh. Tekh. Fiz.* **28** (15), 24 (2002) [*Tech. Phys. Lett.* **28**, 631 (2002)].
6. N. T. Gurin, O. Yu. Sabitov, and A. V. Shlyapin, *Zh. Tekh. Fiz.* **71** (8), 48 (2001) [*Tech. Phys.* **46**, 977 (2001)].
7. N. T. Gurin, A. V. Shlyapin, and O. Yu. Sabitov, *Zh. Tekh. Fiz.* **72** (2), 74 (2002) [*Tech. Phys.* **47**, 215 (2002)].
8. N. T. Gurin, A. V. Shlyapin, and O. Yu. Sabitov, *Zh. Tekh. Fiz.* **73** (4), 100 (2003) [*Tech. Phys.* **48**, 479 (2003)].
9. M. F. Bulanyĭ, B. A. Polezhaev, and T. A. Prokof'ev, *Fiz. Tekh. Poluprovodn. (St. Petersburg)* **32**, 673 (1998) [*Semiconductors* **32**, 603 (1998)].
10. M. F. Bulanyĭ, A. V. Kovalenko, and B. A. Polezhaev, in *Proceedings of the International Conference on Luminescence in Honor of the 110th Anniversary of S. I. Vavilov, Moscow, 2001* (FIAN, Moscow, 2001), p. 98.
11. N. D. Borisenko, M. F. Bulanyĭ, F. F. Kodzhesperov, and B. A. Polezhaev, *Zh. Prikl. Spektrosk.* **55**, 452 (1991).
12. A. N. Gruzintsev, Doctoral Dissertation (Chernogolovka, 1997).
13. A. N. Gruzintsev, *Mikroelektronika* **28**, 126 (1999).

14. A. N. Georgobiani, A. N. Gruzintsev, S. Sujun, and L. Zindong, *Neorg. Mater.* **35**, 1429 (1999).
15. *Physics of II–VI Compounds*, Ed. by A. N. Georgobiani and M. K. Sheinkman (Nauka, Moscow, 1986) [in Russian].
16. N. D. Borisenko, M. F. Bulanyĭ, F. F. Kodzhesperov, and B. A. Polezhaev, *Zh. Prikl. Spektrosk.* **52**, 36 (1990).
17. W. E. Howard, O. Sahni, and P. M. Alt, *J. Appl. Phys.* **53**, 639 (1982).
18. J. C. Hitt, P. D. Keir, J. F. Wager, and S. S. Sun, *J. Appl. Phys.* **83**, 1141 (1998).
19. N. T. Gurin, *Zh. Tekh. Fiz.* **66** (5), 77 (1996) [*Tech. Phys.* **41**, 448 (1996)].
20. P. D. Keir, C. Maddix, B. A. Baukov, *et al.*, *J. Appl. Phys.* **86**, 6810 (1999).
21. *Electroluminescent Sources of Light*, Ed. by I. K. Vereshchagin (Énergoatomizdat, Moscow, 1990) [in Russian].
22. N. T. Gurin and O. Yu. Sabitov, *Zh. Tekh. Fiz.* **69** (2), 64 (1999) [*Tech. Phys.* **44**, 184 (1999)].
23. S. Shin, P. D. Keir, J. F. Wager, and J. Viljanen, *J. Appl. Phys.* **78**, 5775 (1995).
24. A. Zeinert, C. Barthou, P. Benalloul, and J. Benoit, *Semicond. Sci. Technol.* **12**, 1479 (1997).
25. V. S. Vavilov, *Effects of Radiation on Semiconductors* (Fizmatgiz, Moscow, 1963; Consultants Bureau, New York, 1965).

*Translated by M. Lebedev*

---

OPTICS,  
QUANTUM ELECTRONICS

---

## Polarization Properties of Thick Anisotropic Diffraction Holograms Recorded with Infrared-Polymerizable Media

R. S. Akopyan, A. V. Galstyan, G. G. Zakharyan, and Yu. S. Chilingaryan

*Yerevan State University, ul. A. Manukyana 1, Yerevan, 375025 Armenia*

*e-mail: rhakob@www.physdep.r.am*

Received April 29, 2004

**Abstract**—The polarization properties of thick anisotropic holographic gratings are studied theoretically and experimentally. The dependences of the diffraction efficiency, ellipticity, and polarization orientation of the diffraction beam on the azimuth angle of polarization of an incident Bragg beam are derived. The experimental data are shown to agree well with the analytical calculations. It is found that the diffraction characteristics can be controlled in a wide range of incident polarization. © 2005 Pleiades Publishing, Inc.

### INTRODUCTION

The photopolymers that polymerize in the near-IR range are attracting much attention as promising media for high-density memory devices [1–9]. Unlike photographic films, photoresistors, gelatins, etc., photopolymers allow real-time observation of structure recording. Of special interest are the composites called polymer-dispersed liquid crystals (PDLCs) [10–13]. These media offer the mechanical properties of polymers and, at the same time, are anisotropic as liquid crystals (LCs). The anisotropy of LC molecules embedded in polymers makes it possible to control the properties of recorded structures with static electric fields, temperature variation, mechanical strains, etc., which change the orientation of LC molecules [13, 14]. Light diffraction by a volume phase grating based on multilayer or holographic materials has been carefully studied [15]. In particular, holographic polymer systems have been the subject of extensive investigation over a period of several decades [16–18], since they are candidates for various optical applications, such as optical recording [19], detection of acoustic waves [20], planar screens and screens of desired curvature [10, 21], tunable color filters for remote control [22], fiber-optic switchers [11], and lenses with controllable focal length [12]. These materials can also be used in designing optical computers, etc. Thus, diffraction gratings recorded on PDLCs are of both scientific and applied interest [13]. In the case of PDLCs, a hologram is recorded via polymerization (which is initiated in exposed regions) and molecular diffusion, as a result of which the refractive index is periodically modulated. These media offer post-exposure control of the diffraction efficiency and make it possible to fabricate electrically or optically controlled holographic multipliers, storage elements, and lenses with dynamically varying focal length.

To prepare holographic PDLCs, a homogeneous mixture of light-sensitive LC monomers is illuminated

by the interference pattern of two coherent waves. As the material polymerizes, the concentration of the monomers in the exposed regions decreases. When it reaches a dynamically equilibrium value, monomer molecules start diffusing from unexposed to exposed regions, displacing LC molecules from the latter. The LC molecules should be selected such that they mix up with the initial monomer solution but do not mix up with the polymer or with the partially polymerized solution, as a result of which phase separation between the LCs and monomer/polymer occurs. Eventually, a polymer matrix with periodic density modulation occurs where LC molecules are dispersed as 3D domains (drops) (the drops appear primarily in the unexposed regions) [14]. In a number of special cases, clearly separated submicrometer 2D areas of the polymer and LC are formed [7]. Since the orientation of LC molecules is extremely sensitive to hydrodynamic and diffusion fluxes, the LC director will be aligned largely with the wavevector of the final lattice. As was noted above, the LC concentration in the unexposed regions exceeds that in the exposed regions. Therefore, the LC and polymer are the major contributors to the effective refractive index in the unexposed and exposed regions, respectively. The efficiency of refractive index modulation, as well as the diffraction efficiency of PDLC gratings, is strongly dependent on the concentration [23] and shape of the LC drops, LC orientation within the drops, temperature, etc. Since PDLC materials are highly anisotropic, an understanding of the effect of LCs on the angular [24–26] and polarization dependences of the resulting systems is of great importance. The temperature behavior of PDLCs has also been given much attention. For example, the diffraction efficiency of PDLCs as a function of temperature at an LC concentration of 28% was studied in [23] and the temperature dependences of the diffracted and transmitted intensities for two polarizations of the incident beam were considered in [27]. The polarization properties,

however, are less well studied [27]: only the diffracted and transmitted intensities as functions of the angle between the linear polarization vector and the plane of incidence at 27°C were experimentally examined.

The aim of this work is to experimentally and theoretically study the polarization properties of PDLC gratings. Specifically, we will consider how the diffraction efficiency and the polarization of the diffracted wave depend on the azimuth angle of the linear polarization of the wave incident at the Bragg angle. Because of the presence of anisotropic LC molecules, the diffraction properties become strongly dependent on the azimuth angle. This offers possibilities of controlling the diffracted wave parameters.

In Section 1, we describe the computerized experimental setup used to study the materials which the PDLCs were made of. In Section 2, we report experimental data for the polarization properties and give detailed analysis of the results. Emphasis will be placed on the dependence of the diffraction efficiency on the azimuth angle of the incident beam polarization, as well as on the dependences of the ellipticity of the dif-

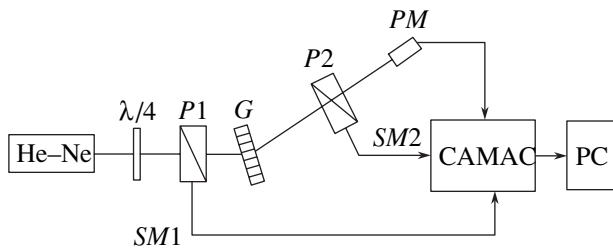


Fig. 1. Schematic of the computerized experimental setup.

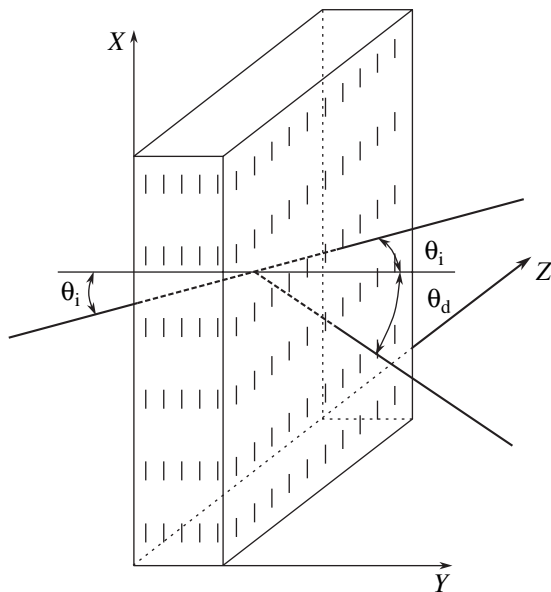


Fig. 2. Schematic of the diffraction grating and the distribution of the liquid crystal.

fracted wave and the orientation of its polarization ellipse on the same azimuth angle. In Section 3, we give a theoretical description of the system under study. The analytical dependence of the diffraction efficiency on the azimuth angle of polarization is derived in Section 3.1, and the state of polarization of the diffracted wave as a function of the azimuth angle of the linear polarization vector of the incident wave is studied in Section 3.2. In Section 4, we discuss the experimental and theoretical results and draw relevant conclusions.

## 1. EXPERIMENTAL SETUP

The setup used in the experiments is schematically shown in Fig. 1. A beam from a He-Ne laser with a wavelength of 628 nm that is initially linearly polarized at an angle of 45° relative to the plane of incidence (plane  $XY$  in Fig. 2) passes through a  $\lambda/4$ -plate, becoming circularly polarized. Then, the beam passes through polarizer  $P1$ , which is mounted on PC-controlled (CAMAC interface) step motor  $SM1$ . The minimal angle by which step motor  $SM1$  can rotate polarizer  $P1$  is 0.77°. Using this computerized system, one can preset a linear polarization of the incident beam. Next, the light strikes holographic grating  $G$  at the Bragg angle ( $\theta_B = 18.3^\circ$ ). The grating (Fig. 2) generates two, diffracted and transmitted, waves, which run symmetrically about the  $Y$  axis (both at the Bragg angle). The diffracted wave passes through polarizer  $P2$ , which is mounted on PC-controlled step motor  $SM2$  and rotates with the same step as  $P1$ . Then, the diffracted wave arrives at photomultiplier  $PM$ , which is connected to an analog-to-digital converter (ADC) via the CAMAC interface. Polarizer  $P2$  rotates from 0° to 90° in 4° increments (except for the first step, which is 2°). In the first experiment, polarizer  $P2$  is removed and photomultiplier  $PM$  records the diffracted beam intensity at each polarization of the incident beam. In the second experiment,  $P2$  rotates by 360° with a minimal step and the ADC converts the readings of  $PM$  at each polarization of the incident beam, recovering the state of polarization of the diffracted beam. If, for example, the dependence of the intensity striking the photomultiplier on the angle of polarizer  $P2$  has the form of an eight, the polarization is linear and the angle of polarization equals the slope of the eight. Thus, for each angle of incidence, we obtain the angle of polarization of the emergent (diffracted) beam. If the diffracted beam is elliptically polarized, this angle is the angle between the major semiaxis of the ellipse and the plane of incidence.

## 2. EXPERIMENTAL DATA

Figure 3 shows the experimental dependence (data points) of diffracted efficiency  $\eta$  on azimuth angle of polarization  $\alpha$  of the incident beam. The efficiency varies smoothly from  $\eta_p = 0.45$  (the azimuth angle of polarization is  $\alpha = 0$ ) to  $\eta_s = 0.14$  (the azimuth angle of

polarization is  $\alpha = 90^\circ$ ). It is seen from this figure that the efficiency changes more or less sharply when  $\alpha$  lies in the interval  $50^\circ$ – $60^\circ$ .

Figure 4 demonstrates the experimental dependence (data points) of angle of orientation of polarization ellipse  $\beta$  on azimuth angle of polarization of the incidence beam  $\alpha$ . The orientation of the polarization ellipse of the diffracted wave increases slowly from 0 to  $5^\circ$  as the azimuth angle of the incident wave varies from 0 to  $50^\circ$ . When  $\alpha$  reaches  $50^\circ$ – $60^\circ$ ,  $\beta$  sharply grows to  $85^\circ$  and then increases slowly to  $90^\circ$  when  $\alpha$  varies from  $60^\circ$  to  $90^\circ$ .

Figure 5 plots the experimental dependence (data points) of ellipticity  $\mu$  on azimuth angle of polarization of the incidence beam  $\alpha$ . The ellipticity of polarization of the diffracted beam grows nearly linearly from 0 to 0.96 when  $\alpha$  increases from  $0^\circ$  to roughly  $55^\circ$  and then drops (also nearly linearly) to 0.

Thus, in the interval  $\alpha = 0^\circ$ – $55^\circ$ , the orientation of the ellipse remains nearly independent of the orientation of linear polarization (being closer to  $p$  polarization): only ellipticity  $\mu$  increases. At  $\alpha = 55^\circ$ , the polarization of the diffracted wave is nearly circular. In the interval  $\alpha = 50^\circ$ – $60^\circ$ , the somewhat oblate circle of polarization sharply changes the orientation (roughly by  $80^\circ$ ). For  $\alpha = 60^\circ$ – $90^\circ$ , the ellipticity starts decreasing but the orientation remains almost unchanged (being closer to  $s$  polarization).

### 3. THEORETICAL CONSIDERATION

#### 3.1. Diffraction Efficiency Versus Polarization

Consider a thick anisotropic holographic direct transmission grating that is recorded on a PDLC. The thickness and period of the grating are  $d$  and  $\Lambda$ , respectively. Let the  $Y$  axis be directed along the normal to the grating surface and the  $X$  axis be aligned with the vector of the grating (Fig. 2). Light strikes the PDLC at angle  $\theta_i$  (outside the grating), the plane  $XY$  being the plane of incidence. It is assumed that the incident light with wavelength  $\lambda_0$  in free space and wavevector  $\mathbf{k}_0$  (the absolute value of the wavevector is  $k_0 = 2\pi/\lambda_0$ ) is monochromatic and linearly polarized. Let the electric field of the incident light wave be  $E_0$ . According to the approximation of slowly varying amplitudes in the theory of coupled waves [28–30], the outgoing (diffracted) wave is given by

$$E_{dp}(d) = -iE_{0ip} \frac{\chi_{dp} \sin \sqrt{v_p^2 + \xi_p^2}}{\chi_{ip} \sqrt{1 + \frac{\xi_p^2}{v_p^2}}} \exp[i\xi_p d], \quad (1)$$

$$E_{ds}(d) = -iE_{0is} \frac{\chi_{ds} \sin \sqrt{v_s^2 + \xi_s^2}}{\chi_{is} \sqrt{1 + \frac{\xi_s^2}{v_s^2}}} \exp[i\xi_s d]. \quad (2)$$

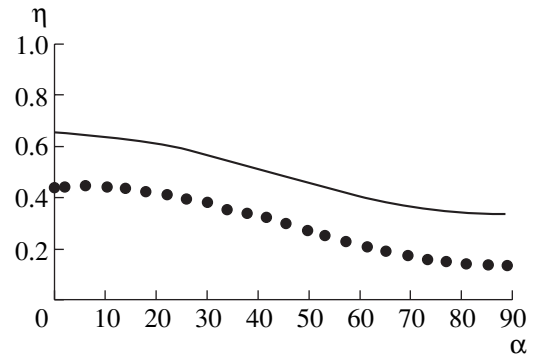


**Fig. 3.** Diffraction efficiency  $\eta$  vs. azimuth angle  $\alpha$  of incident linear polarization ( $d = 26.4 \mu\text{m}$ ,  $\Lambda = 1.0 \mu\text{m}$ ,  $\lambda = 628 \text{ nm}$ ,  $\epsilon_{\text{pol}} = 2.2535$ ,  $\epsilon_{\perp} = 2.3$ ,  $\epsilon_{\parallel} = 2.9474$ , and  $c = 0.35$ ).

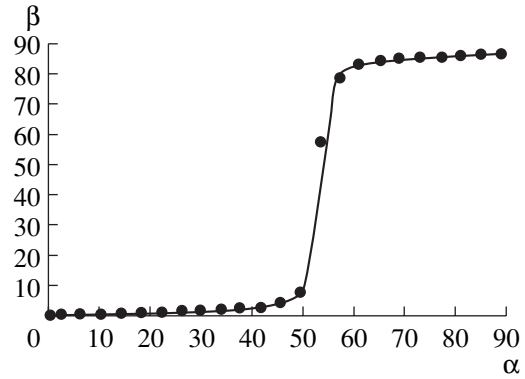


**Fig. 4.** Orientation  $\beta$  of diffracted beam polarization vs. angle  $\alpha$  of incident linear polarization. The parameters are the same as in Fig. 3.

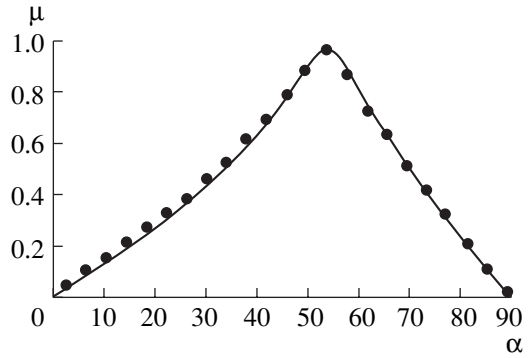


**Fig. 5.** Ellipticity  $\mu$  of polarization of the diffracted beam vs. angle  $\alpha$  of incident linear polarization. The parameters are the same as in Fig. 3.

Here,  $\chi_{ip, dp}$  and  $\chi_{is, ds}$  are the coupling coefficients for the incident and diffracted waves:

$$\chi_{ip, dp} = \frac{k_0 A_p}{4g_{ip, dp} n_{ip, dp} \cos \varphi_{ip, dp}} \quad \text{for the } p \text{ wave}, \quad (3)$$

$$\chi_{is, ds} = \frac{k_0 A_s}{4g_{is, ds} n_{is, ds} \cos \varphi_{is, ds}} \quad \text{for the } s \text{ wave}. \quad (4)$$

In (3) and (4),  $A_p$  and  $A_s$  describe the modulation of the  $p$  and  $s$  waves:

$$A_p = \varepsilon_{\perp}^1 \sin \varphi_{ip} \sin \varphi_{dp} - \varepsilon_{\parallel}^1 \cos \varphi_{ip} \cos \varphi_{dp} \quad (5)$$

for the  $p$  wave,

$$A_s = \varepsilon_{\perp}^1 \quad \text{for the } s \text{ wave,} \quad (6)$$

$$\varepsilon_{\perp, \parallel}^1 = (\varepsilon_{\perp, \parallel}^{\text{LC}} - \varepsilon_{\text{pol}})(c - a),$$

where  $\varepsilon_{\perp, \parallel}^{\text{LC}}$  are the normal and parallel components of the permittivity of the LC;  $\varepsilon_{\text{pol}}$  is the permittivity of the polymer;  $c$  is the volume concentration of the LC;  $a$  is the part of the LC concentration that is not modulated; and  $g_{ip, dp}$  and  $g_{is, ds}$  are the cosines of the angles between the wavevectors and Poynting vectors:

$$g_{ip, dp} = \frac{\varepsilon_{\parallel}^0 \sin^2(\theta_{ip, dp}) + \varepsilon_{\perp}^0 \cos^2(\theta_{ip, dp})}{\sqrt{(\varepsilon_{\parallel}^0)^2 \sin^2(\theta_{ip, dp}) + (\varepsilon_{\perp}^0)^2 \cos^2(\theta_{ip, dp})}} \quad (7)$$

for the  $p$  wave,

$$g_{is, ds} = 1 \quad \text{for the } s \text{ wave.} \quad (8)$$

In (3) and (4),  $n_{ip, dp}$  and  $n_{is, ds}$  are the mean refractive indices for the incident and diffracted beams, respectively:

$$n_{ip, dp}^2 = \frac{\varepsilon_{\perp}^0 \varepsilon_{\parallel}^0}{\varepsilon_{\parallel}^0 \cos^2(\theta_{ip, dp}) + \varepsilon_{\perp}^0 \sin^2(\theta_{ip, dp})} \quad (9)$$

for the  $p$  wave,

$$n_{is, ds}^2 = \varepsilon_{\perp}^0 \quad \text{for the } s \text{ wave.} \quad (10)$$

Hereafter,  $\theta_{ip, dp}$  and  $\theta_{is, ds}$  are the angles of incidence and diffraction inward to the sample for the  $p$  and  $s$  components, respectively;  $\varphi_{ip, dp}$  and  $\varphi_{is, ds}$  are the angles between the normal to the surface (the  $Y$  axis) and Poynting vector for the incident and diffracted beams, respectively:

$$\varphi_{ip, dp} = \theta_{ip, dp} + \arccos(g_{ip, dp}) \quad \text{for the } p \text{ wave,} \quad (11)$$

$$\varphi_{is, ds} = \theta_{is, ds} \quad \text{for the } s \text{ wave.} \quad (12)$$

In (1) and (2),

$$v_{p, s} = d \sqrt{\chi_{ip, is} \chi_{dp, ds}} \quad (13)$$

is the parameter that characterizes the depth of modulation and

$$\xi_{p, s} = \frac{d g_{dp, ds} \Delta_{p, s}}{4 k_0 n_{dp, ds} \cos \varphi_{dp, ds}} \quad (14)$$

is the detuning parameter that characterizes the offset from the Bragg condition. According to Kogelnik [28],

$$\Delta_{p, s} = \frac{k_{dp, ds}^2 - k_{ip, is}^2}{2 k_{ip, is}} \quad (15)$$

is the phase detuning from the Bragg condition. In (15),  $k_{ip, is} = k_0 n_{ip, is}$  and  $k_{dp, ds} = k_0 n_{dp, ds}$  are the wavenumbers of the transmitted and diffracted waves for the  $s$  and  $p$  components, respectively. Next, in (1) and (2),  $E_{0ip} = E_0 \cos \alpha$  and  $E_{0is} = E_0 \sin \alpha$  are the magnitudes of the  $s$  and  $p$  components of the incident beam, respectively, where  $\alpha$  is the azimuth angle of the linear polarization of the incident beam. The diffraction efficiency is given by [29]

$$\eta_{p, s} = \frac{E_{dp, ds}(d) E_{dp, ds}^*(d) n_{dp, ds} g_{dp, ds} \cos \varphi_{dp, ds}}{E_{ip, is}(0) E_{ip, is}^*(0) n_{ip, is} g_{ip, is} \cos \varphi_{ip, is}}. \quad (16)$$

In view of (1) and (2), expression (16) can be recast in the more convenient form

$$\eta_{p, s} = \frac{\sin^2 \sqrt{\xi_{p, s}^2 + v_{p, s}^2}}{1 + \xi_{p, s}^2 / v_{p, s}^2}. \quad (17)$$

Since the  $s$  and  $p$  components in a diffraction grating propagate without interacting with each other, the diffraction efficiency for any polarization of the incident beam can be expressed via the  $s$  and  $p$  components as follows:

$$\eta = \frac{\eta_s f_s \sin^2 \alpha + \eta_p f_p \cos^2 \alpha}{f}, \quad (18)$$

where  $f_s = n_{is} g_{is} \cos(\varphi_{is}) / n_{ds} g_{ds} \cos(\varphi_{ds})$ ,  $f_p = n_{ip} g_{ip} \cos(\varphi_{ip}) / n_{dp} g_{dp} \cos(\varphi_{dp})$ ,  $f = \cos(\theta_i) / \cos(\theta_d)$ , and  $\theta_i$  and  $\theta_d$  are the angles of the transmitted and diffracted waves outside the grating. For Bragg incidence, we have  $\theta_i = \theta_d = \theta_B$ .

Figure 3 shows the analytical dependence (continuous curve) of the diffraction efficiency on the azimuth angle of polarization of the incident beam in the case of Bragg incidence ( $\Delta = 0$ ). It is obvious that the diffraction efficiency for  $\alpha = 0$  ( $p$ -polarized wave) is greater than at  $\alpha = 90^\circ$  ( $s$ -polarized wave). It is seen that, in general, the theoretical curve fits well the data points but runs above the points. This is because absorption by the grating is neglected. Furthermore, the modulation of the refractive index is assumed to be sinusoidal, which also is an approximation. As a result, the experimental efficiency is somewhat lower than the theoretical value.

### 2.3. Variation of the State of Polarization

Let us consider the variation of the state of polarization in a thick anisotropic holographic grating. We assume that an incident wave is linearly polarized at azimuth angle  $\alpha$ . Our aim is to elucidate how the state of polarization (namely, the polarization orientation and ellipticity) of the diffracted wave depends on angle  $\alpha$ . In other words, our aim is to calculate the magnitudes of the  $s$  and  $p$  components of the diffracted wave at  $y = d$  and also the phase difference between these components because of the anisotropy of the grating. If

we decompose the linearly polarized wave with amplitude  $E_0$  into the  $p$  and  $s$  components, the electric field amplitudes of the diffracted and incident waves at  $y = 0$  are  $E_{0ip} = E_0 \cos \alpha$  and  $E_{0id} = 0$  for the  $p$  wave and  $E_{0is} = E_0 \sin \alpha$  and  $E_{0ds} = 0$  for the  $s$  wave. Hence, the  $p$  and  $s$  components of the outgoing (diffracted) wave can be described by formulas (1) and (2), respectively. For Bragg incidence,  $\Delta = 0$  or  $\xi = 0$ ; therefore, the  $p$  and  $s$  components of the diffracted wave can be written as

$$\begin{aligned} E_{dp} &= -iE_0 \sin v_p \cos \alpha, \\ E_{ds} &= -iE_0 \sin v_s \sin \alpha. \end{aligned} \quad (19)$$

If  $\alpha = 0$ , we have the  $p$  component alone (the  $s$  component is absent); if  $\alpha = 90^\circ$ , the  $p$  component disappears and we have only the  $s$  component. The total field of the diffracted light can be represented as

$$\begin{aligned} \mathbf{E}_d(d) &= \mathbf{E}_{ds} \exp(i(k_0 r_{ds} - \omega t)) \\ &+ \mathbf{E}_{dp} \exp(i(k_0 r_{dp} - \omega t)) \end{aligned} \quad (20)$$

or

$$\begin{aligned} \mathbf{E}_d(d) &= \mathbf{e}_{ds} R_{ds} \exp\left(i\left(k_0 r_{ds} - \omega t - \frac{\pi}{2}\right)\right) \\ &+ \mathbf{e}_{dp} R_{dp} \exp\left(i\left(k_0 r_{dp} - \omega t - \frac{\pi}{2}\right)\right), \end{aligned} \quad (21)$$

where  $\mathbf{e}_{ds}$  and  $\mathbf{e}_{dp}$  are the unit vectors in the directions of  $\mathbf{E}_{ds}$  and  $\mathbf{E}_{dp}$ , respectively, and

$$\begin{aligned} R_{ds} &= E_0 \sin v_s \sin \alpha, \\ R_{dp} &= E_0 \sin v_p \sin \alpha, \end{aligned} \quad (22)$$

are the diffraction wave amplitudes for the  $s$  and  $p$  components, respectively. In (20) and (21),  $r_{ds}$  and  $r_{dp}$  are the optical paths the  $s$  and  $p$  waves travel.

The phase difference between the  $s$  and  $p$  components of the diffracted wave has the form

$$\delta = k_0 r_{ds} - k_0 r_{dp}. \quad (23)$$

It follows from Fig. 6 that  $\delta$  can be calculated as follows. Since

$$r_{ds} = AC + n_{ds}AF, \quad r_{dp} = n_{dp}CF,$$

we have

$$AC = d(\tan \theta_{ds} - \tan \theta_{dp}) \sin \theta_i,$$

$$AF = \frac{d}{\cos \theta_{ds}}, \quad CF = \frac{d}{\cos \theta_{dp}}.$$

Eventually,

$$\begin{aligned} \delta &= \frac{2\pi}{\lambda} \left[ \frac{d}{\cos \theta_{ds}} n_{ds} + d(\tan \theta_{ds} - \tan \theta_{dp}) \sin \theta_i \right. \\ &\quad \left. - \frac{d}{\cos \theta_{dp}} n_{dp} \right]. \end{aligned} \quad (24)$$

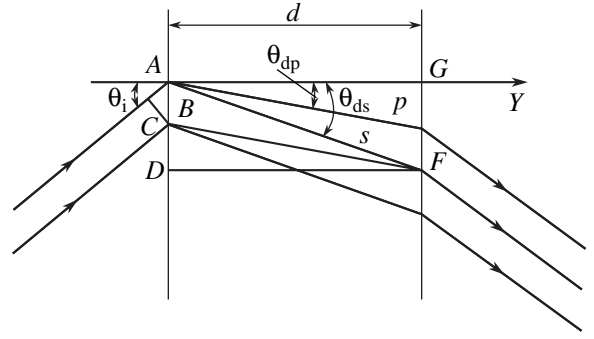


Fig. 6. On the calculation of the optical path difference for the  $s$  and  $p$  waves in the diffraction grating.

From (22) and (23), we can find the angle of elliptical polarization (i.e., the angle between the major semi-axis of the ellipse and the plane of incidence) for the diffracted beam [31]:

$$\beta = \frac{1}{2} \arctan\left(\frac{2R_{ds}R_{dp} \cos \delta}{R_{dp}^2 - R_{ds}^2}\right). \quad (25)$$

We define the ellipticity as the minor-to-major semi-axis ratio:  $\mu = R_{\min}/R_{\max}$ . Clearly, ellipticity  $\mu$  and angle of orientation  $\beta$  depend on the azimuth angle of polarization  $\alpha$  of the incidence beam. Figure 4 shows the analytical  $\alpha$  dependence on  $\beta$  (continuous curve) for grating parameters  $d = 26.4 \mu\text{m}$ ,  $\Lambda = 1.0 \mu\text{m}$ ,  $\lambda = 628 \text{ nm}$ ,  $\epsilon_{\text{pol}} = 2.2535$ ,  $\epsilon_{\perp} = 2.3$ ,  $\epsilon_{\parallel} = 2.9474$ , and  $c = 0.35$ . The analytical curve fits well the data points. In Fig. 5,  $\mu$  is plotted against  $\alpha$  for the same values of the parameters.

#### 4. CONCLUSIONS

In this work, we theoretically and experimentally studied the diffraction efficiency and state of polarization of the diffracted wave versus the azimuth angle of polarization of linearly polarized light that is incident at the Bragg angle on a thick anisotropic hologram. The detailed description of the setup used in the experiments is given. It turned out that one can control the diffraction efficiency of the anisotropic hologram within certain limits by varying the incident polarization. The orientation of the diffracted beam ellipse is found to be closer to  $0^\circ$  or  $90^\circ$  in most cases. A sharp change in the orientation from  $0^\circ$  to  $90^\circ$  is observed in a narrow range of the azimuth angle of incident polarization. In normal uniaxial crystals, a sharp change in the orientation of the ellipse takes place at  $45^\circ$ , with the ellipticity being maximal at this angle. In thick anisotropic diffraction gratings, this change somewhat lags (the angle of sudden change is roughly  $55^\circ$ ), since the diffraction efficiency for the  $p$ -polarized wave is higher than for the  $s$ -polarized wave in these materials (as follows from Fig. 3). As a result, the orientation is closer to  $p$  polarization. Hence, for the amplitudes of the diffracted  $p$



and  $s$  waves be the same, the angle of incident polarization must exceed  $45^\circ$ . Also, under this condition, the sharp change in the state of polarization will be observed at  $45^\circ$ . In thick anisotropic diffraction gratings, the ellipticity reaches a maximum near  $55^\circ$  for the same reason.

#### ACKNOWLEDGMENTS

The authors thank T. Galstian and S. Harbur (Laval University, Quebec, Canada) for submitting PDL-based near-infrared-sensitive diffraction gratings.

This work was partially supported by the CRDF (grant no. AP2-2302-YE-02).

#### REFERENCES

- P. Pilot, Y. Boiko, and T. V. Galstian, Proc. SPIE **3635**, 143 (1999).
- I. Banyasz, Opt. Commun. **181**, 215 (2000).
- P. Pilot and T. V. Galstian, in *Proceedings of the International Conference on Applications of Photonic Technology ICAPT-2000, Quebec, 2000*; Proc. SPIE **4087**, 1302 (2000).
- F. Bouguin and T. V. Galstian, Proc. SPIE **4342**, 492 (2001).
- T. Galstian and A. Tork, US Patent No. 6.398.981 (June 4, 2002).
- P. Nagtegaale and T. V. Galstian, Synthetic Metals **127**, 85 (2002).
- R. Caputo, A. V. Sukhov, Ch. Umeton, and R. F. Ushakov, Zh. Éksp. Teor. Fiz. **118**, 1374 (2000) [JETP **91**, 1190 (2000)].
- Yu. N. Denisyuk, N. M. Ganzhermi, and D. F. Chernykh, Pis'ma Zh. Tekh. Fiz. **26** (9), 25 (2000) [Tech. Phys. Lett. **26**, 369 (2000)].
- N. M. Ganzherli, Yu. N. Denisyuk, S. P. Konop, and I. A. Maurer, Pis'ma Zh. Tekh. Fiz. **26** (16), 22 (2000) [Tech. Phys. Lett. **26**, 707 (2000)].
- J. Qi, M. DeSarkar, G. T. Warren, *et al.*, J. Appl. Phys. **91**, 4795 (2002).
- L. H. Domash, Y. M. Chen, C. Gozewski, *et al.*, Proc. SPIE **3010**, 214 (1997).
- L. H. Domash, Y. M. Chen, C. Gozewski, *et al.*, Proc. SPIE **2689**, 188 (1996).
- T. J. Bunning, L. V. Natarajan, V. P. Tondiglia, *et al.*, Annu. Rev. Mater. Sci. **30**, 83 (2000).
- R. L. Sutherland, L. V. Natarajan, V. P. Tondiglia, *et al.*, Chem. Mater. **5**, 1533 (1993).
- P. Yeh, *Optical Waves in Layered Media* (Wiley, New York, 1988).
- N. Noiret, C. Meyer, D. J. Lougnot, *et al.*, Pure Appl. Opt. **3**, 55 (1994).
- G. Zhao and P. Mouroulis, J. Mod. Opt. **41**, 1929 (1994).
- J. T. Sheridan and J. R. Lawrence, J. Opt. Soc. Am. A **17**, 1108 (2000).
- H. Lee, X. Gu, and D. Psaltis, J. Appl. Phys. **65**, 2191 (1998).
- D. A. Larson, T. D. Black, M. Green, *et al.*, J. Opt. Soc. Am. A **7**, 1745 (1990).
- M. J. Escuti, J. Qi, and G. P. Crawford, Opt. Lett. **28**, 522 (2003).
- K. Fontecchio, C. C. Bowley, and G. P. Crawford, Proc. SPIE **3800**, 36 (1999).
- Y. Liu, B. Zhang, Y. Jia, *et al.*, Opt. Commun. **218**, 27 (2003).
- J. J. Butler, M. A. Rodriguez, M. S. Malcuit, *et al.*, Opt. Commun. **155**, 23 (1998).
- R. I. Sutherland, V. P. Tondiglia, L. V. Natarajan, *et al.*, Appl. Phys. Lett. **79**, 1420 (2001).
- P. Pilot, Y. B. Boiko, and T. V. Galstian, Proc. SPIE **3638**, 26 (1999).
- A. Y.-G. Fuh, C.-R. Lee, and Y.-H. Ho, Appl. Opt. **41**, 4585 (2002).
- H. Kogelnik, Bell Syst. Tech. J. **48**, 2909 (1969).
- G. Montemezzani and M. Zgonik, Phys. Rev. E **55**, 1035 (1997).
- T. V. Galstian, R. S. Akopyan, A. V. Galstyan, *et al.*, J. Opt. Soc. Am. B (in press).
- C. C. Davis, *Lasers and Electro-Optics: Fundamentals and Engineering* (Cambridge Univ. Press, Cambridge, 1996).

*Translated by V. Isaakyan*

## OPTICS, QUANTUM ELECTRONICS

# Excitation of Raman Optical Processes in an Ultradispersed Medium by Radiation from a Pulsed–Periodic Laser

V. S. Gorelik and I. A. Rakhmatullaev

Lebedev Physics Institute, Russian Academy of Sciences,  
Leninskii pr. 53, Moscow, 119991 Russia  
e-mail: gorelik@sci.lebedev.ru

Received March 30, 2004

**Abstract**—A new method of taking Raman and two-photon-excited luminescence spectra in an ultradispersed medium is proposed. In this method, optical fibers serve to introduce an exciting radiation into and extract the secondary radiation from an ultradispersed medium placed in a cavity-type metallic cell. The spectra are initiated with a pulsed–periodic light source (copper vapor laser) and are recorded using a gating system. The contrast of the secondary radiation spectra is high with respect to the exciting radiation, allowing for molecular analysis of ultradispersed media by means of a single small-size monochromator. © 2005 Pleiades Publishing, Inc.

### INTRODUCTION

Ultradispersed media are being widely used in the production of pharmaceutical preparations, chemicals, food, perfumes, etc. Molecular analysis of the constituents and structure of such media is therefore of great importance. A promising approach in this field is the analysis of relevant Raman spectra and their nonlinear analogues using advanced lasers as exciting radiation sources.

Note that, for many materials, the effective cross section of spontaneous Raman scattering (RS) is extremely low ( $\sim 10^{-28}$  cm<sup>2</sup>). Therefore, for Raman spectra to be reliably detected, the power density of the exciting radiation must be relatively high. Still higher intensities of the light sources are needed for the analysis of the nonlinear analogues of spontaneous RS: hyper-Raman scattering (HRS) and two-photon-excited luminescence (TPEL) [1–5].

Pulsed–periodic metal vapor lasers (in particular, a copper vapor laser) proved to be effective light sources when used in experiments on detecting spontaneous RS and its nonlinear analogues [5].

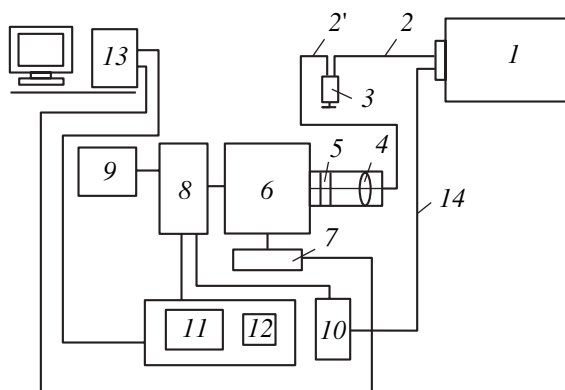
The Raman spectra of condensed media are routinely detected by focusing laser radiation inside the medium. At a high radiation intensity, this leads to a number of adverse effects that alter the initial parameters of the medium, such as photodestruction, local heating, and photoinduced phase transformations.

In this work, we propose a new method of exciting Raman optical processes in ultradispersed media. In this method, a silica fiber applies an exciting radiation to a scattering medium placed inside a cavity-type metallic cell and other fibers extract the secondary radiation from the cell.

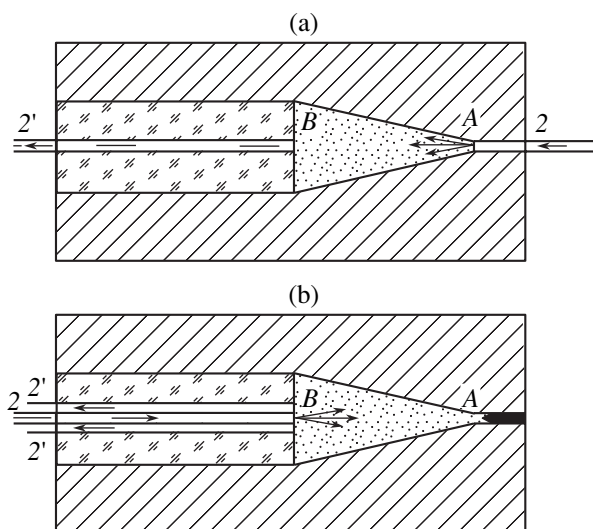
### EXPERIMENTAL

Figure 1 demonstrates the schematic of the experimental setup. It consists of copper vapor laser 1 generating short pulses (20 ns) with a repetition rate of 16 kHz in the visible range ( $\lambda = 510.6$  and 578.2 nm). A color filter selects one of the laser lines ( $\lambda = 510.6$  nm) with a mean power of 0.5 W. Optical fiber 2 applies the laser radiation to cell 3 with the sample. The design of the cells used is shown in Fig. 2.

Figure 2a demonstrates the cell used in the transmission experiments. The exciting radiation is introduced into the conic cavity that is cut out in an aluminum cylinder. Silica fiber 2, applying the exciting radiation,



**Fig. 1.** Schematic of the experimental setup for studying secondary radiation from the interior of condensed media excited with a pulsed–periodic laser. (1) Laser, (2) and (2') optical fibers, (3) cell with sample, (4) lens, (5) color filter, (6) monochromator, (7) monochromator-controlling unit, (8) PMT, (9) power supply of PMT, (10) gate pulse shaper, (11) amplifier, (12) delay line, (13) computer, and (14) optical fiber.



**Fig. 2.** Design of the (a) transmission and (b) reflection cells with cone-shaped cavities. (2, 2') Optical fibers delivering the laser radiation to the cell and extracting the secondary radiation from the cell, respectively.

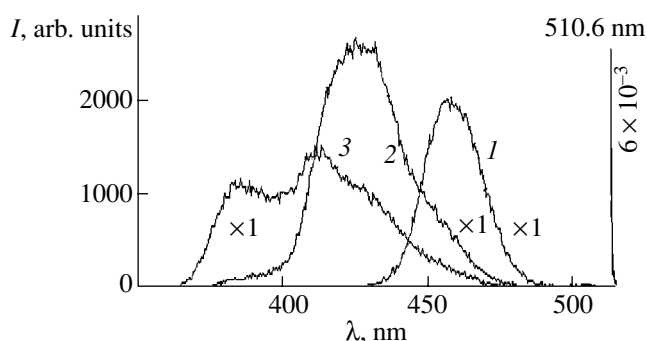


**Fig. 3.** TPEL spectra of (1) POPOP, (2) PPO, and (3) stilbene taken in the reflection mode in the cell coupled with the fiber. The PMT voltage is 1600 V.

ends up at point A near the vertex of the cone. The sample, an ultradispersed polycrystalline medium, is placed into the conic cavity. Owing to multiple scattering events in the cavity, the intensity of the Raman optical processes turns out to be much higher than in the no-cavity scheme. The metal (aluminum) surface with a high thermal conductivity provides effective heat removal from the area where the exciting radiation is the most intense. At point B, the secondary radiation enters fiber 2', which guides it to the entrance slit of MSD-2 monochromator 6 through collecting lens 4 (Fig. 1).

Figure 2b shows the cell used in the reflection experiments. In this case, a metallic plug is placed near point A (the vertex of the cone). The laser radiation is delivered using fiber 2 coaxial with the cell. The secondary radiation is extracted from the cell with off-axis fibers 2'. PS-11 or OS-11 absorption color filters 5 (Fig. 1) are

placed in front of the entrance slit of the monochromator for exciting light rejection. After passing through the exit slit of the monochromator, the signal is detected using FEU-106 photoelectric multiplier tube (PMT) 8. Power supply 9 of the PMT generates a stabilized voltage ( $U = 2$  kV) needed for the amplification of electric pulses due to Raman and luminescence photons arriving at the photocathode of the PMT. The signal from the PMT is amplified further by amplifier 11. The amplifier is time-gated using gate pulse shaper 10 and delay line 12. A reference light pulse is applied to pulse shaper 10 through optical fiber 14, and the pulse shaper generates a 20-ns-wide gating pulse, which can be delayed relative to the exciting (laser) pulse by 0–100 ns with delay line 12. This gating pulse is used to activate the amplifier. Control unit 7 accomplishes discrete spectral scanning with a given step and accumulation time at each point. Computer 13 obtains digital data on the secondary radiation spectrum and controls the step motor of the MSD-2 monochromator, which turns the diffraction grating of the monochromator at regular intervals.

The detection system with gating enables one to detect secondary radiation signals with a high (up to  $10^{-15}$  W) sensitivity. Using the delay line with time gating makes it possible to analyze the spectra of “fast” and “slow” processes in the time interval 0–100 ns.

We experimented with the following ultradispersed organic substances: (i)  $C_{24}H_{16}O_2$  (POPOP), (ii)  $(C_6H_5CH)_2$  (stilbene), and (iii)  $C_{15}H_{11}NO$  (PPO).

The experiments were performed at room temperature.

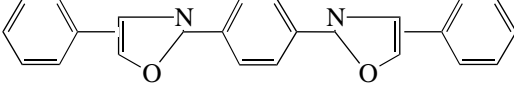
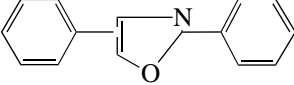
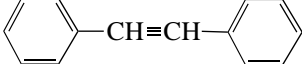
## RESULTS

Figure 3 shows the TPEL spectra of POPOP, PPO, and stilbene (curves 1–3, respectively) that were taken in the reflection mode. In this case, the PS-11 color filter placed in front of the entrance slit of the monochromator suppresses the exciting radiation with a wavelength of 510.6 nm and transmits the near-UV and blue radiation. It is seen that the TPEL spectrum of POPOP represents a relatively narrow band in the visible range (430–500 nm) with  $\lambda_{max} = 460$  nm. The TPEL spectrum of PPO is shifted toward shorter wavelengths (380–480 nm) and peaks at  $\lambda_{max} = 425$  nm. The TPEL spectrum of stilbene exhibits two peaks ( $\lambda = 385$  and 415 nm) and occupies the spectral range 370–480 nm (Fig. 3).

Figure 4a demonstrates the Raman spectra of PPO and stilbene (curves 1 and 2, respectively) taken in the reflection mode. Here, the OS-11 color filter was placed in front of the entrance slit of the monochromator. The Raman spectrum of PPO exhibits several peaks, the most intense one being at  $1553$   $cm^{-1}$ . The Raman spectrum of stilbene also contains several peaks, the most intense one being at  $1593$   $cm^{-1}$ .

Figure 4b shows the Raman spectrum of POPOP taken in the reflection mode (curve 1) with the OS-11

Comparative characteristics of the Raman and TPEL spectra for the aromatic compounds

Substance	$\nu$ , $\text{cm}^{-1}$	$K_S$	$\lambda$ , nm	$K_L$	Structural formula
POPOP	1550	0.38	460	0.09	
PPO	1553	0.31	425	0.16	
Stilbene	1593	0.28	415	0.08	

Note:  $K_S = I_S/I_0$  is the effective primary radiation-to-RS conversion coefficient;  $K_L = I_L/I_0$  is the effective primary radiation-to-TPEL conversion coefficient; and  $I_0$ ,  $I_S$ , and  $I_L$  are the maxima of the primary radiation, RS, and TPEL intensities.

color filter placed before the entrance slit of the monochromator. The Raman spectrum of stilbene (curve 2) is shown for comparison. Among the substances under study, POPOP exhibits the highest Raman signal (see table).

Figure 5 compares the Raman spectra of POPOP that were taken in the transmission mode with delays of 0.25 and 50 ns. In this case, the filters in front of the entrance slit of the monochromator were absent, since the intensity of the exciting radiation exceeds the Raman signal intensity only slightly. The intensity of the continuous background decreases abruptly with

increasing delay time, whereas the Raman spectrum is observed even at long delays (50 ns).

A number of the characteristics of the Raman and TPEL spectra are listed in the table.

## DISCUSSION

In the case of two-photon absorption of light coming from a single source, the exponential law of intensity decay,  $I(x) = I_0 \exp(-k_1 x)$ , is changed to the hyperbolic dependence [6]

$$I_x = I_0 / (1 + k_2 x),$$

where  $\beta I_0 = k_2$  is the two-photon absorption coefficient,  $\beta$  is the two-photon absorption constant (whose dimension in the SI system is  $\text{m}^2/\text{W}$ ).

In this work, the diameter of the fibers was  $100 \mu\text{m}$  and the power of laser pulses, on the order of  $10^4 \text{ W}$ . Thus, the radiation intensity at the fiber exit was  $I_0 = 10^8 \text{ W}/\text{cm}^2$ . For such an intensity and  $\beta = 5 \times 10^{-11} \text{ m}^2/\text{W}$  (this value is typical of molecular media [7]), we have  $k_2 = 50 \text{ m}^{-1} = 0.5 \text{ cm}^{-1}$ . Hence, for the

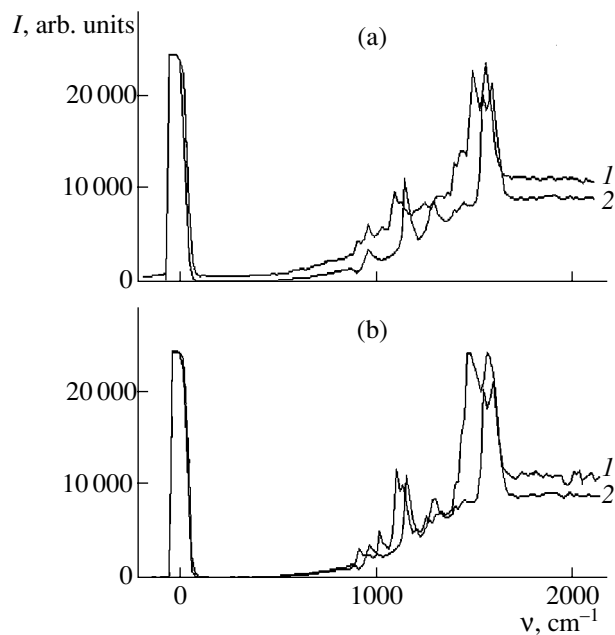


**Fig. 4.** (a) Raman spectra of (1) PPO and (2) stilbene measured in the reflection mode. (b) Raman spectra of (1) POPOP and (2) stilbene taken in the reflection mode (the latter is shown for comparison). The PMT voltage is 1600 V.

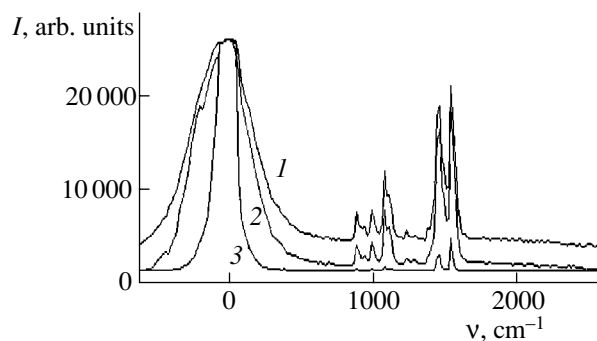


**Fig. 5.** Raman spectra of POPOP taken in the transmission mode for delay times of (1) 0, (2) 25, and (3) 50 ns. The PMT voltage is 1600 V.

given excitation parameters, an intense TPEL signal may be expected to arise in a cell  $\approx 1$  cm long.

The TPEL spectra observed can be viewed as a result of the two-photon excitation of electronic states followed by the transition of a molecule to the vibrational sublevels of the ground ( $S_0$ ) state. The short-wave edge of these spectra corresponds to the  $\pi^*-\pi$  electronic transition in a benzene ring. The long-wave edge of the TPEL spectrum may be assigned to the vibrational sublevels of the molecular ground state.

### CONCLUSIONS

We developed a method of fiber-optic excitation of Raman processes in condensed media and took Raman and TPEL spectra from aromatic substances (PPO, POPOP, and stilbene). Laser heating of the samples is insignificant, which allows for multiple nondestructive measurements. The secondary radiation from the samples is sufficiently high owing to a cavity-type metallic cell used in the experiments. In particular, the effective exciting radiation-to-RS conversion coefficients,  $K_S$ , were found to be 0.38, 0.31, and 0.28 for POPOP, PPO, and stilbene, respectively. The effective exciting radiation-to-TPEL conversion coefficients,  $K_L$ , were 0.09, 0.16, and 0.08 for POPOP, PPO, and stilbene, respectively.

Thus, our method makes it possible to nondestructively detect secondary radiation signals from the inte-

rior of ultradispersed media with a high contrast with respect to the primary (exciting) radiation.

### ACKNOWLEDGMENTS

This work was supported by the Russian Foundation for Basic Research (grant no. 02-02-16221).

### REFERENCES

1. A. M. Agal'tsov, V. S. Gorelik, and M. M. Sushchinskiĭ, *Opt. Spektrosk.* **58**, 386 (1985) [*Opt. Spectrosc.* **58**, 230 (1985)].
2. A. M. Agaltzov and V. S. Gorelik, *J. Russ. Laser Res.* **17**, 431 (1996).
3. V. A. Babenko, V. S. Gorelik, and A. A. Sychev, *J. Russ. Laser Res.* **20**, 152 (1999).
4. V. S. Gorelik, *Izv. Ross. Akad. Nauk, Ser. Fiz.* **64**, 1181 (2000).
5. A. M. Agal'tsov, V. S. Gorelik, and I. A. Rakhmatullaev, *Opt. Spektrosk.* **79**, 959 (1995) [*Opt. Spectrosc.* **79**, 878 (1995)].
6. V. I. Bredikhin, M. D. Galanin, and V. N. Genkin, *Usp. Fiz. Nauk* **110**, 3 (1973) [*Sov. Phys. Usp.* **16**, 299 (1973)].
7. V. S. Gorelik, A. D. Kudryavtseva, A. I. Sokolovskaya, and N. V. Chernega, *Opt. Spektrosk.* **81**, 409 (1996) [*Opt. Spectrosc.* **81**, 369 (1996)].

*Translated by A. Chikishev*

OPTICS,  
QUANTUM ELECTRONICS

## On-Axis Diffuse Directional Screen Based on a Transmission Gabor Hologram

Yu. N. Denisjuk and N. M. Ganzherli

*Ioffe Physicotechnical Institute, Russian Academy of Sciences,  
Politekhnicheskaya ul. 26, St. Petersburg, 194021 Russia  
e-mail: nina@holo.ioffe.rssi.ru*

Received May 27, 2004

**Abstract**—Holographic single-component diffuse screens based on on-axis transmission holograms are studied theoretically and experimentally. The configurations of extra holographically reconstructed images of the diffuse screen (conjugate image, halo, and zeroth-order spot) are analyzed. A so-called centered hologram is suggested in which the conjugate image of the diffuse screen spatially coincides with the main image, thereby eliminating distortions inserted by the conjugate image. Also, hologram recording using a Mach–Zender interferometer is suggested and implemented. Such an approach makes it possible to eliminate the shadow of an object on the hologram. It is noted that, in recording a planar diffuse screen, the presence of the halo does not distort the image of an object projected through the screen: only the light intensity is partially lost. Analysis of the images projected shows that the luminance of the zeroth-order spot, while relatively low, should be diminished in one way or another. © 2005 Pleiades Publishing, Inc.

### INTRODUCTION

The on-axis hologram suggested by Gabor in 1948 [1, 2] is historically the very first type of hologram. Essentially, this hologram is a variety of thin hologram, which is known to reconstruct not only the main image but also extra images of an object. Unlike the case of the off-axis hologram [3], where all these images are spatially separated, here the additional images are superimposed on the main one, causing its considerable distortion. At the same time, the on-axis hologram offers a number of significant advantages. Specifically, it is well compatible with optical systems, most of which are axisymmetric. In the case considered, where an on-axis hologram is used to project the image through a screen, the axial projection scheme does not introduce distortions of the image projected that arise when projecting beams are inclined to the screen. One of the few ways of creating an on-axis holographic screen is based on using an on-axis hologram.

### RECORDING AND RECONSTRUCTION OF AN ON-AXIS HOLOGRAM

The scheme for recording and reconstructing an on-axis hologram is shown in Fig. 1. The radiation from reference source  $R$  illuminates object  $O$ , which scatters this radiation and forms objective wave  $W_O$ . Reference wave  $W_R$  is formed by the radiation from source  $R$ , which falls on a photographic plate, bypassing the object. After development, photographic plate  $Ph$ , which records the interference pattern, becomes hologram  $H$ .

At the stage of reconstruction, hologram  $H$  is exposed to wave  $W_R$  from reference source  $R$ . Interfering with this wave, the hologram generates four waves  $W'_O$ ,  $W'_R$ ,  $W_O^*$ , and  $W_{HL}$ . Wave  $W'_O$  is an extension of wave  $W_O$ , which is scattered by object  $O$ . Perceiving this wave, the observer sees the three-dimensional image of object  $O$ . Wave  $W'_R$  is an extension of wave  $W_R$ , which is emitted by reference (illuminating) source  $R$ . Wave  $W_O^*$  is the so-called conjugate image of object  $O^*$ . Gabor showed that the position of the conjugate image can be found by merely reflecting object  $O$  in reference wave  $W_R$  as in a mirror [2]. Wave  $W_{HL}$  forms halo  $HL$  of the light scattered.

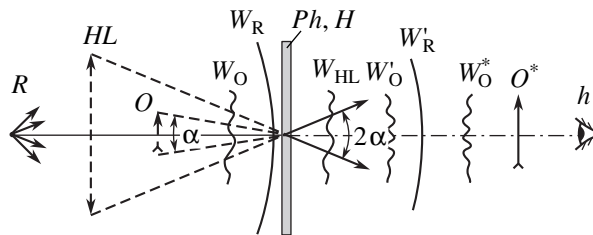


**Fig. 1.** Scheme for recording and reconstruction of an on-axis hologram.  $R$ , point reference source;  $O$ , object;  $W_O$ , wave scattered by object;  $W_R$ , wave from reference source  $R$ ;  $Ph$ , photographic plate (or hologram  $H$  after development);  $W'_O$ , object wave reconstructed;  $W'_R$ , reference wave reconstructed;  $W_O^*$ , wave conjugate to object wave  $W_O$ ;  $O^*$ , conjugate image of object  $O$ ; and  $h$ , observer's eye.

Figure 1 clearly demonstrates the major disadvantage of the on-axis hologram: when viewed from point  $h$ , the reconstructed image of object  $O$  appears considerably distorted, since this image is superimposed on the point image of source  $R$ , conjugate image  $O^*$  of the object, and halo  $HL$ .

### THEORY OF THE THIN (INCLUDING ON-AXIS) HOLOGRAM [1]

The electric fields of the object and reference waves ( $E_O$  and  $E_R$ , respectively) can be written as

$$E_O = A_O(r) \exp i \varphi_O(r), \quad (1)$$

$$E_R = A_R \exp i \varphi_R(r). \quad (2)$$

In (2), it is taken into account that amplitude  $A_R$  of the reference wave is coordinate-independent. Total electric field  $E_t$  acting on the photographic plate is the sum of  $E_O$  and  $E_R$ :

$$E_t(r) = A_O(r) \exp i \varphi_O(r) + A_R(r) \exp i \varphi_R(r). \quad (3)$$

The distribution of intensity  $J_t$  corresponding to field  $E_t$  can be found by multiplying  $E_t$  by its conjugate value:

$$J_t(r) = E_t E_t^* = A_O^2(r) + A_O(r) A_R \exp i [\varphi_R(r) - \varphi_O(r)] + A_O(r) A_R \exp i [\varphi_O(r) - \varphi_R(r)] + A_R^2. \quad (4)$$

Let us assume that, at the stage of development, photographic plate  $Ph$  is subjected to chemical treatment such that its amplitude transmission coefficient  $\tau_H$  is proportional to the intensity of the radiation incident on the plate. In this case, we may write

$$\tau_H \sim \sqrt{T} \sim J_t, \quad (5)$$

where  $T$  is the intensity transmission coefficient.

Relationship (5) implies that the development is positive; that is, the most exposed areas of photographic plate  $Ph$  become the most transparent areas of the hologram developed.

Substituting  $J_t$  from (5) into (4) yields distribution  $\tau_H(r)$  of the amplitude transmission coefficient over the surface of the hologram:

$$\tau_H(r) = A_O^2(r) + A_O(r) A_R \exp i [\varphi_R(r) - \varphi_O(r)] + A_O(r) A_R \exp i [\varphi_O(r) - \varphi_R(r)] + A_R^2. \quad (6)$$

Now we turn to the discussion of the reconstruction process. Assume that the hologram is illuminated by wave  $E_R$  emitted from reference source  $R$  (see expression (2)). The value of electric field  $E_H$  is found by mul-

tiplying  $\tau_H$  (see expression (6)) by  $E_R$ :

$$E_H(r) = A_O^2(r) A_R \exp i \varphi_R(r) + A_O(r) A_R^2 \exp i [2\varphi_R(r) - \varphi_O(r)] + A_O(r) A_R^2 \exp i \varphi_O(r) + A_R^3 \exp i \varphi_R. \quad (7)$$

Since amplitude  $A_R$  of the reference wave is a constant value, it is easy to check that the third term in expression (7) describes wave  $E_O$ , which is reconstructed by the hologram (see expression (1)) and forms the reconstructed image of object  $O$  (Fig. 1).

The fourth term in (7) describes a wave that is identical to reference wave  $E_R$  (expression (2)). This wave forms the image of point source  $R$  (Fig. 1).

The third term in expression (7) corresponds to conjugate image  $O^*$  of the object. As was noted above, the position of this image can be defined by reflecting object  $O$  in reference wave  $W_R$  as in a mirror. The minus sign before phase  $\varphi$  of this term means that conjugate image  $O^*$  is pseudoscopic.

The first term in (7) describes halo  $HL$  of the radiation from the reference source. The halo was scattered by the structure arising as a result of interference between light rays coming from different points of object  $O$  in the course of hologram recording. If the angular size of the object is  $\alpha$ , the halo-producing radiation propagates within angle  $\alpha$  (Fig. 1).

### EXPERIMENT ON RECORDING A SCREEN BUILT AROUND AN ON-AXIS HOLOGRAM

Figure 2 shows the scheme used to record an on-axis holographic screen based on an on-axis transmission hologram. Unlike the early Gabor's scheme, the reference wave bypasses the object. Thus, the shadow of the object is absent on the hologram. The scheme uses a Mach-Zender interferometer, which generates two (object and reference) coaxial beams incident on the hologram.

A laser beam passing through microscopic objective  $MO$  and pinhole  $PH$  is focused into a point. A wave originating at this point is split by beam splitter  $BS_1$  into the object and reference components (branches). Lens  $L_1$  mounted in the path of the object branch forms a plane wave, which is directed toward diffuser  $D$  (clouded glass) by means of mirror  $M_1$ . Beam splitter  $BS_2$  transmits the radiation scattered by the diffuser to a photographic plate to record hologram  $H$ . The spherical wave in the reference branch is directed to lens  $L_2$  by means of mirror  $M_2$  and, having passed through beam splitter  $BS_2$  and the photographic plate with hologram  $H$ , converges into point  $R^*$ .

As a radiation source, we used a He-Ne laser ( $\lambda = 628$  nm) of output 30 mW. The holograms were recorded on PFG-03M domestic high-resolution photographic plates made by the Slavich plant. The plates

exposed were developed in a GP-3 developer, which is recommended by the plate maker.

The image projection scheme using an on-axis holographic screen thus recorded is shown in Fig. 3. Here, lens  $L$ , which projects image  $I$  onto screen  $H$  is centered at point  $R^*$ , into which the spherical reference wave converged in hologram recording. According to the recording scheme depicted in Fig. 2, the hologram illuminated in this way reconstructs the image of diffuser  $D$ , which serves as visibility zone  $VZ$ , through which image  $I$  projected onto the screen can be observed. Along with diffuser  $D$ , hologram  $H$  reconstructs the imaginary conjugate image  $D^*$  of the screen and an imaginary image of halo  $HL$ .

During recording the on-axis hologram, no special efforts to suppress the halo, conjugate image, and zeroth-order spot were made. In spite of this, the image projected onto the holographic screen was virtually distortionless, except for the image of the hologram-reconstructing point source at the center of the screen. This image is somewhat diffuse, since point source  $R^*$  is at a relatively long distance from screen  $H$ , while the system recording the image on the screen is focused on the screen's plane.

Rays  $I_D^*$  and  $I_{HL}$  reconstructed by the on-axis hologram, which forms conjugate image  $D^*$  of the diffuser and the image of halo  $HL$ , are virtually equivalent to the rays that form the image of diffuser  $D$  and thereby do not introduce distortions into the image projected on screen  $H$ . The adverse effect of the rays of halo  $HL$  and conjugate image  $D^*$  lies in the fact that most of them pass outside visibility zone  $VZ$  (scattered light), decreasing the energy efficiency of the projector. The zeroth-order spot falls into the field of view of the observer as a bright spot and should be eliminated in one way or another.

### ON-AXIS HOLOGRAPHIC SCREEN BASED ON A THIN CENTERED HOLOGRAM

The bright zeroth-order spot, which appears in the field of view of the one who observes the scene projected onto the screen, is the only considerable disadvantage of a thin hologram. It is also important that, when the observer looks through visibility zone  $VZ$ , conjugate image  $D^*$  of the diffuser serves as a window that makes image  $I$  of the scene brighter, causing the nonuniform illumination of the field of view. Unfortunately, the conjugate image, unlike the halo and zeroth-order spot, cannot be eliminated by phase modulation of the on-axis hologram structure.

The only way of suppressing the effect of the conjugate image consists in shifting its position in such a way that it does not influence the intensity distribution in field of view  $h$  of the observer (Fig. 1). The position of the conjugate image can be determined using the Gabor's rule, which follows from the second term in (7). Analyzing the positions of conjugate image  $D^*$  of

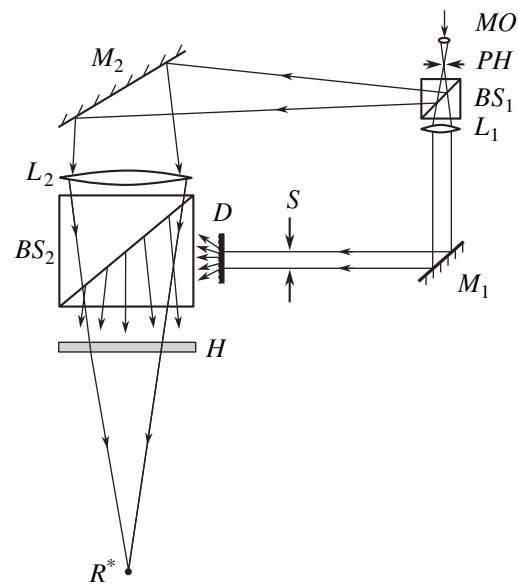


**Fig. 2.** Scheme for recording a screen based on an on-axis transmission hologram.  $MO$ , microscopic objective;  $PH$ , pinhole;  $BS_1$  and  $BS_2$ , beam splitters;  $L_1$  and  $L_2$ , lenses;  $M_1$  and  $M_2$ , mirrors;  $D$ , diffuser (clouded mirror);  $H$ , hologram;  $S$ , diaphragm; and  $R^*$ , point of convergence of the reference wave.

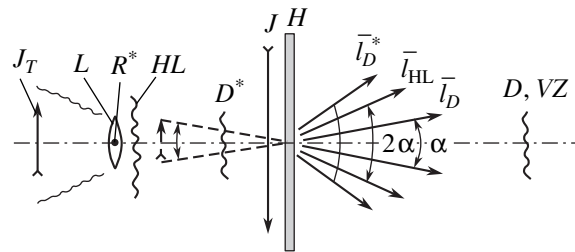


**Fig. 3.** Scheme for image projection with an on-axis holographic screen.  $I_{HL}$ ,  $I_D$ , and  $I_D^*$  are the rays forming the image of halo  $HL$ , diffuser  $D$ , and conjugate image  $D^*$  of the diffuser;  $VZ$ , visibility zone;  $R^*$ , point of convergence of the spherical reference wave during recording of the hologram;  $J$ , image of transparency  $J_T$  projected onto screen  $H$  using lens  $L$  placed at point  $R^*$ .

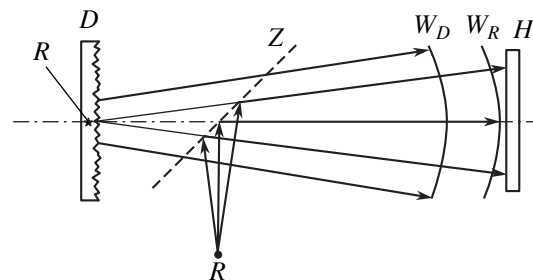


**Fig. 4.** Scheme for recording a centered on-axis hologram.  $D$ , diffuser (object);  $R$ , reference source whose image is transferred to the center of the diffuser by means of semi-transparent mirror  $Z$ ; and  $W_D$  and  $W_R$ , object and reference waves the interference pattern of which is recorded as hologram  $H$ .



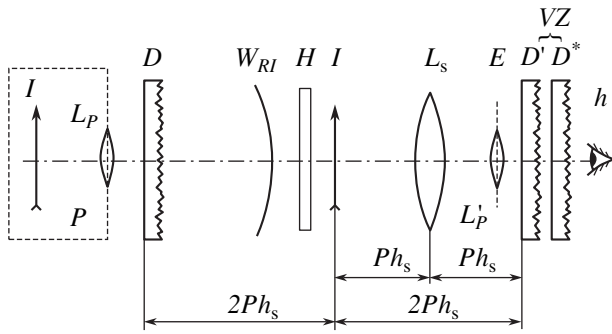


**Fig. 5.** Scheme for projecting image  $I$  using a projector based on a centered hologram;  $L_p$  is the lens of projector  $P$ , which projects image  $I$  on hologram  $H$  of the diffuser;  $D'$  is the reconstructed image of the diffuser, which arises during reconstruction of the hologram;  $D^*$  is the conjugate image of the diffuser;  $W_{RI}$  is the reconstructing wave, whose intensity is modulated by the image;  $H$  is the hologram of the diffuser (screen);  $I$  is the image projected onto screen  $H$ ;  $L_s$  is the lens projecting the reconstructed image onto the observer's eye  $h$ ;  $L'_p$  is the projector lens image;  $HL$  is halo;  $VZ$  is the visibility zone, through which the observer sees image  $I$  (this image appears to be placed at infinity, since it is situated distance  $Ph_s$  from lens  $L_s$ , where  $Ph_s$  is its focal length).

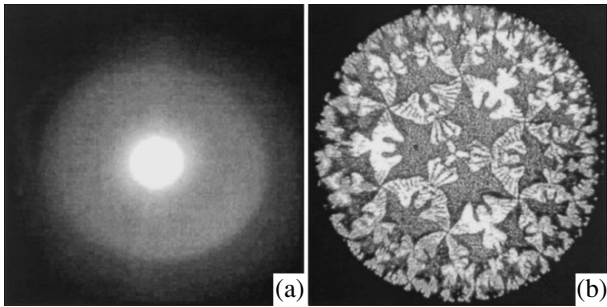


**Fig. 6.** (a) Light distribution over visibility zone  $VZ$  and (b) image  $I$  projected onto screen  $H$ .

the diffuser with this rule, one can easily arrive at the conclusion that the position of conjugate image  $D^*$  coincides with that of main image  $D$  only if reference source  $R$  is placed at the center of diffuser  $D$  during recording of the hologram (Fig. 4). In this case, wave  $W_D$ , which is scattered by diffuser  $D$ , mixes up with spherical reference wave  $W_R$  from source  $R$ , which is transferred to the center of the object by semitransparent mirror  $Z$ . The pattern of interference between waves  $W_D$  and  $W_R$  is recorded on hologram  $H$ . From Fig. 4, it follows that, in reconstructing such a hologram, conjugate image  $D^*$  of the object is bound to coincide with object  $D$ , since the latter is at the center of spherical wave  $W_R$ . In its turn, in constructing conjugate image  $D^*$ , this wave is perceived as a mirror behind which object  $D$  must be imaged. This type of hologram, where the reference source is placed at the center of the object, will be called a centered hologram.

The scheme for object projection through a screen based on a centered hologram is shown in Fig. 5. Lens  $L_p$  of projector  $P$  projects image  $I$  of the scene onto such a screen  $H$ . The projection is accomplished by means of spherical wave  $W_{RI}$ , whose intensity is modulated by the image being projected. Screen  $H$  reconstructs the image of diffuser  $D'$  and also its conjugate  $D^*$ . It should be noted that, if the zeroth order is not eliminated, the screen forms image  $L'_p$  of the projector lens. Observer  $h$  sees the image on screen  $H$  through images  $D'$  and  $D^*$  of the diffuser, which are formed by holographic screen  $H$ .

Since published data on centered on-axis holograms are lacking, we performed a tentative experiment on recording images with such a method. The experimental scheme was the same as that used in recording a centered hologram (Fig. 4) and in projecting an image through centered-hologram-based screen  $H$  (Fig. 5). The hologram was recorded using a He-Ne laser on PFG-03M photographic plates (in this case, their resolution may be much lower).

In this experiment, a centered hologram was recorded and reconstructed following the procedure mentioned above. The intensity distribution over visibility zone  $VZ$  is shown in Fig. 6a. A circular region filled with light that is reconstructed by holographic diffuser  $H$  is seen. At the center of this region, the zeroth-order spot is observed. The conjugate image of the diffuser or any other extra images are absent, as they must be if the principle of operation of such holograms is taken into consideration.

Figure 6b shows an image that is projected onto screen  $H$  and observed through visibility zone  $VZ$ . It is seen that the nonuniform illumination of the visibility zone does not influence the illumination uniformity of the image projected.

Thus, starting from a thin Gabor on-axis hologram, we devised a new type of holograms that partially exclude image distortions typical of a simple on-axis hologram. Specifically, an on-axis screen based on a centered hologram is suggested. It makes it possible to eliminate distortions due to conjugate images arising during reconstruction of thin holograms.

#### ACKNOWLEDGMENTS

This work was supported by the Russian Foundation for Basic Research (grant no. 04-02-17593) and a grant of the President of the Russian Federation (grant no. NSH-98.2003.2).

#### REFERENCES

1. D. Gabor, Proc. R. Soc. London, Ser. A **197**, 454 (1949).
2. D. Gabor, Proc. Phys. Soc. London, Sect. B **64**, 449 (1951).
3. E. N. Leith and J. Upatnieks, J. Opt. Soc. Am. **52**, 1123 (1962).

Translated by V. Isaakyan

## OPTICS, QUANTUM ELECTRONICS

# Self-Modulation of the Radiation from Fiber Lasers with Microcavity Mirrors

V. D. Burkov, F. A. Egorov, and V. T. Potapov

*Institute of Radio Engineering and Electronics (Fryazino branch), Russian Academy of Sciences,  
pl. Vvedenskogo 1, Fryazino, Moscow Oblast, 141120 Russia*

Received December 17, 2003; in final form, June 7, 2004

**Abstract**—The domain of excitation of self-oscillations is experimentally studied in a system consisting of an erbium fiber laser and a microcavity. The dependences of the self-oscillation frequency on the parameters of the system are found. The features of the self-oscillations are analyzed for the case where the laser radiation simultaneously interacts with several microcavities. © 2005 Pleiades Publishing, Inc.

Modern microelectronic technologies allow designers to create optical elements based on micromechanic resonance structures (MRSs), which exhibit unique properties making it possible to effectively control the parameters of optical radiation [1]. Using these optically excited microstructures as the optical elements (e.g., mirrors) of the fiber laser (FL) cavity, one may substantially influence the lasing dynamics. In this case, the laser may interact with the MRS (microcavity) using an optically tunable Fabry–Perot interferometer or a microcavity-based autocollimator. This effect is related largely to passive  $Q$  switching in the FL cavity, as well as to the Doppler shift of the frequency of the radiation reflected from the microcavity mirrors. The variation of the FL radiation intensity strongly depends on the ratio between the natural frequencies  $f$  of elastic (acoustic) oscillations of the microcavity and the frequency  $f_{\text{rel}}$  of relaxation oscillations of the laser. The self-modulation mode arising under the resonance condition ( $f_{\text{rel}} \cong f$ ) or multiple resonance conditions ( $f_{\text{rel}} \cong f/N$ ,  $N = 2, 3, \dots$ ) is of great applied interest. This mode opens the way for designing a variety of self-oscillation fiber-optic measuring systems [2]. The domain of excitation of resonance self-modulation in the parameter space of the FL–microcavity system is of a complicated structure. It consists of the ranges where the regular and stable self-oscillations of the laser share a common frequency  $F \approx f$  with those of the microcavity and the ranges where the oscillations are nearly chaotic. In this work, we experimentally study the ranges of resonance self-modulation excitation and the variation of the lasing modes. In addition, we are interested in the variation of the self-oscillations parameters in separate ranges of the domain of excitation, which should be taken into account in order to optimize the characteristics of measuring devices based on the systems under consideration. We also demonstrate the intriguing nonlinear properties of the systems comprising an FL and

microcavities where two or more microcavities interact with the laser radiation.

In experiments, we employed erbium FLs (radiation wavelength  $\lambda \cong 1540$  nm) with the linear configuration of the optical cavity (Fig. 1). Silicon microcavities of various types served as laser cavity mirrors. In such microcavities, the frequencies and acoustic  $Q$  factors of the elastic oscillation fundamental modes in air were  $f = 20$ –400 kHz and  $Q = 50$ –200, respectively. The active medium represents a section ( $AB$ ) of an  $L \approx 3$  m-long optical fiber doped by  $\text{Er}^{3+}$  and  $\text{Yb}^{3+}$  (sensitizer) ions. It was pumped using a semiconductor laser with a pumping radiation wavelength  $\lambda_p = 980$  nm. By varying the injection current  $I$  of the pumping laser, we set the mean output  $W_{\text{av}}$  of the FL and relative pump power  $r = P/P_{\text{thr}}$  ( $P_{\text{thr}}$  is the threshold pump power) in the ranges  $W_{\text{av}} = 0$ –30 mW and  $r = 0$ –4. In this case, the laser relaxation frequency  $f_{\text{rel}}$  ranged from 0 to 170 kHz.

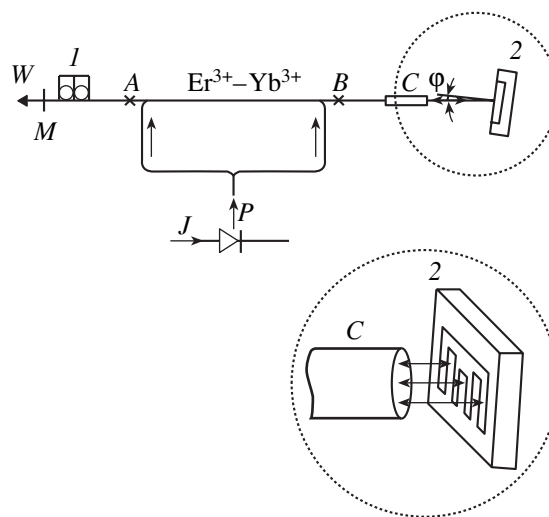


**Fig. 1.** Schematic of a fiber-optic laser with a microcavity mirror: (1) polarization controller and (2) MRS.

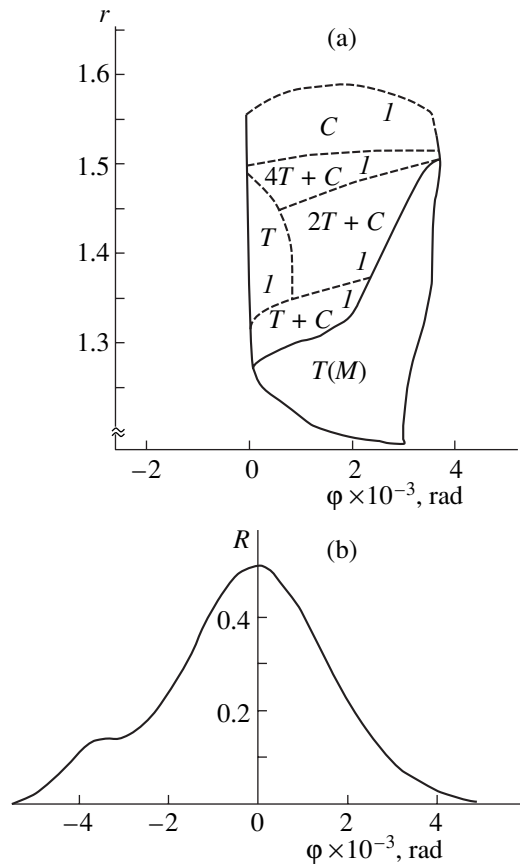


**Fig. 2.** (a) Domain of excitation of self-oscillation and (b) the directional pattern of the collimator (*I* marks the range of hard excitation).

The FL–MRS system under consideration has a wide set of parameters characterizing (i) the active medium and cavity of the laser; (ii) thermo-optical and thermoelastic properties of the MRS, the resonance frequencies,  $Q$  factors, and the arrangement of the microcavities; and (iii) the linear and angular coordinates characterizing the position of the laser beam relative to the microcavity. In this work, we restrict our consideration to the analysis of the systems where an FL is optically coupled with a microcavity via an autocollimator offering a high stability against destabilizing factors [2]. Given the characteristics of the microcavity and the FL optical cavity, the behavior of these systems depends mainly on parameters  $r$  and  $\varphi$  ( $\varphi$  is the angle between the axis of the collimated beam and the normal to the microcavity surface). Figure 2 demonstrates the projections of the sections of the ranges where resonance self-modulation excitation takes place onto plane ( $r, \varphi$ ). The projections are seen to consist of several regions corresponding to characteristic manifestations of the nonlinear dynamics. At low pump levels, we observe stable self-oscillations with the fundamental period  $T = 1/f$  (region *T*), which are excited in the soft mode (*M*). Outside this region, where resonance self-

modulation is excited in the hard mode, we observe regions where the period is sequentially doubled ( $2T$  and  $4T$ ) and which eventually pass into the region of chaotic motion (*C*). The chaotic motion shows up as a significant noise in the laser spectrum. Note that the discrete lines observed against the noise background correspond to the fundamental frequency of unstable cycles, as well to their higher harmonics and subharmonics. The observed sequence of the oscillation modes lets us assume that the regular self-modulation of the laser loses stability in accordance with the Feigenbaum scenario [3].

In the region of synchronous self-oscillations (*T*), the self-modulation frequency is, in essence, the natural frequency of a coupled system of oscillators (which are the microcavity and FL). In this case, the FL can be viewed as a model of an intrinsically nonlinear oscillator characterized by a spectrum of relaxation oscillations. Using the rate equations for an FL [4], as well as the equation for a linear oscillator describing an MRS, and assuming that coupling between the oscillators is weak and the microcavity oscillation amplitude, as well as the laser intensity, is low, one can show that the self-modulation frequency  $F$  can be found as a real root of the equation

$$F^4 - F^2(f^2 + f_{\text{rel}}^2 + ff_{\text{rel}}/Q_{\text{rel}}) + f^2 f_{\text{rel}} + \gamma = 0. \quad (1)$$

Here,  $f_{\text{rel}}$ ,  $Q$ , and  $\gamma$  depend, in particular, on parameters  $r$  and  $\varphi$  and  $Q_{\text{rel}}$  is the quality factor of an oscillator simulating the FL relaxation oscillations.

In Eq. (1), it is assumed that  $Q$  and  $Q_{\text{rel}} \gg 1$  and the coefficient characterizing the coupling of oscillators satisfies the condition  $\gamma/f^2 f_{\text{rel}} \ll 1$ . Under the resonance condition ( $f_{\text{rel}} \approx f$ ), it follows from Eq. (1) that  $F \approx f$ .

Figure 3 demonstrates experimental curves  $F(r, \varphi, f)$  for region *T*. For the given parameters of the microcavity, the relative variation of the self-modulation frequency  $\Delta F/f = [F - f]/f$  is no greater than  $10^{-4}$ , while reaching the value  $\Delta F/f \leq 5 \times 10^{-3}$  near the boundaries of this region.

Note that, when parameters  $r$  and  $\varphi$  remain unchanged, the dependence  $F(f)$  is virtually linear. In this case, the nonlinearity coefficient  $\delta = |\Delta F/f - 1|$  is normally no greater than 0.1% if the relative variation of the microcavity frequency  $|\Delta f/f| \leq 5 \times 10^{-2}$ . This suggests that such a self-oscillation mode is very promising for precision frequency-output fiber-optic sensors. In the absence of external actions on the FL–MRS system, the relative rms fluctuations  $(\langle \Delta F_{\text{fl}}^2 \rangle)^{1/2}/f$  of the self-modulation frequency substantially depend on the MRS quality factor, decreasing with increasing quality factor. For the microcavities used in this work ( $Q = 50$ –

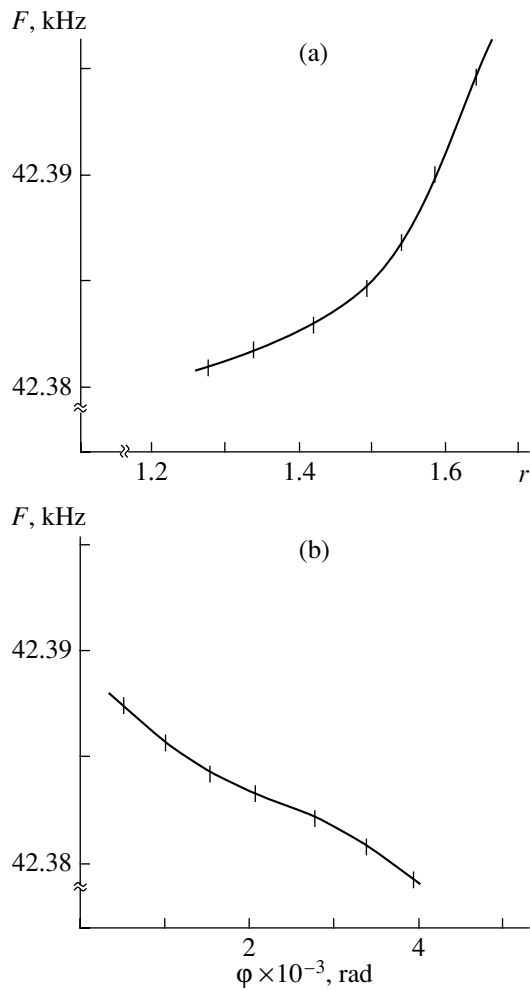


**Fig. 3.** Self-oscillation frequency vs. (a) the pump level and (b) the tilt angle of the microcavity.

200), the relative fluctuations equaled

$$(\langle \Delta F_n \rangle^{1/2})/f = 5 \times 10^{-6} - 5 \times 10^{-5}.$$

It is known [5] that, under normal conditions, the quality factor of the microcavities depends primarily on the scattering of the oscillation energy. In air, the scattering factor is much higher than in a vacuum. At a pressure of no greater than  $10^{-2}$  Pa, the quality factor of silicon microcavities ranges from  $5 \times 10^3$  to  $1 \times 10^5$ . In this case, the relative fluctuations of the self-oscillation frequency of the systems under consideration are estimated as not exceeding  $5 \times 10^{-7}$ .

As follows from Eq. (1), the self-oscillation frequency is a function of the parameters describing, in particular, the relaxation oscillations of a fiber laser, which, in turn, depend mainly on the properties of the active medium and optical cavity of the laser. Since the frequency is a physical quantity that can be measured with a very high precision, the dependence mentioned above may be used for precisely measuring the param-

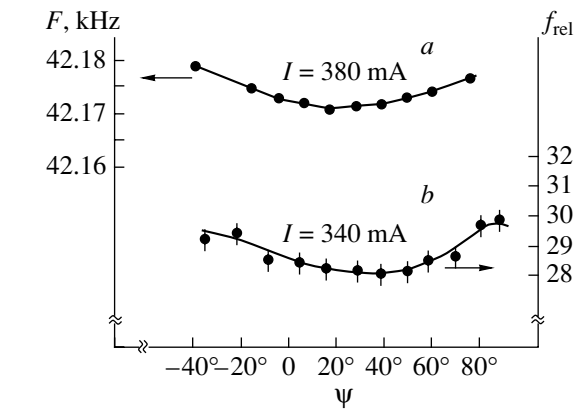


**Fig. 4.** Frequencies of the (a) self-oscillations and (b) relaxation oscillations vs. the state of polarization.

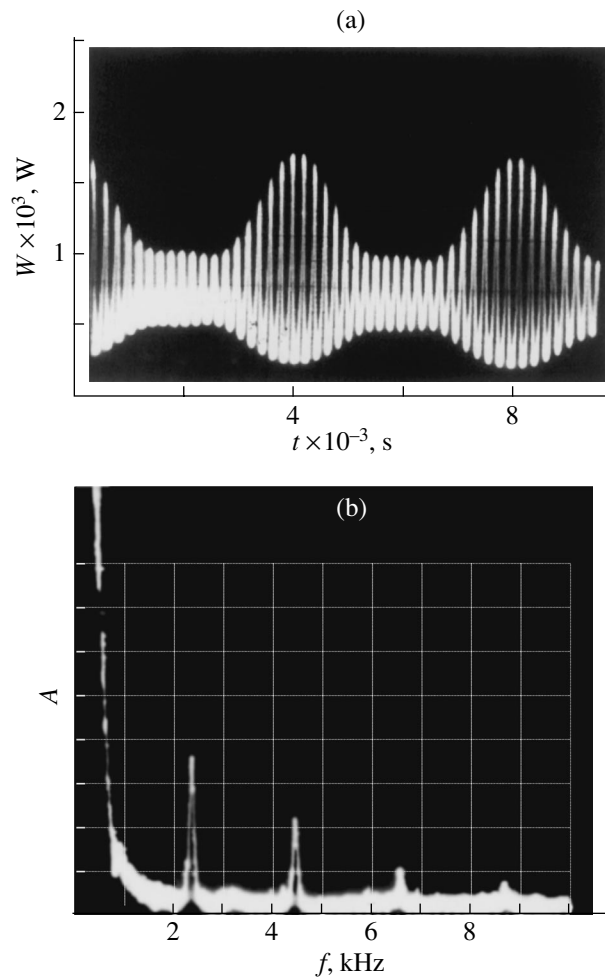


**Fig. 5.** (a) Oscillograms of the FL radiation intensity and (b) the Fourier spectrum of the laser radiation intensity near the difference frequency of microcavities.

eters of the active medium and FL optical cavity. This is confirmed by Fig. 4, which plots the experimentally found frequencies of the self-oscillations and FL relaxation oscillations against the radiation polarization

inside the cavity. The state of polarization was changed with a fiber-optic polarization controller, which was placed in the FL cavity and varied the angle  $\Psi$  between the axes of two fiber loops serving as quarter-wave plates. The polarization dependences of the self-oscillation,  $F(\Psi)$ , and relaxation oscillation,  $f_{\text{rel}}(\Psi)$ , spectra were obtained at pump levels significantly higher (curve *a*) and lower (curve *b*) than the excitation threshold of the self-oscillations (the threshold injection current is  $I_{\text{thr}} = 350$  mA). The data presented show that there exists a distinct correlation between the two functions, the relative errors involved in the polarization-dependent frequency drift being  $\delta_1 = \langle \Delta F^2 \rangle_{\text{fl}}^{1/2} / (F_{\text{max}} - F_{\text{min}}) \approx 0.1$  and  $\delta_2 = \langle \Delta f_{\text{rel,max}}^2 \rangle_{\text{fl}}^{1/2} / (f_{\text{rel,max}} - f_{\text{rel,min}}) \approx 0.3$ . These polarization effects are apparently related to anisotropy of the active medium, since the difference between the Fresnel reflection coefficients of the microcavities is insignificant (no greater than  $3 \times 10^{-4}\%$  for the given tilt angles of the mirrors,  $|\varphi| \leq 0.3^\circ$ ).

The experiments with mirrors based on planar multielement structures (Fig. 1b), when a number of microcavities fit the cross section of the laser beam, are of great interest for development of multichannel measuring systems. In this case, the laser radiation simultaneously interacts with two or more microcavities. If the microcavities are optically excited with the same efficiencies, their frequencies are close to each other ( $f_1 \approx f_2$ ), and they resonantly interact with the laser ( $f_{\text{rel}} \approx f_{1,2}$ ), one can establish the self-modulation mode of lasing. Under such conditions, the simultaneous self-excitation of at least two microcavities occurs. Figure 5 demonstrates the oscillograms and Fourier spectrum of

the FL radiation intensity in the low-frequency range (the difference frequencies of the MRS) for the lasing regime under consideration ( $f_1 \approx 57$  kHz,  $f_2 \approx 60$  kHz). The modulation spectrum of the laser intensity exhibits frequencies  $F_{1,2} \approx f_{1,2}$ , along with difference frequency  $\Delta F = f_1 - f_2$  (and its harmonics), which is due to the nonlinear properties of the FL–MRS<sub>1,2</sub> system. This effect opens up possibilities for designing microcavity fiber-optic difference-scheme sensors, which are highly resistant to factors adversely affecting the measuring system.

#### ACKNOWLEDGMENTS

This work was supported by the “Integration” Federal Program (grant no. B0003).

#### REFERENCES

1. Victor M. Bright, John H. Comtois, J. Robert Ried, and Darren E. Sene, *IEICE Trans. Electron.* **E80-C**, 206 (1997).
2. V. D. Burkov, F. A. Egorov, Ya. V. Malkov, and V. T. Potapov, *Zh. Tekh. Fiz.* **70** (1), 113 (2000) [*Tech. Phys.* **45**, 112 (2000)].
3. P. S. Landa, *Nonlinear Oscillations and Waves* (Nauka, Moscow, 1997) [in Russian].
4. C. Barnard, P. Myslinski, J. Chrostowski, *et al.*, *IEEE J. Quantum Electron.* **30**, 1817 (1994).
5. B. Hok and K. Gustafsson, *Sens. Actuators* **8**, 235 (1985).

*Translated by A. Chikishev*

---

---

**ELECTRON AND ION BEAMS,  
ACCELERATORS**

---

---

# **Multireflection Planar Time-of-Flight Mass Analyzer. I: An Analyzer for a Parallel Tandem Spectrometer**

**A. N. Verentchikov, M. I. Yavor, Yu. I. Hasin, and M. A. Gavrik**

*Institute of Analytical Instrument Making, Russian Academy of Sciences,  
Rizhskii pr. 26, St. Petersburg, 190103 Russia*

*e-mail: iap@ianin.spb.ru*

Received June 1, 2004

**Abstract**—To increase the speed and selectivity of tandem mass-spectrometric analysis, a tandem of two time-of-flight analyzers that operate in a radically new “nested time” mode is proposed. Such an approach makes it possible to perform parallel analysis of the fragment spectra for all parent ions within a single separation cycle using the first (“slow”) analyzer. The method suggested can be implemented with a new “slow” time-of-flight analyzer, which combines lateral confinement of a low-energy ion beam in periodic lenses and multiple reflection of the ions from planar gridless mirrors. Also, the new approach opens the way to considerably extending the effective length of the ion trajectory, while retaining the possibility of operating in the entire mass range and providing high-order time-of-flight ion focusing in energy. As follows from the analytical data and the experimental data obtained on a prototype of the analyzer, the instrument offers a high transmission (no less than  $6 \text{ mm} \times 1.5^\circ$  in either direction transverse to the beam), good resolving power (more than 5000), and wide (six orders of magnitude) dynamic range. © 2005 Pleiades Publishing, Inc.

## INTRODUCTION

Up to the early 1980s, tandem mass spectrometry was represented by expensive and bulky instruments [1, 2], which consisted of two sector magnetic mass spectrometers. The first instrument separates out the ion component to be analyzed, the ions are passed through a fragmentation cell, and the fragments are analyzed in the second spectrometer. Such instruments are usually used for structural analysis of volatiles or for improving the isotopic sensitivity of isotope analysis. Advances in the methods of mass spectrometry and soft ionization (such as electrospray ionization [3–7] and MALDI [8–10]) highlighted the potential of tandem mass spectrometry as a powerful analytical tool. The unique properties of tandem instruments, specifically, a high specificity and selectivity in analysis of multicomponent compounds, became obvious [11]. Over the last decade, tandem instruments have been considerably refined. Tandems, such as a combination of quadrupole and time-of-flight (TOF) spectrometers, linear ion traps, a combination of an ion trap with a Fourier spectrometer, and tandem TOF spectrometers have appeared. In these tandems, the selectivity may be as high as  $10^{-14}$  mol and the rate of fragment analysis reaches one spectrum per second. The new potentialities of tandem analysis have found wide application, e.g., in biotechnology, where multicomponent compounds are analyzed in a wide range of component concentrations.

In spite of the variety of tandem instruments currently available, they suffer from a common disadvantage: only one type of parent ions is analyzed at a given

time instant. All other parent ions are removed from the primary parent beam and are lost. Ion-by-ion analysis extends the time of the experiment; moreover, the sensitivity of the analysis drops when multicomponent mixtures are studied. One of us suggested [12, 13] devices of a new type that make it possible to perform tandem analysis for many parent ions simultaneously (in parallel) and cut the time of analysis by two orders of magnitude. The key unit in these instruments is a “slow” TOF mass analyzer, which separates out parent ions. The design of such an analyzer was presented in [14], and pioneering experiments carried out on its prototype were reported in [15]. In Part I of this work, we generalize the results obtained to date on designing a TOF analyzer of the new type as a component of a parallel tandem TOF mass spectrometer. Part II is devoted to the feasibility of using the analyzer suggested in high-resolution instruments.

## PARALLEL ANALYSIS IN A TIME-OF-FLIGHT TANDEM

To improve the sensitivity and speed of tandem mass analysis, we suggest a mass spectrometer of a new type the operation of which is illustrated in Fig. 1. The device consists of two TOF mass analyzers TOF1 and TOF2, which are separated by a fragmentation cell. Here, parent ions are slowly (within several milliseconds) separated in the first analyzer with subsequent rapid fragmentation and rapid (about  $10 \mu\text{s}$ ) mass analysis of the fragments in the second analyzer. This establishes a basically new (nested-time) operating mode

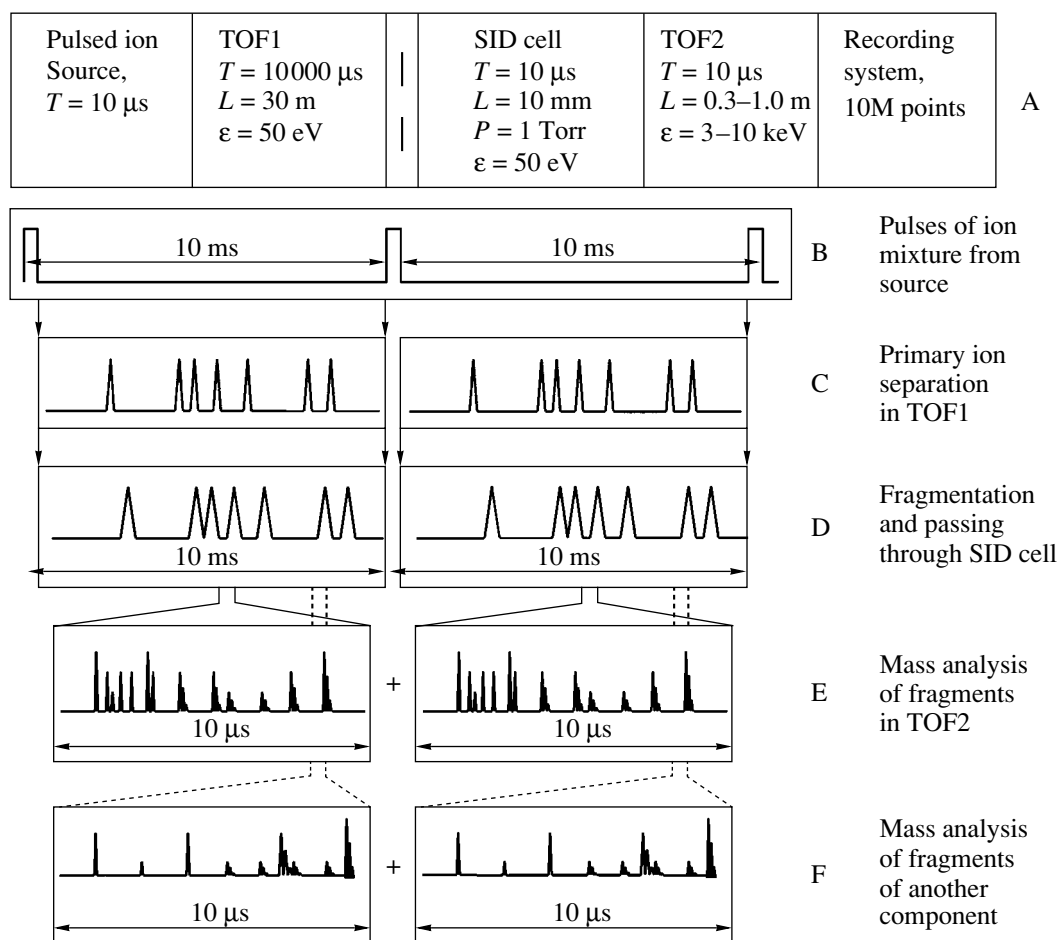


**Fig. 1.** Operating principle of the TOF tandem in the nested time analysis mode.

and, accordingly, opens the possibility for parallel analysis. Such an approach allows for parallel analysis of fragment spectra for all parent ions in one separation cycle carried out in the first analyzer.

To clarify the principle of operation of the tandem instrument, consider its version with the parameters shown in panel A (Fig. 1). Panel B shows a recording cycle where the ions are injected from the ion source at 10-ms intervals. Parent ions are separated in the first TOF analyzer, and a train of ion packets, which are separated according to the masses of the parent ions, enters into the fragmentation cell. The parent ions are partially fragmented in the cell, and the fragments, which quickly pass through the cell, reach the second TOF analyzer virtually simultaneously with their parent ions, remaining within a given packet (plot C). Each new family of ions (parents with their daughter ions) is injected into the second (high-energy) TOF analyzer to form mass spectra for each of the parent ions at its exit (panels D and E).

The time of analysis at either stage is of primary importance. The instrument is intended for problems of pharmacology and proteomics, where multicomponent

mixtures of medium-weight (300–3000 u) molecules (e.g., drugs or peptides) are analyzed. Thus, to separate isotopes in TOF2, it is necessary that the resolution be 3000–5000 or higher. Since the peaks in TOF mass spectrometers are several nanoseconds wide, the time of flight in TOF2 must be no less than 10  $\mu\text{s}$ . Hence, parallel analysis can be accomplished if the difference in times of arrival at TOF2 for isotopic groups from different parents is close to this value. At the same time, to separate these groups at the first stage of the tandem, it is sufficient that the resolving power of TOF1 be on the order of 300–500. Hence, the separation times in the two stages must differ by three orders of magnitude; that is, the separation time in the first analyzer must be of no less than 10 ms, which is the case in the example considered.

A possible design of the tandem is presented in Fig. 2. As a pulsed ion source, one may take that based on matrix-assisted laser desorption/ionization (MALDI). In this case, problems associated with the long-term stability of ions excited may arise. It is preferable to use soft ionization sources, such as those based on electrospray ionization (ESI) or atmospheric-

pressure chemical ionization (APCI). These sources, as well as any other continuous ion sources (e.g., photoionization sources), may be converted to pulsed sources by means of a gas-filled rf accumulator, e.g., a linear quadrupole trap. In this case, the quality of the pulsed beam is affected primarily by the space charge in the accumulator. For a time period of 10 ms between the pulses, an ESI source with a valid ion current of 20 pA delivers about 1 million ions to the trap. For a typical ion packet comprising  $10^6$  ions of mass 1000 u that are accelerated to 50 eV when injected from the accumulator, the parameters of the beam are as follows: the energy spread is less than 10 eV; time spread, less than 3  $\mu$ s; and spatial phase volume, less than  $2 \text{ mm} \times 1^\circ$ .

For the efficient operation of the tandem with the ion packets mentioned above, TOF1 must provide a time of flight of 10 ms and a mass resolution of 500–1000. For an ion energy of 50 eV and an ion mass of 1000 u, such a duration is provided only if the ion trajectory is about 30 m. With today's TOF instruments, the necessary parameters are unachievable. In reflectrons, the flight length does not exceed several meters. In the case of multiple reflections, the mass range shrinks catastrophically and the geometric losses of the ion beam increase considerably. Moreover, TOF instruments operate at ion energies of several kiloelectron volts in order to avoid ion and resolution losses when the relative energy spread is sufficiently high. Thus, a new-generation analyzer should be developed to slowly (for a time of 10 ms) separate parent ions.

Ion fragmentation in a parallel tandem is assumed to take place in a surface-induced dissociation (SID) cell with accelerated ion transmission, which makes it possible to decrease the time broadening of ion packets to less than 10  $\mu$ s. Under these conditions, information on the separation time in the first analyzer is kept. Fast collision relaxation (within several microseconds) is possible only if the gas pressure in the cell is high ( $P = 0.2$ – $1.0$  Torr). In this case, one can decrease length  $L$  of the cell to 5–10 mm, thereby accelerating the ion transmission. Although the cell is short, the product  $PL > 0.1$  Torr cm remains sufficient for cooling the ions [16, 17]. The transport of the ions through the cell can be accelerated still further by applying a longitudinal electrostatic field. For a drift velocity of 500 m/s, the transport time of the ions is below 20  $\mu$ s and the time spread is expected to be lower than 10  $\mu$ s. Alternatively, the time broadening can be reduced by introducing a traveling wave of the longitudinal field. Such a more sophisticated solution loosens the requirements imposed on the length of and the pressure in the fragmentation cell.

Finally, the mass analysis of the fragments may be carried out in the fast TOF mass analyzer with orthogonal ion injection. For a typical length of the ion trajectory of 0.3 m and an energy of 5 keV, the time of flight will equal the desired 10  $\mu$ s. With such fast analysis, the resolution of the analyzer is expected to be from 2000

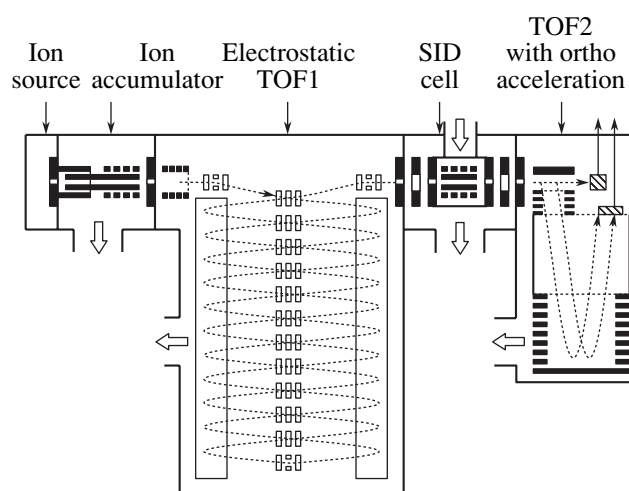


Fig. 2. Design of the TOF tandem suggested.

to 3000. If a higher resolution is required, its operation must be slowed down. This can be achieved either by extending the period of the pulses from the source or by decreasing the resolution at the first stage (i.e., at the stage of parent separation).

From the above consideration of a TOF tandem operating in the nested time mode, it follows that its components, except for TOF1, are merely slight modifications of well-known and reliably operating mass-spectrometric units. Thus, the major problem in implementing the tandem is the development of a TOF analyzer with a separation time of about 10 ms. A slow multireflection TOF analyzer operating in the entire mass range is the central issue of this article.

#### ION-OPTICAL SCHEME OF A MULTIREFLECTION ANALYZER

A long transport time of ions in the analyzer means an increase in the transport length. With the overall dimensions of the instrument kept at a reasonable level, the problem can be solved by increasing the number of reflections of the ion beam from electrostatic mirrors. In currently available multireflection and multiturn TOF mass analyzers with cyclic ion beam motion [18, 19], an increase in the number of turns inevitably shrinks the mass range being analyzed. The entire mass range is retained in an analyzer where the ion beam follows an open zigzag trajectory [20]. We employed zigzag motion in a slow analyzer that is based on two gridless parallel 2D ion mirrors that face each other and are extended in drift direction  $Z$  (Fig. 3). In this analyzer, ions describe a zigzag trajectory, reflecting from the mirrors and slowly shifting perpendicularly to the mirrors (in the drift direction). The axial zigzag trajectory of the ion beam lies in symmetry plane  $XZ$  of the mirrors. The design of our analyzer radically differs from the instrument suggested in [20] in that the mirrors and lenses of the former produce field distributions that



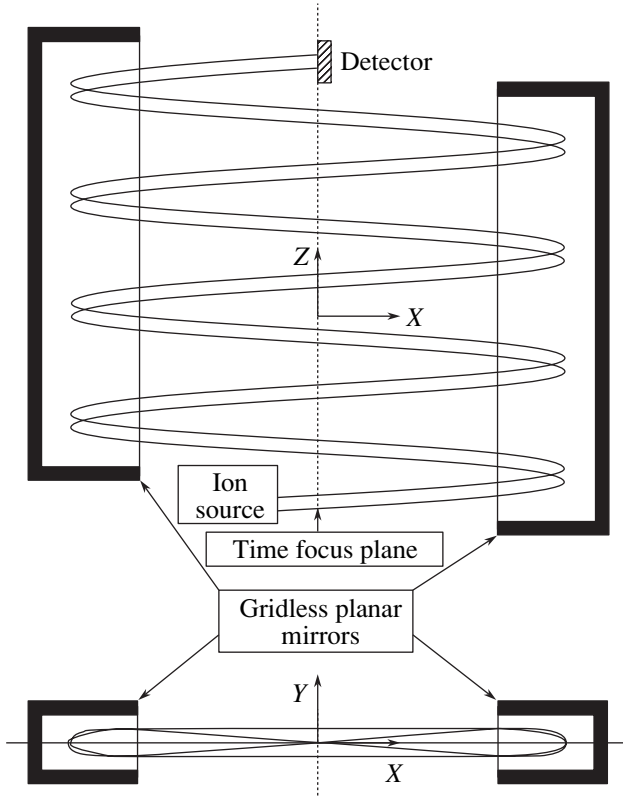


**Fig. 3.** Basic diagram of the planar multireflection TOF analyzer suggested in this work.

allow us to combine high-order time focusing of ions in energy and spatial spread with reliable beam confinement after multiple reflections. The stable motion of the beam is due to its passage through periodic electrostatic field structures [21, 22].

In a simplified version of the analyzer, the primary time focus, which is produced by the ion source, and an ion detector are placed in the middle between the mirrors, i.e., in plane  $YZ$  (Fig. 3). The mirrors make the ion motion from one intersection with this plane to another isochronous, i.e., independent of the ion energy and spatial coordinates in plane  $XY$ . Also, the ion motion in this plane must be stable.

Let us consider the projection of the ion path in the drift space between the mirrors onto plane  $XY$ . We fix the mass of an ion and expand coordinate  $y$  of this projection, slope  $b = dy/dx = \tan \beta$ , and time of flight  $t$  in  $y_0$ ,  $b_0$  ( $y_0$  and  $b_0$  are the initial values), and parameter  $\delta = (K - K_0)/K_0$  (where  $K$  and  $K_0$  are the energy of the given ion and the mean ion energy in the beam, respectively):

$$\begin{aligned} y(x) &= (y|y)y_0 + (y|b)b_0 + (y|y\delta)y_0\delta + (y|b\delta)b_0\delta + \dots, \\ b(x) &= (b|y)y_0 + (b|b)b_0 + (b|y\delta)y_0\delta + (b|b\delta)b_0\delta + \dots, \\ t(x) &= t_0 + (t|\delta)\delta + (t|yy)y_0^2 + (t|yb)y_0b_0 \end{aligned} \quad (1)$$

$$+ (t|bb)b_0^2 + (t|\delta\delta)\delta^2 + (t|\delta\delta\delta)\delta^3 + \dots$$

Here,  $t_0$  is the time of flight of a mean-energy ion and coefficients  $(t|y)$ ,  $(t|b)$ ,  $(t|y\delta)$ , and  $(t|b\delta)$  vanish, since the system is symmetric about plane  $XZ$ .

Note that the motion of an ion from plane  $YZ$  to the same plane after single reflection from the mirror is essentially the passage of the ion through a mirror-symmetric ion-optical cell. In such cells, the ion trajectories are stable [23] if  $-1 < (y|y) < 1$  at the exit from the cell. The stability is the highest in the middle of this range, i.e., at

$$(y|y) = 0. \quad (2)$$

Condition (2) means that a trajectory issuing from plane  $YZ$  parallel to the  $X$  axis returns (in a linear approximation) to this plane at  $y = 0$  (parallel-to-point focusing). Simultaneously, point-to-parallel focusing takes place owing to the symmetry of the system:

$$(b|b) = 0. \quad (3)$$

It is known [23] that the expansion coefficients for function  $t(x)$  in expansion (1) are related to the coefficients for functions  $y(x)$  and  $b(x)$  via the so-called symplecticity conditions. These conditions, along with the conditions of symmetry about planes  $XZ$  and  $YZ$ , and Eqs. (2) and (3) yield a number of relationships for the expansion coefficients in (1) as applied to our ion-optical system.

(1) Once an ion has passed two cells of the systems (i.e., after two sequential reflections from the mirrors), the condition  $(t|yb) = 0$  is met simultaneously with the condition  $(y|y) = 0$ .

(2) If the conditions  $(y|y) = 0$  and  $(t|yy) = 0$  are met after an ion has passed one cell, the condition  $(t|bb) = 0$  is also satisfied.

(3) If the condition  $(t|bb) = 0$  is satisfied after an ion has passed one cell, the conditions  $(y|y\delta) = (b|b\delta) = 0$  are also satisfied. That is, in the second-order approximation, conditions (2) and (3) of spatial focusing are not violated for ions with other-than-mean energies.

Thus, if parallel-to point focusing (2) takes place in one of the cells and one finds a field configuration in the mirror such that condition

$$(t|yy) = 0, \quad (4)$$

is fulfilled after an ion has traveled this cell, it follows from the above relationships that the time of flight of any ion becomes independent (in the second-order approximation) of initial coordinates  $y_0$  and  $b_0$  once the ion has twice reflected from and returned back to plane  $YZ$ . In addition, the spatial motion of the ions becomes more stable in this situation because of the absence of spatial chromatic aberrations (i.e., because the focal length of each of the cells does not depend on the energy in the second-order approximation).

All the results listed above are valid provided that only two conditions (2) and (4) are fulfilled. However, for the analyzer to be efficient as a TOF system, it is also necessary that the time it takes for an ion to pass each of the cells be energy-independent in an aberration order as high as possible. For example, the fact that the ion motion is isochronous in energy in the third order means that three conditions are met:

$$(t|\delta) = 0, \quad (t|\delta\delta) = 0, \quad (t|\delta\delta\delta) = 0. \quad (5)$$

Using numerical experiments aimed at optimizing the 2D gridless mirrors, we managed to find four-electrode configurations of the mirrors for which all the conditions listed are met. Here, the fulfillment of the five conditions set by (2), (4), and (5) is provided by appropriately selecting the electrode potentials of the mirror and mirror spacing.

An example of the axial distribution of the electrostatic potential in the mirror optimized and of paraxial ion trajectories in it are presented in Fig. 4. The axial distribution is provided by the electrodes, which, except for the extreme right (reflecting) electrode, consist of parallel conducting equidistant plates. The reflecting electrode is half as wide and is equipped with a closing plate (cap), which connects a pair of its parallel plates. The extension of the mirror field is limited by the space between two parallel grounded screens, where the field decays. The screens are made with the same gap as the other electrodes of the mirror. The electrode adjacent to the screen is under an accelerating potential that forms a negative lens. Due to this lens, condition (2) of first-order spatial focusing is fulfilled. The rest of the electrodes of the mirror produce a non-uniform field structure that decelerates the ions, with the electrostatic field strength dropping along the ion trajectory as an ion moves toward the turning point. Such a field structure provides third-order time focusing in the energy spread in the beam.

The negative lens of the mirror can provide first-order spatial focusing (2) when operating in different modes. As follows from the numerical experiments, the optimal operating mode of the mirror is that when an ion starting from plane  $YZ$  toward the mirror in the direction parallel to the  $X$  axis meets this axis near the turning point of the beam inside the mirror and then returns to this axis after crossing plane  $YZ$  (Fig. 4). It is in this mode that condition (4) can be satisfied by the numerical optimization of the electrostatic field distribution and, hence, that the time of flight through the cell becomes independent of a spatial spread of the ions in a packet in the second-order approximation.

High-order time focusing in energy and reliable confinement of the beam in the analyzer allow one to attain high parameters at low ion energies. Reliable confinement of the ion beam in the focusing mirrors makes it possible to increase the ion path length and thus improve the resolution of the analyzer.

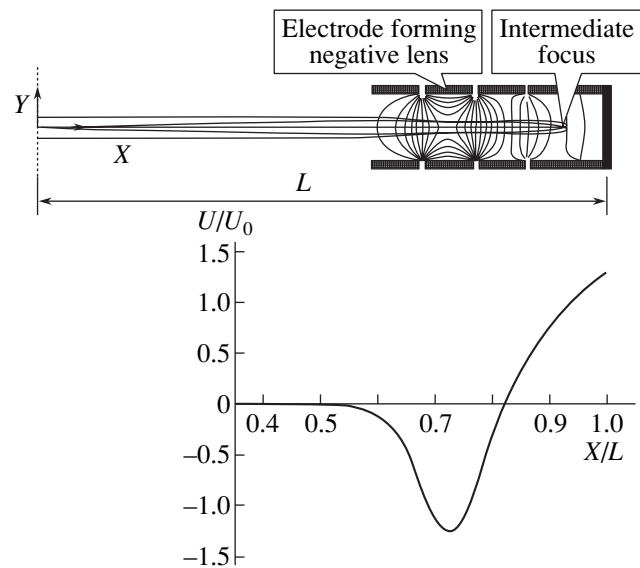


**Fig. 4.** Paraxial trajectories and electrostatic field equipotentials in a single cell (four-electrode gridless mirror) and the electrostatic field potential distribution along the mirror axis ( $U_0$  is the accelerating potential responsible for the kinetic energy of the ions).

A feasible design of the analyzer is depicted in Fig. 5. The modifications that differentiate this design from that shown in Fig. 3 are as follows.

(1) Weak 2D lenses, which focus the beam in plane  $XZ$ , are placed between the mirrors in order to considerably increase the number of reflections of the ion beam without overlaps at different turns in the drift direction. These lenses distort the time characteristics of the analyzer only slightly.

(2) The analyzer is configured with an extra exit deflector, which returns the ions that have traveled the total length of the mirrors to the analyzer and cause them to move in the opposite direction (Fig. 5). This deflector does not limit the mass range of the analyzer and does not introduce significant distortions into the time characteristics of the analyzer when the ion path is long.

(3) To inject ions from the ion source into the analyzer and direct ions separated in time of flight into the collision cell, the positions of the primary time focus and collision cell are shifted relative to plane  $YZ$ . This shift introduces minor distortions into the time characteristics of the analyzer, since the total ion path length changes insignificantly.

The operation of the analyzer in the low ion energy mode was evaluated with the SIMION 7.0 program [24]. To this end, we numerically studied the model of the analyzer where the spacing between the turning points in the opposite mirrors was taken to be equal to 220 mm along the  $X$  axis and the total length of the mirrors in the  $Z$  direction, 1.2 m. The ion beam entered into the intermirror space at an angle of  $3^\circ$  to the  $X$  axis, and

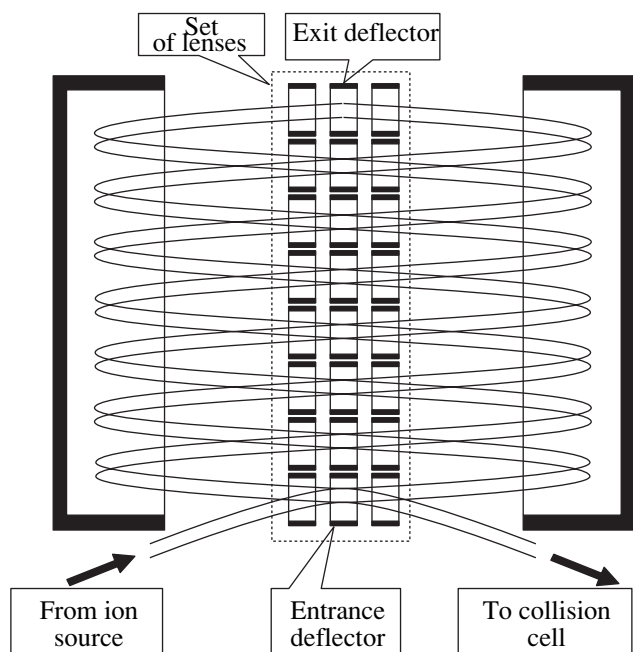


**Fig. 5.** Design of the analyzer with focusing lenses in the drift space and an exit deflector.

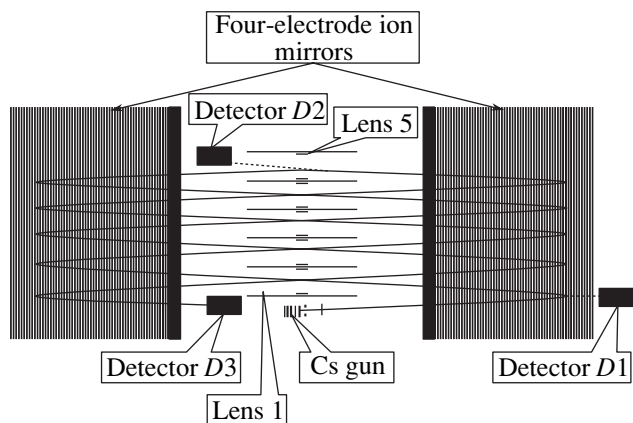


**Fig. 6.** Arrangement of basic components in the prototype of the analyzer.

the number of reflections from the mirrors at the midpoint of the path (i.e., from the source to the exit deflector) equaled 78. For a mean ion energy of 50 eV and an ion mass of 1000 u, the time of flight through the analyzer was 11.4 ms. The analyzer provided 100% rated transmission of an ion beam with a relative energy spread of 20%, initial diameter of 2 mm, and initial angular divergence of  $1^\circ$ . For these ion beam parameters, the peak-base mass resolution of the instrument (i.e., the resolution at the zero initial time spread in the beam) was found to be 500. At the peak half-maximum, the resolution was 4000.

The ion beam was also stable against external perturbations introduced into the field structure. For exam-

ple, the readings of the analyzer subjected to a magnetic field (each of its components along the coordinates was 10 G) were almost the same as without the field. The transmission losses in this case were estimated as 20%. Similar results were observed when one of the mirrors was turned by  $0.1^\circ$  in plane XZ, where the ion beam moved along a zigzag trajectory. It should be emphasized that such stability is provided by the periodic focusing of the beam using the mirrors (in plane XY) and lenses (in plane XZ).

## EXPERIMENTAL SETUP

The performance of the TOF analyzer was studied on its prototype, in which the mirror spacing was larger than that mentioned in the previous section but the number of reflections of the beam from the mirrors was reduced. The arrangement of the basic components of the prototype is shown in Fig. 6.

The prototype consists of two identical parallel planar ion mirrors and a set of lenses that are placed on the symmetry axis between the mirrors. Each of the mirror electrodes is made of nine 1-mm-thick stainless steel sheets that run normally to plane XZ. The sheets have  $228 \times 32$ -mm windows cut by spark cutting, through which the ion beam propagates; are separated by 2-mm-high precision insulating washers; and are tied up by insulating rods. The total nonparallelism of the mirror assembly, as well as the tolerance on the mirror spacing, does not exceed  $10 \mu\text{m}$  at a 600-mm distance between the “caps” of the reflecting electrodes.

The set of electrostatic lenses comprises five identical 2D lenses spaced 30 mm apart. Ten identical 10-mm-wide insulated plates, which serve as the focusing electrodes of the lenses, are mounted on the inner surfaces of the sections of the lens unit. All the focusing electrodes are supplied independently; therefore, any of the lenses can be used as a deflector.

When studying the performance of the analyzer, we used a specially designed compact low-energy cesium gun as a source of a test ion beam (for details, see [25]). This gun provides an ion beam emittance that is close to the analyzer's acceptance. A pulsed ion beam is generated by applying a modulating voltage to the control electrode of the gun. In the pulsed mode, the energy spread in the outgoing beam varies from 4% for an ion energy of 100 eV to 20% for an energy of 10 eV. Three detectors (VÉU6 secondary electron multipliers) arranged as shown in Fig. 6 are used in the prototype. Detector D1 is mounted immediately after the window in the reflecting electrode of the mirror and detects the gun-generated beam with the mirror switched off. Detector D2 receives the ion beam that has passed the analyzer in one direction. To this end, only a focusing voltage is applied to the electrodes of the fifth lens. Detector D3 is the basic detecting unit, which detects the ion beam that has passed the analyzer there and

back with the deflecting voltage on the fifth lens chosen appropriately.

The system uses a pulse amplifier with a bandwidth of no less than 100 MHz and a gain of  $10^3$ . The noise amplitude at the output of the amplifier is 5–10 mV or lower, and the duration of the pulsed response of the system to a single ion is 40–50 ns. The pulse parameters were recorded and measured with an averaging oscilloscope or with an AR-100 ADC [26], which has a time resolution of 1–10 ns and a vertical scale of 8 bit.

The chamber of the analyzer was evacuated to a pressure of  $3 \times 10^{-7}$  Torr with a turbomolecular pump of capacity 250 l/s and a mechanical pump. All joints of the vacuum chamber were sealed with Viton gaskets. A sorption trap was placed into the evacuating manifold.

### ADJUSTMENT OF THE ANALYZER

The adjustment of ion beam transport through the analyzer and the estimation of the analyzer performance were performed in the continuous operating mode of the ion source at an ion beam energy of 100 eV. The adjustment quality was monitored with detectors *D1–D3*. Detector *D2* was adjusted to a maximal ion current by applying low (no higher than 1 V) deflecting potentials to the electrodes of the lenses. The values of the ions measured by *D2* and *D3* (both detectors operated as collectors) led us to conclude that five extra reflections on the return path of the beam do not cause a noticeable decrease in the beam intensity.

When the cesium gun operated in the pulse modulation mode at an ion energy of 100 eV, a  $\text{Cs}^+$  ion peak with a time of flight of 500  $\mu\text{s}$  was observed on the screen of the oscilloscope, which agrees well with the results of numerical simulation.

In the early experiments with the analyzer, less intense peaks, along with the  $\text{Cs}^+$  peak, were also present on the oscillogram. They were spaced at regular time intervals and their amplitudes heavily depended on the lens voltage. The 3D simulation of the analyzer revealed that such an effect may result from a combination of three reasons: (i) a high angular divergence of the beam in the horizontal plane, which may be due to the elastic reflection of the ions from the lens electrodes; (ii) a high angular divergence of the beam in the vertical plane and the distortion of the beam near the mirrors; and (iii) insufficient focusing (the degree of focusing is lower than the rated one) of the beam, which is observed when the lens field structure is not strictly two-dimensional because of a finite height of the lenses.

We managed to virtually completely suppress this effect, making a series of refinements. First, a 3-mm-high mask was placed at the site where the beam enters into the mirror; second, masks with a  $20 \times 60$ -mm window that prevent the beam from striking the lens elements were placed before the lenses; and, third, the lens field structure was made closer to two-dimensional by

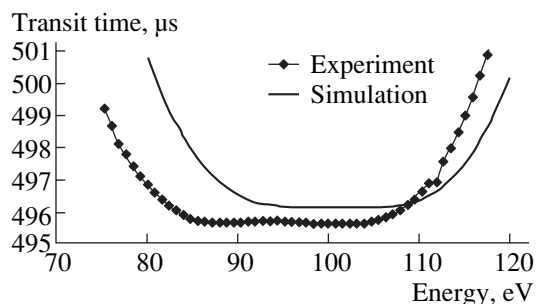


Fig. 7. Analytical and experimental dependences of the transit time on the ion energy.

modifying the configuration of the focusing electrodes of the lenses.

These refinements, combined with a proper selection of the lens electrode and cesium gun potentials and widening of the amplifier bandwidth, allowed us to find the operating conditions of the analyzer under which only the well-focused cesium peak with a 130-ns FWHM was observed on the screen of the oscilloscope. For a time of flight of 500  $\mu\text{s}$ , this value corresponds to a mass resolution of 2000. The peak width depends largely on the beam modulation efficiency in the ion source and is limited from below by a relatively low intensity of the low-energy beam.

Since the analyzer was designed for operation on a time scale realizable only at low ion energies, it was important to check the capabilities of its ion mirrors to provide extremely high time focusing in energy. Figure 7 shows the energy dependence of the time of flight of cesium ions that was simulated with the SIMION program and the same (experimental) dependence taken on the prototype at ion energies of  $100 \pm 20$  eV. When taking the experimental dependence, we kept the mirror electrode potential constant and close to the rated values and controlled the ion energy by varying the voltages applied to the ionizer and gun modulator. The curves demonstrate the range of TOF focusing in energy, and the shape of the experimental curve allows us to argue that third-order TOF focusing in energy is achievable.

Of no less importance is testing the analyzer performance at ion energies below 100 eV. It turned out that the analyzer is efficient in the ion energy range from 100 to 10 eV. The cesium gun was adjusted to such energies by varying the signal on detector *D1* with the mirrors switched off. For each ion energy, the mirror electrode potentials were taken such that the cesium ion peak was the highest when its width was minimal. The discrepancy between the optimal values of the electrode potentials found experimentally and the rated ones was within 2%.

As the ion energy was decreased, the signal intensity tended to decline. This may be because the divergence of the gun-generated ion beam increases and the beam is partially lost on the diaphragms and masks of the

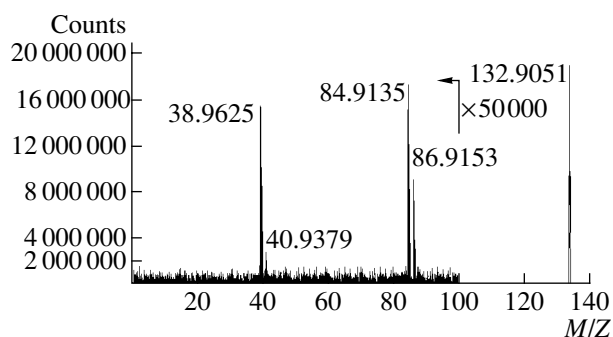


**Fig. 8.** Mass spectrum of the ions emitted by the cesium gun. The intensities for  $M/Z < 100$  are increased 50 000 times.

analyzer. To check this assumption, we performed a series of measurements of the ion current on detector *D3* with the current on detector *D1* fixed. It was found that the signal amplitude on both detectors vary in a similar way according to the quality and features of gun adjustment in the given series of measurements. Namely, at low energies, the amplitude drops in inverse proportion to the energy, as might be expected in view of the increasing beam divergence.

#### PERFORMANCE OF THE ANALYZER

After the adjustment, the parameters of the analyzer were the following: the energy losses were no higher than 10% at ion energies from 100 to 40 eV, 20% for 20 eV, and about 40% for 10 eV; and the mass resolution was 3000–5000. As the energy declines from 100 to 20 eV, the time of flight increases and, hence, the relative influence of the ion beam duration drops. Accordingly, the resolution of the instrument rises. At energies below 20 eV, additional factors adversely affecting the resolution may appear. These are interference on the electrodes and the effect of the electrode surface's imperfect condition.

The capabilities of the analyzer in recording ion spectra were examined with an AR-100 ADC [26]. We recorded the trace amounts of alkali metal ions that were contained in cesium aluminate. Prior to estimating the yield of these ions, we carried out preliminary measurements with an MX7302 quadrupole mass spectrometer. Potassium and rubidium ions were detected in amounts of 1–10 ppm relative to cesium ions. Sodium ions were not revealed.

To extend the dynamic range, the spectra were recorded, while by the ADC, in the counting mode. The multiplication factor of the VÉU-6 multiplier was selected in such a way that the response to a single ion had an amplitude of 10–20 mV for the noise amplitude ranging from 2 to 5 mV. The counting threshold was set at 5 mV in order to cut off analog noise and exclude the jitter of the last digit in the ADC. The ADC scale (a total of 500 mV, 2 mV per bit) was selected so as to avoid

ADC saturation by the most intense cesium peak (100 ions per shot at a maximal signal amplitude of less than 30 ions, i.e., less than 500 mV). In spite of the counting mode of operation, the cesium peak intensity equaled several tens of millions of counts per minute at a pulse repetition rate of 1 kHz, so that the spectrum gained good statistics and a wide dynamic range. An example of such a mass spectrum taken at an ion energy of 10 eV is given in Fig. 8.

The results obtained demonstrate that the scattered-ion-induced background in the mass spectra may be extremely low, indicating that our efforts to suppress this background were effective. The peak intensity of scattered ions, which are associated with spurious reflections in the channel of the analyzer, was depressed to a level below  $10^{-5}$  of the cesium ion intensity. In each of the spectra,  $^{39}\text{K}^+$ ,  $^{41}\text{K}^+$ ,  $^{85}\text{Rb}^+$ , and  $^{87}\text{Rb}^+$  isotope ions were reliably detected. The ratio between the peak intensities of these elements and the peak intensity of cesium was nearly the same as the ratio between their amounts ( $10^{-5}$ – $10^{-6}$ ). For example, the  $^{41}\text{K}^+$  ion peak intensity is only  $3 \times 10^{-6}$  of the cesium ion peak intensity. At such low intensities of trace amounts, the mass of any ion can be determined with an accuracy of higher than 0.0001 u provided that one of the components is used as an internal standard; e.g., the masses of  $^{39}\text{K}^+$ ,  $^{41}\text{K}^+$ , and  $^{87}\text{Rb}^+$  can be determined by calibration against the  $\text{Cs}^+$  and  $^{85}\text{Rb}^+$  peaks. The afore-said is equally related to all mass spectra recorded throughout the range 100–10 eV.

The frequency stability of the power supply at low frequencies is of great importance for a multireflection analyzer. For an ion energy of 100 eV, the ion velocity is 12 mm/ $\mu\text{s}$ ; the time of motion in the field of one 25-mm-long electrode, 2  $\mu\text{s}$  (500 kHz); the turn time (i.e., the time taken for two reflections from the mirrors), 100  $\mu\text{s}$  (10 kHz); and the total transit time, 500  $\mu\text{s}$  (2 kHz). Therefore, low-frequency (<2 kHz) interference is bound to change the electrode potentials. As was expected, the peaks are shifted to the greatest extent (about 1  $\mu\text{s}/\text{V}$ ) when the potential of the reflecting electrode of the mirror is varied. The amplitude ripple in our power supplies was lower than 10 mV; accordingly, the shift of the peaks was usually smaller than 10 ns. High-frequency (>1 MHz) voltage oscillations alter the peak position insignificantly. In the range 1 kHz–1 MHz, resonant frequencies may occur, which affect the ion motion most considerably and, as a consequence, noticeably degrade the resolution of the analyzer. Tests where a variable voltage of controllable amplitude and frequency was imposed on the voltage applied to the electrodes of the mirror showed that the resolution of the instrument may degrade catastrophically at some frequencies (close to 60 and 200 kHz in our experiments) when the variable voltage amplitude is about 100 mV.

## CONCLUSIONS

We suggest a concept of tandem mass-spectrometric analysis that is based on parallel recording of fragments of all parent ions by using TOF analyzers as both stages of the tandem. In terms of this concept, the parents are separated by a slow TOF analyzer, through which ions of mass about 1000 u are transported within 10 ms. For such a tandem, a unique planar reflecting TOF analyzer is designed and its prototype is built. At low ion energies (on the order of 100 eV), this analyzer operates in the entire mass range. It is shown that the ion motion is stable and the ion current losses after five turns of the beam in the analyzer are low. The performance of the prototype is close to that predicted with an analytical model as regards adjustment regimes and stability against potential variations. Specifically, third-order TOF focusing in energy is demonstrated. The acceptance of the instrument is estimated as  $6 \text{ mm} \times 1.5^\circ$ . It is also shown that the analyzer goes on reliably operating when the ion energy decreases to 10 eV. Even for such (extremely low for mass-spectrometric studies) energies, the mass spectra with a resolution of 5000 can be recorded. A further decrease in the ion energy is limited by the magnetic fields of the turbomolecular pump and pressure sensor, as well as by voltage ripples (about 10 mV) on the electrodes. The ripples may be attributed to resonant frequencies in the range 10–100 kHz, which make the ion motion unstable. One more feature of the multireflection TOF analyzer is an extremely low signal of scattered ions, allowing one to record mass spectra with a dynamic range of  $10^6$ .

## ACKNOWLEDGMENTS

The authors thank M.S. Svedentsov for the development of the program aimed at optimizing the field structures of gridless ion mirrors and the group headed by A.F. Kuz'min for the careful measurement of the amount of attendant alkali metal ions emitted by hot cesium aluminate.

## REFERENCES

1. J. V. Jonson and R. A. Yost, *Anal. Chem.* **57**, 758 (1985).
2. F. W. McLafferty, *Tandem Mass Spectrometry* (Wiley, New York, 1983).
3. M. L. Aleksandrov, L. N. Gall', N. V. Krasnov, *et al.*, *Dokl. Akad. Nauk SSSR* **277**, 374 (1984) [*Sov. Phys. Dokl.* **29**, 39 (1984)].
4. M. L. Aleksandrov, L. N. Gall', N. V. Krasnov, *et al.*, *Zh. Anal. Khim.* **40**, 160 (1985).
5. M. Yamashita and J. B. Fenn, *J. Phys. Chem.* **84**, 4671 (1984).
6. C. M. Whitehouse, R. N. Dreyer, M. Yamashita, *et al.*, *Anal. Chem.* **57**, 675 (1985).
7. J. B. Fenn, M. Mann, C. K. Meng, *et al.*, *Science* **246**, 64 (1989).
8. K. Tanaka, H. Waki, Y. Ido, *et al.*, *Rapid Commun. Mass Spectrom.* **2**, 151 (1988).
9. M. Karas and F. Hillenkamp, *Anal. Chem.* **60**, 2299 (1988).
10. M. Karas and F. Hillenkamp, *Advances in Mass Spectrometry*, Ed. by P. Longevialle (Heyden, London, 1989), p. 416.
11. R. Aebersold and M. Mann, *Nature* **422**, 198 (2003).
12. A. Verentchikov, GB Patent No. 2,390,935 (July 16, 2002).
13. A. N. Verentchikov, *Nauchn. Priborostroenie* **14** (2), 34 (2004).
14. M. I. Yavor and A. N. Verentchikov, *Nauchn. Priborostroenie* **14** (2), 38 (2004).
15. Yu. I. Hasin, A. N. Verentchikov, M. A. Gavrik, *et al.*, *Nauchn. Priborostroenie* **14** (2), 59 (2004).
16. D. J. Douglas and J. B. French, *J. Am. Soc. Mass Spectrom.* **3**, 398 (1992).
17. D. J. Douglas and J. B. French, US Patent No. 4,963,736 (December 12, 1988).
18. H. Vollnik and A. Casares, *Int. J. Mass. Spectrom.* **227**, 217 (2003).
19. M. Toyoda, D. Okumura, M. Ishihara, *et al.*, *J. Mass Spectrom.* **38**, 1125 (2003).
20. L. M. Nazarenko, L. Sekunova, and E. M. Yakushev, Patent Appl. No. 1,725,289 A1 (Russia, 1992).
21. A. Verentchikov and M. Yavor, in *Proceedings of the 51st ASMS Conference on Mass Spectrometry and Applied Topics, Montreal, 2003*; [www.asms.org](http://www.asms.org).
22. A. N. Verentchikov and M. I. Yavor, *Nauchn. Priborostroenie* **14**, 46 (2004).
23. G. Vol'nik, *Optics of Charged Particles* (Énergoatomizdat, St. Petersburg, 1992) [in Russian].
24. D. A. Dahl, *SIMION 3D, Version 7.0: User's Manual* (Idaho National Eng. Envir. Lab., 2000).
25. Yu. I. Hasin, M. A. Gavrik, V. N. Demidov, *et al.*, *Nauchn. Priborostroenie* **14** (2), 72 (2004).
26. Ya. I. Lyutvinskiĭ, D. M. Petrov, A. N. Verentchikov, *et al.*, *Nauchn. Priborostroenie* **14** (2), 80 (2004).

Translated by V. Isaakyan

---

---

**ELECTRON AND ION BEAMS,  
ACCELERATORS**

---

---

# Multireflection Planar Time-of-Flight Mass Analyzer. II: The High-Resolution Mode

**A. N. Verentchikov, M. I. Yavor, Yu. I. Hasin, and M. A. Gavrik**

*Institute of Analytical Instrument Making, Russian Academy of Sciences,  
Rizhskii pr. 26, St. Petersburg, 190103 Russia*

*e-mail: iap@ianin.spb.ru*

Received June 1, 2004

**Abstract**—The feasibility of the high-resolution operating mode in a planar multireflection time-of-flight analyzer that is suggested in Part I of this work is demonstrated. Time-of-flight aberrations, which limit the resolution, are estimated. A resolution as high as 200 000 at a time of flight of 70 ms is achieved in experiments. It is shown that the maximal resolution is limited by the duration of the ion packet generated by the source. The resolution can be improved by closing the ion beam trajectory with the formation of repeating cycles. The number of the cycles depends on the beam intensity losses due to scattering by the residual gas. It seems likely that the resolution can be improved further by using a higher vacuum, refining the ion source, and applying more stable power supplies. © 2005 Pleiades Publishing, Inc.

## INTRODUCTION

In Part I of this work [1], we studied a multireflection time-of-flight (TOF) mass analyzer where ions describe a zigzag trajectory sequentially reflecting from two 2D electrostatic mirrors. This analyzer is aimed at extending the time of flight of the ions in order to analyze parent ions in a tandem mass spectrometer that provides parallel recording of fragment spectra [2, 3] and still operates with the entire mass range at a moderate resolution. However, a large time of flight requires that the analyzer operate at low ion energies (no higher than 100 eV). To solve this problem, specially designed high-quality gridless ion mirrors were suggested [4], which provide third-order TOF focusing in energy and second-order TOF focusing in lateral spatial spread of the beam ions. The reliable confinement of the ion beam in the plane of zigzag motion is provided by beam focusing in a periodic set of 2D lenses placed between the mirrors. In the perpendicular plane, the ions are confined with the help of focusing mirrors.

Owing to the high-order TOF focusing of the ion beam, time aberrations in the analyzer are low. In the experiments with the prototype of the analyzer, no beam intensity losses were noticed after the beam had reflected from the mirrors ten times [5]. It is therefore natural to expect that a further extension of the ion path will considerably improve the resolution compared with that achieved in [1], specifically, in view of the fact that multireflection and multiturn TOF mass analyzers developed by other teams of researchers have demonstrated a resolution on the order of several tens of thousands [6] or even several hundreds of thousands [7]. The aim of this work is to demonstrate the feasibility of the high-resolution mode in a planar multireflection TOF analyzer.

## ESTIMATION OF TIME-OF-FLIGHT ABERRATIONS IN THE ANALYZER

Let the length of the zigzag trajectory of the ions in the analyzer depicted in Figs. 3 and 5 in [1] be so large that the initial segment of the trajectory from the ion source to midplane  $YZ$  of the analyzer (i.e., to initial entering into the lens unit in Fig. 5 in [1]) and the final segment of the trajectory between the midplane and detector are minor contributors to TOF aberrations. We also assume that, for each length the ions travel when passing through one “cell” of the analyzer (i.e., the length from the midplane and back to it after one reflection from the mirror), the parallel-to-point focusing conditions  $(y|y) = 0$  and  $(\zeta|\zeta) = 0$  are met for the coefficients

$$y(x) = (y|y)y_0 + (y|b)b_0 + (y|y\delta)y_0\delta + (y|b\delta)b_0\delta + \dots,$$

$$\zeta(x) = (\zeta|\zeta)\zeta_0 + (\zeta|a)a_0 + (\zeta|\zeta\delta)\zeta_0\delta + (\zeta|a\delta)a_0\delta + \dots$$

of expansion in initial values  $y_0$  and  $\zeta_0$ . Here,  $\delta = (K - K_0)/K_0$ ,  $K$  is the ion energy, and  $K_0$  is the mean ion energy in the beam. Coordinate  $\zeta = z - z_0$  is measured from axial trajectory  $z_0(x)$  of the beam.

The passage of two cells by an ion will be called a “turn” of the ion. Then, with regard for the mirror symmetry of the cells and parallel-to-point focusing, the ion trajectory will change sign (in a linear approximation) of its coordinates  $y$  and  $\zeta$ , as well as of the related slopes ( $a = d\zeta/dx = \tan\alpha$  and  $b = dy/dx = \tan\beta$ ), after each turn with their absolute values remaining unchanged.

After two turns, the trajectory transforms into itself in a linear approximation. Accordingly, after  $N$  turns of an ion, its total time aberration will equal  $N$  one-turn time aberrations.

As was shown in [1], the planar multireflection analyzer offers third-order TOF focusing in energy and second-order TOF focusing in spread in the  $Y$  direction; that is, the conditions

$$\begin{aligned}(t|\delta) &= (t|\delta\delta) = (t|\delta\delta\delta) = 0, \\ (t|y) &= (t|b) = (t|y\delta) = (t|b\delta) \\ &= (t|yy) = (t|yb) = (t|yy) = 0\end{aligned}$$

are fulfilled for the coefficients of expansion of the TOF for an ion with a fixed mass:

$$\begin{aligned}t(x) &= t_0 + (t|y)y_0 + (t|b)b_0 + (t|\zeta)\zeta_0 + (t|b)b_0 + (t|\delta)\delta \\ &+ (t|yy)y_0^2 + (t|yb)y_0b_0 + (t|bb)b_0^2 + (t|y\delta)y_0\delta \\ &+ (t|b\delta)b_0\delta + (t|\delta\delta)\delta^2 + (t|\delta\delta\delta)\delta^3 + \dots,\end{aligned}$$

where  $t_0$  is the TOF of a mean-energy ion.

Furthermore, at small drift angles  $\varepsilon = dz_0(x)/dx$ , i.e., at a small inclination of the beam axial trajectory to the  $X$  axis in the intermirror space, the following conditions are met:

$$\begin{aligned}(t|\zeta) &\approx 0, \quad (t|a) \approx 0, \quad (t|\zeta a) \approx 0, \\ (t|\zeta\delta) &\approx 0, \quad (t|a\delta) \approx 0\end{aligned}$$

(these coefficients would be exactly equal to zero in the case of symmetry at  $\varepsilon = 0$ , that is, if the beam would execute a reciprocating motion along the optical axis parallel to the  $X$  axis).

Thus, the basic contributors to TOF aberrations in the analyzer are (i) second-order geometric aberrations  $(t|\zeta\zeta)$  and  $(t|aa)$  due to the 2D lenses, which focus the beam in plane  $XZ$ ; (ii) third-order chromatic aberrations  $(t|yy\delta)$  and  $(t|yb\delta)$  due to the mirrors and  $(t|aa\delta)$ ,  $(t|\zeta\zeta\delta)$  due to the 2D lenses (coefficients  $(t|yb\delta)$  and  $(t|\zeta a\delta)$  vanish after each turn owing to the mirror symmetry of the cells; and (iii) fourth-order chromatic aberration  $(t|\delta\delta\delta\delta)$ . It is these aberrations growing proportionally to the number of turns that specify the ultimate resolution of the instrument.

To estimate the aberration-related limit of the resolution of the analyzer prototype (for details, see [1]), we calculated the aberration coefficients mentioned above. Their values are listed in Table 1. Table 2 gives the aberration-related resolution limits (calculated under the assumption that the pulse width at the exit to the analyzer is negligible) at the peak half-maximum for several typical initial values of the beam parameters.

From Table 2, it follows that second-order TOF angular aberration  $(t|aa)$  is the basic ion-optical factor that governs the aberration-related limit of the resolution. With the angular divergence of the beam in plane  $XZ$  not exceeding  $0.5^\circ$  and the beam being initially sev-

**Table 1.** Values of the basic nonzero TOF aberration coefficients for one turn of ions with a rated energy of 100 eV and a mass of 1000 u (the transit time equals 278  $\mu$ s)

$(t aa)$	$(t \zeta\zeta)$	$(t bb\delta)$	$(t yy\delta)$	$(t aa\delta)$	$(t \zeta\zeta\delta)$	$(t \delta\delta\delta\delta)$
331	0.00088	3333	0.05	-300	-0.0017	4479

Note: The times are given in microseconds; linear dimensions, in millimeters; angles, in values of their tangents; and energies, in fractions of the rated value.

**Table 2.** Aberration-limited maximal mass resolution  $R_m$  at the peak half-maximum for typical spreads of the initial ion parameters in the beam

$2\Delta y = 2\Delta\zeta$ , mm	$2\Delta a = 2\Delta b$ , deg	$2\Delta\delta$ , %	$R_m$
1	0.5	1	1 300 000
1	1	1	300 000
2	0.5	1	600 000
2	1	1	150 000
1	0.5	5	500 000
1	1	5	60 000
2	0.5	5	300 000
2	1	5	40 000
1	0.5	10	300 000
1	1	10	30 000
2	0.5	10	200 000
2	1	10	20 000

eral millimeters across, one may expect the resolution to be as high as several hundreds of thousands even if the energy spread in the beam is appreciable.

It should be noted that, in reference to the lateral spatial spread of the ions, the TOF aberration coefficients listed above are several times smaller than those reported in [7] for a multiturn analyzer that demonstrated a resolution of 350 000. In addition, the planar analyzer considered offers much better energy focusing compared with that described in [7]. This fact lets us conclude that a planar analyzer resolution as high as several hundreds of thousand is quite feasible.

## EXPERIMENTAL RESULTS

In experiments aimed at studying the high-resolution mode, we used the same prototype as in Part I of this work [1]. A cesium gun [8] generating an ion beam of energy 100 eV served as a test source. The energy spread in the ion beam, which resulted largely from the pulse modulation, was within 3–4%. The exit slit of the ion source was 1 mm wide, and the angular divergence of the beam in the analyzer, which was limited by the windows in the masks before the lens unit, was estimated as somewhat exceeding  $1^\circ$ . For such parameters of the output beam, the calculated aberration-limited



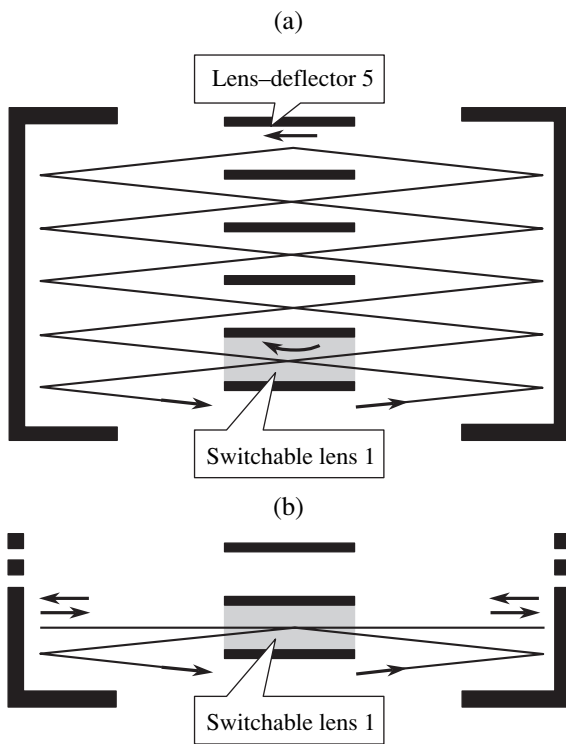


**Fig. 1.** Ion trajectory closing conditions in the analyzer: (a) zigzag motion of the ions and (b) reciprocating motion of the ions.

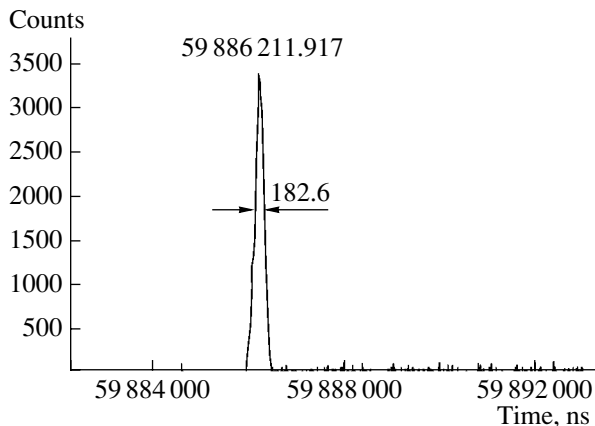


**Fig. 2.** Typical time signal recorded at long transit times.

resolution of the analyzer at the peak half-maximum is roughly equal to 150 000. The basic limiter here is second-order angular aberration ( $t_{aa}$ ) in the lenses.

With such an ion source, the minimal duration of the ion pulse ( $>100$  ns) at the primary time focus cannot provide the one-pass length that provides a high resolution. To remedy the situation, the ion trajectories in the analyzer were closed to form repeating cycles by changing over the operating mode of lens 1 in the lens unit [1, Fig. 6]. The closing was accomplished in two ways (Fig. 1).

(1) In the first case, the ions were injected into the analyzer when lens 1 first operated in the normal (focusing) mode and then (after the ions have passed through it) the potentials of its electrodes were switched to the deflecting mode. As a result, the ion beam turned around in lens-deflector 5 and returned to lens 1, which directed it again to the analyzer (Fig. 1a). After the beam had executed a number of zigzag cycles between lenses 1 and 5, the former was switched back to the pure focusing mode and the ion beam left the analyzer for the detector.

(2) In the other case, lens 1 initially served as a deflector, so that the mirror-reflected beam arriving at the lens was directed normally to the mirrors (Fig. 1b). Once the beam has passed lens 1, its electrode potentials were switched to the focusing mode without deflecting the beam. In other words, the beam executed reciprocating motion in the analyzer, traveling along the same rectilinear optical axis passing through lens 1. After a number of cycles (turns), lens 1 was switched again to the initial (deflecting) mode and the beam left the analyzer for the detector.

When the ion trajectories cycle, the effective mass range narrows in proportion to the number of cycles, since the detector cannot discriminate between the ions that executed  $N$  and  $N + 1$  cycles. This restriction, along with the lean spectral composition of the ions emitted by the gun, made simultaneous recording of several ionic components at long transit times impossible. Therefore, the resolution of the analyzer under the closed trajectory conditions was estimated relative to the Cs peak width in the detector. For this width not to be influenced by self-bunching [9] due to the space charge of the beam, the recording procedure was carried out at small amounts of ions (down to single ions) in a pulse. In this case, the peaks were recorded with the AR-100 ADC in the accumulation mode [10]. A typical signal waveform is shown in Fig. 2. Here, the sharpness of the peak (the absence of extended tails) and the low noise level at very large transit times are noteworthy.

Figure 3 plots the FWHM of the peak, its amplitude, and the mass resolution of the analyzer against the transit time of the ions under the second cycling conditions. The time a single 100-eV  $\text{Cs}^+$  ion takes to make a complete turn (two reflections from the mirrors) is about 100  $\mu\text{s}$ ; that is, the ions in the analyzer made 700 turns, traveling a distance of 700 m (1 m per turn). The adjustment of the analyzer was kept unchanged for any transit time (which was controlled by the time lens 1 was switched from the deflecting to focusing mode and vice versa). Since the adjustment was optimized for long transit times, the time signal somewhat broadens and its amplitude slightly decreases at short transit times, as follows from Figs. 3a and 3c.

Surprisingly, an ultimate resolving power of about 200 000, which was invariably demonstrated by the analyzer in a series of measurements, exceeded the theoretical predictions mentioned above. Moreover, the

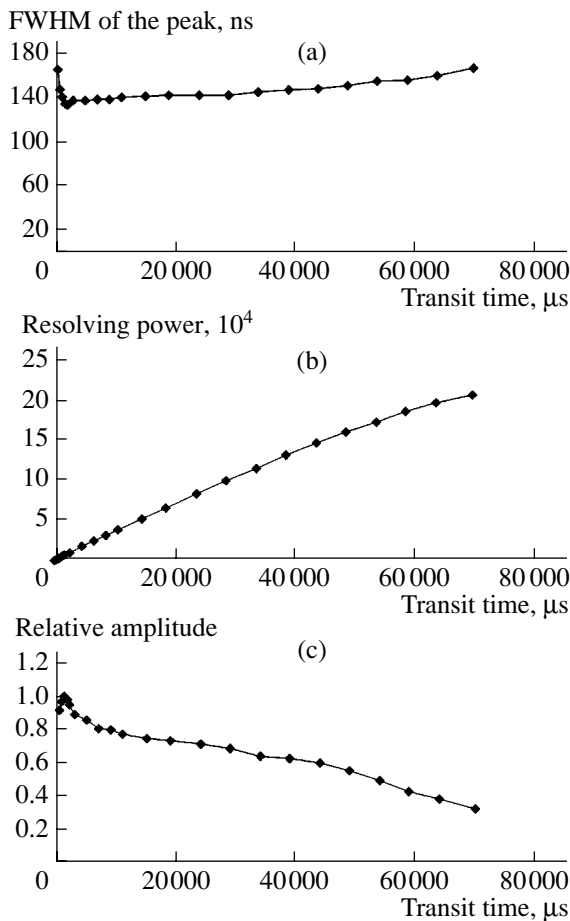


**Fig. 3.** (a) FWHM of the signal detected, (b) resolving power at the half-maximum of the peak, and (c) signal relative amplitude vs. the transit time.

increase in the pulse duration and the linear growth of the resolution with increasing transit time up to its maximal value (Figs. 3a, 3b) clearly indicate that the aberration-limited value of the resolution was not reached. The maximal resolution was apparently limited by factors other than aberration, of which the following two seem to be basic.

The first is the instability of the power supplies that feed the electrodes of the ion source, mirrors, and lenses. The signals that are sequentially recorded at large transit times and correspond to moderate amounts of accumulated responses to the arrival of single ions exhibit high-frequency oscillations of the positions of their maxima. Since these oscillations correlate with the time instant the signals are recorded, they may be related to the variation of the transit time with the electrode potential, primarily, with the potential of the reflecting electrode of the mirrors. The amplitude of the oscillations is comparable to the duration of the signals, causing broadening of the time peaks.

The second reason lies in the fact that the amplitude of the signal decreases with increasing transit time,

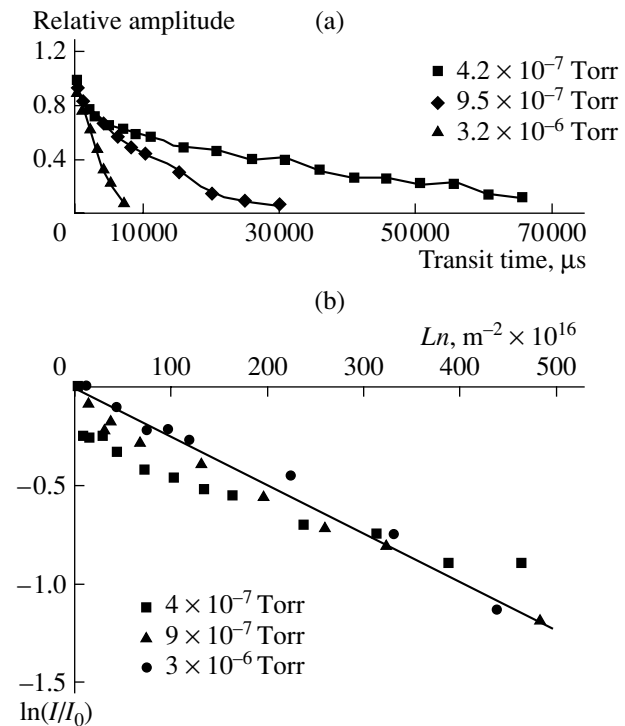


**Fig. 4.** (a) Signal relative amplitude at the detector vs. the transit time for different pressures in the analyzer and (b) the logarithm of the relative intensity vs. the product of the transit length and residual gas concentration in the chamber.

which limits the measuring capabilities of the system. In the analyzer, some of the ions (namely, those the energies and coordinates of which diverge significantly from the mean values) may be lost at the masks of the lenses and mirrors. Such an assumption finds an indirect confirmation in that the maximal experimental resolution of the analyzer exceeds the aberration-limited maximum predicted.

Ion scattering by a residual gas also results in ion losses. To estimate this contribution, we carried out the measurements at different pressures with the adjustment of the analyzer kept unchanged. It was found that the resolution does not change when the pressure in the chamber varies by one order of magnitude from  $4 \times 10^{-6}$  to  $3 \times 10^{-7}$  Torr. However, the transmission of the instrument heavily depended on the pressure, as follows from Fig. 4a. One may therefore expect that the transit time will increase (accordingly, the resolution will be improved) in a higher vacuum. The ion beam intensity as a function of the transit time is plotted in Fig. 4b. As is seen from this figure, the loss of 100-eV ions is described well by the exponential law  $\ln(I/I_0) = -Ln\sigma$ , where  $I$  is the intensity of the ion beam after it has traveled distance  $L$ ,  $I_0$  is the beam intensity at the entrance to the analyzer,  $n$  is the volume concentration of gas molecules, and  $\sigma$  is the scattering cross section. The curve in Fig. 4b is drawn for cesium ion scattering by nitrogen molecules ( $\sigma = 25 \text{ \AA}^2$ ).

Note that the measurements performed under the first cycling (closing) conditions showed a lower (about 110 000) maximal resolution. This finding is supposed to be associated with a periodic deflection of the ion beam in the first and last (fifth) lenses of the lens unit, which adversely affects the performance of the instrument. First, such a deflection causes a spatial dispersion of the ions in energy and, thereby, expands the spatial phase volume of the beam (hence, deteriorates the transmission of the analyzer). Second, the deflection introduces extra TOF aberrations, specifically, the first-order dependence of the transit time on angle of inclination  $\alpha$  and spatial coordinate  $\zeta$  of the ions.

### CONCLUSIONS

In Part II of this work, we showed theoretically and experimentally that the planar multireflection TOF analyzer described in Part I is promising for reaching a very high mass resolution (on the order of several hundreds of thousands) at a sufficiently high acceptance. This statement is based on the fact that the analyzer is equipped with specially designed high-quality gridless ion mirrors, allowing the ions to stably make several hundreds of turns. It may be expected that use of a larger number of lenses in order to extend the length of the unclosed cycle of the ion motion will make it possi-

ble to set the high-resolution mode without (or with minor) restrictions on the mass range.

### REFERENCES

1. A. N. Verentchikov, M. I. Yavor, Yu. I. Khasin, *et al.*, Zh. Tekh. Fiz. **75** (1), 74 (2005) [Tech. Phys. **50**, 73 (2005)].
2. A. Verentchikov, GB Patent No. 2,390,935 (July 16, 2002).
3. A. N. Verentchikov, Nauchn. Priborostroenie **14** (2), 24 (2004).
4. M. I. Yavor and A. N. Verentchikov, Nauchn. Priborostroenie **14** (2), 38 (2004).
5. Yu. I. Khasin, A. N. Verentchikov, M. A. Gavrik, *et al.*, Nauchn. Priborostroenie **14** (2), 59 (2004).
6. H. Wollnik and A. Casares, Int. J. Mass. Spectrom. **227**, 217 (2003).
7. M. Toyoda, D. Okumura, M. Ishihara, *et al.*, J. Mass Spectrom. **38**, 1125 (2003).
8. Yu. I. Khasin, M. A. Gavrik, V. N. Demidov, *et al.*, Nauchn. Priborostroenie **14** (2), 72 (2004).
9. D. Strasser, T. Geyer, H. B. Pedersen, *et al.*, Phys. Rev. Lett. **89**, 283204 (2002).
10. Ya. I. Lyutvinskiĭ, D. M. Petrov, A. N. Verentchikov, *et al.*, Nauchn. Priborostroenie **14** (2), 80 (2004).

*Translated by V. Isaakyan*

ELECTRON AND ION BEAMS,  
ACCELERATORS

# Tunable Wakefield Dielectric-Filled Accelerating Structure

A. M. Altmark, A. D. Kanareykin, and I. L. Sheinman

St. Petersburg State Electrotechnical University, ul. Prof. Popova 5, St. Petersburg, 197376 Russia

e-mail: lab@physics.etu.spb.ru

Received November 2, 2003; in final form, June 29, 2004

**Abstract**—The feasibility of the frequency spectrum of Vavilov–Cherenkov radiation being controlled in a wakefield dielectric-filled accelerating structure via an outer ferroelectric layer is studied. The spectrum and amplitude of the field excited in the structure versus the permittivity of the ferroelectric are found. Dielectric losses in the ferroelectric are estimated. It is shown that these losses impose limitations on the ferroelectric layer thickness and the range within which the frequency spectrum of the waveguide can be controlled. The structure under consideration is optimized for the AWA wakefield accelerator. The multilayer construction of the waveguide, in combination with specially shaped ferroelectric-permittivity-controlling electrodes, allows designers to tune the spectrum of the waveguide and suppress electron-bunch-deflecting waveguide modes. Thereby, there appears the possibility of controlling the transverse stability of the beam. © 2005 Pleiades Publishing, Inc.

## INTRODUCTION

Wakefield acceleration of charged particles (a method where wake fields downstream of electron bunches passing through a dielectric waveguide are used) is nowadays the subject of extensive theoretical and experimental investigation [1–4].

Wakefield acceleration implies energy transfer from a high-current electron bunch to a high-energy low-charged one. In an accelerating structure, the former generates an electromagnetic field with a longitudinal component amplitude as high as 100 MV/m. This component is used to accelerate a subsequent low-current bunch [1].

In this work, we consider an accelerating structure [1–4] that represents a circular metallic dielectric-filled bunch-directing waveguide the inner evacuated channel of which has a radius  $R_c$ . The outer side of the dielectric wall with a radius  $R_w$  is metallized (Fig. 1). The basic requirement for the waveguide structure of a wakefield accelerator is electromagnetic loss minimization in the waveguide material. To this end, ceramic materials with a high figure of merit ( $Q = 10^5$  at a frequency of 10 GHz) and the dielectric loss tangent  $\tan\delta$  not exceeding  $10^{-4}$  are employed. The permittivity  $\epsilon_1$  of the waveguide material depends on the structure and ranges widely from 4 to 36 [3, 4].

The fulfillment of the phase relationships (the low-current bunch must be kept within the accelerating phase of the wave) imposes strict tolerances on the waveguide parameters and bunch position. If ultrarelativistic bunches are accelerated, the increase in the beam energy does not violate the wave–bunch phase relationships. However, the problem of compensating for frequency shifts due to a discrepancy between the

actual and rated parameters of the structure, as well as to a mismatch between the waveguide sections of the accelerator, still persists. Varying the permittivity of the waveguiding system, one can control the wave–bunch phase relationships and provide the most favorable energy conditions for acceleration. In [5], a method of controlling the frequency spectrum of the waveguide in a wakefield dielectric-filled accelerator was suggested. In this method, the frequency spectrum is tuned with a ferroelectric film applied on the outer side of the dielectric waveguide.

In this work, we perform computer simulation of a two-layer waveguide (Fig. 2), the frequency spectrum of which can be tuned as described above. Unlike the conventional dielectric-filled accelerating structures [1–4], the system suggested incorporates an additional ceramic (ferroelectric) layer placed between a linear dielectric of radius  $R_d$  and a metallic wall of radius  $R_w$  [6, 7]. The spectrum of this waveguide can be tuned by varying the permittivity  $\epsilon_2$  of the ferroelectric. Permittivity  $\epsilon_2$  changes when the ferroelectric is subjected to an external electric field. In other words, the spectrum of the wake field can be influenced in real time (i.e., during the experiment).

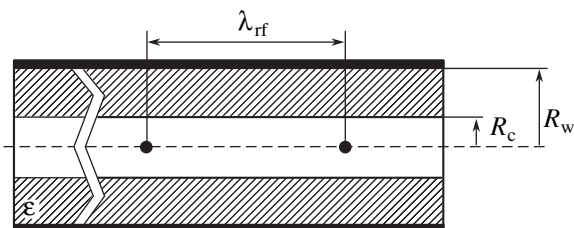


Fig. 1. Single-layer dielectric waveguide.

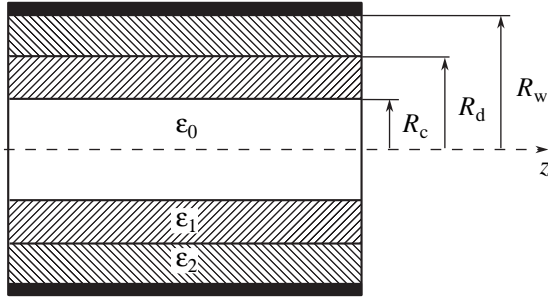


Fig. 2. Dielectric waveguide with a ferroelectric layer.

### WAKE (VAVILOV-CHERENKOV) FIELD IN A DIELECTRIC WAVEGUIDE WITH A FERROELECTRIC LAYER

An expression for the field produced by a point electron bunch in a single-layer waveguide was derived in [8–10]. To derive this expression for a multilayer waveguide, we will use the Maxwell equations and related boundary conditions in the waveguide:

$$\nabla \times \mathbf{E} = -\frac{1}{c} \frac{\partial \mathbf{B}}{\partial t}, \quad (1)$$

$$\nabla \times \mathbf{H} = \frac{1}{c} \frac{\partial \mathbf{D}}{\partial t} - \frac{4\pi en\mathbf{V}}{c}, \quad (2)$$

$$\nabla \cdot \mathbf{B} = 0, \quad (3)$$

$$\nabla \cdot \mathbf{D} = -4\pi en, \quad (4)$$

$$\mathbf{B} = \mu \mathbf{H}, \quad (5)$$

$$\mathbf{D} = \varepsilon \mathbf{E}. \quad (6)$$

Here,  $\mathbf{E}$  and  $\mathbf{H}$  are the electric and magnetic field strengths, respectively;  $\mathbf{D}$  and  $\mathbf{B}$  are the electric and magnetic inductions;  $c$  is the speed of light in a vacuum; and  $e$ ,  $n$ , and  $\mathbf{V}$  are the charge, density, and velocity of electrons, respectively.

Let a point electron bunch with charge  $q$  move with velocity  $V = \beta c$  along the cylindrical waveguide at distance  $r_0$  from its axis. Then, the electron density will have the form

$$n = \frac{q}{e} \delta(z - Vt) \frac{\delta(r - r_0)}{|\mathbf{r} - r_0|} \delta(\theta).$$

The components of the electric and magnetic fields can be expressed through longitudinal components  $E_z$  and  $H_z$ . For  $E_z$  and  $H_z$ , the Maxwell equations appear as

$$\left( \nabla^2 - \frac{\varepsilon_0}{c^2} \frac{\partial^2}{\partial t^2} \right) E_z = -\frac{4\pi e}{\varepsilon_0} \left( \frac{\varepsilon_0 \beta}{c} \frac{\partial n}{\partial t} + \frac{\partial n}{\partial z} \right), \quad (7)$$

$$\left( \nabla^2 - \frac{\varepsilon_0}{c^2} \frac{\partial^2}{\partial t^2} \right) H_z = 0. \quad (8)$$

Let us expand all the quantities entering into Eqs. (1)–(8) in a series in mode number  $\nu$  (hereafter, subscript  $\nu$  will be omitted for simplicity) and apply the Fourier transformation in the cylindrical coordinate system  $(r, \theta, z)$  to  $E_z$ :

$$E_z(r, \theta, z, t) = \sum_{\nu=-\infty}^{\infty} \exp(j\nu\theta) \times \int_{-\infty}^{\infty} \tilde{E}_{z\nu}(r, \omega) \exp(j(z - Vt)\omega/V) d\omega.$$

Then, we have

$$n = \frac{1}{4\pi^2 V} \sum_{\nu=-\infty}^{\infty} \exp(j\nu\theta) \int_{-\infty}^{\infty} \exp(j\zeta\omega/V) n_{\nu}(r, \omega) d\omega = \frac{1}{4\pi^2 V} \sum_{\nu=-\infty}^{\infty} \exp(j\nu\theta) \times \iint \exp(j\zeta\omega/V) J_{\nu}(\rho r) J_{\nu}(\rho r_0) \rho d\rho d\omega,$$

where  $J_{\nu}$  is the Bessel function of order  $\nu$  and  $\zeta = z - Vt$ .

Equation (7) can be recast as

$$\left( \nabla^2 - \frac{\varepsilon_0 \omega^2}{c^2} \right) E_{z\nu}(r, \omega) = \phi_{\nu}(r, \omega), \quad (9)$$

where

$$\nabla^2 = \frac{1}{r} \frac{\partial}{\partial r} \left( r \frac{\partial}{\partial r} \right) - \frac{\omega^2}{c^2} - \frac{\nu^2}{r^2},$$

$$\phi_{\nu}(r, \omega) = \frac{je\omega(1 - \varepsilon_0\beta^2)}{V^2\pi\varepsilon_0} \int_0^{\infty} \rho J_{\nu}(\rho r) J_{\nu}(\rho r_0) d\rho.$$

A partial solution to (9) can be found in the form

$$E_{z\nu}^{\text{part}}(r, \omega) = -\frac{jq\omega(1 - \beta^2)}{\pi V^2} \int_0^{\infty} \frac{\rho J_{\nu}(\rho r) J_{\nu}(\rho r_0)}{(\rho^2 + (\omega/c)^2(1 - \beta^2))} d\rho.$$

Then, integration over  $\rho$  yields

$$E_{z\nu}^{\text{part}}(r, \omega) = -\frac{jq\omega}{\pi V^2 \gamma^2} \begin{cases} I_{\nu}(\gamma\omega r/V) K_{\nu}(\gamma\omega r_0/V) & r < r_0 \\ K_{\nu}(\gamma\omega r/V) I_{\nu}(\gamma\omega r_0/V) & r \geq r_0, \end{cases}$$

where  $\gamma = (1 - \beta^2)^{-1/2}$  and  $I_{\nu}$  and  $K_{\nu}$  are the modified Bessel function and the Macdonald function of order  $\nu$ , respectively.

We will consider the case  $r \geq r_0$ . The general solution to (9) has the form

$$E_{zv}^{\text{gen}} = \begin{cases} AI_v(\chi_0 r), & 0 \leq r \leq R_c, \\ C_1 J_v(\chi_1 r) + D_1 N_v(\chi_1 r), & R_c \leq r \leq R_d, \\ E(J_v(\chi_2 r) - N_v(\chi_2 r)J_v(\chi_2 R_w)/N_v(\chi_2 R_w)), & R_d \leq r \leq R_w; \end{cases} \quad (10)$$

$$H_{zv}^{\text{part}} = \begin{cases} BI_v(\chi_0 r), & 0 \leq r \leq R_c, \\ C_2 J_v(\chi_1 r) + D_2 N_v(\chi_1 r), & R_c \leq r \leq R_d, \\ F(J_v(\chi_2 r) - N_v(\chi_2 r)J_v(\chi_2 R_w)/N_v(\chi_2 R_w)), & R_d \leq r \leq R_w, \end{cases} \quad (11)$$

where

$$\chi_0 = k \sqrt{\frac{(1 - \beta^2 \epsilon_0)}{\beta^2}}, \quad \chi_1 = k \sqrt{\frac{(\beta^2 \epsilon_1 - 1)}{\beta^2}}, \\ \chi_2 = k \sqrt{\frac{(\beta^2 \epsilon_2 - 1)}{\beta^2}}, \quad k = \frac{\omega}{c}.$$

The complete solution inside the waveguide can be written as a sum of the general and partial solutions:

$$E_{zv} = E_{zv}^{\text{gen}} + E_{zv}^{\text{part}} = AI_v(\chi_0 r) + \eta K_v(\chi_0 r),$$

where

$$\eta = -\frac{jqk\chi_0^2}{\pi c} I_v(\chi_0 r_0).$$

Let us apply the boundary conditions of continuity of the tangential electric and magnetic field components  $E_{\theta v}$ ,  $H_{\theta v}$ ,  $E_{zv}$ , and  $H_{zv}$  at the vacuum–dielectric and dielectric–ferroelectric interfaces. Expressing  $E_{\theta v}$  and  $H_{\theta v}$  through  $E_{zv}$  and  $H_{zv}$ , we arrive at

$$E_{\theta v} = \frac{1}{\chi^2} \left( \frac{vk}{r\beta} E_{zv} - jk \frac{\partial H_{zv}}{\partial r} \right), \quad (12)$$

$$H_{\theta v} = \frac{1}{\chi^2} \left( \frac{vk}{r\beta} H_{zv} + jk \epsilon_0 \frac{\partial E_{zv}}{\partial r} \right). \quad (13)$$

The radial component of the electric field can be written in the form

$$E_{rv} = \frac{1}{\chi^2} \left( \frac{vk}{r} H_{zv} - \frac{jk}{\beta} \frac{\partial E_{zv}}{\partial r} \right).$$

Eventually, we obtain a set of eight equations for coefficients  $A$ ,  $B$ ,  $E$ ,  $F$ ,  $C_1$ ,  $D_1$ ,  $C_2$ , and  $D_2$ . In view of (12) and (13), this set can be reduced to a set of four

equations for  $C_1$ ,  $D_1$ ,  $C_2$ , and  $D_2$ :

$$\begin{bmatrix} m_{11} & m_{12} & m_{13} & m_{14} \\ m_{21} & m_{22} & m_{23} & m_{24} \\ m_{31} & m_{32} & m_{33} & m_{34} \\ m_{41} & m_{42} & m_{43} & m_{44} \end{bmatrix} \begin{bmatrix} C_1 \\ D_1 \\ C_2 \\ D_2 \end{bmatrix} = \begin{bmatrix} 0 \\ \Psi \\ 0 \\ 0 \end{bmatrix}, \quad (14)$$

where

$$\Psi = \frac{-jk}{\chi_0} \left( K_v'(\chi_0 R_c) - \frac{I_v'(\chi_0 R_c)}{I_v(\chi_0 R_c)} \right),$$

$$m_{11} = \frac{vk J_v(\chi_1 R_c)}{\beta R_c} \left( \frac{1}{\chi_0^2} + \frac{1}{\chi_1^2} \right),$$

$$m_{21} = j \left( \frac{\epsilon_1 J_v'(\chi_1 R_c)}{\chi_1} + \frac{\epsilon_0 J_v(\chi_1 R_c) I_v'(\chi_0 R_c)}{\chi_0 I_v(\chi_0 R_c)} \right),$$

$$m_{31} = \frac{-vk J_v(\chi_1 R_d)}{\beta R_d} \left( \frac{1}{\chi_0^2} + \frac{1}{\chi_1^2} \right),$$

$$m_{41} = -jk \left( \frac{J_v'(\chi_1 R_d) \epsilon_1}{\chi_1} + \frac{J_v(\chi_1 R_d) \Delta_{21}}{\chi_2 \Delta_{22}} \right),$$

$$m_{12} = \frac{vk K_v(\chi_1 R_c)}{\beta R_c} \left( \frac{1}{\chi_0^2} + \frac{1}{\chi_1^2} \right),$$

$$m_{22} = j \left( \frac{\epsilon_1 N_v'(\chi_1 R_c)}{\chi_1} + \frac{\epsilon_0 N_v(\chi_1 R_c) I_v'(\chi_0 R_c)}{\chi_0 I_v(\chi_0 R_c)} \right),$$

$$m_{32} = \frac{-vk N_v(\chi_1 R_d)}{\beta R_d} \left( \frac{1}{\chi_0^2} + \frac{1}{\chi_1^2} \right),$$

$$m_{42} = -jk \left( \frac{N_v'(\chi_1 R_d) \epsilon_1}{\chi_1} + \frac{N_v(\chi_1 R_d) \Delta_{21}}{\chi_2 \Delta_{22}} \right),$$

$$m_{13} = -j \left( \frac{J_v(\chi_1 R_c) I_v'(\chi_0 R_c)}{\chi_0 I_v(\chi_0 R_c)} + \frac{J_v'(\chi_1 R_c)}{\chi_1} \right),$$

$$m_{23} = \frac{vk J_v(\chi_1 R_c)}{\beta R_c} \left( \frac{1}{\chi_0^2} + \frac{1}{\chi_1^2} \right),$$

$$m_{33} = jk \left( \frac{J_v'(\chi_1 R_d)}{\chi_1} + \frac{J_v(\chi_1 R_d) \Delta_{11}}{\chi_2 \Delta_{12}} \right),$$

$$m_{43} = \frac{vk J_v(\chi_1 R_d)}{\beta R_d} \left( \frac{1}{\chi_1^2} + \frac{1}{\chi_2^2} \right),$$

$$m_{14} = j \left( \frac{-N_v(\chi_1 R_c) I_v'(\chi_0 R_c)}{\chi_0 I_v(\chi_0 R_c)} + \frac{-N_v'(\chi_1 R_c)}{\chi_1} \right),$$

$$m_{24} = \frac{vk N_v(\chi_1 R_c)}{\beta R_c} \left( \frac{1}{\chi_0^2} + \frac{1}{\chi_1^2} \right),$$

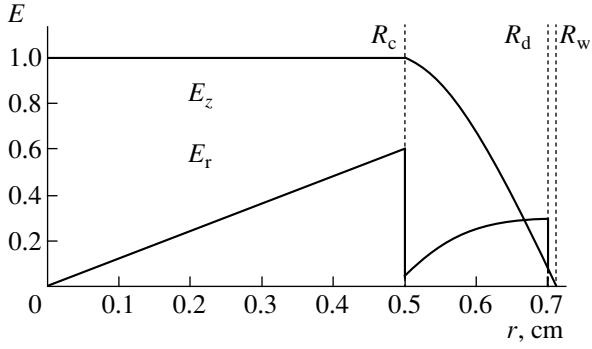


**Fig. 3.** Normalized radial and longitudinal electric field components vs. radial coordinate in the three-layer dielectric waveguide.

$$m_{34} = jk \left( \frac{N'_v(\chi_1 R_d)}{\chi_1} + \frac{N_v(\chi_1 R_d) \Delta_{11}(k, \nu)}{\chi_2 \Delta_{12}(k, \nu)} \right),$$

$$m_{44} = \frac{\nu k N_v(\chi_1 R_d)}{\beta R_d} \left( \frac{1}{\chi_1^2} + \frac{1}{\chi_2^2} \right),$$

$$\Delta_{11} = J'_v(\chi_2 R_d) N'_v(\chi_2 R_w) - J'_v(\chi_2 R_w) N'_v(\chi_2 R_d),$$

$$\Delta_{12} = -(J'_v(\chi_2 R_d) N'_v(\chi_2 R_w) - J'_v(\chi_2 R_w) N'_v(\chi_2 R_d)),$$

$$\Delta_{21} = -(J'_v(\chi_2 R_d) N'_v(\chi_2 R_w) - J'_v(\chi_2 R_w) N'_v(\chi_2 R_d)),$$

$$\Delta_{22} = J'_v(\chi_2 R_d) N'_v(\chi_2 R_w) - J'_v(\chi_2 R_w) N'_v(\chi_2 R_d).$$

Coefficients  $A$  and  $B$  in (10) and (11) are expressed as follows:

$$A = \frac{C_1 J'_v(\chi_1 R_c) + D_1 N'_v(\chi_1 R_c)}{I'_v(\chi_0 R_c)} - \eta \frac{K'_v(\chi_0 R_c)}{I'_v(\chi_0 R_c)},$$

$$B = \frac{C_2 J'_v(\chi_1 R_c) + D_2 N'_v(\chi_1 R_c)}{I'_v(\chi_0 R_c)},$$

where

$$C_1 = \frac{\text{Det}_1}{\text{Disp}}, \quad D_1 = \frac{\text{Det}_2}{\text{Disp}}, \quad C_2 = \frac{\text{Det}_3}{\text{Disp}}, \quad D_2 = \frac{\text{Det}_4}{\text{Disp}},$$

$$\text{Disp}(k, \nu)$$

$$= \begin{bmatrix} m_{11}(k, \nu) & m_{12}(k, \nu) & m_{13}(k, \nu) & m_{14}(k, \nu) \\ m_{21}(k, \nu) & m_{22}(k, \nu) & m_{23}(k, \nu) & m_{24}(k, \nu) \\ m_{31}(k, \nu) & m_{32}(k, \nu) & m_{33}(k, \nu) & m_{34}(k, \nu) \\ m_{41}(k, \nu) & m_{42}(k, \nu) & m_{43}(k, \nu) & m_{44}(k, \nu) \end{bmatrix}.$$

Determinants  $\text{Det}_1$ ,  $\text{Det}_2$ ,  $\text{Det}_3$ , and  $\text{Det}_4$  are found from determinant  $\text{Disp}$  by replacing the corresponding column by the column of free terms in Eq. (14). The dispersion relation of waves in the waveguide can be written in the form

$$\text{Disp}(k) = 0. \quad (15)$$

The Vavilov–Cherenkov field in an evacuated channel is given by

$$E_z^{\text{gen}}(r, \theta, \zeta) = \sum_{\nu=0}^{\infty} \exp(j\nu\theta) \int_{-\infty}^{\infty} E_{z\nu}(k, \nu) dk \quad (16)$$

$$= 4q \sum_{\nu=0}^{\infty} \exp(j\nu\theta) \sum_{m=0}^{\infty} \Phi_{E_z}(k_{\nu, m}, r, \nu) \cos\left(\frac{k_{\nu, m} \zeta}{\beta}\right),$$

$$H_z^{\text{gen}}(r, \theta, \zeta) = \sum_{\nu=0}^{\infty} \exp(j\nu\theta) \int_{-\infty}^{\infty} H_{z\nu}(k, \nu) dk \quad (17)$$

$$= 4q \sum_{\nu=0}^{\infty} \exp(j\nu\theta) \sum_{m=0}^{\infty} \Phi_{H_z}(k_{\nu, m}, r, \nu) \cos\left(\frac{k_{\nu, m} \zeta}{\beta}\right).$$

Here,  $\zeta = z - ct$  is a distance back of a bunch,

$$\Phi_{E_z}(k, r, \nu) = \Phi_1(k, \nu) I'_v(\chi_0 r_0) I'_v(\chi_0 r),$$

$$\Phi_{H_z}(k, r, \nu) = \Phi_2(k, \nu) I'_v(\chi_0 r_0) I'_v(\chi_0 r),$$

$$\Phi_1(k, \nu) = \frac{1 - \beta^2}{\beta^2}$$

$$\times \frac{k(\text{Det}_1 J'_v(\chi_1 R_c) + \text{Det}_2 N'_v(\chi_1 R_c) - K'_v(\chi_0 R_c) \text{Disp})}{I'_v(\chi_0 R_c) \frac{d}{dk} \text{Disp}},$$

$$\Phi_2(k, \nu) = \frac{1 - \beta^2 k(\text{Det}_3 J'_v(\chi_1 R_c) + \text{Det}_4 N'_v(\chi_1 R_c))}{\beta^2 I'_v(\chi_0 R_c) \frac{d}{dk} \text{Disp}}.$$

The field of a Gaussian bunch can be determined by taking the integral of convolution of point charge field (16) with the charge distribution in the bunch. Assuming that the charge in the bunch is normally distributed, we find

$$E_{z,r}(r, \zeta) = \int_{-\infty}^{\zeta} \frac{1}{\sqrt{2\pi\sigma_b}} \exp\left(-\frac{\zeta^2}{2\sigma_b^2}\right) E_{z,r}(r, s - \zeta) ds, \quad (18)$$

where  $\sigma_b$  is the length of the bunch.

The amplitude–frequency characteristic of the field depends on the bunch length in such a way that an extension of a bunch suppresses high-frequency modes. For example, if a 0.4-cm-long bunch propagates in a waveguide with  $R_c = 0.5$  cm and  $R_d = 0.7$  cm, the net field strength is roughly equal to the strength of the lowest frequency (i.e., first, or  $E_{01}$ ) mode.

Figure 3 plots  $E_z$  and  $E_r$  against radial coordinate  $r$ . As follows from this figure, the accelerating field in the evacuated channel is uniform along the radial coordinate. Outside the channel, the field drops and vanishes at the metallic wall; i.e., longitudinal field  $E_z$  in the ferroelectric is almost ten times lower than in the evacuated channel. The radial component  $E_r$  of the electric

field experiences jumps at the interfaces according to the boundary conditions. In the ferroelectric, it is negligibly small.

### THE EFFECT OF THE FERROELECTRIC ON THE WAKE FIELD

As a ferroelectric film, one can take a film of MgO-doped barium titanate–strontium titanate solid solution ( $\text{Ba}_{0.6}\text{Sr}_{0.4}\text{TiO}_3$ ) at a working temperature of 300 K. When the dopant concentration is 1%, such a composition makes it possible to vary permittivity  $\epsilon_2$  at a frequency of 10 GHz from 800 (for  $\tan\delta_2 \approx 2 \times 10^{-3}$ ) to 1820 (for  $\tan\delta_2 \approx 6 \times 10^{-3}$ ). The same variation of the permittivity is observed when the control electrostatic field ranges from  $4 \times 10^6$  V/m to zero [11]. The increase in the control electrostatic field to  $10^7$  V/m causes permittivity  $\epsilon_2$  to decrease to 365. It is noteworthy that these results are valid for thin-film devices (1- to 5- $\mu\text{m}$ -thick), while the ferroelectric we are dealing with may be as thick as 100  $\mu\text{m}$  (in contrast to a 1- $\mu\text{m}$ -thick film, see [11]). “Thick” ferroelectric films and a bulk ferroelectric as control elements were used, e.g., in [12–15], where a possible rise in the loss tangent in the bulk material (compared with the thin film) due to its inhomogeneity was noted. In a recent work [16], the loss tangent in bulk MgO-doped  $\text{BaSrTiO}_3$  was reported to be  $5 \times 10^{-3}$  at 10 GHz. We are planning to employ MgO-doped  $\text{BaSrTiO}_3$  filled with an inert nonferroelectric, a standard linear high- $Q$  ceramic material, in order to shrink the range of the permittivity from 800–1800 to 180–320 [7]. Such a decrease in the permittivity of the ferroelectric would allow us not only to decrease the loss tangent in the material but also to reduce energy losses in the metallic wall (sheath) adjacent to the ferroelectric. In the dependences of the energy losses that follow, the value of  $\tan\delta_2$  is taken to be equal to  $5 \times 10^{-3}$  throughout the range of  $\epsilon_2$ .

Note that the loss tangent in ferroelectrics ( $\tan\delta_2 \approx 5 \times 10^{-3}$ ) is 1–1.5 orders of magnitude higher than in materials used as a dielectric ( $\tan\delta_1 \sim 10^{-4}$ ).

Figure 4 plots the fundamental frequency of the wake field of the bunch versus permittivity  $\epsilon_2$  in a three-layer dielectric waveguide with an inner radius  $R_c = 0.5$  cm and ferroelectric film thickness  $h = R_w - R_d = 0.015$  cm for three values of the permittivity of the waveguide material ( $\epsilon_1 = 5, 7,$  and  $9$ ). The radius of the dielectric,  $R_d$ , was taken such that the field frequency in the middle of the ferroelectric permittivity ( $\epsilon_2$ ) range be equal to 11.42 GHz, which is the working frequency of the experiment to be carried out. It follows from Fig. 4 that, for  $\epsilon_1 = 5$ , we can vary the frequency within  $\pm 14\%$  of the wake field center frequency  $f = 11.42$  GHz. As the permittivity of the dielectric increases, the tuning range of the frequency narrows. If the ferroelectric-to-

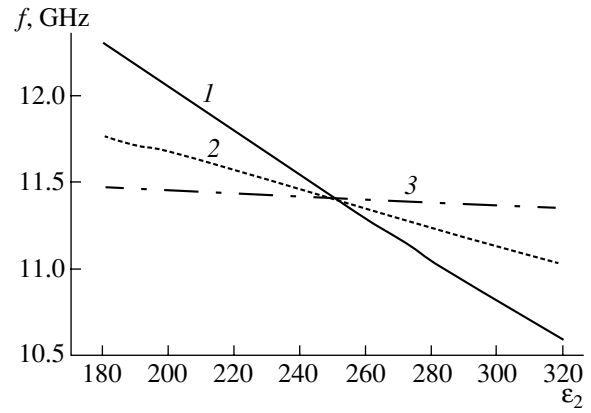


**Fig. 4.** Wake field frequency vs. permittivity  $\epsilon_2$  of the ferroelectric. (1)  $\epsilon_1 = 5$  and  $R_d = 0.72$  cm, (2)  $\epsilon_1 = 7$  and  $R_d = 0.713$  cm, and (3)  $\epsilon_1 = 9$  and  $R_d = 0.703$  cm.

dielectric thickness ratio is increased, the frequency tuning range may be substantially expanded; in this case, however, electric losses in the system grow and the performance of the accelerator degrades.

### LOSSES IN THE WAVEGUIDE

Electric losses are convenient to consider when permittivity is represented as a sum of the real,  $\epsilon = \epsilon' - j\epsilon''$ , and imaginary,  $\epsilon'' = \sigma/\omega$ , parts, where  $\sigma$  is the conductivity of a material and  $\omega$  is the circular frequency. Dielectric loss tangent is then written in the form

$$\tan\delta = \frac{\epsilon''}{\epsilon'} = \frac{\sigma}{\omega\epsilon'}. \quad (19)$$

Total losses  $w_t$  in the waveguide include dielectric losses in the dielectric and ferroelectric,  $w_d$ , and magnetic losses  $w_m$  due to a finite conductivity of the metallic sheath:  $w_t = w_d + w_m$ .

The dielectric losses in the waveguide are found by integration of the specific losses over the dielectric and ferroelectric volume:  $w_d = \sigma_d \int_V \mathbf{E} \cdot \dot{\mathbf{E}} dV$ .

The conductivity of the dielectric,  $\sigma_d$ , is found from (19):

$$\tan\delta = \frac{\sigma_d}{\omega\epsilon'}$$

Then, we have

$$w_d = \omega\epsilon_1 \tan\delta_1 \int_V \mathbf{E} \cdot \dot{\mathbf{E}} dV + \omega\epsilon_2 \tan\delta_2 \int_V \mathbf{E} \cdot \dot{\mathbf{E}} dV. \quad (20)$$

To find the dielectric losses in the dielectric and ferroelectric, we substitute the components of field  $\mathbf{E}$  that are given by expression (18) for the wake field downstream of a charged relativistic bunch into (20) and



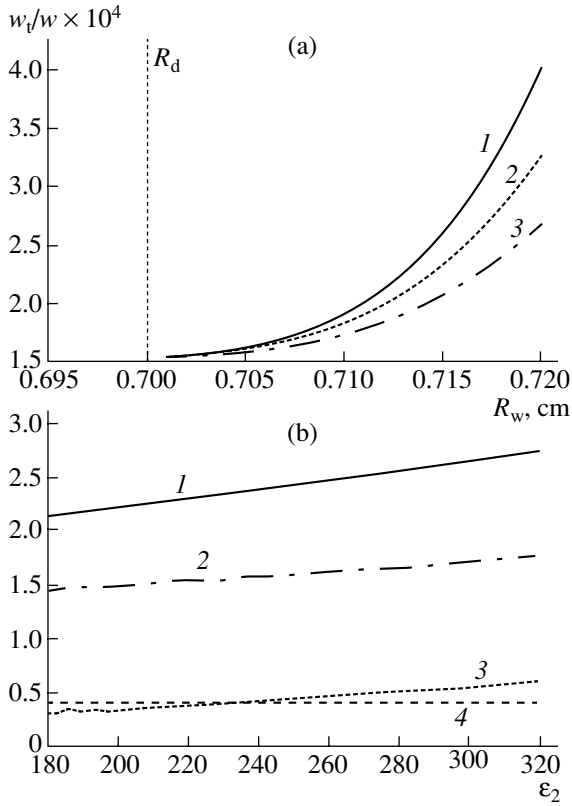


**Fig. 5.** (a) Relative energy losses vs. outer radius of the waveguide:  $\epsilon_2 = (1)$  320, (2) 250, and (3) 180. (b) Relative energy losses vs. permittivity  $\epsilon_2$  of the ferroelectric: (1) total losses, (2) magnetic losses, (3) ferroelectric losses, and (4) dielectric losses.  $R_c = 0.5$  cm,  $R_d = 0.7$  cm, and  $R_w = 0.715$  cm.

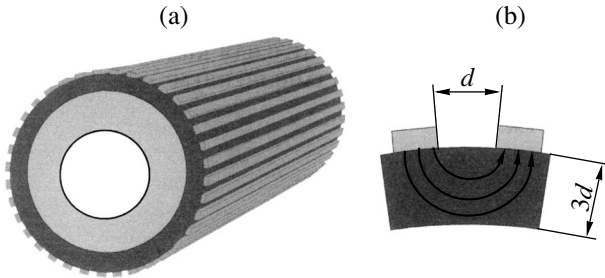


**Fig. 6.** Geometry of the microstrip electrodes for the ferroelectric- and ceramic-filled tunable accelerating structure.  $d = 60$   $\mu\text{m}$ . (a) General view and (b) a fragment.

obtain

$$w_d = \omega \epsilon_1 \tan \delta_1 \int_{R_c}^{R_d} (E_z(r)^2 + E_r(r)^2) 2\pi r l dr$$

$$+ \omega \epsilon_2 \tan \delta_2 \int_{R_d}^{R_w} (E_z(r)^2 + E_r(r)^2) 2\pi r l dr,$$

where  $l$  is the length of the waveguide.

The losses in the conductor (metallic sheath) are found as the real part of the complex Poynting vector flux piercing the total surface area of the conductor from the inside and depend on the tangential component  $H_\tau$  of the magnetic field at the boundary of the conductor:

$$w_m = \frac{1}{2\sigma_m \Delta} \oint_S H_\tau^2 ds.$$

Skin depth  $\Delta$  depends on the electromagnetic field circular frequency  $\omega$  and conductivity  $\sigma_m$  of the metal,

$$\Delta = \frac{c}{\sqrt{2\pi\omega\mu\delta_m}}.$$

Figure 5a plots the ratio of the total energy losses ( $w_l$ ) to the energy stored in the waveguide ( $w$ ) against its outer radius  $R_w$  for  $\epsilon_1 = 9.4$ . The relative energy losses are seen to grow with the ferroelectric layer thickness. Note also that the ferroelectric layer not only dissipates a major part of the energy but also increases the losses in the metallic sheath. Thus, the ferroelectric and the metallic sheath are major contributors to the total energy losses and their combined contribution increases drastically with increasing permittivity of the ferroelectric (Fig. 5b). Eventually, this fact limits the thickness of the ferroelectric film and makes frequency tuning of a wakefield waveguide less effective.

## GEOMETRY OF THE FERROELECTRIC-PERMITTIVITY-CONTROLLING ELECTRODES

Figure 6a shows an electric-field-controlled dielectric accelerating structure with a ferroelectric layer.

When applied to the electrodes made on the outer side of the ferroelectric layer, a dc field (of strength 10 V/ $\mu\text{m}$  for the material used) alters the permittivity of the ferroelectric and, thereby, tunes the fundamental frequency of the structure. The electrodes will supposedly be made by advanced electrode technology, including lithography and precision etching. It is being widely used in production of thin-film ferroelectric tunable phase shifters and filters [11–13]. It is hoped that, using this technology, we will be able to make the electrode configuration such that it (i) supports the modes necessary for effective acceleration (mode  $E_{0N}$  for the structure considered); (ii) provides a maximal strength (to 10 V/ $\mu\text{m}$  for the ferroelectric material used) of the dc (control) field penetrating into the ferroelectric in order to extend the range of controllability and, at the same time, keeps the control field uniform; and (iii) minimizes insertion losses.

Figure 6b shows the particular dimensions of the microelectrode system designed for an accelerating waveguide operating at 10–13 GHz. For a 180- to 220- $\mu\text{m}$ -thick ferroelectric film intended for controlling a ceramic waveguide with a center frequency of 11 GHz, the optimal relationship is  $h = 3d$  according to our cal-

culation, where  $h$  is the thickness of the film and  $d$  is width of the strip. The electrode spacing must also be roughly equal to  $d$ . For the frequency range 10–13 GHz, the appropriate value of this parameter ranges from 50 and 60  $\mu\text{m}$ . A dc voltage of 0.5–1.0 kV is applied across the spacing to generate a control field on the order of 10 V/ $\mu\text{m}$ .

### MODE-SELECTION CONTROLLABLE WAKEFIELD ACCELERATING STRUCTURE

The transverse fields excited in wakefield waveguides are no lower than longitudinal ones. These fields, causing the beam to deviate from the waveguide axis and directing some of the particles on the walls of the structure, are responsible for charge losses in the bunch and may initiate the breakdown of the dielectric [17].

Figure 7 demonstrates the design of a multilayer ferroelectric- and ceramic-loaded tunable accelerating waveguide to be used in further experiments. It consists of a high- $Q$  ceramic layer covering the evacuated channel of inner radius  $R_c$  and outer radius  $R_d$ , a thin ferroelectric layer of radius  $R_f$  with longitudinal insulated microstrip electrodes on its top, and an absorbing (ferrite) layer covered by a metallic wall of radius  $R_w$ .

The longitudinal arrangement of the control microelectrodes is aimed at supporting only the longitudinal accelerating electric modes of the microwave wake field. Then, the microstrips applied on the ferroelectric may be used not only as electrodes generating the dc control voltage but also as a system suppressing transverse (deflecting) modes [18].

When designing the layout described above, we used the Chojnacki filtering method [19]. According to this method, the transverse modes of a waveguide can be suppressed by making the outer sheath of the waveguide longitudinally anisotropic instead of using continuous isotropic metallization. The idea of suppressing transverse modes in a waveguide by making the conductivity of its sheath purely longitudinal with the help of longitudinal insulated conductors was first suggested in [19], and computer simulation and experimental implementation of this concept were performed in [20].

Hybrid modes in dielectric waveguides persist when both the axial and azimuth surface electric current in the sheath are supported. If the outer conductors carry the axial current alone (as in Fig. 6a), the deflecting modes could be absorbed outside the waveguide space bounded by the longitudinal electrodes, decaying as surface waves in a microwave absorber placed around the structure. It is thus expected that, owing to the specific geometry of the microstrip electrodes, the waveguide will support only mode  $E_{0N}$  with the longitudinal electric field component, which is just necessary for effective acceleration.

To elucidate the influence of the ferrite layer on the field structure, let us write expressions for  $E_z$  and  $H_z$  for

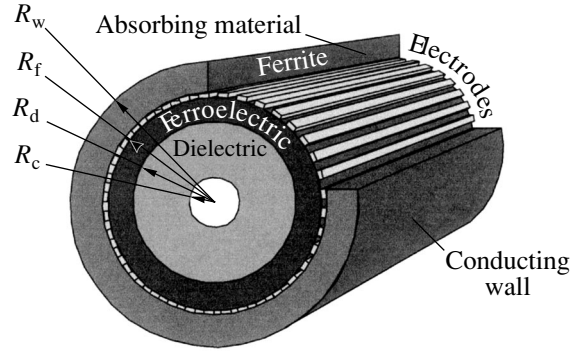


**Fig. 7.** Tunable accelerating waveguide where transverse deflecting modes are suppressed.

each of the parts of the waveguide:

$$E_{z\nu}^{\text{gen}} = \begin{cases} AI_\nu(\chi_0 r), & 0 \leq r \leq R_c, \\ C_1 J_\nu(\chi_1 r) + D_1 N_\nu(\chi_1 r), & R_c \leq r \leq R_d, \\ E \left( J_\nu(\chi_2 r) - \frac{J_\nu(\chi_2 R_w)}{N_\nu(\chi_2 R_w)} N_\nu(\chi_2 r) \right), & R_d \leq r \leq R_f, \\ 0, & R_f \leq r \leq R_w, \end{cases} \quad (21)$$

$$H_{z\nu} = \begin{cases} BI_\nu(\chi_0 r), & 0 \leq r \leq R_c, \\ C_2 J_\nu(\chi_1 r) + D_2 N_\nu(\chi_1 r), & R_c \leq r \leq R_d, \\ E_2 (J_\nu(\chi_2 r) + F_2 N_\nu(\chi_2 r)), & R_d \leq r \leq R_f, \\ G \left( J_\nu(\chi_3 r) - \frac{J_\nu(\chi_3 R_w)}{N_\nu(\chi_3 R_w)} N_\nu(\chi_3 r) \right), & R_f \leq r \leq R_w, \end{cases} \quad (22)$$

where

$$\chi_3 = k \sqrt{\frac{(\beta^2 \epsilon_3 \mu_3 - 1)}{\beta^2}},$$

$\mu_3 = \mu_{r3} - j\mu_{i3}$  is the complex permeability of the ferrite ( $\mu_{r3}$  and  $j\mu_{i3}$  are the real and imaginary parts, respectively), and  $\epsilon_3$  is the permittivity of the ferrite.

Using the continuity conditions for the tangential components of the electric and magnetic fields at the interfaces, as well as the fact of vanishing of the longitudinal component of the electric field because of the conducting electrodes present at the ferroelectric–ferrite interface, we obtain from expressions (12), (13), (21), and (22) a dispersion relation and the fields for the multilayer structure considered.

The numerical simulation and experimental implementation showed [20] that the axially conducting boundary does not influence the accelerating fields, while the transverse fields exponentially decay over several periods (Fig. 8).

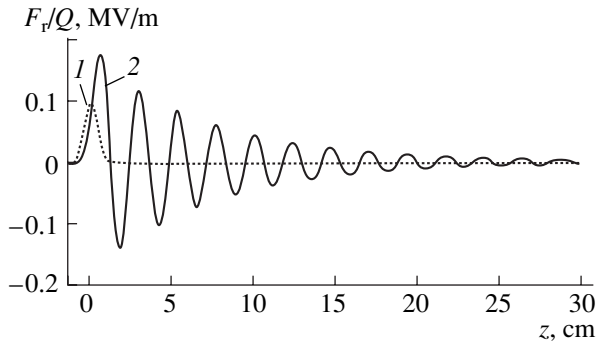


**Fig. 8.** Decay of the radial deflecting field with distance back of a bunch: (1) bunch charge distribution and (2) radial component of the wake field.  $R_c = 0.5$  cm,  $R_d = 0.58$  cm,  $R_f = 0.582$  cm,  $R_w = 0.6$  cm,  $\epsilon_1 = 16$ , and  $\epsilon_2 = 200$ . The ferrite parameters are  $\mu_{3i} = 3$ ,  $\mu_{3r} = 3$ , and  $\epsilon_3 = 20$ .

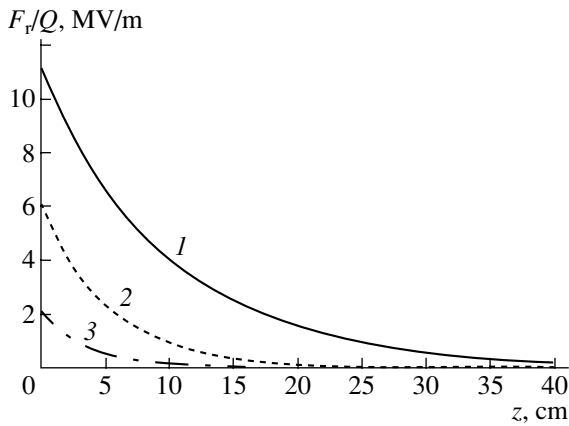


**Fig. 9.** Amplitude of the radial deflecting field in the waveguide vs. distance  $z$  back of a bunch for the ferrite thickness  $D_{\text{fer}} =$  (1) 0.002, (2) 0.004, and (3) 0.05 cm.

Figure 9 plots the radial field of the first transverse mode in the waveguide versus distance  $z$  back of a 0.4-cm-long bunch that carries a charge  $Q = 100$  nC and is offset from the waveguide axis by  $r_0 = 0.001$  cm for three ferrite thicknesses  $D_{\text{fer}}$  (for the ferrite parameters, see [19]). As the thickness of the ferrite layer grows, so does the energy absorption in it (the deflecting mode amplitude inside the waveguide exponentially decays). Moreover, the deflecting mode amplitude declines in the evacuated channel of the waveguide as well. This effect is related to the field penetration outside the waveguide space bounded by the longitudinal electrodes. When the accelerating electron bunches and those being accelerated are  $z = 25\text{--}27$  cm apart (this distance roughly equals  $10\lambda$ , where  $\lambda$  is the wavelength at the fundamental frequency of the waveguide, 11.41 GHz), the radial field of the first mode is reduced by a factor of 100 or more and becomes comparable to, or lower than, the deflecting force associated with the zeroth mode. The latter, according to our calculation, does not exceed 100 V/m in the geometry under discus-

sion and is negligibly small compared with the radial force of the first mode in the absence of the extra ferrite layer in a standard waveguide.

Thus, when combined with the additional absorbing sheath, the longitudinal electrode system used to control the permittivity of the ferroelectric provides suppression of transverse deflecting modes, while retaining the possibility of controlling the waveguide frequency spectrum.

It should be noted that the ferrite properties considerably depend on the permanent magnetic field strength in the accelerator (focusing systems, etc.). However, deflecting field suppression will allow designers to completely or partially get rid of the conventional beam-focusing magnetic system and, thereby, greatly simplify the construction of an accelerating waveguide.

## CONCLUSIONS

We demonstrated that the frequency spectrum of the wake field generated by an electron bunch in an accelerating structure can be controlled by varying the permittivity of a thin ferroelectric layer applied on the dielectric (ceramic) waveguide. The ferroelectric permittivity is varied by varying the amplitude of the electric field applied to microelectrodes made on the outer surface of the control layer.

A decrease in the ferroelectric permittivity increases the wake field frequency and amplitude in the accelerating structure. At the same time, energy losses impose restrictions on the ferroelectric thickness and render frequency tuning in a wakefield waveguide less effective. The ferroelectric thickness is selected starting from desired frequency tuning range and wake field frequency.

The specially shaped ferroelectric-permittivity-controlling electrodes, combined with an extra absorbing sheath, allow for not only frequency tuning but also suppression of deflecting modes in the waveguide to provide the lateral stability of the beam.

The technology of multilayer tunable waveguides that is proposed in this paper can be extended to high-power high-frequency accelerating systems, such as tunable microwave switches and pulse compressors [21]. Moreover, a novel field of research arises: nonlinear effects in the multilayer systems [22], where the high-frequency wake field generated by an electron bunch in a dielectric-loaded waveguide interacts with the ferroelectric layer, thereby accomplishing control over the system. In this case, various nonlinear effects like shock waves, self-focusing, and many others may be worth studying.

It should be noted that the possibility of rapid tuning of the waveguide frequency (and, hence, the phase velocity of the accelerating wave) is a great advantage of ceramic-loaded waveguides over standard evacuated ones. The former can be widely used in systems where strict wave-beam synchronization is required.

## ACKNOWLEDGMENTS

This work was supported by the Ministry of Education of the Russian Federation and the Committee for Science and Higher Education of St. Petersburg (grant no. PD02-1.2-104), as well as by DoE of SBIR (grant no. DE-FG02-02ER83418).

## REFERENCES

1. W. Gai, P. Schoesson, B. Cole, *et al.*, Phys. Rev. Lett. **61**, 2756 (1988).
2. R. Keinigs, M. Jones, and W. Gai, Part. Accel. **24**, 223 (1989).
3. A. D. Kanareykin, I. L. Sheinman, E. A. Nenasheva, *et al.*, in *Proceedings of the International Conference on Physics at the Turn of the 21st Century, St. Petersburg, 1998*, pp. 57–58.
4. G. Power, M. E. Conde, W. Gai, *et al.*, Phys. Rev. ST Accel. Beams **3**, 101302 (2000).
5. A. D. Kanareykin and E. A. Nenasheva, Patent Appl. No. 2,003,107,001, Russia (March 5, 2003).
6. A. D. Kanareykin, I. L. Sheinman, and A. M. Altmark, Pis'ma Zh. Tekh. Fiz. **28** (21), 75 (2002) [Tech. Phys. Lett. **28**, 916 (2002)].
7. A. D. Kanareykin, W. Gai, J. Power, *et al.*, AIP Conf. Proc. **647**, 565 (2002).
8. B. M. Bolotovskii, Usp. Fiz. Nauk **75**, 295 (1961) [Sov. Phys. Usp. **4**, 781 (1961)].
9. King-Yuen Ng, *Wake Fields in a Dielectric-Lined Waveguide*, Fermilab Report No. FN-533 (1990), pp. 1–11.
10. M. Rosing and W. Gai, Phys. Rev. D **42**, 1829 (1990).
11. H.-D. Wu and F. S. Barnes, Integr. Ferroelectr. **22**, 300 (1998).
12. O. G. Vendik, *Ferrielectrics in Microwave Technology* (Sov. Radio, Moscow, 1979) [in Russian].
13. F. W. Van Keuls *et al.*, Integr. Ferroelectr. **34**, 165 (2001).
14. L. Sengupta and S. Sengupta, IEEE Trans. Ultrason. Ferroelectr. Freq. Control. **44**, 792 (1997).
15. L. Sengupta, in *Proceedings of the International Microwave Symposium (IMS-2000), Boston, MA, 2000*.
16. E. A. Nenasheva, A. D. Kanareykin, N. F. Kartenko, and S. F. Karmanenko, J. Electroceram. (2003).
17. W. Gai, A. Kanareykin, A. Kustov, and J. Simpson, Phys. Rev. E **55**, 3481 (1997).
18. A. M. Altmark, A. D. Kanareykin, and I. L. Sheinman, Pis'ma Zh. Tekh. Fiz. **29** (20), 58 (2003) [Tech. Phys. Lett. **29**, 862 (2003)].
19. E. Chojnacki *et al.*, J. Appl. Phys. **69**, 6257 (1991).
20. W. Gai and Ching-Hung Ho, J. Appl. Phys. **70**, 3955 (1991).
21. V. P. Yakovlev, O. A. Nezhevenko, J. L. Hirshfield, in *Proceedings of the Particle Acceleration Conference, Portland, 2003*, pp. 1150–1152.
22. P. Schoessow, in *Proceedings of the 4th Workshop on Advanced Accelerator Concepts, Lake Arrowhead, CA, 1989*, Ed. by C. Joshi (AIP, 1989), p. 371.

*Translated by V. Isaakyan*

## EXPERIMENTAL INSTRUMENTS AND TECHNIQUES

# Optimization of Feed Flow Parameters in Separation of Neodymium Isotopes by Atomic Vapor Selective Laser Photoionization and Analysis of Results

S. K. Kovalevich, V. P. Labozin, and G. O. Tsvetkov

Russian Research Center Kurchatov Institute, pl. Kurchatova 1, Moscow, 123182 Russia

e-mail: secretariat@imp.kiae.ru

Received April 8, 2004

**Abstract**—Experimental data for separation of neodymium isotopes by atomic vapor selective laser photoionization are analyzed. Atom scattering in the working volume and the Doppler shift of the atom absorption line are shown to be the basic deselection processes in the experimental cell studied. A data processing technique that allows one to determine the effect of either deselection process on the product enrichment and yield is suggested. The experimental dependence of the target isotope concentration in photoions present in the separating chamber on the angular divergence (collimation) of the atomic vapor flow along the laser beam is found. A method for determining the vapor flow optimal angular collimation is developed. © 2005 Pleiades Publishing, Inc.

## INTRODUCTION

In this work, we analyze the experimental data [1–5] for separation of neodymium isotopes by the atomic vapor laser isotope separation (AVLIS) method. In this method, the flow of atoms evaporated passes through a laser-irradiated space where the selective photoionization of a target isotope takes place. The ions thus produced are extracted from the vapor flow and are directed to the collector by means of an electric field. The remaining (neutral) atoms of the flow are trapped by the waste collector. The experiments on neodymium isotope separation were aimed at tackling the question of whether this method is promising for the preparation of a product containing up to 70% of the  $^{150}\text{Nd}$  isotope. This product in amounts of several tens of kilograms is needed for fundamental research on double  $\beta$  decay [6, 7]. The natural occurrence of  $^{150}\text{Nd}$  is 5.6%. Since this element does not produce volatile compounds, its isotopes cannot be separated by the conventional centrifugal method.

## EXPERIMENTAL SETUP AND METHOD

Figure 1 shows the setup used for research and pilot experiments on recovery. Neodymium is evaporated from a 30-cm-long crucible heated to 1700–1900 K [1]. The design of the evaporator allows for the mounting of a collimator to limit the angular divergence of the vapor flow in the direction of the laser beam. In the experiments, the collimation half-width of the flow was varied from  $15^\circ$  to  $60^\circ$ .

The laser system consists of copper vapor lasers and tunable dye lasers. The former generate a pulsed radia-

tion (yellow and green components) of total output 300 W. The pulse duration is 30 ns; the pulse repetition rate, 10 kHz [8]. This radiation is used to pump three chains of the dye lasers (according to the number of photoionization steps). The radiation from the dye lasers (a total output of 100 W) is directed to the separating chamber [2]. The multipass optics installed in the chamber allows the laser beam to pass over the neodymium evaporator up to 20 times, thereby increasing the volume of the vapor irradiated. The photoionization scheme used in the experiments is depicted in Fig. 1.

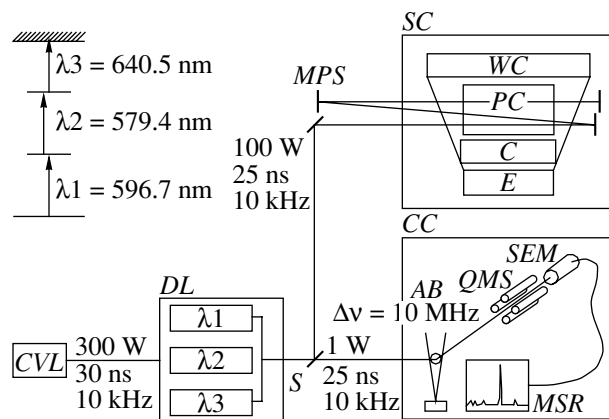


**Fig. 1.** Schematic of the setup for research and pilot experiments on neodymium isotope recovery. CVL, copper vapor lasers; DL, dye lasers; S, splitter; MPS, multipass system; SC, separating chamber; E, evaporator; C, collimator; PC, product collector; WC, waste collector; CC, control chamber; AB, atomic beam; QMS, quadrupole mass spectrometer; SEM, secondary electron multiplier; and MSR, mass spectrum recorder.

**Table 1**

Isotopic composition, %	$I/D$	$C = 150$	$C = 148$	$C = 146$	$D = 145$	$C = 144$	$C = 143$	$C = 142$
Natural		5.6	5.7	17.2	8.3	23.8	12.2	27.2
Measured in mass spectrometer		91.6	4.59	2.6	0.03	0.9	0.03	0.06
Measured on collector		34.3	11.2	12.9	5.4	14.2	7.0	15.3
Mixing of composition in mass spectrometer with natural composition in proportion $I/D$	1	48.6	5.1	9.9	4.2	12.3	6.1	13.6
	0.8	43.8	5.2	10.7	4.6	13.6	6.8	15.1
	0.7	41.0	5.2	11.2	4.9	14.4	7.2	16.0
	0.6	37.9	5.3	11.7	5.2	15.2	7.6	17.0
	0.5	34.3	5.2	12.3	5.5	16.2	8.1	18.2

A waste collector is placed immediately above the working volume.

A minor part ( $\approx 1\%$ ) of the radiation is directed to a control chamber, where it interacts with a thin neodymium atom beam (the Doppler broadening of the line is  $\Delta v_D \approx 100$  MHz). The interaction takes place directly in the ion source of a quadrupole mass spectrometer. The fraction of the power directed into the control chamber and the volume of the space of interaction are taken such that the laser radiation intensities in the separating chamber and the control mass spectrometer equal each other. The composition of the photoions is monitored throughout the experiment at a rate of one mass spectrum per minute.

The time of recovery was, as a rule, 1 h. When the experiment was over, the product obtained on the photoion collector and the neodymium in the waste collector were washed away. The isotopic composition and amount of neodymium in the samples were determined in an independent laboratory. In this way, the external parameters of the process were found: product flux  $P$ , concentration  $C_p$  of the target isotope in the product, waste flux  $W$ , and concentration  $C_w$  of the target isotope in the waste. Feed flow  $F$  was found by the formula

$$F = P + W. \quad (1)$$

### DESELECTING PROCESSES

When recovery is carried out by the AVLIS method, an increase in the output enhances the effect of deselection processes, such as atom scattering in the working space and resonant charge exchange. When working with neodymium vapor flows, which are highly divergent, one should take into account that the Doppler broadening of the spectral line becomes comparable to the isotopic shift. Because of the action of the deselection processes, the target isotope concentration in the product turns out to be lower than the concentration measured in the control mass spectrometer.

Table 1 summarizes the results of experiments with multimode lasers for which the lasing linewidth is  $\approx 1$  GHz [9]. The first row lists the natural occurrence of neodymium isotopes; the second, the mass spectrum

obtained in the control mass spectrometer and averaged over the time of recovery; and the third, the isotopic composition in the sample washed away from the photoion collector. It is seen that the concentration of the  $^{150}\text{Nd}$  target isotope is much lower than the concentration in the mass spectrometer. This may be explained by the arrival of a neutral atom flux with the natural composition at the collector.

Let us try to obtain the desired composition of the product on the collector by adding the natural composition to the composition determined in the control mass spectrometer under the assumption that the isotopic concentration of photoions in the separator equals the concentration of photoions in the mass spectrometer. The concentration of an  $i$ th isotope on the collector is given by

$$C_{pi} = \frac{IC_{\text{photo}i} + DC_{fi}}{I + D} = \frac{(I/D)C_{\text{ms}i} + C_{fi}}{I/D + 1}, \quad (2)$$

where  $C_{\text{photo}i}$  is the concentration of an  $i$ th isotope in photoions in the separator,  $C_{\text{ms}i}$  is the concentration of the  $i$ th isotope in the mass spectrometer, and  $I/D$  is the ratio between the selective flux ( $I$ ) of photoions and the flux of neutral atoms ( $D$ ) with the natural composition.

The results of such addition are given in lower rows of Table 1. One can conclude that the isotopic composition observed on the collector cannot be obtained by merely adding the natural composition to that determined in the mass spectrometer. Consequently, the initial isotopic composition of photoions in the separator differs from that in the mass spectrometer. The adding procedure is inefficient because of a high concentration of the  $^{148}\text{Nd}$  isotope on the collector. This isotope is next to the  $^{150}\text{Nd}$  target isotope in the spectrum. It may be therefore supposed that the composition of photoions in the separator changes because of the Doppler effect. Indeed, the laser beam in the mass spectrometer interacts with the atomic (vapor) flow, which has an angular divergence of  $4^\circ$ . This corresponds to a Doppler half-width of the absorption line of  $\approx 100$  MHz. On the other hand, the vapor flow in the separator has a maximal angular divergence along the laser beam,  $\approx 120^\circ$  (a Doppler width of  $\approx 1$  GHz). Thus, in the experiment

**Table 2**

Isotopic composition, %	<i>I/D</i>	<i>C</i> = 150	<i>C</i> = 148	<i>C</i> = 146	<i>D</i> = 145	<i>C</i> = 144	<i>C</i> = 143	<i>C</i> = 142
Natural		5.6	5.7	17.2	8.3	23.8	12.2	27.2
Measured in mass spectrometer		75.45	15.01	4.9	1.17	2.1	0.49	0.9
Measured on collector		23.8	7.3	13.7	6.5	18.4	9.4	20.9
Mixing of composition in mass spectrometer with natural composition in proportion <i>I/D</i>	0.353	23.8	8.1	14.0	6.4	18.1	9.1	20.3

considered, the Doppler width of the vapor flow in the separator turns out to be roughly equal to the spectral width of the laser radiation and to the isotopic shift between the  $^{150}\text{Nd}$  and  $^{148}\text{Nd}$  isotopes in the first transition.

To check the above supposition, we mounted a collimator in the path of the atomic flow, which limited its maximal angular divergence to  $30^\circ$ . The results of such an experiment are presented in Table 2, from which it follows that the desired composition on the collector can be obtained by mixing the two compositions. This suggests that the isotopic compositions in the mass spectrometer and separator are roughly the same in the given experiment. Since the experiments with different angles of collimation of the vapor flow were carried out at comparable atomic concentrations and under the same conditions, we can conclude that the decrease in the target isotope concentration in photoions compared with the concentration measured in the mass spectrometer results from the overlap of the absorption lines of different isotopes due to the Doppler effect.

#### DATA PROCESSING TECHNIQUE

To clarify the effect of the deselection processes, it is important to determine ratio *I/D*, where *I* is the enriched component and *D* is the component with the natural composition. Knowing this ratio, one can find the isotopic composition of photoions in the separator, the coefficient of extraction of the target isotope by means of photoionization, and the atom scattering coefficient in the working space. Unfortunately, ratio *I/D* cannot be found only with the external parameters of the separating cell. However, this important quantity can be determined by comparing the concentrations of even isotopes in the product and in the mass spectrometer.

Our procedure of determining *I/D* consists in the following. The concentration of an *i*th isotope in the mass spectrometer is given by

$$C_{msi} = \frac{C_{fi}\eta_{msi}}{\sum_i C_{fi}\eta_{msi}}, \quad (3)$$

where  $\eta_{msi}$  is the ionization efficiency for the *i*th isotope in the mass spectrometer.

Similarly, the concentration of an *i*th isotope in the photoions that are present in the separator is expressed as

$$C_{photoi} = \frac{C_{fi}\eta_i}{\sum_i C_{fi}\eta_i}, \quad (4)$$

where  $\eta_i$  is the ionization efficiency for the *i*th isotope in the separator.

Ratio  $\alpha_i = C_{photoi}/C_{msi}$ , where  $C_{photoi}$  is the concentration of the *i*th isotope at the stage of photoionization in the separator and  $C_{msi}$  is the concentration of the same isotope that is measured in the mass spectrometer, is numerically equal to the ratio of the related photoionization efficiencies for this isotope times a factor that is the same for all the isotopes:

$$\alpha_i = \frac{C_{photoi}}{C_{msi}} = \frac{\eta_i}{\eta_{msi}} \frac{\sum_i C_{fi}\eta_{msi}}{\sum_i C_{fi}\eta_i}. \quad (5)$$

The isotopic composition of photoions in the separator differs from that measured in the mass spectrometer because of the Doppler effect, which is a spectrally dependent deselection effect. In other words, the smaller isotopic shift  $\Delta v_{150-i}$  between a given isotope and the target isotope, which the laser wavelength are tuned to, the greater the change in the ionization efficiency. Since the inequalities

$$\Delta v_{150-148} < \Delta v_{150-146} < \Delta v_{150-144} < \Delta v_{150-142}, \quad (6)$$

are valid for the used transitions in neodymium, the inequalities

$$\alpha_{148} > \alpha_{146} > \alpha_{144} > \alpha_{142} \quad (7)$$

or

$$0 < \frac{\alpha_i}{\alpha_{i+1}} = \frac{C_{photoi}}{C_{photoi+1}} \frac{C_{msi+1}}{C_{msi}} < 1 \quad (8)$$

must hold.

With Eq. (2), concentration  $C_{photoi}$  can be expressed via concentration  $C_{pi}$  of an *i*th isotope in the product

and ratio  $I/D$ , which is the same for all the isotopes:

$$C_{\text{photo}i} = \frac{(I/D + 1)C_{pi} - C_{fi}}{(I/D)}, \quad (9)$$

where  $C_{fi}$  is the natural concentration of the  $i$ th isotope.

Ratio  $I/D$ , in turn, can be found by using the following procedure (note that the accuracy of determining  $I/D$  is the highest when the concentrations of the  $^{144}\text{Nd}$  and  $^{142}\text{Nd}$  isotopes are used). Substituting (9) into (8) yields an inequality for  $I/D$ :

$$\frac{C_{f142}}{C_{p142}} - 1 \leq I/D \leq \frac{C_{ms144}C_{f142} - C_{ms142}C_{f144}}{C_{ms144}C_{p142} - C_{ms142}C_{p144}} - 1. \quad (10)$$

Inequality (10) implies, on the one hand, that the photoionization efficiency for the  $^{142}\text{Nd}$  isotope cannot be less than zero. On the other hand, this inequality implies that the difference between the photoionization efficiencies for the  $^{142}\text{Nd}$  isotope in the separator and in the mass spectrometer cannot exceed this difference for the  $^{144}\text{Nd}$  isotope. In most of the experiments, inequality (10) determines ratio  $I/D$  accurate to several percent. Knowing  $I/D$ , one can find the rest of the internal parameters of the separating cell, namely, (i) experiment-averaged concentration  $C_{\text{photo}}$  of the target product at the photoionization stage (by formula (9)), (ii) enriched component  $I$ , (iii) component  $D$  with the natural composition, and (iv) coefficient of extraction  $K_{\text{extr}}$  of the target product by means of photoionization (i.e., the fraction of the target product gathered on the collector by means of selective photoionization):

$$I = \frac{P \cdot I/D}{1 + I/D}, \quad (11)$$

$$D = \frac{P}{1 + I/D}, \quad (12)$$

$$K_{\text{extr}} = \frac{IC_{\text{photo}}}{FC_f}. \quad (13)$$

The application of such an approach to experimental data is exemplified in Table 3. This table lists the natural isotopic composition of neodymium, the experiment-averaged isotopic composition measured in the mass spectrometer, and the isotopic composition of the sample, as well as the analytical compositions of photoions in the separator for each of the samples. Samples 75–79 were obtained in one experiment and taken from different sites on the collector. It is seen that the analytical isotopic compositions of photoions are virtually the same for all the samples, which confirms the validity of the method. The lowest row lists the analytical isotopic composition of photoions that is averaged over samples. It should be noted that, in this example, the error of measuring the  $^{142}\text{Nd}$  and  $^{144}\text{Nd}$  isotope concentrations is a major contributor to the total inaccuracy of determining the isotope concentrations. The target product concentration in the waste, which was calcu-

lated using the value of  $K_{\text{extr}}$  obtained, served as a reference value (this calculated value was in good agreement with that measured in the waste collector).

The validity of inequality (7) is confirmed by the calculations of selective photoionization that were performed in [10, 11]. In the works cited, the solution of the equations for the atomic density matrix, which describes the behavior of an atomic ensemble in high monochromatic fields with regard for the Doppler broadening of the transitions, was considered. Formulas for calculating the photoionization probability of nontarget isotopes as a function of the isotopic shift, laser radiation intensity, and width of the Doppler-broadened line were suggested.

Direct measurement of the isotopic composition of photoions in the separator is difficult, since the effective operation of the mass spectrometer under the conditions of an intense metal vapor flow must be provided. Because of this, the technique suggested in this work seems to be a convenient means for finding the internal parameters of the separating cell.

#### ANALYSIS OF EXPERIMENTAL DATA

Experiments show that the flow of the component  $D$  with the natural composition toward the collector depends on feed flow  $F$  and can be represented as

$$D = K_{\text{sc}}F. \quad (14)$$

Experiments also show that proportionality (scattering) coefficient  $K_{\text{sc}}$  depends on the feed flow. Figure 2 demonstrates the experimental values of  $K_{\text{sc}}$  (symbols) that were obtained by directly measuring the amount of Nd arrived at the collector after evaporation without photoionization and using formula (13). For comparison, Fig. 2 also shows the analytical dependence of the Nd atom scattering coefficient in the working space on feed flow  $F$ . The calculation was carried out as follows. The working space was partitioned into elements. For each of the elements, the atom concentration and its

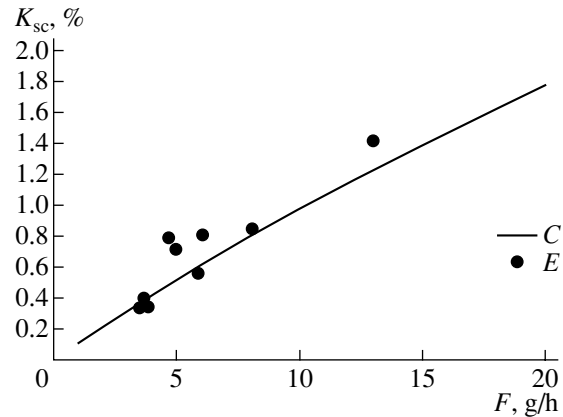


Fig. 2. Scattering coefficient  $K_{\text{sc}}$  vs. feed flow  $F$ . E, experiment; C, calculation.



**Table 3**

	150	148	146	145	144	143	142	
Isotopic composition, %	5.6	5.7	17.2	8.3	23.8	12.2	27.2	
Composition measured in mass spectrometer, %	91.58	4.59	2.61	0.27	0.86	0.03	0.08	
Isotopic composition in sample 75, %	Measured $C_p$	$34.1 \pm 0.2$	$11.1 \pm 0.2$	$12.9 \pm 0.2$	$5.4 \pm 0.2$	$14.2 \pm 0.2$	$7.0 \pm 0.2$	$15.3 \pm 0.2$
	Calculated composition of photoions, $C_{photo}$ $I/D = 0.78 \pm 0.03$	$70 \pm 2$	$18 \pm 1$	$7.4 \pm 0.2$	$1.7 \pm 0.2$	$2.4 \pm 0.5$	$0.4 \pm 0.3$	$0.1 \pm 0.1$
Isotopic composition in sample 76, %	Measured $C_p$	$56.3 \pm 0.2$	$16.3 \pm 0.2$	$9.3 \pm 0.2$	$3.0 \pm 0.2$	$6.4 \pm 0.2$	$2.9 \pm 0.2$	$5.8 \pm 0.2$
	Calculated composition of photoions, $C_{photo}$ $I/D = 3.7 \pm 0.2$	$71 \pm 2$	$19 \pm 1$	$7.1 \pm 0.2$	$1.5 \pm 0.2$	$1.3 \pm 0.5$	$0.3 \pm 0.1$	$0.1 \pm 0.1$
Isotopic composition in sample 77, %	Measured $C_p$	$35.3 \pm 0.2$	$10.9 \pm 0.2$	$12.5 \pm 0.2$	$5.2 \pm 0.2$	$13.9 \pm 0.2$	$7.0 \pm 0.2$	$15.2 \pm 0.2$
	Calculated composition of photoions, $C_{photo}$ $I/D = 0.79 \pm 0.03$	$73 \pm 2$	$18 \pm 1$	$7.0 \pm 0.2$	$1.3 \pm 0.2$	$1.4 \pm 0.5$	$0.4 \pm 0.3$	$0.1 \pm 0.1$
Isotopic composition in sample 78, %	Measured $C_p$	$16.5 \pm 0.2$	$7.7 \pm 0.2$	$15.4 \pm 0.2$	$7.2 \pm 0.2$	$20.1 \pm 0.2$	$10.3 \pm 0.2$	$22.8 \pm 0.2$
	Calculated composition of photoions, $C_{photo}$ $I/D = 0.19 \pm 0.01$	$73 \pm 4$	$18 \pm 1$	$6.0 \pm 0.5$	$1.5 \pm 0.3$	$1.0 \pm 1.0$	$0.5 \pm 0.5$	$0.1 \pm 0.1$
Isotopic composition in sample 79, %	Measured $C_p$	$9.6 \pm 0.2$	$6.4 \pm 0.2$	$16.6 \pm 0.2$	$7.9 \pm 0.2$	$22.5 \pm 0.2$	$11.5 \pm 0.2$	$25.6 \pm 0.2$
	Calculated composition of photoions, $C_{photo}$ $I/D = 0.065 \pm 0.005$	$71 \pm 9$	$17 \pm 2$	$7.3 \pm 2$	$1.7 \pm 1.0$	$2 \pm 2$	$1 \pm 1$	$0.1 \pm 0.1$
Calculated composition of photoions averaged over all samples, %	71.8	18.0	6.8	1.5	1.4	0.4	0.1	

related collision frequency were determined. Then, the probability that the atoms scattered will fall on the collector was found. Only single collisions were taken into account. Comparison between the experimental and analytical data shows that the atomic scattering in the working space is the basic source of the natural-concentration component. The effect of resonant charge exchange on the product concentration is insignificant compared with the effect of atomic scattering, as follows from our calculation using the charge exchange cross section from [12]. Thus, atomic scattering in the working space and the Doppler effect are the main deselection processes in the separating cell considered in this work.

Figure 2 shows that scattering coefficient  $K_{sc}$  is a nearly linear function of the feed flow in the geometry of our experiments. The same result can also be obtained in terms of the elementary kinetic theory. In fact, the number of collisions experienced by an atom per unit time is  $n\sigma V$  (1/s), where  $n$  is the atomic concentration in the working space (1/cm<sup>3</sup>),  $\sigma$  is the atomic scattering cross section (cm<sup>2</sup>), and  $V$  is the mean thermal velocity of the atoms (cm/s). Considering that the number of atoms per unit volume is  $n$ , we get the total number of collisions in a unit volume per unit time:  $\nu = n^2\sigma V$  (1/cm<sup>3</sup> s). Then, assuming that the fraction of the

scattered atoms that arrive at the collector is  $k_g$ , we can find the scattered atom flux (vapor flow) toward the collector:

$$D = k_g \nu S h m = k_g n^2 \sigma V S h m, \text{ g/h}, \quad (15)$$

where  $S$  is the cross-sectional area of the vapor flow (cm<sup>2</sup>),  $h$  is the height of the region from which the scattered atoms come (cm), and  $m$  is the mass coefficient equal to  $9 \times 10^{-19}$  (g s)/h for neodymium.

The flux of the scattered atom toward the collector can be expressed through feed flow  $F$  that enters into the separating cell ( $F = n V S m$  (g/h)):

$$D = k_g n \sigma h F = K_{sc} F, \quad (16)$$

$$K_{sc} = k_g n \sigma h, \quad (17)$$

where  $K_{sc}$  is the atomic scattering coefficient on the collector.

From (17), it follows that the scattering coefficient depends on the atomic concentration and can be expressed as

$$K_{sc} = \theta F, \quad (18)$$

where

$$\theta = k_g \sigma h / (V S \cdot 9 \times 10^{-19}), \text{ h/g}. \quad (19)$$

Factor  $\theta$  depends only on the properties of an evaporating material and the experimental cell geometry. Consideration of atomic scattering in simple terms gives the linear dependence of the scattering coefficient on the feed flow, which is confirmed for the geometry and atomic concentration range that were adopted in our experiments. The value of  $\theta$  measured for our cell with a 30-cm-long evaporator turned out to be  $\theta = 10^{-3}$  h/g. Substituting this value into (19) yields  $k_g = 0.25$ .

Consider how the Doppler effect influences the selectivity and efficiency of photoionization of the target isotope. Figure 3 demonstrates the results of experiments with vapor flows that had different angular divergences  $q$  along the direction of the laser beam. Different divergences were provided by mounting collimating grids with different pitches in the flow. The data points in Fig. 3 were obtained by processing the results of the recovery experiments with formulas (9) and (13). In these experiments, single-mode dye lasers were employed. A single-mode laser with a linewidth of  $\approx 130$  MHz makes it possible to considerably raise the target isotope concentration in the photoions compared with a multimode laser [3, 4]. The results obtained demonstrate how much the selectivity and efficiency of photoionization of the target isotope (in Fig. 3, the latter parameter is represented through the coefficient of extraction of the target isotope) decrease with increasing angular divergence of the vapor flow in the direction of laser radiation for the specific parameters of the radiation that were used in the experiments. The decrease in the ionization efficiency with increasing angle of collimation is associated with an increase in the number of target isotope atoms in the wings of the Doppler-broadened line. For these atoms, the photoionization probability is much lower than for the atoms at the center of the line.

### OPTIMIZATION OF THE VAPOR FLOW PARAMETERS

Consider now how the results obtained may be used in optimizing the vapor flow parameters. With allowance for atomic scattering in the working volume, the target isotope concentration can be represented as [5]

$$C_p = \frac{K_{\text{extr}}C_f + K_{\text{sc}}C_f}{K_{\text{extr}}C_f/C_{\text{photo}} + K_{\text{sc}}}. \quad (20)$$

If the concentration of  $^{150}\text{Nd}$  in the product is  $C_p$ , yield  $P_{C_p}$  is given by

$$P_{C_p} = (K_{\text{extr}}C_f/C_{\text{photo}} + K_{\text{sc}})F. \quad (21)$$

Our aim is to derive an expression for the output of the cell when the target isotope (product) concentration desired equals 0.7. If the product concentration exceeds 0.7, it may be decreased to the desired value by mixing with the natural composition. Eventually, the yield of

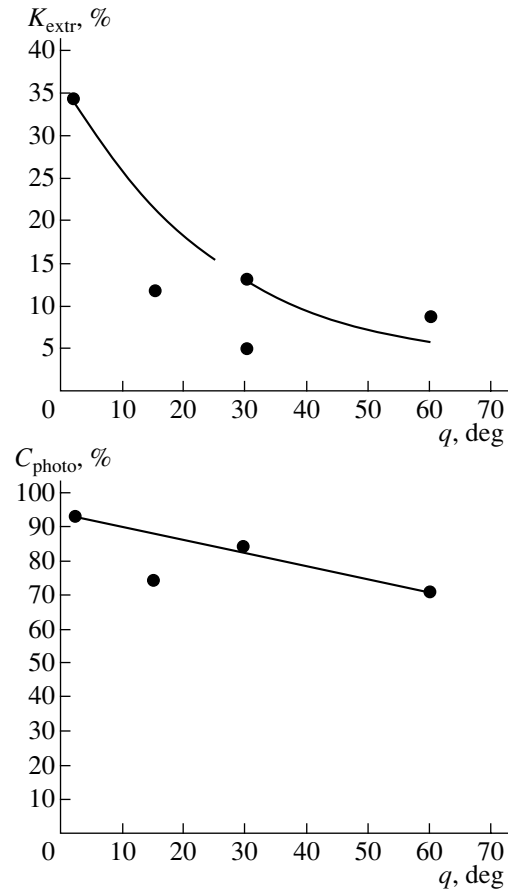


**Fig. 3.** Results of experiments with vapor flows that have different angular divergences along the laser beam.  $q$  is the collimation half-angle. The curves are constructed according to experimental data from [5].

the product with  $^{150}\text{Nd}$  concentration  $C_{150} = 0.7$  appears as

$$P_{0.7} = P_{C_p}(C_p - C_f)/(0.7 - C_f). \quad (22)$$

Substituting  $C_p$  and  $P_{C_p}$  from (20) and (21), respectively, into (22) gives

$$P_{0.7} = FK_{\text{extr}} \frac{C_f}{0.7 - C_f} \frac{C_{\text{photo}} - C_f}{C_{\text{photo}}}, \quad C_p \geq 0.7. \quad (23)$$

The values of feed flow  $F$  in (23) are limited by the inequality  $C_p \geq 0.7$ . Assuming that  $C_p = 0.7$  in formula (20), we can express  $K_{\text{sc}}$  as

$$K_{\text{sc}} \leq K_{\text{extr}} \frac{C_f}{C_{\text{photo}}} \left( \frac{C_{\text{photo}} - 0.7}{0.7 - C_f} \right). \quad (24)$$

Expressing scattering coefficient  $K_{\text{sc}}$  through the feed flow from (18), we impose a restriction on the feed flow that corresponds to the inequality  $C_p \geq 0.7$ :

$$F_{0.7} \leq \frac{K_{\text{sc}}}{\theta} = \frac{1}{\theta} K_{\text{extr}} \frac{C_f}{0.7 - C_f} \left( \frac{C_{\text{photo}} - 0.7}{0.7 - C_f} \right). \quad (25)$$

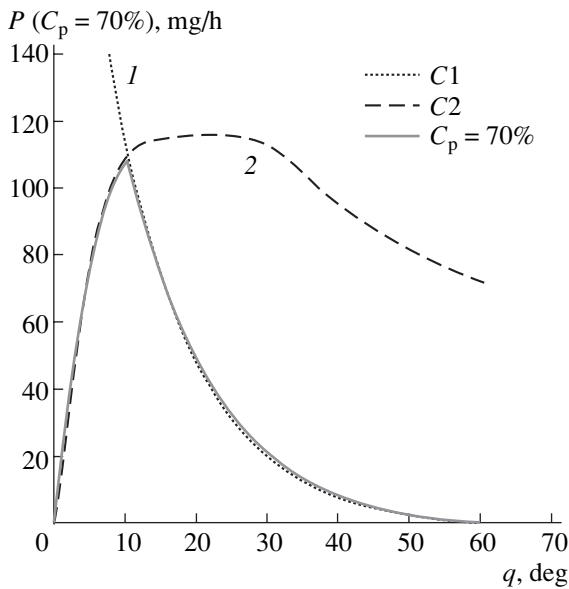


**Fig. 4.** Calculated output  $P$  of the 30-cm-long cell vs. collimation half-angle  $q$  for  $C_p = 70\%$ .

Substituting the value of  $F_{0.7}$  into (23), we arrive at

$$P_{0.7} \leq \frac{1}{\theta} \left( \frac{C_f}{0.7 - C_f} \right)^2 \frac{C_{\text{photo}} - C_f}{C_{\text{photo}}} K_{\text{extr}}^2 \frac{C_{\text{photo}} - 0.7}{C_{\text{photo}}}. \quad (26)$$

Thus, for our experimental cell, the maximal scattering-limited yield of the product with a desired concentration is given by expression (26). For  $C_p = 0.7$ , the yield depends on the coefficient of target isotope extraction by means of photoionization and is inversely proportional to  $\theta$ , which characterizes atomic scattering and the geometric perfection of the separating cell.

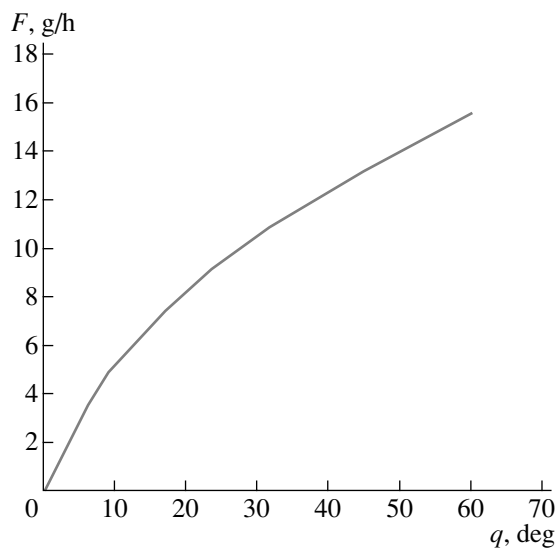


**Fig. 5.** Feed flow  $F$  vs. collimation half-angle  $q$  for a  $30 \times 2 \times 2$ -cm collimator.

The other physical factor influencing the yield of the product with a desired concentration in the separating cell is the Doppler shift of the atom absorption line. It can be shown that there exists an optimal collimation of the vapor flow that provides a maximal yield of the product with a desired enrichment. If, for example, the dependences of  $K_{\text{extr}}$  and  $C_{\text{photo}}$  on collimation angle  $q$  are described by the continuous curves in Fig. 3, then, substituting the functions  $K_{\text{extr}}(q)$  and  $C_{\text{photo}}(q)$  into (26), we get the dependence of the yield on the collimation along the direction of the laser radiation,  $P_{0.7}^{\text{dep}}(q)$  (Fig. 4, curve 1). Expression (26) is a balance between the fluxes of photoions and scattered atoms, which ensures the achievement of desired concentration  $C_{150} = 0.7$ ; hence, this expression reflects a limitation on the yield that is imposed by scattering (the first of the deselecting phenomena). As the collimation angle decreases, the yield calculated by (26) monotonically grows. Expression (26) disregards the fact that feed flow  $F$  that can pass through the collimating grid without collisions decreases with decreasing collimation angle. To take this fact into account, we calculated the dependence  $F(q)$  (Fig. 5). Function  $F(q)$  gives an estimate of the maximal atomic flow that can pass through the given collimator so that atomic collisions have an insignificant effect on the collimation quality (the fraction of noncollimated atoms resulting from collisions in the collimator and evaporated from its surface does not exceed 10%). Substituting known functions  $F(q)$ ,  $K_{\text{extr}}(q)$ , and  $C_{\text{photo}}(q)$  into formula (23), we obtain a collimator-related limitation on the yield,  $P_{0.7}^{\text{col}}(q)$  (Fig. 4, curve 2). Thus, given functions  $F(q)$ ,  $K_{\text{extr}}(q)$ ,  $C_{\text{photo}}(q)$ ,

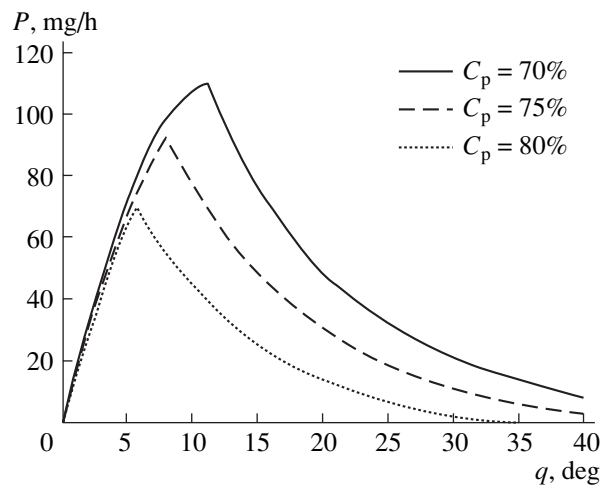


**Fig. 6.** Calculated dependence of output  $P$  of the 30-cm-long cell on collimation half-angle  $q$  for different  $^{150}\text{Nd}$  isotope concentrations in the product.

and  $\theta$ , the output of the setup is

$$P_{0.7} = \min(P_{0.7}^{\text{col}}, P_{0.7}^{\text{dep}}). \quad (27)$$

Function  $P_{0.7}(q)$  specified by (27) is shown in Fig. 4 by the continuous curve. In experiments, the yield of the product with a  $^{150}\text{Nd}$  concentration of 65% was 25 mg/h for a length of the evaporator along the laser beam of 30 cm and a beam collimator half-angle of  $30^\circ$  [5]. This value is in good agreement with the calculation (Fig. 4). The calculation shows that the yield versus collimation angle dependence for  $C_p = 70\%$  has a peak at a collimation half-angle of  $\approx 10^\circ$ . Figure 6 plots the analytical dependences of the yield on the collimation half-angle for different target isotope concentrations in the product. As the concentration grows, the yield drops and the optimal collimation shifts toward smaller angular divergences.

### CONCLUSIONS

Thus, from a series of experiments with vapor flows in which the flows have different angular divergences along the direction of the laser beam with the laser radiation parameters fixed, one can determine an optimal collimation that provides the maximal (for given laser radiation parameters) yield of a product with a desired target isotope concentration. In conducting these experiments with different flow divergences, there is no need for preparing the product with a desired concentration. Moreover, the feed flows may also differ. It is only essential that the laser radiation parameters (wavelength, spectral width, and intensity), as well as the configuration of the irradiation zone and the geometry of the multipass optic, remain unchanged.

Using this technique and measuring the external parameters of the separator (feed flows, the amount of the product and waste, and the product and waste concentrations), we managed to find the internal parameters ( $C_{\text{photo}}$ ,  $K_{\text{extr}}$ , and  $K_{\text{sc}}$ ) and, thereby, separate the influence of laser photoionization, scattering, and Doppler effect on the yield of the product and selectivity of the process. This makes it possible to further refine the setup and reliably predict its separating power.

### ACKNOWLEDGMENTS

The authors thank I.S. Grigoriev for the fruitful discussions.

### REFERENCES

1. A. I. Grigoriev, I. S. Grigoriev, S. K. Kovalevich, *et al.*, in *Proceedings of the 3rd All-Russia Scientific Conference "Physicochemical Processes for Atom and Molecule Selection," Moscow, 1998* (TsNIIatominform, Moscow, 1998), p. 64.
2. I. S. Grigoriev, A. B. D'yachkov, V. P. Labozin, *et al.*, in *Proceedings of the 4th International Scientific Conference "Physicochemical Processes for Atom and Molecule Selection," Moscow, 1999* (TsNIIatominform, Moscow, 1999), p. 93.
3. I. S. Grigoriev, A. B. Diachkov, V. A. Kuznetsov, *et al.*, *Proc. SPIE* **5121**, 411 (2003).
4. I. S. Grigoriev, A. B. Diachkov, S. K. Kovalevich, *et al.*, *Proc. SPIE* **5121**, 406 (2003).
5. A. P. Babichev, I. S. Grigoriev, A. B. D'yachkov, *et al.*, in *Proceedings of the 8th International Scientific Conference "Physicochemical Processes for Atom and Molecule Selection," Moscow, 2003* (TsNIIatominform, Moscow, 2003).
6. V. A. Artem'ev, E. V. Brakhman, S. I. Vasil'ev, *et al.*, *Yad. Fiz.* **59**, 10 (1996).
7. S. R. Elliot and P. Vogel, *Ann. Rev. Nucl. Part. Sci.* **52**, 115 (2002).
8. A. I. Grigoriev, A. P. Dorovskii, V. A. Kochetov, *et al.*, in *Proceedings of the 4th International Scientific Conference "Physicochemical Processes for Atom and Molecule Selection," Moscow, 1999* (TsNIIatominform, Moscow, 2003), p. 91.
9. I. S. Grigoriev, S. M. Mironov, and I. V. Mikhailov, Preprint No. 5860/14, RNTs "Kurchatovskii Institut" (Russian Research Center Kurchatov Institute, 1995).
10. A. V. Eletskaï, Yu. N. Zaitsev, and S. V. Fomichev, Preprint No. 4611/12, IAE (Kurchatov Institute of Atomic Energy, 1988).
11. S. V. Fomichev, *J. Phys. D* **26**, 349 (1992).
12. E. L. Duman and B. M. Smirnov, *Teplofiz. Vys. Temp.* **12**, 502 (1974).

*Translated by V. Isaakyan*